Design and Analysis of Acoustic Metamaterials in Order to Isolate Microelectromechanical Systems Devices from High Frequency Acoustic Noise

by

Brittany Consuegra Griffin

A dissertation submitted to the Graduate Faculty of
Auburn University
in partial fulfillment of the
requirements for the Degree of
Doctor of Philosophy

Auburn, Alabama
August 7th, 2021

[Keywords: Acoustic Metamaterials, High Frequency, Additive Manufacturing, Acoustic Mitigation, Perforated Nozzles, MEMS]

Approved by

Dr. George T. Flowers, Chair, Mechanical Engineering Professor
Dr. Robert Dean, Electrical Engineering Professor
Dr. David Beale, Mechanical Engineering Professor
Dr. Jeffery Suhling, Mechanical Engineering Professor

Abstract

The effects of high frequency acoustic noise can be rather damaging to Microelectromechanical Systems (MEMS) devices. The use of MEMS devices is widespread; therefore, some operational environments for MEMS devices can be harsh with regards to high frequency acoustic noise. This research has developed a compact, configurable, omnidirectional, and passive packaging that isolates MEMS devices from damaging acoustic environments by utilizing acoustic metamaterials (AMM). An AMM is a material that affects sound waves and has properties not found in nature. Commonly, the properties are a function of the material's geometric structure instead of material composition.

In order to ensure acoustic mitigation across a broad spectrum of sensors and applications, sensor packaging was the focus of this research. The packaging developed during this research acoustically isolates the sensor using a combination of perforated nozzles in conjunction with interconnected cavities. The design is modular therefore the packaging can be tailored to fit any size required by the application. The design and experimental testing process was an iterative approach that was broken into three phases.

The first phase focused on a series of nozzles with various features and of various sizes in a single input single output (SISO) configuration. Multiple designs were manufactured and experimentally tested. The testing concluded that a four-stage system of nozzles with radial and axial perforations and a constricted opening at the output plane of the system was the optimal configuration. This configuration is referred to as the Base Feature (BF) AMM. The nozzles in the early SISO configurations were two inches in length, but testing proved the system was

operational when the nozzles were one-quarter inches in length meaning the overall thickness of the BF AMM configuration is one inch. From the control configuration to the BF AMM configuration, the average transmission loss (TL_{avg}) across the acoustic spectrum went from 4.8 dB to 33.7 dB. Additionally, the BF performed well in the 2 kHz to 20 kHz range, with the TL_{avg} over 35 dB. These experimental results for the BF AMM formed the basis for the second phase of testing.

The next phase of testing focused on multiple input multiple output (MIMO) testing. A series of interconnected cavities surrounding the BF AMM were added to the design. The series of nozzles and accompanying interconnected cavities, called a cell, were repeated in parallel to form a panel. The panels consisted of 37 cells and were 7.5 inches in diameter. Multiple configurations of interconnected cavities of varying sizes were tested. The optimal configuration consisted of 12 interconnected cavities surrounding the BF AMM. This configuration is referred to as the Small Cavity AMM configuration. From the control panel to the Small Cavity AMM panel, the TL_{avg} increased from 16.4 dB to 33.8 dB across the acoustic spectrum. The Small Cavity AMM performed exceptionally in the 2 kHz to 20 kHz range, with the TL_{avg} equaling approximately 40 dB. These results formed the basis for the final phase of testing.

The final stage of testing focused on an AMM Sphere. The Small Cavity AMM cell was modified to have curvature for use in the AMM Sphere. The AMM Sphere testing was performed at various distances as well as between multiple sound sources. The AMM Sphere test results were comparable in all the experimental test configurations with a TL_{avg} at approximately 28 dB. The AMM Sphere performed exceptionally well in the 2 kHz to 20 kHz. The system performance when subjected to multiple sound sources was not affected.

Acoustic simulations were performed with MSC ACTRAN. The theory and methodology of the acoustic simulations was thoroughly considered to ensure that any assumptions and the overall model development were accurate. Comparison of the acoustic simulations with the experimental results showed correlation and allowed for validation of the acoustic models. The experimental results were encapsulated within 1 standard deviation of the acoustic simulation mean results. The acoustic models demonstrated the capability to predict performance in operational environments.

Several supplemental features are to be noted. The system is air permeable, therefore, adverse conditions such as stored heat, or the blockage of airflow are not introduced to the system. All of the configurations were tested in the Converging Nozzle and Diverging Nozzle configurations with similar results. This is indicative of the structure having the ability to keep sound in as well as out.

This research has contributed to the field of AMM in several ways. The system's capability to mitigate noise in the upper end of the acoustic spectrum is a significant contribution. Currently, AMM literature above 10 kHz is very rare. Within the current literature, AMM research above 10 kHz tends to be configured for a specific system and operates in a very narrow bandwidth or is theoretical in nature. The system's ability to successfully operate from 2 kHz to 20 kHz is innovative. Additionally, the system operates omnidirectionally and with multiple sound sources. Current literature focuses on systems that operate in laboratory settings where the location of the single sound source is predetermined. Finally, the system can be configured to work with any MEMS device as well as within any application size.

Acknowledgements

I would like to thank the U.S. Army Combat Capabilities and Development Command Aviation and Missile Center for the financial support and resources I received during my research. I am particularly thankful to the Additive Manufacturing Center for Excellence for the significant amount of assistance they provided to me during the course of my research. Specifically, I would like to acknowledge Robert Helem and Dr. Jim Kirsch for all of the guidance and opportunities that they have given me throughout my career.

I would to thank the Auburn University College of Engineering and especially the Mechanical Engineering Department. I wish to thank my committee for their continued support and guidance. I wish to extend my deepest gratitude to Dr. George Flowers. For almost 20 years, he has provided me with exceptional guidance and unwavering support both personally and professionally. As my mentor, he has helped me in more ways than he could ever know. His character has shown me how to be a good engineer as well as a good person.

Throughout my career in both academia and industry, I have received a tremendous amount of love, support, and assistance from my friends, in-laws, brother, and husband. I know that I am genuinely lucky to have them in my life. Along with support and encouragement, they have provided me with all of the things I knew I needed as well as things I did not realize I needed. Thank you all for everything from the much-needed distractions to the in-depth technical discussions. I cannot begin to express my gratitude to my husband, Massey Griffin. He has given me unconditional love, support, and encouragement that I will forever cherish. Sweet Husband, thank you for all that you've done for me. I love you!

Table of Contents

List of Figures

List of Tables

Nomenclature

ACTRAN	Acoustic Transmission
AFC	Army Futures Command
AMM	Acoustic Metamaterial
AP	Axial Perforations
ASA	Acrylonitrile Styrene Acrylate
AvMC	Aviation and Missile Center
bdf	bulk data input file
BF	Base Feature
c	Speed of Sound
C_1	Integration Constant One
C_2	Integration Constant Two
CAD	Computer-Aided Design
CN	Converging Nozzle
COOP	Constricted Opening at the Output Plane
DAQ	Data Acquisition
DBLNSF	Distance-Based Linearized Navier-Stokes-Fourier
DEVCOM	Combat Capabilities Development Command
DN	Diverging Nozzle
f	Frequency
FDM	Fused Filament Fabrication
FFT	Fast Fourier Transform
GWN	Gaussian White Noise

IFC	Infinite Fluid Component
k	Wave Number
L	Length
$\dot{m}$	Mass Flow Rate
MEMS	Microelectromechanical Systems
MIMO	Multiple Input Multiple Output
MSC	MacNeal-Schwendler Corporation
MUMPS	MultiFrontal Massively Parallel Solver
P	Pressure
P_0	Acoustic Reference Pressure
PCB	PicoCoulomB
PID	Property Identification
PIF	Prototype Integration Facility
PPE	Personal Protective Equipment
PSD	Power Spectral Density
R	Radius
RAP	Radial and Axial Perforations
RMS	Root Mean Square
RP	Radial Perforations
S	Cross Sectional Area
SCN	Series of Converging Nozzles
SDN	Series of Diverging Nozzles
SISO	Single Input Single Output
SP	Straight Pipe

SPL	Sound Pressure Level
t	Time
TEDS	Transducer Electronic Data Sheet
Tet	tetrahedron
TL	Transmission Loss
TL_{avg}	Average Transmission Loss
TM	Transfer Matrix
TM_{11}	Transfer Matrix Dimension (1,1)
TM_{12}	Transfer Matrix Dimension (1,2)
TM_{21}	Transfer Matrix Dimension (2,1)
TM_{22}	Transfer Matrix Dimension (2,2)
Tria	triangle
u	Velocity
u'	Perturbation Velocity
u_0	Average Mean Velocity
V	Volume
x	X-Direction Position
x_t	Parasolid
Z	Acoustic Impedance
ρ	Perturbation Density
ρ_0	Atmospheric Density
ϕ	Angle of Nozzle Walls/Grazing Angle
ω	Angular Frequency

Chapter 1: Introduction

"Like diseases, noise is never eliminated, just prevented, cured, or endured, depending on its nature, seriousness, and the cost/difficulty of treating."

-Jacob Fraden [1]

Throughout academia and industry, high frequency acoustic noise is an ongoing concern. In particular, the effects of high frequency acoustic noise can be quite damaging to Microelectromechanical Systems (MEMS) devices. Due to their small size and low cost, MEMS devices are utilized in almost all new technology. To list all of the applications which utilize MEMS device would be lengthy, but a few examples include mobile phones, vehicles, aircraft, and robotics. Since the use of MEMS devices is becoming more and more widespread, the operational environment of these devices is becoming increasingly broad and often as a result, harsher. In particular, a harsh operational environment with regards to high frequency acoustic noise has become increasingly common.

This research has developed a compact, omnidirectional, and passive packaging that isolates MEMS devices from damaging acoustic environments by utilizing acoustic metamaterials (AMM). The goal was be to design the packaging in order to create a "filter" so that the damaging acoustic environment will not penetrate into the environment surrounding the sensor. The invention can be used on any device subjected to harsh acoustic noise. The applications can range from existing hardware to future military systems as well as numerous commercial

applications where a reduction in acoustic noise is desired. Since the design is based on a modular cell, the packaging can be tailored to fit any size required by the application.

All phases of the concept development are discussed in detail in this dissertation. The design is methodically built up from simple well-understood concepts in a way that considers each layer of complexity. This allows the final, complex design to be easily understood by the reader.

In order to maintain focus on the overall goals of the research, several requirements were established for this research. The requirements for the final design are as follows:

- Operational in the 10 kHz - 20 kHz acoustic bandwidth
- Compact with a minimal footprint
- Configurable
- Passive
- Omnidirectional

This dissertation is organized in such a way that each new phase of research builds on the previous phase. In chapter 1, the research starts with a literature review of the effects of high frequency acoustic noise on MEMS devices and AMM. This chapter then discusses the significance of this research and fundamental assumptions used throughout the research. Acoustic principles and equations are then discussed.

Chapter 2 utilizes the information from chapter 1 to discuss the design of the prototypes. The prototypes are grouped into 3 main categories. The first category discusses single input single output (SISO) systems, the second category discusses multiple input multiple output (MIMO) systems, and the third category discusses the AMM Spherical system. The SISO

prototypes consist of different configurations of nozzles. The nozzle configurations include a single nozzle, a series of nozzles, Radial and Axial Perforations (RAP), and a Constricted Opening at the Output Plane (COOP). These prototypes were utilized to determine the fundamental design performance. The SISO systems were then enclosed, downsized, and enhanced. The SISO systems were replicated into a multiple input multiple output (MIMO) system. The MIMO prototypes then had AMM in the form of interconnected cavities added into the design to further enhance performance. The AMM consists of either a series of interconnected cavities of varying sizes or additive manufacturing infill material. The interconnected cavity AMM design includes a series of connected nozzles and cavities in order to dissipate acoustic energy. The interconnected cavities allow sound waves to travel throughout the structure while the geometry provides significant energy dissipation. The Infill AMM works in the same manner. The top performing MIMO prototype was then modified for incorporation into an AMM Sphere, which allowed for the verification of all the design requirements.

Chapter 3 discusses the experimental testing of the prototypes. The test inputs, equipment, methodology, and results are discussed for the SISO, MIMO, and AMM Sphere prototypes. Test results are compared so that the top performing design for each category of prototype can be identified. The prototypes are tested across the entire acoustic bandwidth. The results are presented so that each prototype can be evaluated in four sections of the acoustic bandwidth as well as the entire spectrum. The bandwidths evaluated are 20 Hz to 5 kHz, 5 kHz to 10 kHz, 10 kHz to 15 kHz, 15 kHz to 20 kHz, and 20 Hz to 20 kHz.

Chapter 4 describes the acoustic simulation of the prototypes. The acoustic software MacNeal-Schwendler Corporation (MSC) ACoustic TRANsmission (ACTRAN) was utilized for the

analysis. The theory and methodology of MSC ACTRAN is discussed to ensure that the assumptions and model development were accurate. The models and test results for the SISO and MIMO are discussed in detail.

Chapter 5 describes a comparison of the results from the experimental testing discussed in chapter 3 with the results from the acoustic analysis discussed in chapter 4. The results are compared in the 5 bandwidths of the acoustic spectrum listed in the chapter 3 summary above.

Chapter 6 discusses the overall conclusions of the dissertation and a summary of the results. In addition, recommendations for future work are outlined.

1.1 Literature Review

1.1.1 Acoustic Noise Effects on MEMS sensors

"Machines built by human beings will function correctly if we provide them with a very specific environment. But, if that environment is changed, they won't function at all."

-Ralph Merkle [2]

A vulnerability of MEMS devices is exposure to high frequency acoustic noise. Due to the small size of a MEMS proof mass, the natural frequency of some MEMS devices can be within the 10 kHz to 20 kHz bandwidth. [3] This bandwidth is becoming increasingly common in the operational environments of these devices. When a MEMS's proof mass is externally excited at its natural frequency, the output of the MEMS device is often distorted and inaccurate.

Using the packaging of MEMS devices in order to isolate the device from the environment is common in the MEMS field. Overall requirements of the packaging are often broad, such as to protect the sensor from external influences and environmental effects. Common materials such as metal, plastic, and ceramics fail to satisfy these requirements with regards to acoustic noise. Furthermore, the mechanical interface often interferes with the sensor. For example, the mounting of the packaging may inherently couple with the measurement of the sensor. This results in most environmentally isolating packaging being very sensor specific. Thus, the overall performance of the sensor is often directly dependent on the overall packaging of the sensor. [4]

In addition to packaging, filtering techniques are often employed. The many techniques of filtering rely on the measurement and the damaging noise occupying different frequency bandwidths. If the bandwidths indeed overlap, filtering is not an option. This issue is further compounded if the interference noise is inherently random and broadband in nature. In this regard, broadband acoustic noise is often unfilterable. [5]

Research done by Khazzaaleh et al. describes a MEMS gyroscope subjected to acoustic noise near the device's natural frequency. While the applied acoustic environment was barely in an audible range, the added energy to the device caused the stationary gyroscope to sense rotation upwards of 6˚/sec. Furthermore, attempts to isolate the device from such environments proved unsuccessful. [6]

In order to question the integrity of MEMS sensors, 2 different types of acoustic environments were applied to a MEMS accelerometer by Trippel et al. Both environments resulted in the exploitation of the sensor's inherent vulnerabilities. The research team was then

able to manipulate the acoustic environment to induce controlled outputs, effectively hi-jacking the output of the MEMS devices. [7] Similar work done by Son et al., showed that acoustic noise could be targeted at drones. The targeted noise was able to cause MEMS gyroscopes to fail, resulting in the drones crashing. [8]

1.1.2 Acoustic Metamaterials

"Technology is always changing. There was a time where oil painting was a new technology. That changed painting."

-Joe Bradley [9]

Attempts to mitigate acoustic noise can be seen throughout history. In ancient Rome, Julius Caesar made a decree announcing that "no on shall drive a wagon along the streets of Rome or along those streets in the suburbs where there is continuous housing after sunrise or before the tenth hour of the night." [10] Traditional acoustic mitigation techniques utilize extremely dense and bulky materials. As electronic technology decreases in size and weight, the desire for compact acoustic mitigation increases.

This need for new methods of acoustic mitigation has increased growth in the field of AMM. AMM is a fast growing, fascinating field that at times seems to be governed by Clarke's Third Law stating, "Any sufficiently advanced technology is indistinguishable from magic." [8] In reality, AMM are artificial materials engineered to have properties that may not be found in nature. AMM usually gain their properties from the system's geometric structure rather than the system's material composition. [11] In essence, an AMM is simply designed to manipulate sound waves. Consequently, the structure of an AMM is subwavelength in nature. For example,

at 20 kHz, the acoustic wavelength is 0.67“. The AMM designs presented in this research have features as small as 0.04”. The AMM structure is considerably smaller than the 20 kHz wavelength.

The concept of metamaterials was conceived in the 1960s by Victor Veselgao [12], but the field of AMM did not take off until the 1990s. By utilizing specially designed materials with a negative bulk modulus, negative density, or negative refractive index, specialty fields of AMM such as but not limited to sonic crystals, split-ring resonators, acoustic cloaking, acoustic refractive index manipulation, and acoustic lenses have emerged. [13] These technologies are indeed fascinating, but this literature review will focus purely on passive AMM structures with the goal of mitigating acoustic transmission that operate in ambient air environments.

The types of AMM listed in the previous paragraph are effective, but often difficult to manufacture. In order to make structures that are more manufacturable, the use of additive manufacturing technology is create AMM structures has become increasingly prevalent. Commonly, layers of solid structure interlaced with surface gaps, volumetric gaps, or scattering structures are utilized. Examples of scattering structures include cylinders, columns, or similar geometrical structures of various sizes and spacing. Scattering structures may consist of arrays of thin plates with perforations. Several examples of scattering structures are shown in Figure 1-1. The scattering structures size and locations are varied in order to tune the AMM’s effective frequency bandwidth. The scattering structures interact with the acoustic waves resulting in behavior similar to waves traveling through a propagation material with different properties than the environmental medium. [14]

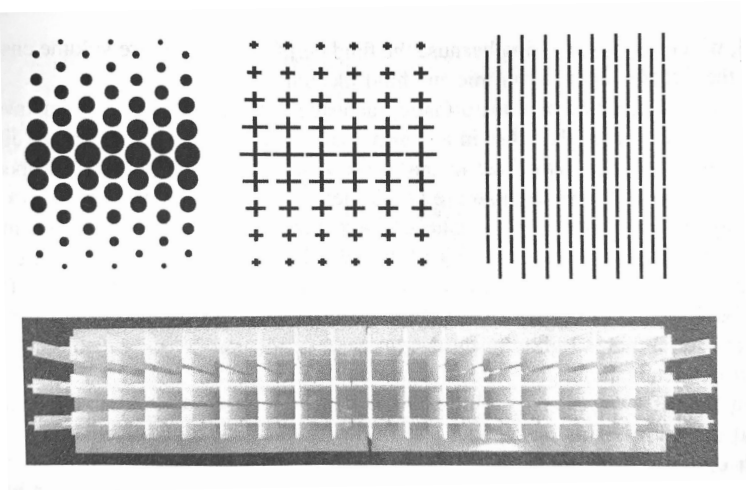

Figure 1-1 - Examples of AMM Scattering Structures [14]

Scattering structures cause the incident wave to scatter into secondary waves. The scattered waves consist of waves in the incident and reflected directions. The waves in the reflected direction may interact with the waves in the incident direction, causing a loss in momentum for the overall sound wave. [15]

Structures that cause acoustic wave scattering by utilizing tortuosity in the form of interconnected cavities or maze-like structures have shown promise in reducing acoustic transmission. Work done by Zhang et al. demonstrates the ability to mitigate sound below 8.2 kHz utilizing a structure of interconnected tubes with dimensions in the range of millimeters. [16] Tang et al. utilize a structure consisting of perforated honeycomb corrugation hybrid core. The structure provided mechanical stiffness and strength as well as sound absorption below 2 kHz. The honeycomb corrugation hybrid core structure schematic is shown in Figure 1-2. [17]

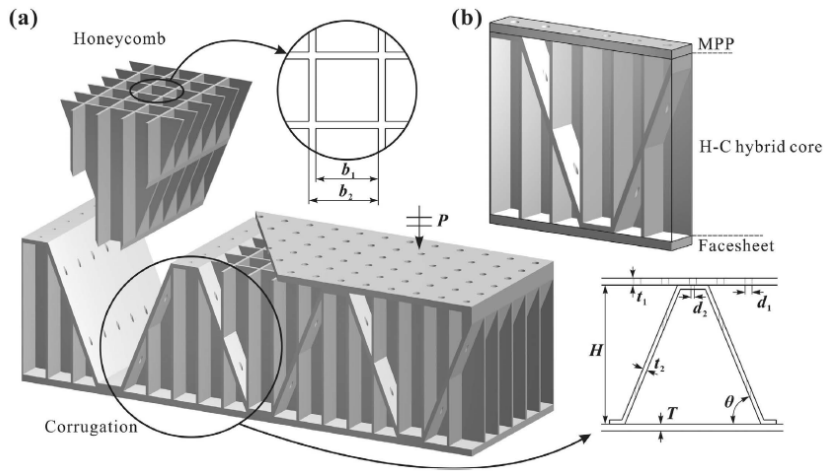

Figure 1-2 - Structure Schematic for a Perforated Honeycomb Corrugation Hybrid Core [17]

Helmholtz resonators are common in the field of AMM. Arranged in a chain along a channel, the configuration of the resonators produces a negative effective density. However, the resonators are limited to specific frequencies based on the structure and resonator geometry. Casarini et al. created a small scale AMM capable of creating band gaps of up to 6.5 kHz. Research showed that additional Helmholtz resonators deepened the band gap. [18]

Excess heat may damage electronics, so a related issue is air permeability for heat dissipation. Efforts to reduce acoustic transmission while maintaining maximum air permeability have improved. Utilizing a multi-material bilayer structure located transversely to the direction of wave propagation, sound mitigation can be realized. The structure consists of the bilayer material configured in multiple channels of AMM shaped like coils. At 450 Hz, the structure transmission coefficient is 0.06. Tuning of the system by utilizing varying the system's overall refractive indices is possible. [19]

Analysis using models comprised of interchangeable springs connecting multiple mass in mass structures were shown to be promising in creating band gaps. The masses configured as a

nesting are connected by springs. The virtual spring-mass in mass system is configured to have a negative effective mass. The acoustic band gaps created by the structure are dependent on the outermost masses within the system. [20] Acoustic band gaps are sections of the acoustic bandwidth where the transmitted sound energy is essentially zero.

Utilizing a series of concentric ring oscillators, Chen et al. were able to analytically prevent acoustic wave transmission by inducing a negative mass density. The multi-material oscillators act as acoustic scatterers and create acoustic band gaps in the 1 kHz to 3 kHz range. The models generated by the research showed that additional oscillators were able to create additional band gaps in the output data. [21]

1.2 Research Significance

The research discussed in section 1.1 does not represent the entire body of knowledge with regards to passive AMM which focus on the mitigation of acoustic transmission. However, the examples discussed are indicative of the current state of the technology. AMM structures can create multiple bandgaps. However, the bandgaps are not particularly wide. The ability to tune an AMM system in order to create bandgaps at certain frequencies is comparable to the specific packaging required for MEMS devices discussed in section 1.1.1. Additionally, MEMS devices can have a wide range of natural frequencies. Therefore, narrow bandgaps may not be able to address a wide range of natural frequencies.

AMM current literature does not address the upper end of the acoustic spectrum. The examples discussed in section 1.1 have a maximum operating range of 8.2 kHz. Considering most MEMS devices have natural frequencies above 10 kHz, there are many opportunities for

improvement in the 10 kHz to 20 kHz bandwidth. The research discussed in this dissertation had the original goal of being operational in the 10 kHz to 20 kHz bandwidth. However, experimental testing has shown significant acoustic mitigation in the 2 kHz to 20 kHz bandwidth. Instead of being marginally operational in a narrow bandwidth, the AMM developed in this research provides significant acoustic mitigation in three-quarters of the acoustic bandwidth.

Presently, AMM technology operates in laboratory conditions, while some technology only exists in theory. The specific laboratory conditions dictate the location of the sound source, the orientation of the AMM, and the size of the AMM working space. There is no indication that such technologies will not eventually operate in environments outside of laboratory conditions, but currently the opportunities for advancement are abundant. The research described in this dissertation considers structures that employ repeating geometry that can be easily configured in series and in parallel. This configurability allows the technology to be configurable to fit any application. The configurability allows devices to be encapsulated by the AMM in order to become omnidirectional. This omnidirectionally allows the technology to be utilized in uncontrolled environments. Experimental testing consisting of multiple sound sources in multiple directions further demonstrated the ability of the design to work in uncontrolled environments. Details of the experimental test results are presented and discussed in chapter 3.

1.3 Acoustic Principles and Equations

1.3.1 Assumptions

Several assumptions are made throughout the research as discussed below. The acoustic waves are operating in an environment with no airflow. The velocity of the propagating medium, u, is defined by adding the average mean velocity, u_0, to the

perturbation velocity, v. For this research, $u_0 = 0$. The fluid is air at an ambient temperature. The following values were used for air at ambient conditions: [22] [23]

Parameter	Symbol	Value
Atmospheric Density	ρ_0	1.225 kg/m^3
Speed of Sound	c	343 m/s
Acoustic Reference Pressure	P_0	20 µPa
Damping Coefficient	-	0.01

Table 1-1 - Properties of Air at an Ambient Temperature

The analytical equations derived in sections 1.3.3 and 1.3.4 disregard higher order terms that exist in the derivation. Higher order terms are defined as second order or higher derivatives. Sections 1.3.3 and 1.3.4 do not include damping or viscosity. Consequently, no boundary layers are calculated in these sections of this dissertation.

1.3.2 Acoustic Principles

In order to define a particular acoustic system, the wave equation for that system must be described. The general wave equation is derived by combining common acoustic relationships, the conservation of mass equation, conservation of momentum equation, and the isentropic relationship of an ideal gas equation. Variables used throughout this dissertation are defined in Table 1-2.

Variable	Symbol
Acoustic Impedance	Z
Angular Frequency	w
Cross-Sectional Area	S
Density	ρ
Frequency	f
Mass Flow Rate	$\dot{m}$
Position	x
Pressure	P
Radius	R
Sound Pressure Level	SPL
Speed of Sound	c
Time	t
Transmission Coefficient	τ
Transmission Loss	TL
Velocity	u
Volume	V
Wave number	k

Table 1-2 - Acoustic Variables

Common acoustic equations used in this dissertation are listed in Table 1-3. [22] [24] [25] [26]

Common Equations	
$P(x) = Ae^{-ikx} + Be^{ikx}$	1.1
$P(x,t) = P(x)e^{i\omega t}$	1.2
$u(x) = \frac{P(x)}{\rho c} = \frac{Ae^{-ikx} - Be^{ikx}}{\rho c}$	1.3
$\dot{m} = \rho u S$	1.4
$Z = \rho c$	1.5
$\tau = \frac{P_1^2}{P_2^2}$	1.6
$TL = -10\, log_{10}\, \tau$	1.7
$k = \frac{w}{c}$	1.8
$w = 2\pi f$	1.9
$\lambda = \frac{c}{f}$	1.10
$SPL = 20\, log_{10} \frac{P_{RMS}}{P_0} = 20\, log_{10} \frac{P}{\sqrt{2}P_0}$	1.11

Table 1-3 - Common Acoustic Equations

In order to use the variables listed in Table 1-2, considerations must be made with regards to pressure, velocity, and density. Utilizing perturbation theory allows the sound waves to be characterized properly. These variables are defined in Table 1-4. [27]

Variable	Perturbation Equation
Pressure	$P_{Total} = P_0 + P$
Velocity	$u_{Total} = u_0 + u$
Density	$\rho_{Total} = \rho_0 + \rho$

Table 1-4 - Perturbation Equations

The Conservation of Mass/Continuity Equation is defined as: [28]

$$\frac{d}{dt}(\rho V) = \dot{m_{in}} - \dot{m_{out}} \quad 1.12$$

The Conservation of Momentum Equation is defined as: [28]

$$\frac{\partial(\rho u)}{\partial t} + \nabla \cdot (\rho u u) = -\nabla P \quad 1.13$$

The Isentropic Relationship of an Ideal Gas is: [28]

$$dP = c^2 d\rho \quad 1.14$$

The general form of the Wave Equation is: [27]

$$\frac{\delta^2 P}{\delta t^2} - c^2 \frac{\delta^2 P}{\delta x^2} = 0 \quad 1.15$$

Equations 1.1 thru *1.14* will allow for the derivation of customizable linear wave equations as well as the derivation of variables at any location within a control volume.

Utilizing a transfer matrix (TM), is a common way to numerically simulate a system consisting of multiple features and components, such as mufflers. The AMM discussed in this dissertation consists of many components. Therefore, the use of TMs was investigated. System TM methodology begins by determining a TM for each component. Once the TM for each

component is determined, the overall system TM can be determined. The component TM determines the relationship between the input pressure and velocity with the output transfer velocity. A basic schematic diagram of this approach is shown in Figure 1-3. [29]

Figure 1-3 - Schematic for a Nondescript Acoustic Feature

The relationships between the input and output pressure and velocities can be rearranged into the following form:

$$P_n = TM_{11}P_{n+1} + TM_{12}u_{n+1} \tag{1.16}$$

and

$$u_n = TM_{21}P_{n+1} + TM_{22}u_{n+1} \tag{1.17}$$

Equations 1.16 and 1.17 can be combined into:

$$\begin{Bmatrix} P_n \\ u_n \end{Bmatrix} = \begin{bmatrix} TM_{11} & TM_{12} \\ TM_{21} & TM_{22} \end{bmatrix} \begin{Bmatrix} P_{n+1} \\ u_{n+1} \end{Bmatrix} \tag{1.18}$$

The TM is defined as:

$$[TM] = \begin{bmatrix} TM_{11} & TM_{12} \\ TM_{21} & TM_{22} \end{bmatrix} \tag{1.19}$$

For systems with multiple components, the indivdual TM must be combined to get a system TM. For a system with 2 componets, the first component has a TM of the form:

$$\begin{Bmatrix} P_n \\ u_n \end{Bmatrix} = \begin{bmatrix} TM_{11} & TM_{12} \\ TM_{21} & TM_{22} \end{bmatrix} \begin{Bmatrix} P_{n+1} \\ u_{n+1} \end{Bmatrix} \tag{1.20}$$

which can be rewritten as:

$$\begin{Bmatrix} P_n \\ u_n \end{Bmatrix} = [T_n] \begin{Bmatrix} P_{n+1} \\ u_{n+1} \end{Bmatrix} \quad 1.21$$

The second component has a TM of the form:

$$\begin{Bmatrix} P_{n+1} \\ u_{n+1} \end{Bmatrix} = \begin{bmatrix} TM_{11} & TM_{12} \\ TM_{21} & TM_{22} \end{bmatrix} \begin{Bmatrix} P_{n+2} \\ u_{n+2} \end{Bmatrix} \quad 1.22$$

Which can be rewritten as:

$$\begin{Bmatrix} P_{n+1} \\ u_{n+1} \end{Bmatrix} = [T_{n+1}] \begin{Bmatrix} P_{n+2} \\ u_{n+2} \end{Bmatrix} \quad 1.23$$

The goal of this development is to define a relationship between P_n and u_n with P_{n+2} and u_{n+2}. Substituting equation 1.23 into equation 1.21 yields:

$$\begin{Bmatrix} P_n \\ u_n \end{Bmatrix} = [T_n][T_{n+1}] \begin{Bmatrix} P_{n+2} \\ u_{n+2} \end{Bmatrix} \quad 1.24$$

where the overall system TM, T, is defined as:

$$[T] = [T_n][T_{n+1}] \quad 1.25$$

1.3.3 Straight Pipe Transfer Matrix Derivation

In order to determine the TM for a Straight Pipe (SP), schematics for the system were created. Figure 1-4 shows the schematic for the SP with the input and output boundary conditions as well as the overall length of the nozzle (L) and radius (R). Boundary conditions include Pressure (P), velocity (u), and position (x).

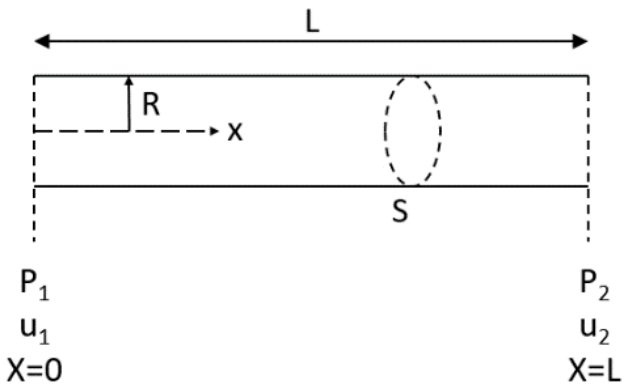

Figure 1-4 - Straight Pipe Schematic

For the purposes of this research, a SP is used as a basic system for comparison of the proposed AMM designs. The cross-sectional area, s, is equal at the input and the output. Therefore:

$$s = s_1 = s_2 = \pi R^2 \tag{1.26}$$

The general equation for the pressure, P(x), of a sound wave as a function of x is:

$$P(x) = Ae^{-ikx} + Be^{ikx} \tag{1.27}$$

At the input of the system, the pressure equation becomes:

$$P(O) = P_1 = A + B \tag{1.28}$$

At the output of the system, the pressure equation becomes:

$$P(L) = P_2 = Ae^{-ikL} + Be^{ikL} \tag{1.29}$$

The general equation for the velocity, u(x), of a sound wave as a function of x is:

$$u(x) = \frac{P(x)}{\rho c} = \frac{Ae^{-ikx} - Be^{ikx}}{\rho c} \tag{1.30}$$

At the input of the system, the velocity equation becomes:

$$u(0) = u_1 = \frac{A - B}{\rho c} \tag{1.31}$$

At the output of the system, the velocity equation becomes:

$$u(L) = u_2 = \frac{Ae^{-ikL} - Be^{ikL}}{\rho c} \tag{1.32}$$

Solving for the constants A and B yields:

$$A = \frac{1}{2}P_1 + \frac{1}{2}\rho c u_1 \tag{1.33}$$

$$B = \frac{1}{2}P_1 - \frac{1}{2}Pcu_1 \tag{1.34}$$

Substituting equation 1.33 and equation 1.34 into equation 1.29 yields:

$$P_2 = \left(\frac{1}{2}P_1 + \frac{1}{2}\rho c u_1\right)e^{-ikL} + \left(\frac{1}{2}P_1 - \frac{1}{2}\rho c u_1\right)e^{ikL} \tag{1.35}$$

Simplification of equation 1.35 yields:

$$P_1 = \frac{P_2 + \rho c u_1 i \sin kL}{\cos kL} \tag{1.36}$$

Substituting equation 1.33 and equation 1.34 into equation 1.32 yields:

$$u_2 \rho c = \left(\frac{1}{2}P_1 + \frac{1}{2}\rho c u_1\right)e^{-1kL} - \left(\frac{1}{2}P_1 - \frac{1}{2}\rho c u_1\right)e^{ikL} \tag{1.37}$$

Simplification of equation 1.37 yields:

$$u_1 = \left(\frac{i \sin kL}{\rho c}\right)P_2 + (\cos kL)u_2 \tag{1.38}$$

Equation 1.38 is of the form:

$$u_1 = TM_{21}P_2 + TM_{22}u_2 \tag{1.39}$$

Substituting equation 1.38 into equation 1.36 yields:

$$P_1 = \frac{P_2 + \rho c i \sin kL\left[\frac{i \sin kL}{\rho c}P_2 + \cos kL u_2\right]}{\cos kL} \tag{1.40}$$

Simplification of equation 1.40 yields:

$$P_1 = P_2 \cos kL + (\rho c i \sin kL)u_2 \tag{1.41}$$

Equation 1.41 is now of the form:

$$P_1 = TM_{11}P_2 + TM_{12}u_2 \tag{1.42}$$

Equations 1.38 and 1.41 can be rearranged into the TM:

$$\begin{Bmatrix} P_1 \\ u_1 \end{Bmatrix} = \begin{bmatrix} \cos kL & \rho c i \sin kL \\ \dfrac{i \sin kL}{\rho c} & \cos kL \end{bmatrix} \begin{Bmatrix} P_2 \\ u_2 \end{Bmatrix} \tag{1.43}$$

A MATLAB code listed in Appendix A-1 verified equation 1.43 by deriving the TM independently. The MATLAB code shown in Appendix A-2 was used to generate Figure 1-5. The MATLAB code shown in Appendix A-2 calculated the TL by utilizing equations 1.6 and 1.7. Recorded input noise from experimental testing was utilized for the input into the TM. The generation of the experimental input and output noise is discussed in detail in chapter 3.

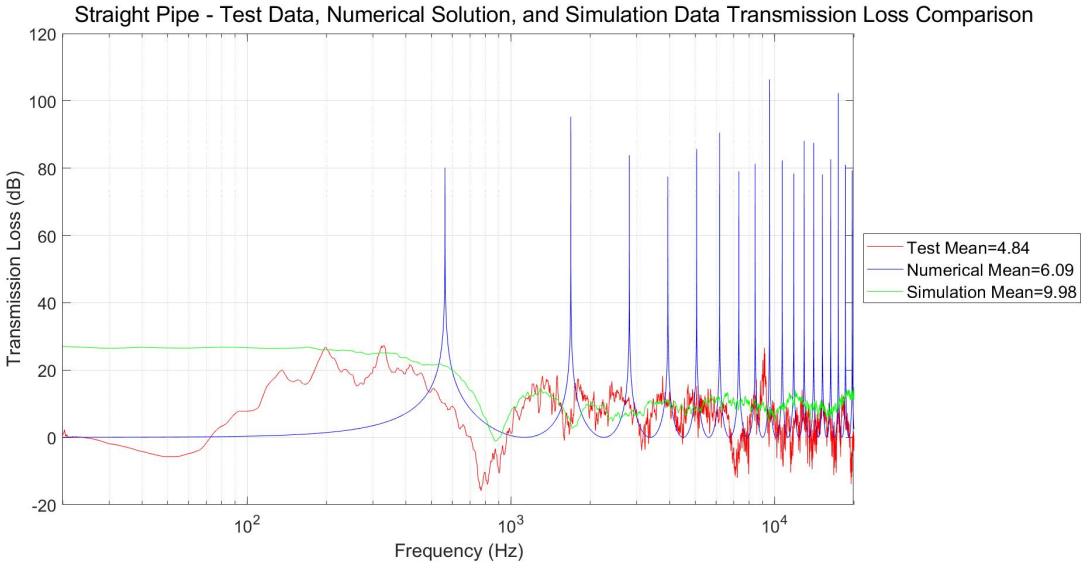

Figure 1-5 - Straight Pipe - Numerical, Simulation, and Test Transmission Loss Comparison

Figure 1-5 shows the analytical results correlated with the experimental TL data below 700 Hz. The plot compares the TL calculated using experimental test results shown in red, acoustic simulation results shown in green, and numerical results shown in blue. Above 700 Hz,

the analytical solution breaks down and cannot be used for any meaningful assessment. The acoustic software simulation begins to correlate reasonably well with the experimental test data above 1 kHz, but does not appear to produce meaningful results below 1 kHz.

1.3.4 Nozzle Transfer Matrix Derivation

In order to determine the TM for a simple nozzle, schematic diagrams for the system were developed. Figure 1-6 shows the schematic for the nozzle with the input and output boundary conditions as well as the overall length of the nozzle (L). Boundary conditions include Pressure (P), velocity (u), cross-sectional area (S), and position (x). Figure 1-7 further defines the nozzle geometry in terms of radius (R), overall length (L), position (x), and the angle of the nozzle walls (ϕ).

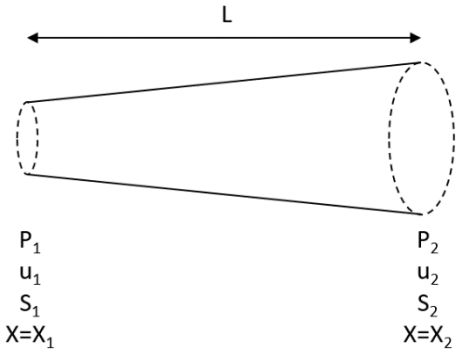

Figure 1-6 - Nozzle Schematic

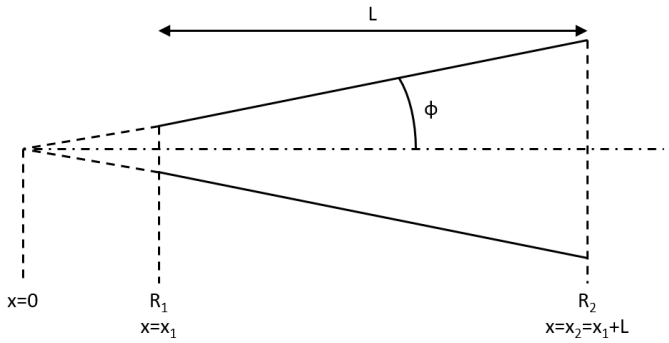

Figure 1-7 - Nozzle Geometry Schematic

Figure 1-8 shows an incremental control volume for the nozzle in terms of mass flow rate into the volume ($\dot{m}_i$), mass flow rate out of the volume ($\dot{m}_o$), change in radius (dr), and change in the x-direction (dx).

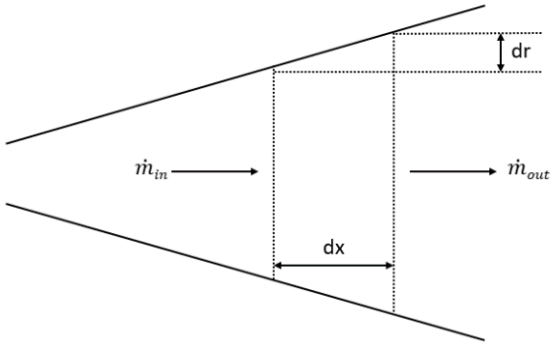

Figure 1-8 - Nozzle Control Incremental Volume Schematic

In order to determine the TM for the system, a modified wave equation was determined. Determine the cross-sectional area as a function of x:

$$tan\,\phi = \frac{R_2}{x_1 + L} = \frac{R_1}{x_1} = \frac{R}{x} \tag{1.44}$$

$$x_1 = \frac{R_1 L}{R_2 - R_1} \tag{1.45}$$

$$R = x\left(\frac{R_2 - R_1}{L}\right) \tag{1.46}$$

$$S(x) = \pi R^2 = \pi x^2 \left(\frac{R_2 - R_1}{L}\right)^2 = \frac{S_2 x^2}{x_2^2} \tag{1.47}$$

Later in the derivation, the following relationship is required:

$$\frac{dS(x)}{dx} = \frac{d}{dx}\left(\pi x^2 \left(\frac{R_2 - R_1}{L}\right)^2\right) = \frac{S_2(2x)}{x_2^2} \tag{1.48}$$

$$\frac{1}{S(x)}\frac{dS(x)}{dx} = \frac{2}{x} \tag{1.49}$$

The cross-sectional area into the system (S_i) and out of the system (S_o) along with the control volume (V) are defined by:

$$S_i = \pi R^2 \tag{1.50}$$

$$S_0 = \pi(R + dR)^2 \tag{1.51}$$

$$V = (S + dS)dx = \pi(R + dR)^2 dx \tag{1.52}$$

The mass flow rates in ($\dot{m}_i$) and out ($\dot{m}_o$) of the control volume are:

$$\frac{\dot{m}_i}{S_i} = \rho u \tag{1.53}$$

$$\frac{\dot{m}_0}{S_0} = pu + \frac{d(\rho u)}{\partial x} dx \tag{1.54}$$

The Conservation of Mass equation is:

$$\frac{d}{dt}(\rho V) = \dot{m_{in}} - \dot{m_{out}} \tag{1.55}$$

Substitution of equation 1.53 and equation 1.54 into 1.55 along with simplification and disregarding higher order terms yields:

$$\frac{d}{dt}(\rho V) = puS - (S + dS)\left(\rho u + \partial \frac{\rho u}{\partial x} dx\right) \tag{1.56}$$

$$\frac{d\rho}{dt} + \rho_0 \frac{du}{dx} + \frac{\rho_0 u}{s} \frac{ds}{dx} = 0 \tag{1.57}$$

The Conservation of Momentum equation is:

$$\frac{\partial(\rho u)}{\partial t} + \nabla \cdot (\rho u u) = -\nabla P \tag{1.58}$$

Simplification of equation 1.58, including disregarding higher order terms, yields:

$$\rho_0 \frac{du}{dt} + \nabla \cdot (\rho u u) + \frac{dP}{dx} = 0 \tag{1.59}$$

$$\rho_0 \frac{du}{dt} + \frac{dP}{dx} = 0 \qquad 1.60$$

Taking the partial derivative of equation 1.60 with respect to x yields:

$$\frac{\partial^2 u}{\partial x \partial t} = \frac{\partial}{\partial x}\left(-\frac{1}{p_0}\frac{\partial P}{\partial x}\right) = -\frac{1}{\rho_0}\frac{d^2 P}{dx^2} \qquad 1.61$$

The isentropic relationship of an ideal gas is:

$$dP = c^2 d\rho \qquad 1.62$$

In order to obtain the wave equation of the nozzle configuration, substitute equation 1.62 into equation 1.57:

$$\frac{1}{c^2}\frac{dP}{dt} + \rho_0 \frac{\partial u}{dx} + \frac{p_0 u}{s}\frac{dS}{dx} = 0 \qquad 1.63$$

Taking the partial derivative of equation 1.63 with respect to t yields:

$$\frac{1}{c^2}\frac{d^2 p}{dt^2} + \rho_0 \frac{\partial^2 u}{\partial x \partial t} + \frac{\rho_0}{S}\frac{\partial S}{\partial x}\frac{\partial u}{\partial t} = 0 \qquad 1.64$$

Taking the partial derivative of equation 1.60 with respect to x and substitution into equation 1.63 yields:

$$\frac{\partial^2 u}{\partial x \partial t} = \frac{d}{dx}\left(-\frac{1}{\rho_0}\frac{dp}{dx}\right) = -\frac{1}{\rho_0}\frac{d^2 p}{dx^2} \qquad 1.65$$

Substituting equation 1.65 into equation 1.64 yields:

$$\frac{1}{c^2}\frac{\partial^2 P}{dt^2} + \rho_0\left(\frac{-1}{\rho_0}\frac{d^2 P}{dx^2}\right) + \frac{\rho_0}{S}\frac{\partial S}{\partial x}\left(-\frac{1}{\rho}\frac{\partial P}{\partial x}\right) = 0 \qquad 1.66$$

Simplification yields the wave equation for a varying cross-section control volume:

$$\frac{d^2 P}{dt^2} - c^2\frac{d^2 P}{dx^2} - \frac{c^2}{S}\frac{dS}{dx}\frac{dP}{dx} = 0 \qquad 1.67$$

The equation for pressure as a function of x and time is:

$$P(x,t) = P(x)e^{i\omega t} \tag{1.68}$$

Insertion of equation 1.68 into equation 1.67 yields:

$$\frac{d^2\left(P(x)e^{i\omega t}\right)}{dt^2} - c^2\frac{d^2\left(P(x)e^{i\omega t}\right)}{dx^2} - \frac{c^2}{S}\frac{dS}{dx}\frac{d}{dx}\left(P(x)e^{i\omega t}\right) = 0 \tag{1.69}$$

Simplification yields:

$$k^2P(x) + \frac{d^2P(x)}{dx^2} + \left(\frac{1}{S}\frac{dS}{dx}\right)\left(\frac{dP(x)}{dx}\right) = 0 \tag{1.70}$$

Substitution of equation 1.49 into equation 1.70 yields:

$$\frac{d^2P(x)}{dx^2} + \frac{2}{x}\frac{dP(x)}{dx} + k^2P(x) = 0 \tag{1.71}$$

The second term is nonlinear. Linearization of equation 1.71 using Q(x) as a substituted variable yields:

$$P(x) = \frac{Q(x)}{x} = Q(x)x^{-1} \tag{1.72}$$

$$\frac{d^2(Q(x)x^{-1})}{dx^2} + \frac{2}{x}\frac{d(Q(x)x^{-1})}{dx} + \frac{k^2Q(x)}{x} = 0 \tag{1.73}$$

Simplification of equation 1.73 yields:

$$\frac{d^2Q}{dx} + k^2Q = 0 \tag{1.74}$$

The equation is now linear harmonic oscillation. A solution to equation 1.74 is:

$$Q(x) = C_1e^{-ikx} + C_2e^{ikx} \tag{1.75}$$

Substitution of equation 1.72 and equation 1.75 into equation 1.68 yields:

$$P(x,t) = \frac{Q(x)}{x}e^{i\omega t} \tag{1.76}$$

$$P(x,t) = \frac{\left(c_1 e^{-ikx} + c_2 e^{ikx}\right) e^{i\omega t}}{x} \tag{1.77}$$

For the velocity, u, consider the perturbation velocity, u', in the momentum equation:

$$\rho_0 \frac{\partial u'}{dt} + \frac{\partial P}{\partial x} = 0 \tag{1.78}$$

$$\rho_0 \frac{du'}{dt} + \frac{d}{dx}\left(\frac{C_1 e^{-ikx}}{x} + \frac{C_2 e^{ikx}}{x}\right) e^{i\omega t} = 0 \tag{1.79}$$

$$\rho_0 \frac{du'}{dt} + e^{i\omega t}\left(\frac{C_1 e^{-ikx}}{x}(-ik) + \frac{C_1 e^{-ikx}}{-x^2} + \frac{C_2 e^{ikx}}{x}(ik) + \frac{C_2 e^{ikx}}{-x^2}\right) = 0 \tag{1.80}$$

$$\rho_0 \frac{du'}{dt} + e^{i\omega t}\left(\frac{C_1 e^{-ikx}}{x}\left(-ik - \frac{1}{x}\right) + \frac{C_2 e^{ikx}}{x}\left(ik - \frac{1}{x}\right)\right) = 0 \tag{1.81}$$

Integration of equation 1.81 with to get u'(x,t) yields:

$$-\int \rho_0 d\, u' = \int e^{i\omega t}\left(\frac{C_1 e^{-ikx}}{x}\left(-ik - \frac{1}{x}\right) + \frac{C_2 e^{ikx}}{x}\left(ik - \frac{1}{x}\right)\right) d\, t \tag{1.82}$$

$$u'(x,t) = \frac{i e^{i\omega t}}{\rho_0 \omega x}\left[C_1 e^{-ikx}\left(-ik - \frac{1}{x}\right) + C_2 e^{ikx}\left(ik - \frac{1}{x}\right)\right] \tag{1.83}$$

The overall velocity, u, is defined as:

$$u(x,t) = \rho_0 S(x)\left(u_0 + u'(x,t)\right) \tag{1.84}$$

Substitution of equation 1.83 and equation 1.47 into equation 1.84 to obtain velocity, u, yields:

$$u(x,t) = \frac{\rho_0 \pi x^2 \left(\frac{R_2 - R_1}{L}\right)^2}{\rho_0 \omega x} i e^{i\omega t}\left[C_1 e^{-ikx}\left(-ik - \frac{1}{x}\right) + C_2 e^{ikx}\left(ik - \frac{1}{x}\right)\right] \tag{1.85}$$

Simplification of equation 1.85 yields:

$$u(x,t) = \frac{\pi (R_2 - R_1)^2 x e^{i\omega t}}{L^2 c}\left[C_1 e^{-ikx}\left(1 - \frac{i}{kx}\right) - C_2 e^{ikx}\left(1 + \frac{i}{kx}\right)\right] \tag{1.86}$$

Substitution of S_2 into equation 1.86 yields:

$$u(x,t) = \frac{S_2 x e^{i\omega t}}{c x_2^2}\left[C_1 e^{-ikx}\left(1 - \frac{i}{kx}\right) - C_2 e^{ikx}\left(1 + \frac{i}{kx}\right)\right] \qquad 1.87$$

Equations for P(x, t) (equation 1.77) and u(x, t) (equation 1.87) with constants C_1 and C_2 have now been derived. Rewrite the equations to in the standard form as:

$$P(x,t) = T_{11}C_1 + T_{12}C_2 \qquad 1.88$$

$$u(x,t) = T_{21}C_1 + T_{22}C_2 \qquad 1.89$$

In order to solve for C_1 and C_2 and obtain the TM, consider matrices $G(x_1,t)$ and $G(x_2,t)$ where:

$$\begin{Bmatrix} P(x_1,t) \\ u(x_1,t) \end{Bmatrix} = [G(x_1,t)]\begin{Bmatrix} C_1 \\ C_2 \end{Bmatrix} \qquad 1.90$$

$$\begin{Bmatrix} P(x_2,t) \\ u(x_2,t) \end{Bmatrix} = [G(x_2,t)]\begin{Bmatrix} C_1 \\ C_2 \end{Bmatrix} \qquad 1.91$$

Solving for C_1 and C_2 and substitution into equations 1.90 and 1.91 to determine $P(x_1,t)$ and $u(x_1,t)$ yields:

$$\begin{Bmatrix} P(x_1,t) \\ u(x_1,t) \end{Bmatrix} = [G(x_1,t)][G(x_2,t)]^{-1}\begin{Bmatrix} P(x_2,t) \\ u(x_2,t) \end{Bmatrix} \qquad 1.92$$

Therefore, the TM is defined as:

$$[T] = [G(x_1,t)][G(x_2,t)]^{-1} \qquad 1.93$$

Rearranging equation 1.77 and equation 1.86 yields

$$G(x,t) = \begin{bmatrix} \dfrac{e^{i\omega t}e^{-ikx}}{x} & \dfrac{e^{i\omega t}e^{ikx}}{x} \\ \dfrac{S_2 x}{c x_2^2} e^{i\omega t}e^{-ikx}\left(1 - \dfrac{i}{kx}\right) & -\dfrac{S_2 x}{c x_2^2} e^{i\omega t}e^{ikx}\left(1 + \dfrac{i}{kx}\right) \end{bmatrix} \qquad 1.94$$

In order to solve for the TM, a MATLAB code was developed. That code is listed in Appendix A-3. Results from using this code produced the TM as:

$$\begin{pmatrix} -\dfrac{sin(Lk) - kx_2 cos(Lk)}{kx_1} \\ \dfrac{s_1 s_2 i(sin(Lk) + kx_1 cos(Lk) - kx_2 cos(Lk) + k^2 x_1 x_2 sin(Lk))}{ck^2 x_2^2} \end{pmatrix} \quad 1.95$$

$$\begin{pmatrix} \dfrac{cx_2 i sin(Lk)}{s_2 x_1} \\ \dfrac{s_1(sin(Lk) + kx_1 cos(Lk))}{ks_2 x_2} \end{pmatrix}$$

The code shown in A-4 was used to generate Figure 1-9. Recorded input noise from experimental testing was utilized for the input into the TM. The MATLAB code shown in Appendix A-4 calculated the TL by utilizing equations 1.6 and 1.7. Generation of the input noise and test output noise is discussed in detail in chapter 3. Figure 1-9 shows a comparison of the TL calculated using experimental test results shown in red, acoustic simulation results shown in green, and analytical results shown in blue.

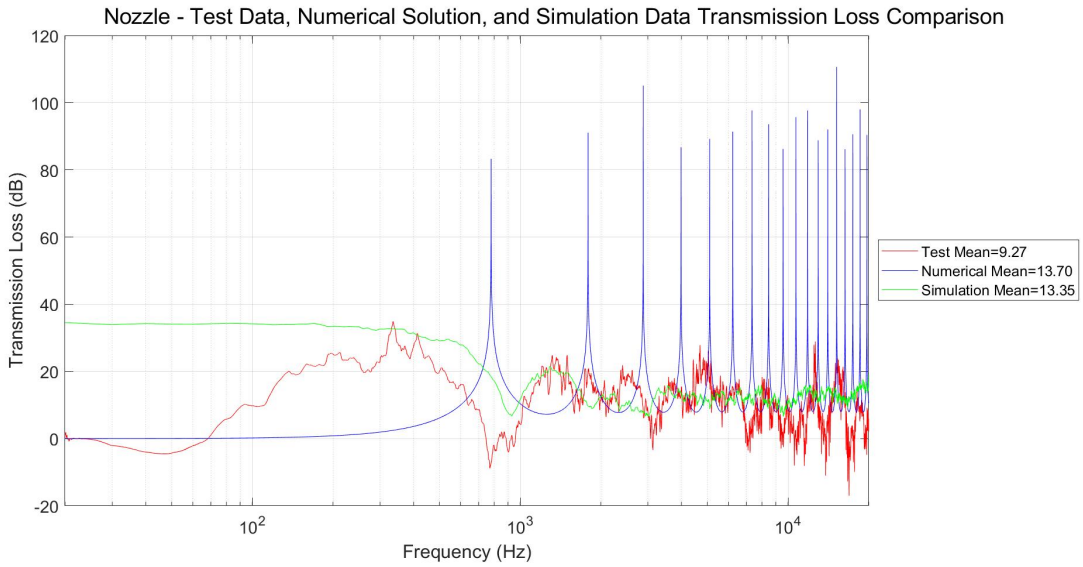

Figure 1-9 - Nozzle - Numerical, Simulation, and Test Transmission Loss Comparison

Figure 1-9 shows that the analytical results correlate with the TL for the experimental test data below 600 Hz. Above 600 Hz, the analytical solution does not correlate with experimental test data and cannot be used for any meaningful assessment.

1.3.5 Transfer Matrix Assessment

The results shown in Figure 1-5 and Figure 1-9 demonstrate that TM approach does not correlate above approximately 600 Hz. While it is common to use TM for systems that are easily represented in 2 dimensions, the AMM actually works in 3 dimensions. The equation for pressure would become: [29]

$$P(x,y,x,t) = e^{i\omega t}\left(C_1 e^{-ik_z z} + C_2 e^{ik_z z}\right)\left(e^{-ik_x x} + C_3 e^{ik_x x}\right)\left(e^{-ik_y y} + C_2 e^{ik_y y}\right) \qquad 1.96$$

With the condition of:

$$k_0^2 = k_x^2 + k_y^2 + k_z^2 \qquad 1.97$$

In order to solve equations 1.96 and 1.97, assumptions have to be made. At the nozzle walls, pressure boundary conditions equaling zero would partially allow for determining

constants in equation 1.96. Assumptions regarding the values of k_{0xyz} would have to be made to in order to determine a solution. However, the relationships between the components of k can be hard to substantiate. For non-planar waves, k_x and k_y can be defined in terms of cross-sectional mode shapes m and n as well as system geometry. Therefore, $k_x = f(m,r)$ and $k_y = f(n,r)$. In order for a wave to propagate, the limitation $k_0^2 - k_x^2 - k_y^2 > 0$ would need to be met. Substituting for k using wavelength gives a relationship between geometry, modes, and frequency. If the frequency increases so that the limitation described above is exceeded, then the solution is said to be "cut-off." This means that the solution is only valid for waves below the cut-off frequency. [29]

Attempts to simplify the equations have used the assumption that $k_x = k_y = 0$. However, the resulting solution would only be valid for planar waves. In the case of planar waves, the solution is a function of the cross-sectional mode shapes m and n with respect to k_z. Furthermore, for cylindrical shapes such as pipe or nozzles, the coordinate system would need to be a cylindrical coordinate system, further complicating the Laplacian as well as equations 1.96 and 1.97. In order to solve this system of equations, Bessel and Neumann functions are required. [29]

In order to increase the bandwidth of validity for the numerical solutions, the input and output areas can be divided into a number of points equaling the number of modes in the "cut-off" frequency range. Consequently, considering a higher frequency range requires the equations to include higher modes. Therefore, the number of points required increases. Solutions can be determined by solving the equations at each point for each permutation of

modes m and n. The number of equations to solve is a function of frequency, points, modes, and geometry. In order to increase the numerical solution into the desired frequency range, the number of equations required would be quite substantial. [29]

To further improve the numerical solutions, higher order terms, viscosity, damping, and boundary layers would need to be included in the derivation of the TM. By the time these parameters and the number of equations required to solve the system in a desirable frequency range are developed, a new acoustic software package only for this particular system would have been created. Therefore, the solution was to use commercial acoustic simulation software. MSC ACTRAN was chosen as the software package.

The explanation for why the numerical solution only works at lower frequencies can also explain why the acoustic software package does not correlate at low frequency. The MSC ACTRAN software package is designed to work in complex systems with non-planar waves. Consequently, the software functions above the cut-off frequency where the effect of planar waves is minimal.

1.4 Research Organization and Methodology

During the initial phases of this research, it was determined that the simulation portion of the research would require verification. Further investigation into the acoustic simulation software revealed that the traditional methodology of performing analysis before prototype manufacturing and experimental testing would be an arduous task. Since the acoustic simulation models require a very fine mesh for the high frequency analysis, typical simulation runs required

approximately 72 hours of runtime. The design, analysis, build, and then test approach would be very time consuming and the results could not be validated prior to manufacturing.

The approach for this research then switched from the traditional approach of model, analyze, build, and test to a more intuitive and test-based approach. Prototype designs with a variety of increasingly complex features were built and tested. Once the effective features and designs were identified, analysis could be done in a more efficient manner. Further details regarding the acoustic simulation methodology are described in section 4.1.

After the literature review, the design phases for the SISO prototypes were outlined. The SISO designs focused on examining intuitive acoustic mitigation and fundamental features. The fundamental features prototypes were then analyzed utilizing MSC ACTRAN. The results of the acoustic simulations were compared with test results in order to validate the software. Experimental testing of the fundamental features allowed the SISO designs to further increase in complexity by enclosing the prototypes, adding an additional stage, and downsizing the prototypes. The test results were evaluated in order to determine the top performing SISO configuration.

The same approach used on the SISO prototypes was then applied to the MIMO prototypes. Prototypes were built and tested. Then the top performing configurations were determined. Acoustic simulations were conducted using MSC ACTRAN. The simulations were verified using the experimental test results.

The top performing MIMO design was then modified for incorporation into the AMM Sphere. The AMM Sphere design was then tested in order to verify compliance with the research requirements outlined in the beginning of this chapter.

Chapter 2: Prototypes

"When people talk about innovation in this decade, they really mean design."

-Bruce Nussbaum [30]

To meet the goals outlined in chapter 1, a methodology to create a complex system was created. The methodology needed to be able to quantify each feature in order to ensure the system did not have ineffective features. Consequently, the design process methodically added complexity one feature at a time to a well-understood system. This approach allowed each feature to be quantified and measured. The foundation for all of the designs discussed throughout this dissertation was a SP, which acted as the control for the research.

The initial design phase concentrated on the fundamental features for the SISO systems. All of the SISO prototypes had an overall length of 6", minor diameter of 1", and a major diameter of 2.5". Following the design for the SP, the design was modified to create 2 different designs. The first design consisted of a nozzle and the second design consisted of a SP with 3 rows of Radial Perforations (RP). The subsequent design then incorporated the nozzle and RP. A separate design consisted of a series of 3 nozzles. Depending on the direction of the nozzle, the configuration was either a Series of Converging Nozzles (SCN) or a Series of Diverging Nozzles (SDN). Each nozzle section is referred to as a stage. The subsequent design incorporated RP into the series of nozzles. However, the length of each nozzle did not support 3 rows of perforations; therefore, 2 rows of perforations were integrated. The subsequent design then incorporated axial perforations (AP). Finally, a Constricted Opening at the Output Plane (COOP) was added to the design. The SISO fundamental features prototypes were then manufactured.

Experimental testing was then conducted on the SISO fundamental features prototypes in order to determine which design was the top performer. The designs were compared using the TL of each configuration. The configuration with the SDN with RAP was used as the Base Feature (BF) AMM design moving forward. The prototype with the COOP was designed and manufactured after the experimental testing of the SISO fundamental features prototypes. The experimental testing for this prototype was conducted later in the design stage. Therefore, that feature is not included in the BF AMM until the MIMO design and testing phase of the research. Details about the SISO fundamental features experimental testing can be found in section 3.5.1.9.

In order to meet the goal of a compact and configurable system, the BF AMM was enclosed and downsized. In order to enclose the system, a series of walls with a hexagonal outer shape were created in order to surround the BF AMM. Furthermore, a wall between the outer enclosure walls and the nozzle base at the end of each stage was added to the design. The outer cell walls and the stage division walls created the enclosure of the system. The designs were then downsized from 2” stages to 0.25” stages. There were 4 downsizing prototypes with each design scaled by a factor of 2 from the previous prototype.

An additional stage for the prototypes was considered. The additional stage consisted of a SP with a diameter that matched the nozzle input diameter. The additional stage was added as the initial stage to the SISO systems. The SISO designs then became a 4-stage design.

Experimental testing was then conducted on the enclosed, downsized, and additional stage SISO prototypes in order to determine which prototype was the top performing design. The designs were compared using the TL of each configuration. The configuration with the SDN

with RAP with an Additional Stage was used as the BF AMM design moving forward. Details can be found in section 3.5.5.

A main requirement of the research outlined in chapter 1 states that the design needed to be configurable. In order to be fully configurable, the design needed to have variable thickness, length, and width. To ensure this goal was attained in the MIMO prototypes, the overall system was divided into 3 categories.

The first category is denoted as a stage. A stage consists of a perforated nozzle surrounded by a series of interconnected cavities and an enclosure. The stages were designed to have perforations to allow the stage to be connected to previous, subsequent, or adjacent stages. Depending on the location of the stage in the MIMO system, previous, subsequent, or adjacent perforations may not be required. For example, an initial stage would not require perforations to connect to the previous stage. A cross-section of an example stage CAD model is shown in Figure 2-1.

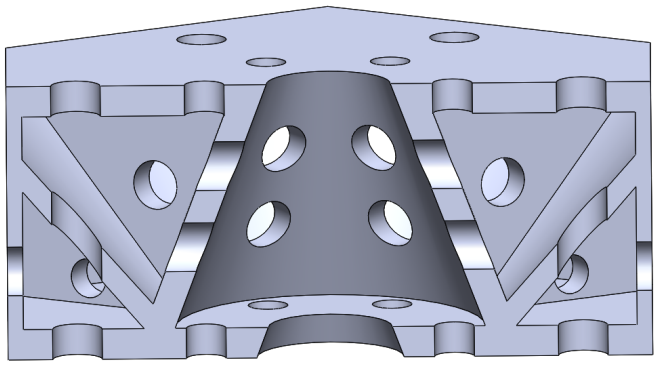

Figure 2-1 - Example Stage Cross-Section

The second category is designated as a cell. As many stages as desired can be stacked in series. These stacked stages form a cell. This research uses an initial stage consisting of a SP and

interconnected cavities followed by 3 stages of perforated nozzles with interconnected cavities for the basis of a cell. A cross-section of a CAD model for an example cell is shown in Figure 2-2.

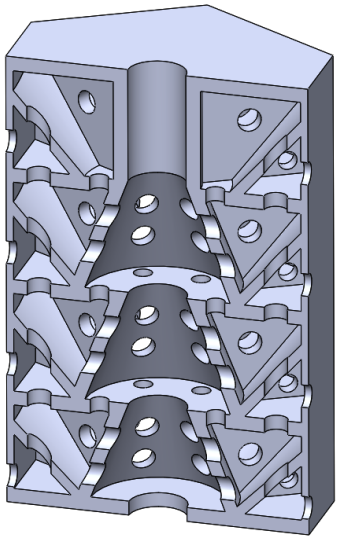

Figure 2-2 - Example Cell Cross-Section

The third category is designated as a panel. These cells are placed in parallel and can be configured to any shape or size. The cells were designed to have hexagonal outer cell walls, therefore the cells are arranged into a honeycomb structure. This honeycomb structure can be manufactured to be of any size or shape, allowing the system to be fully configurable. The MIMO panels used in this research were designed to have an outer diameter of 7.5" with 37 cells per panel. Figure 2-3 shows an example of the CAD model for an experimental test panel.

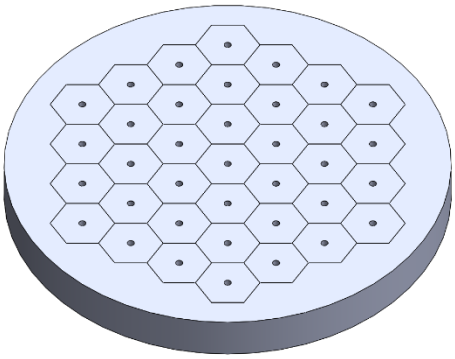

Figure 2-3 - Example Test Panel

Building from this concept of AMM structure consisting of stages, cells, and panels, the intermediate design phase focused on creating MIMO systems. Using the experimental testing results described in section 3.5.5, the BF AMM was combined with the traditional AMM in the form of interconnected cavities. The interconnected cavities were created in the area surrounding the BF AMM and the enclosure walls.

In order to quantify the performance of the MIMO prototypes, a control panel consisting of SPs and a panel consisting of the BF AMM were created. Both designs utilized 0.25" stages. After the BF AMM MIMO prototype was manufactured, the concept of a COOP was conceived. The SISO prototype was then manufactured and tested. Experimental testing, outlined in section 3.5.1.9, indicated that the feature was substantially beneficial to the overall performance. Therefore, the subsequent MIMO prototypes contained the feature.

The first AMM configuration, referred to as a Large Cavity AMM, added a bisecting wall from the base of the nozzle to the top of the stage, in order to create 2 large cavities surrounding the nozzle. Perforations were added to the bisecting wall in order to connect the outer and inner cavities. The Small Cavity AMM added 6 vertical walls to the Large Cavity AMM configuration.

Each wall connected the nozzle to a corner of the outer cell walls. The addition of the 6 vertical walls divided the inner and outer cavities into 6 sections, yielding 12 cavities surrounding the nozzle. Perforations were made in the vertical walls to connect each inner and outer cavity to adjacent cavities.

During the manufacturing of the Large Cavity AMM and Small Cavity AMM prototypes, a fifth configuration of AMM utilizing infill was designed and manufactured. The Large and Small Cavity AMM prototypes required extensive manufacturing times and a significant amount of additive manufacturing support structure. The support structure had to be removed prior to experimental testing. The support material is soluble and the removal process requires the structure to be immersed in a detergent bath while in either an ultrasonic, heat, or agitation bath. [31] [32]

The use of infill material instead of interconnected cavities allows for a substantial increase in the ease of manufacturing as well as a decrease in production time. Infill material, referred as Infill AMM in this dissertation, is commonly used in additive manufacturing as a way to save print material, weight, and to expedite the manufacturing process. In a region of large, solid additive manufactured material, thick outer cell walls are utilized with infill between the walls. The infill consists of material printed in various overlapping patterns of geometry. These overlapping patterns allow for the creation of a controlled acoustic material, which can act as an acoustic foam. The infill patterns allow the structure to be manufactured without the need of additive manufacturing support structures. The infill pattern of the AMM used in this research consisted of a porous hexagonal pattern. The Infill AMM surrounded the nozzles and replaced the outer cell walls, the stage division walls, and the interconnected cavity AMM walls.

Experimental testing was performed on the MIMO prototypes in order to determine which prototype was the top performer. The designs were compared using the TL of each configuration. The top performing MIMO design was the Small Cavity AMM. Details can be found in section 3.6.6.

The final phase of the research focused on taking the Small Cavity AMM design and adapting it into the AMM Sphere. The geometry and dimensions of the cell were maintained, but the cell was modified to fit into a hollow sphere with an inner radius of 6" and an outer radius of 7". The AMM Sphere had an internal platform for instrumentation to verify functionality. The AMM Sphere provided the compact, omnidirectional, passive packaging that is the overall goal of the research.

All of the designs were developed using Dassault Systèmes Solidworks 2019.

2.1 Manufacturing

The prototypes were manufactured using a Stratasys Fortus 450 Gen2 [33] [34] utilizing Acrylonitrile Styrene Acrylate (ASA) thermoplastic [35] in the United States Army Futures Command (AFC) Combat Capabilities Development Command (DEVCOM) Aviation and Missile Center (AvMC) Prototype Integration Facility (PIF) Additive Manufacturing Center of Excellence. The prototypes were printed using a tip size of 0.005". Figure 2-4 shows the additive manufacturing machine. The prototypes were manufactured with support material [32] as required. Best practices were used when removing the support structure prior to experimental testing. [31]

2.2 Single Input Single Output Systems Fundamental Features

The research began with designing a series of nozzles with different features to see how each feature effected acoustic noise. Changes in the fundamental SP design included RP, AP, CN, DN, SCN, SDN, and a COOP. The dimensions of the nozzle configurations are shown in Table 2-1.

Figure 2-4 - Stratasys Fortus 450 Gen2 Additive Manufacturing Machine [36]

Geometry Feature	Dimension Value (in)
Overall Length	6
Stage Length	2
Input Diameter	1
Output Diameter	2.5
Perforated Hole Diameter	0.25
Wall Thickness	0.25

Table 2-1 - SISO - Geometry Details

Eight different SISO prototypes were manufactured. The prototypes containing nozzles were tested in both the converging and diverging directions yielding a total of 14 different test configurations. In order for each prototype to fit into the test apparatus, each end consisted of a flanged end. Instead of a purely circular flange, half of the flange was square. The square end feature allowed for a better seal around the nozzle during experimental testing.

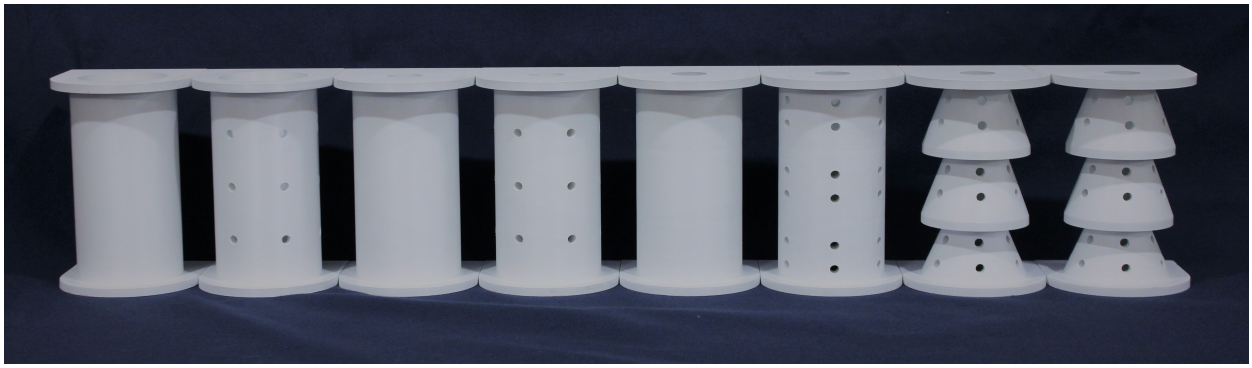

Figure 2-5 - SISO Fundamental Features Prototypes

2.2.1 Straight Pipe

A control prototype was designed. The SP prototype had an inner diameter of 2.5” and a length of 6”. The wall thickness throughout the structure was 0.25”. Figure 2-6 shows a cross-section from the CAD model and Figure 2-7 shows an isometric view of the finished prototype.

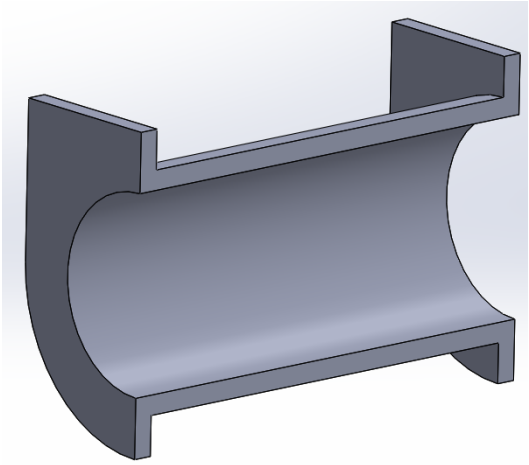

Figure 2-6 - SISO - Straight Pipe - CAD

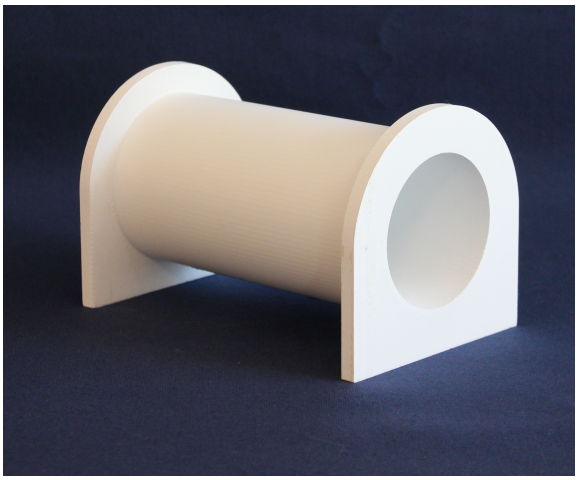

Figure 2-7 - SISO - Straight Pipe - Prototype

2.2.2 Straight Pipe with Radial Perforations

The SP was modified to have 3 rows of RP. Each row consisted of 6 RP equidistant around the structure. The perforations had a diameter of 0.25". The wall thickness, diameter, and length were maintained at .25", 2.5", and 6" respectively. Figure 2-8 shows a cross-section from the CAD model and Figure 2-9 shows an isometric view of the finished prototype.

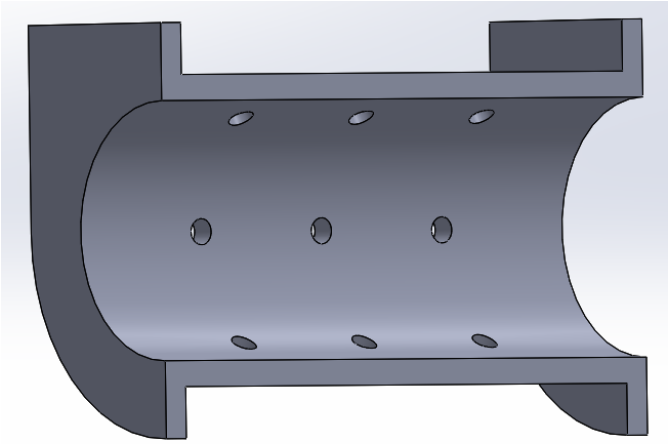

Figure 2-8 - SISO - Straight Pipe with Radial Perforations - CAD

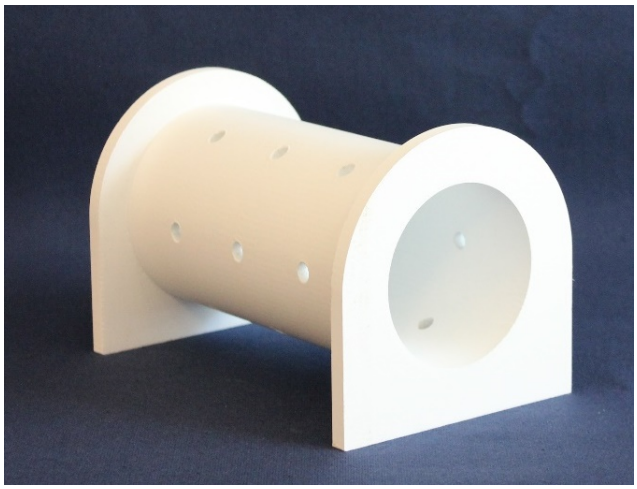

Figure 2-9 - SISO - Straight Pipe with Radial Perforations - Prototype

2.2.3 Nozzle

The minor diameter of the nozzle was 1” and the major diameter was 2.5”. The length was maintained at 6”. The nozzle was tested in the converging and diverging configurations. Figure 2-10 shows a cross-section of the nozzle from the CAD model. Figure 2-11 shows the finished prototype from the forward (minor diameter) view and Figure 2-12 shows the finished prototype from the aft (major diameter) view.

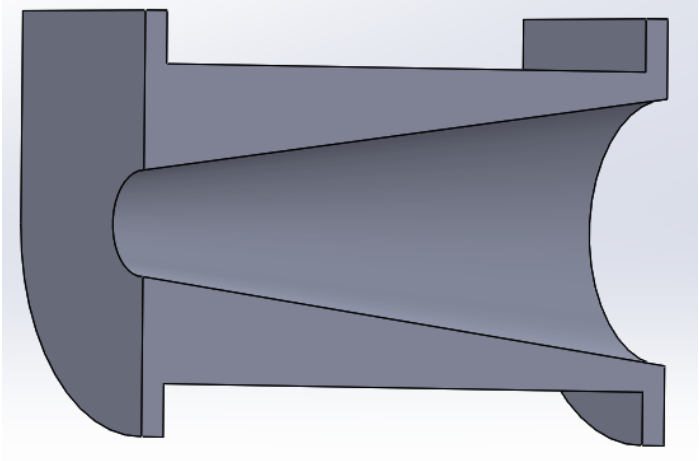

Figure 2-10 - SISO - Nozzle - CAD

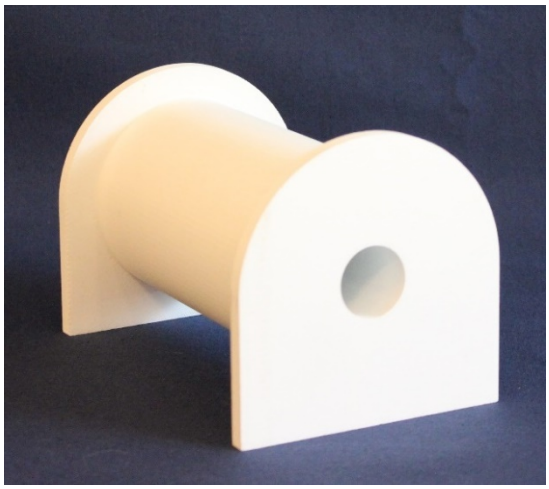

Figure 2-11 - SISO - Nozzle - Prototype - Forward View

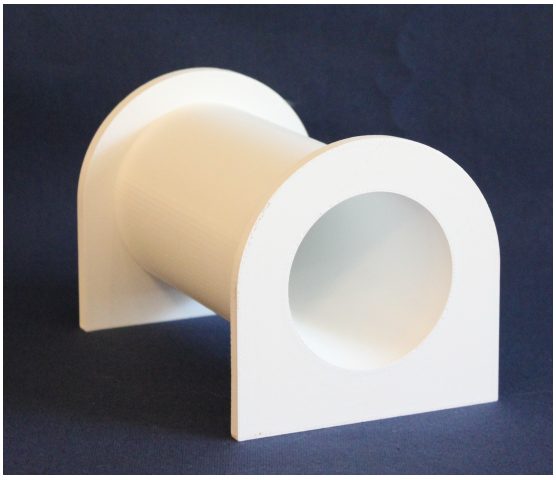

Figure 2-12 - SISO - Nozzle - Prototype - Aft View

2.2.4 Nozzle with Radial Perforations

The CN/DN was modified to have 3 rows of RP. Each row consisted of 6 RP equidistant around the structure. The perforations had a diameter of 0.25". The minor diameter, major diameter, and length were maintained at 1", 2.5", and 6" respectively. Figure 2-13 shows a cross-section of the design from the CAD model. Figure 2-14 shows an isometric view of the finished prototype, Figure 2-15 shows the finished prototype from the forward (minor diameter) view, and Figure 2-16 shows the finished prototype from the aft (major diameter) view.

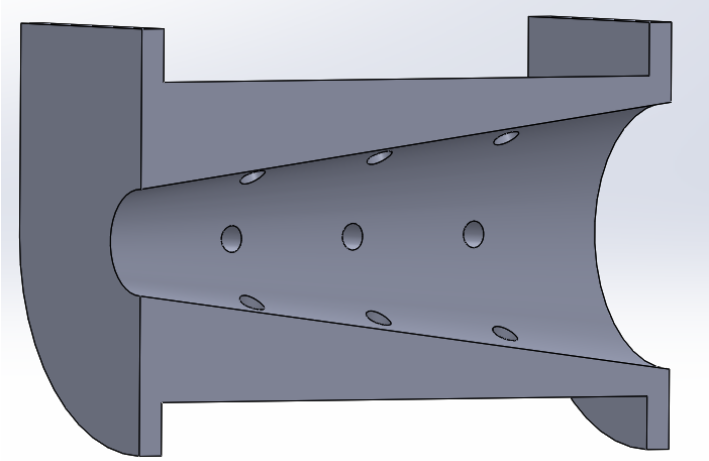

Figure 2-13 - SISO - Nozzle with Radial Perforations - CAD

Figure 2-14 - SISO - Nozzle with Radial Perforations - Prototype

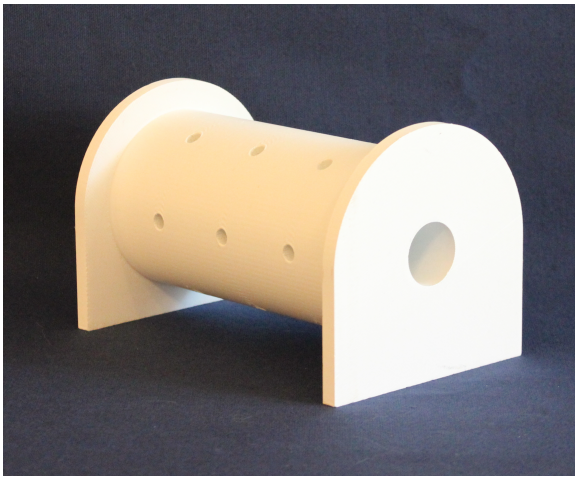

Figure 2-15 - SISO - Nozzle with Radial Perforations - Prototype - Forward View

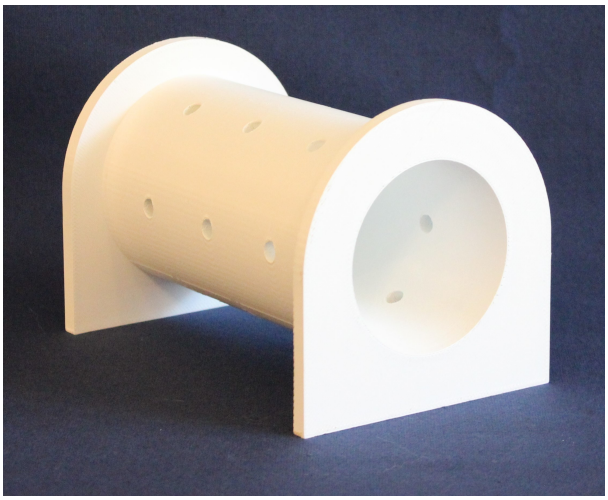

Figure 2-16 - SISO - Nozzle with Radial Perforations - Prototype - Aft View

2.2.5 Series of Nozzles

The SCN/SDN was divided into 3 stages. Each stage consisted of a nozzle 2” in length. The overall length was maintained at 6”. Figure 2-17 shows a cross-sectional view from the CAD model. Figure 2-18 shows the finished prototype from the forward (minor diameter) view and Figure 2-19 shows the finished prototype from the aft (major diameter) view.

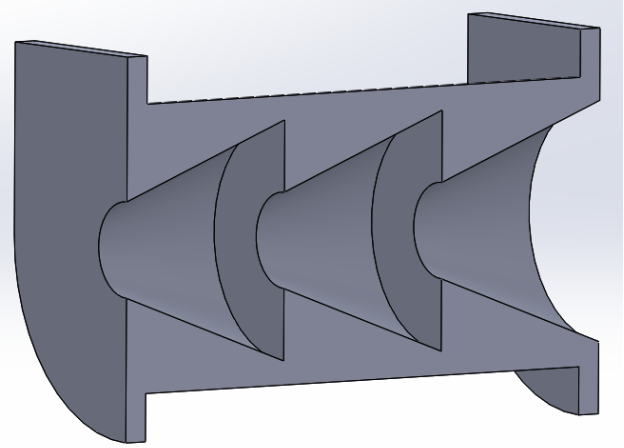

Figure 2-17 - SISO - Series of Nozzles - CAD

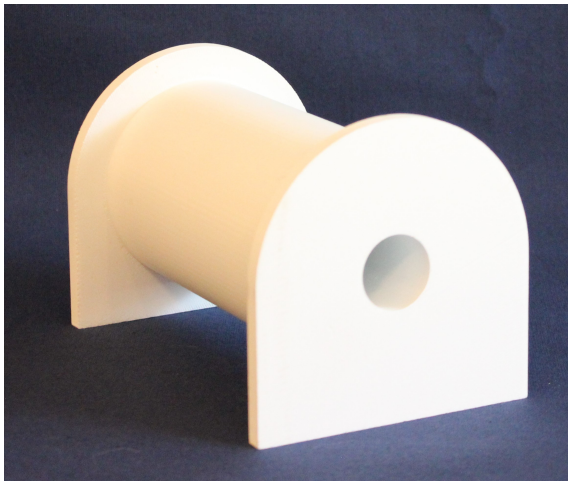

Figure 2-18 - SISO - Series of Nozzles - Forward View

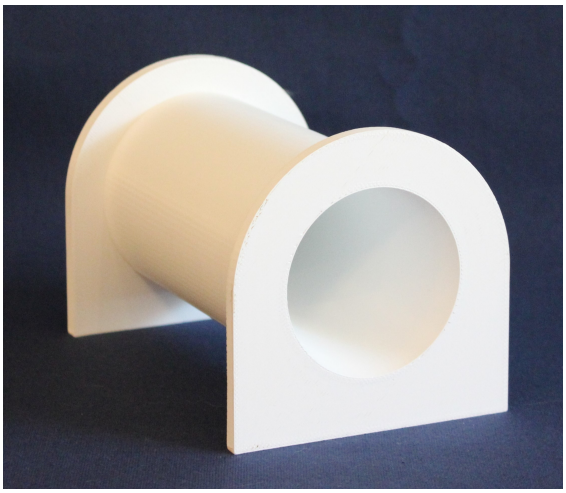

Figure 2-19 - SISO - Series of Nozzles - Aft View

2.2.6 Series of Nozzles with Radial Perforations

The SCN/SDN with RP maintained 3 2” stages with a minor diameter of 1” and a major diameter of 2.5”. Each stage was modified to have 2 rows of RP. Each row consisted of 6 RP equidistant around the structure. Figure 2-20 shows a cross-section from the CAD model. Figure 2-21 shows the finished prototype from an isometric view, Figure 2-22 shows the finished prototype from a forward (minor diameter) view, and Figure 2-23 shows the finished prototype from an aft (major diameter) view.

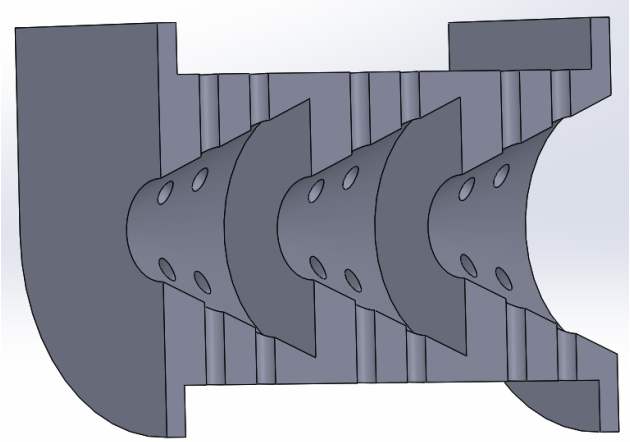

Figure 2-20 - SISO - Series of Nozzles with Radial Perforations - CAD

Figure 2-21 - SISO - Series of Nozzles with Radial Perforations - Prototype

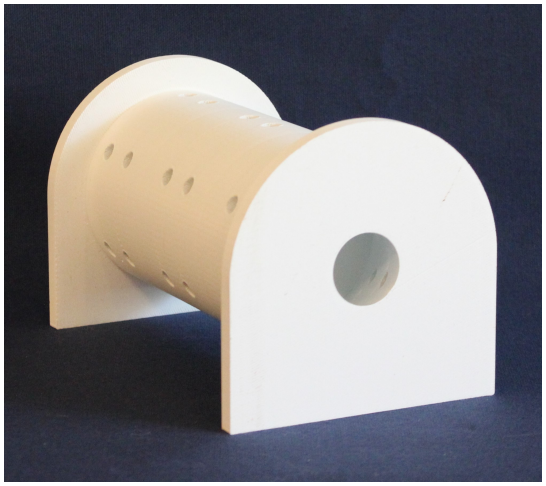

Figure 2-22 - SISO - Series of Nozzles with Radial Perforations - Prototype - Forward View

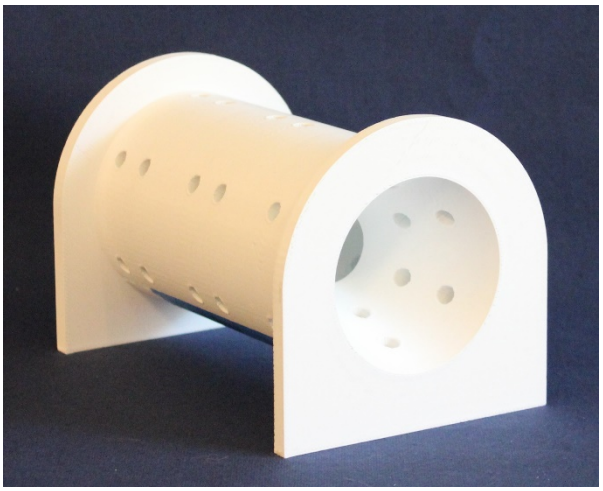

Figure 2-23 - SISO - Series of Nozzles with Radial Perforations - Prototype - Aft View

2.2.7 Series of Nozzles with Radial and Axial Perforations

The SCN/SDN with RAP maintained a minor diameter of 1” and a major diameter of 2.5”. Each 2” stage maintained the RP, and a series of 6 AP were added to the first 2 stages. Figure 2-24 shows a cross-sectional view from the CAD model. Figure 2-25 shows the finished prototype from an isometric view, Figure 2-26 shows the finished prototype from a forward (minor diameter) view, and Figure 2-27 shows the finished prototype from an aft (major diameter) view.

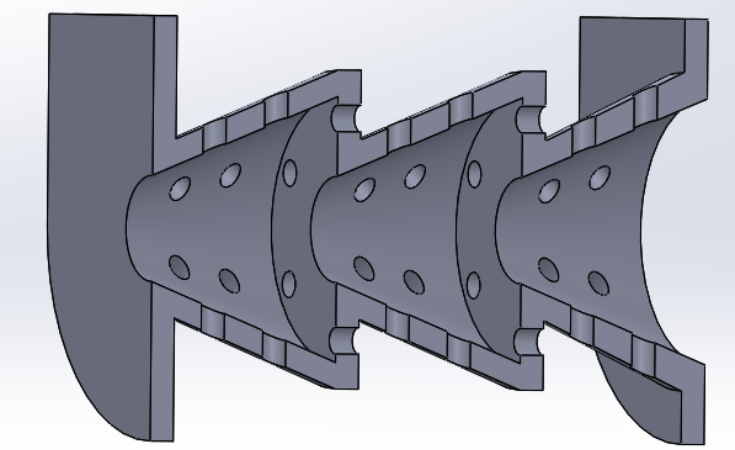

Figure 2-24 - SISO - Series of Nozzles with Radial and Axial Perforations - CAD

Figure 2-25 - SISO - Series of Nozzles with Radial and Axial Perforations - Prototype

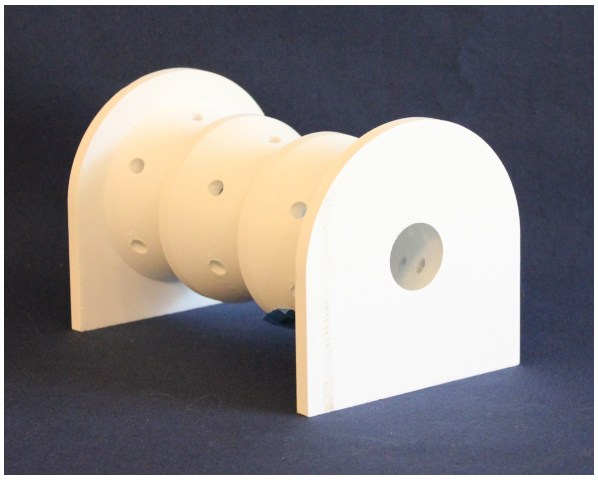

Figure 2-26 - SISO - Series of Nozzles with Radial and Axial Perforations - Prototype - Forward View

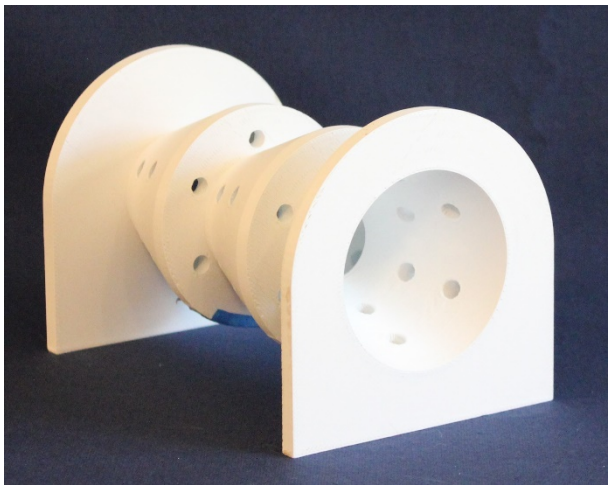

Figure 2-27 - SISO - Series of Nozzles with Radial and Axial Perforations - Prototype - Aft View

2.2.8 Series of Diverging Nozzles with Radial and Axial Perforations and a Constricted Opening at the Output Plane

The SDN with RAP was modified to have a COOP. On the DN, the output plane is defined as the location in the nozzle with the major diameter. With the constricted opening, the 2.5" diameter was decreased to 1" in diameter. Figure 2-28 shows a cross-sectional view from the CAD model. Figure 2-29 shows the finished prototype from an isometric view, Figure 2-30 shows the finished prototype from a forward (minor diameter) view, and Figure 2-31 shows the finished prototype from an aft (major diameter) view.

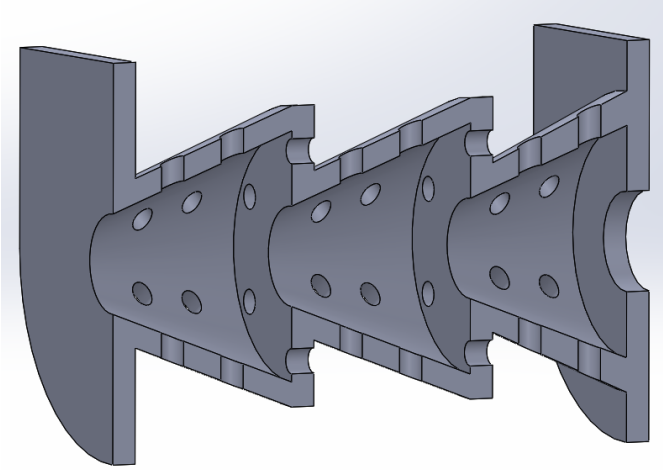

Figure 2-28 - SISO - Series of Diverging Nozzles with Radial and Axial Perforations and a Constricted Opening at the Output Plane - CAD

Figure 2-29 - SISO - Series of Diverging Nozzles with Radial and Axial Perforations and a Constricted Opening at the Output Plane - Prototype

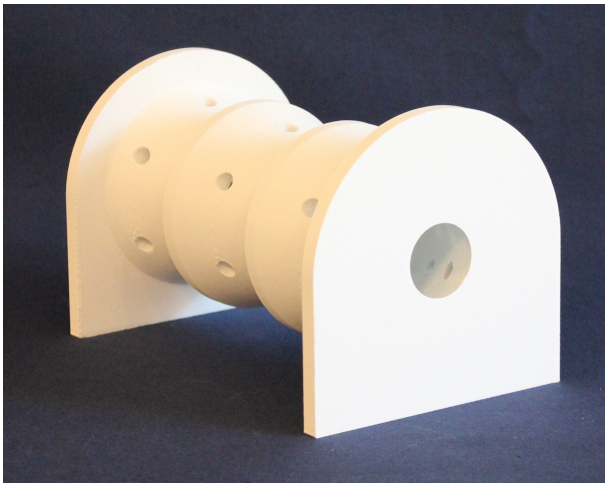

Figure 2-30 - SISO - Series of Diverging Nozzles with Radial and Axial Perforations and a Constricted Opening at the Output Plane - Prototype - Forward View

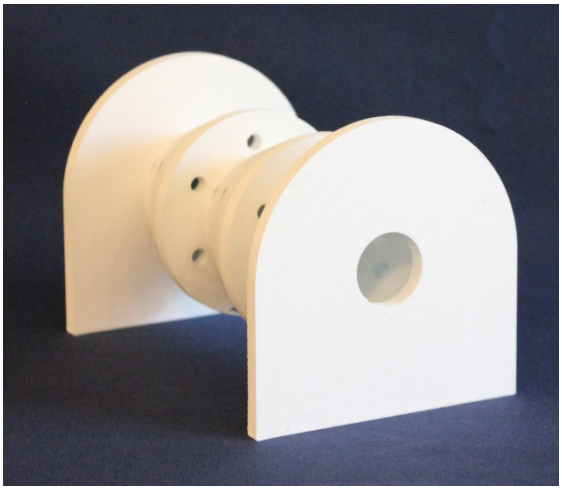

Figure 2-31 - SISO - Series of Diverging Nozzles with Radial and Axial Perforations and a Constricted Opening at the Output Plane - Prototype - Aft View

2.3 Enclosing of the Single Input Single Output Systems

Experimental testing of the prototypes described in section 2.2 demonstrated that the configuration of a SDN with RAP was the top performing design. This configuration will be referred to as the BF AMM configuration. Experimental testing details can be found in section 3.5.1.9. The design featuring a COOP was not yet conceived at this point in the research. Consequently, it is not included in this section of the research.

In order to accommodate the MIMO AMM design, the SISO prototypes required an enclosure around the nozzles, which provided the base structure for the AMM design. A series of outer cell walls with a hexagonal outer shape were created to surround the BF AMM and a wall at the end of each stage connecting the nozzle base to the enclosure outer cell walls was added to the design. The outer cell walls and the stage division walls created the enclosure of the system.

Figure 2-32 and Figure 2-33 show a BF AMM CAD model with no enclosure and enclosure walls, respectively. The outer cell walls are shown surrounding the nozzle. The outer cell walls are configured in a hexagonal shape with an inscribed circle with a radius of 3". The stage division walls are the horizontal walls located on the exit planes of the first and second stage nozzles shown in Figure 2-33. Figure 2-34 shows the finished prototype.

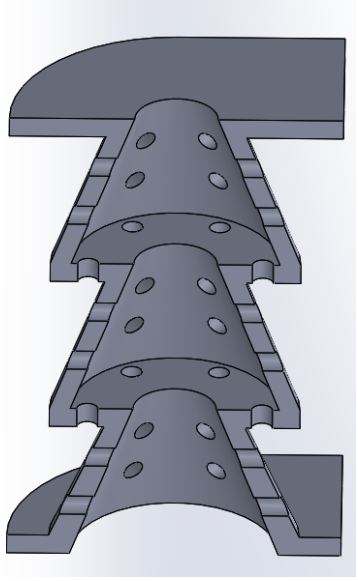

Figure 2-32 - SISO - Series of Nozzles with Radial and Axial Perforations - CAD

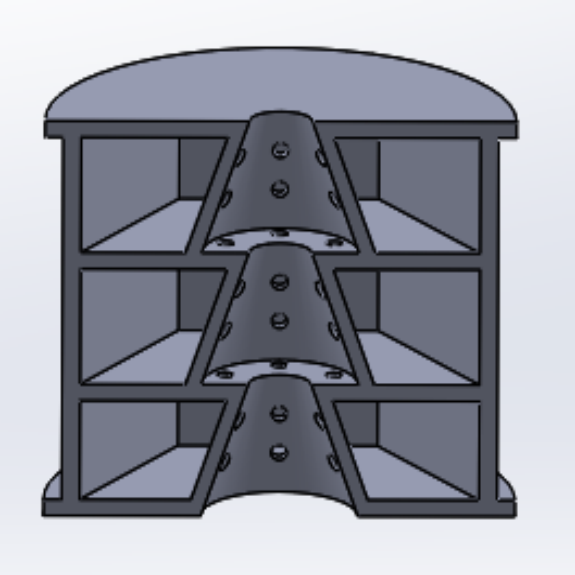

Figure 2-33 - SISO - Enclosed Series of Nozzles with Radial and Axial Perforations - CAD

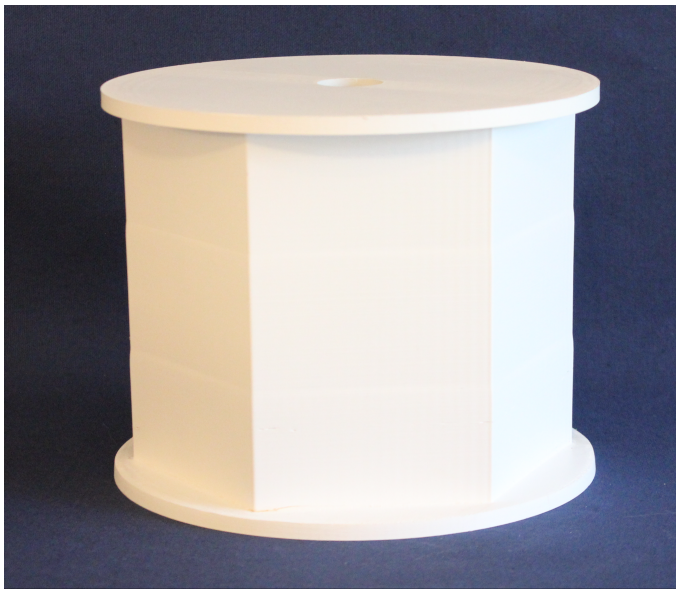

Figure 2-34 - SISO - Enclosed Series of Nozzles with Radial and Axial Perforations Prototype

2.4 Single Input Single Output Downsizing

The SISO systems discussed in sections 2.2 through 2.3 have an overall length of 6". In order to meet the requirement of a compact design with a minimal footprint, the design needed to be downsized. Four prototypes were designed, manufactured, and tested in order to demonstrate that the design could be downsized and maintain performance. The naming of

each prototype refers to the length of its stage. The first prototype, referred to as the 2” stage, kept the dimensions discussed in previous sections. The second prototype, referred to as the 1” stage, scaled down dimensions from the previous section by a factor of 2. This process was repeated for the 0.5” stage and the 0.25” stage. Dimensions for each configuration are detailed in Table 2-2. All dimensions are in inches.

Geometry Feature	2” Stage	1” Stage	0.5” Stage	0.25" Stage
Geometry Factor	1	2	4	8
Overall Length	6”	3”	1.5”	0.75”
Stage Length	2”	1”	0.5”	0.25”
Input Diameter	1”	0.5”	0.25”	0.125”
Output Diameter	2.5”	1.25”	0.625”	0.3125”
Perforated Hole Diameter	0.25”	0.125”	0.0625”	0.04”
Wall Thickness	0.25”	0.125”	0.0625”	0.03125”
Hexagonal Radius	3”	1.5”	.75”	.375”

Table 2-2 - Geometry Details of SISO Downsizing

The 0.5” stage and the 0.25” stage prototypes were designed to have 6 support columns surrounding the enclosed nozzle to ensure the prototypes would not be damaged during handling or testing. The CAD models of the downsizing prototypes are shown in Figure 2-35 in an isometric view. Figure 2-36 shows an isometric cross-sectional view from the CAD models. Figure 2-37 shows a cross-sectional view of the downsizing prototypes CAD models. Figure 2-38 shows the finished prototypes.

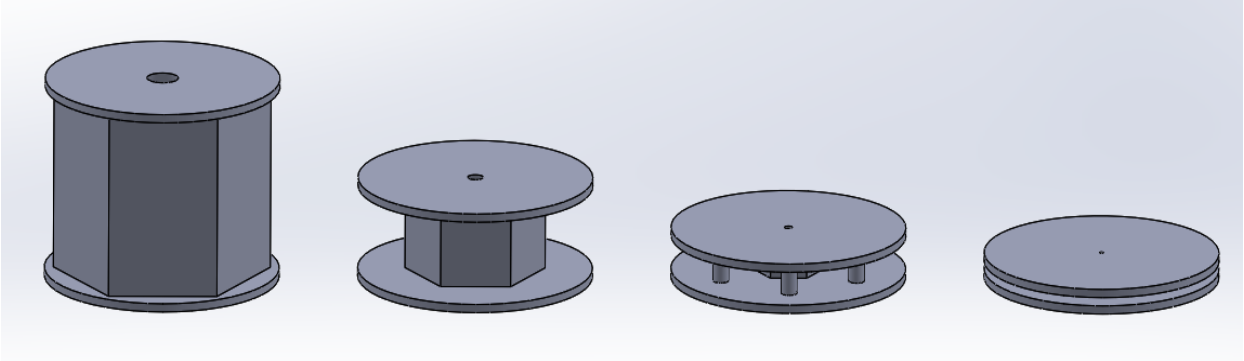

Figure 2-35 - SISO - Downsizing Prototypes - Isometric CAD View

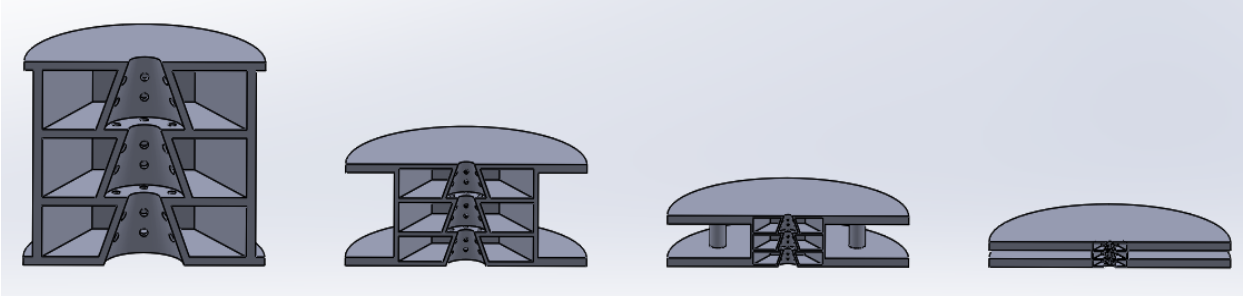

Figure 2-36 - SISO - Downsizing Prototypes - Cross-Section Isometric CAD View

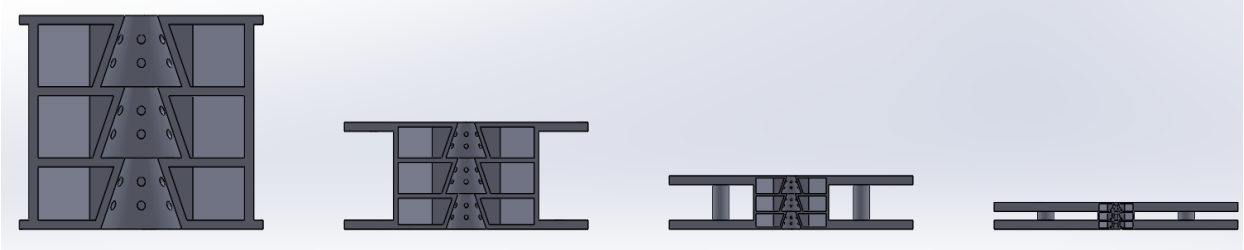

Figure 2-37 - SISO - Downsizing Prototypes - Cross-Section CAD View

Figure 2-38 - SISO - Downsizing Prototypes

The 2” downsizing prototype is the same prototype discussed in section 2.3. Geometry details can be found in Table 2-2. Figure 2-38 shows a cross-sectional view from the CAD model. Figure 2-40 shows the finished prototype.

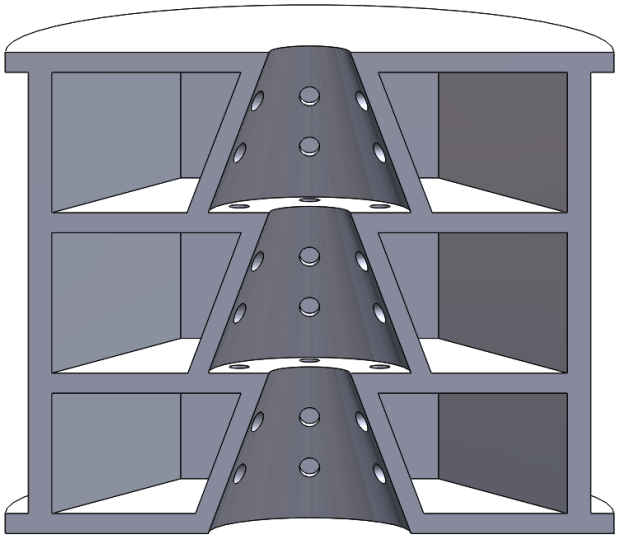

Figure 2-39 - SISO - Two Inch Stages Downsizing Prototype - CAD

Figure 2-40 - SISO - Two Inch Stages Downsizing Prototype

The 1” stage prototype geometry was determined by scaling the 2” stage prototype by a factor of 2. Geometry details can be found in Table 2-2. Figure 2-41 shows a cross-sectional view from the CAD model. Figure 2-42 shows the finished prototype.

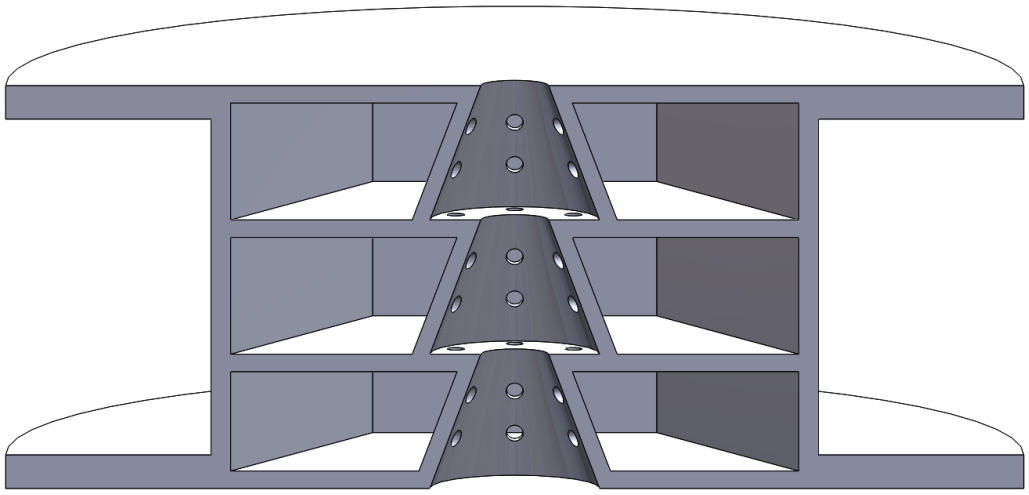

Figure 2-41 - SISO - One Inch Stages Downsizing Prototype - CAD

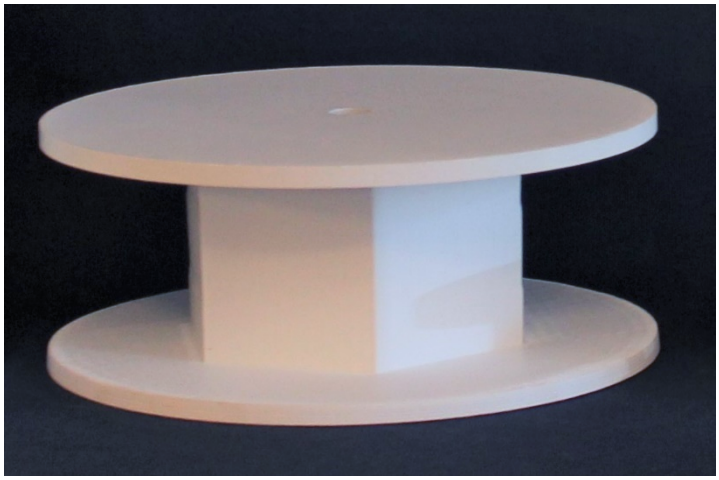

Figure 2-42 - SISO - One Inch Stages Downsizing Prototype

The 1/2” stage prototype geometry was determined by scaling the 1” stage prototype by a factor of 2. Geometry details can be found in Table 2-2. Six support posts were added to the

design in order to ensure the prototype was not damaged during handling. Figure 2-43 shows a cross-sectional view from the CAD model. Figure 2-44 shows the finished prototype.

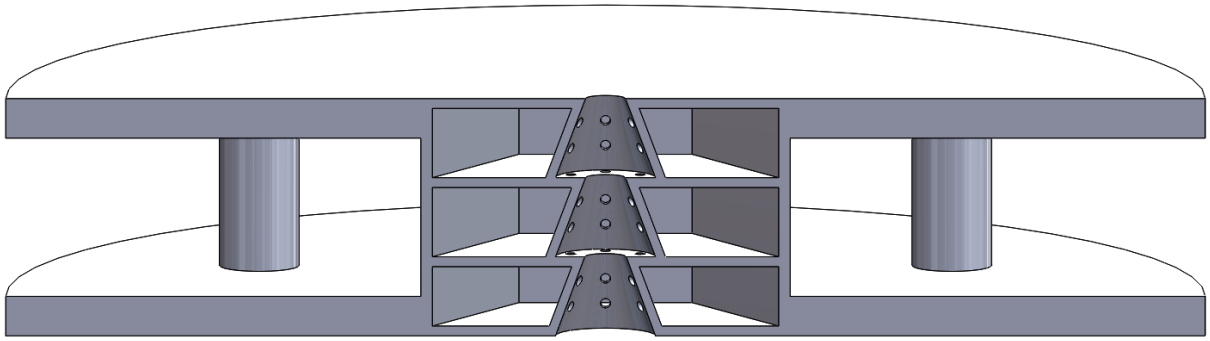

Figure 2-43 - SISO - Half Inch Stages Downsizing Prototype - CAD

Figure 2-44 - SISO - Half Inch Stages Downsizing Prototype

The 1/4” stage prototype geometry was determined by scaling the 1/2” stage prototype by a factor of 2. The perforations for the 1/4” stage prototype were not scaled by a factor of 2. The additive manufacturing machine could not manufacture the perforations with the specified diameter of 0.03125”. The printer tip of could only manufacture perforations with a diameter of 0.04”. Geometry details can be found in Table 2-2. Six support posts were added to the design in order to ensure the prototype was not damaged during handling. Figure 2-45 shows a cross-sectional view from the CAD model. Figure 2-46 shows the finished prototype.

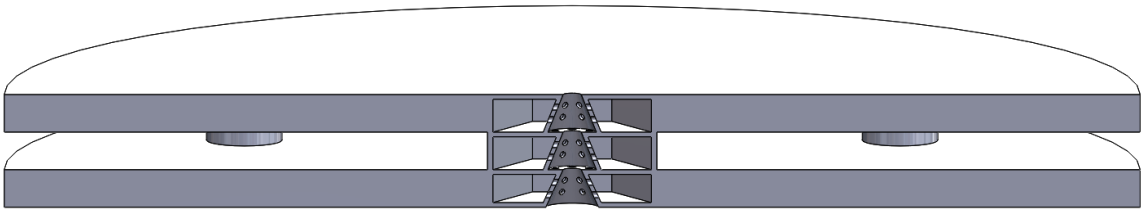

Figure 2-45 - SISO - Quarter Inch Stages Downsizing Prototype - CAD

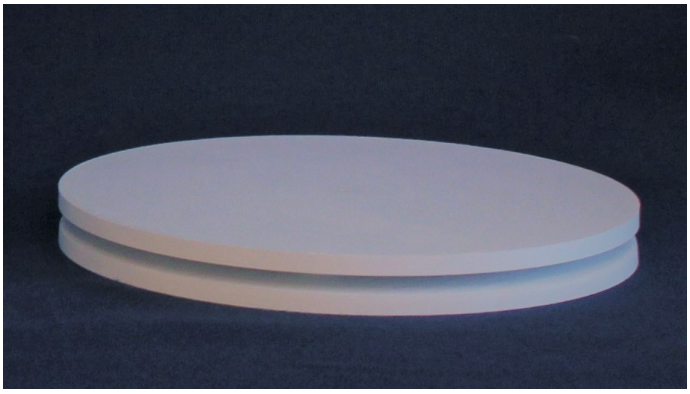

Figure 2-46 - SISO - Quarter Inch Stages Downsizing Prototype

2.5 Single Input Single Output Additional Stage

During preliminary testing and design, an additional stage consisting of a SP for the prototypes was considered. Experimental testing concluded that the additional stage was beneficial to system performance. Therefore, a fourth stage was added to the design. Test results are discussed in section 3.5.4. The fourth stage was added as the initial stage and consisted of a SP with a diameter equal to the nozzle input diameter.

The quarter inch stage prototype discussed in section 2.4 was the basis of the design for the additional stage prototype. The geometry outlined in Table 2-2 with the exception of the overall length remained constant. The change in the overall length between the 3- and 4-stage prototypes is outlined in Table 2-3.

Stage Length	Overall Length 3 Stage	Overall Length 4 Stage
0.25”	0.75”	1”

Table 2-3 - Length Comparison for 3- and 4-stage Prototypes

Figure 2-47 shows a cross-sectional view from the CAD model for the 4-stage prototype with 1/4” stages. Figure 2-48 shows the finished prototype.

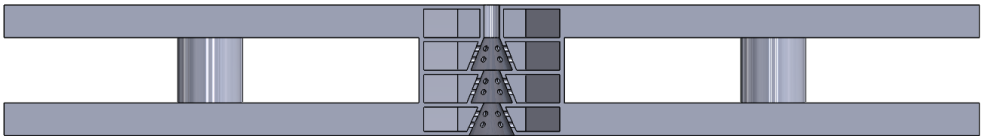

Figure 2-47 - SISO - Four Stage Prototype with Quarter Inch Stages - CAD

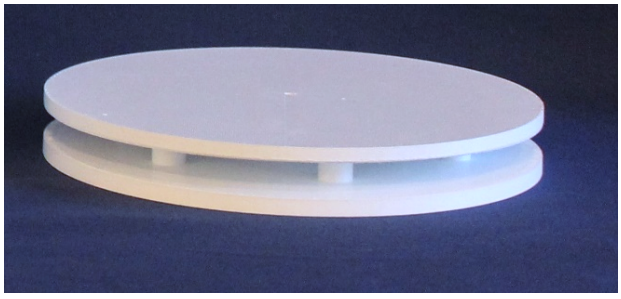

Figure 2-48 - SISO - Four Stage Prototype with Quarter Inch Stages - Prototype

2.6 Multiple Input Multiple Output Systems

The next phase of the prototypes combined AMM consisting of interconnected cavities with the top performing SISO prototype. The experimental testing results used to determine the top performing SISO prototype are discussed in section 3.5.5.

Two panels 7.5” in diameter consisting of 37 cells of either SP or BF AMM were designed and manufactured. After the SP and BF AMM prototypes were manufactured, the concept of a COOP was conceived. The SISO prototype with a COOP was then manufactured and tested. Experimental testing, outlined in section 3.5.1.9, indicated the feature was substantially

beneficial to the overall performance. The subsequent MIMO prototypes contained the feature making the top performing SISO prototype the SDN with RAP with a COOP. This configuration will now be referred to as the BF of the AMM. The BF configuration consisted of 0.25" stages. The enclosure walls consisting of outer cell walls and stage division walls served as the foundation of the AMM. Using these walls, a series of interconnected cavities, which is the AMM of the structure, were created. The dimensions of the MIMO configurations are shown in Table 2-4.

2.6.1 Straight Pipe

In order to access the performance of the MIMO systems, a control panel consisting of SP cells was created. The dimensions are shown in Table 2-4. Figure 2-49 shows a cross-sectional view from the cell CAD model. Figure 2-50 shows a vertical cross-sectional view from the CAD model. Figure 2-51 shows a horizontal cross-sectional view from the CAD model. Figure 2-52 shows an isometric view from the CAD model. Figure 2-53 shows the finished prototype.

Geometry Feature	Value (in)
Overall Thickness	1
Stage Length	0.25
Input Diameter	0.125
Output Diameter	0.3125
Perforated Hole Diameter	0.04
Wall Thickness	0.03125
Hexagonal Radius	.375

Table 2-4 - Geometry Details of MIMO Prototypes

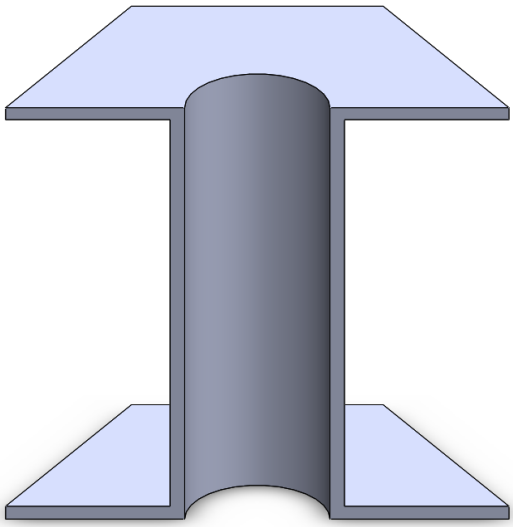

Figure 2-49 - MIMO - Straight Pipe Cell - CAD

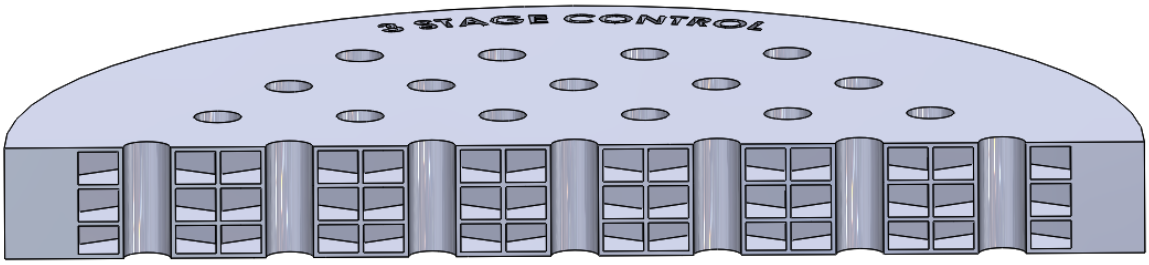

Figure 2-50 - MIMO - Straight Pipe Panel - CAD - Vertical Cross-Section View

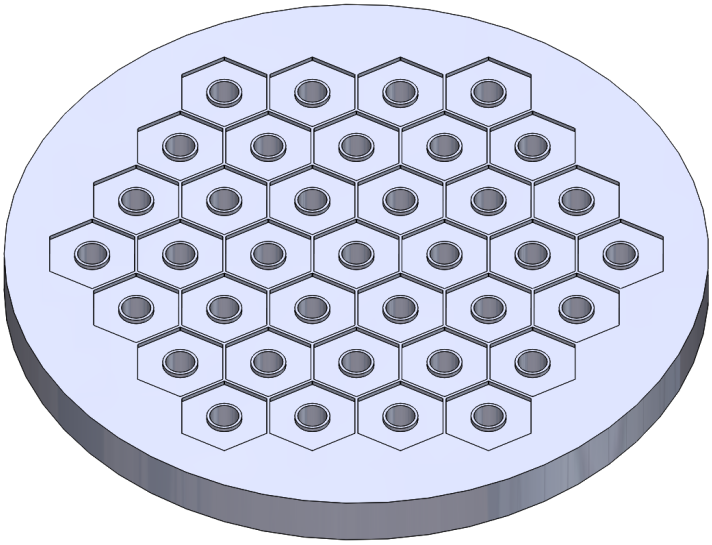

Figure 2-51 - MIMO - Straight Pipe Panel - CAD - Horizontal Cross-Section View

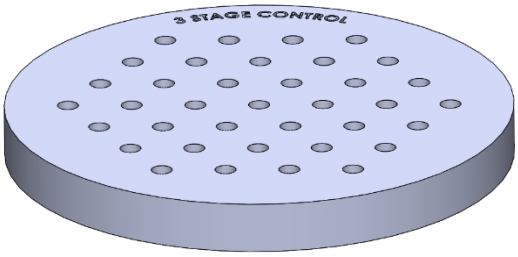

Figure 2-52 - MIMO - Straight Pipe Panel - CAD

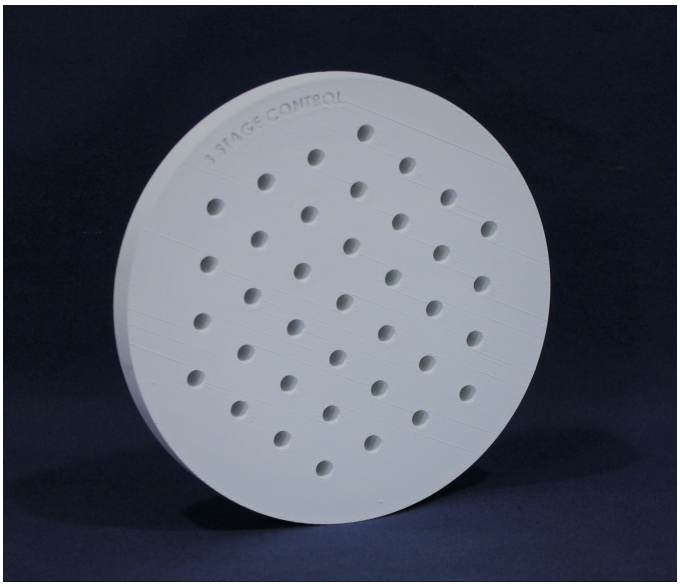

Figure 2-53 - MIMO - Straight Pipe Panel - Prototype

2.6.2 Base Feature Acoustic Metamaterials

In order to establish a control for the performance of the interconnected cavity AMM designs, a panel consisting of cells of the BF AMM was created. The panel does not include stage division walls, cell walls, or the COOP feature as discussed in section 2.6. The dimensions are shown in Table 2-4. Figure 2-54 shows a cross-sectional view from the cell CAD model. Figure 2-55 shows a vertical cross-sectional view from the CAD model. Figure 2-56 shows a horizontal cross-sectional view from the CAD model. Figure 2-57 shows an isometric view from the CAD model. Figure 2-58 shows the forward view of finished prototype and Figure 2-59 shows the aft view of the finished prototype.

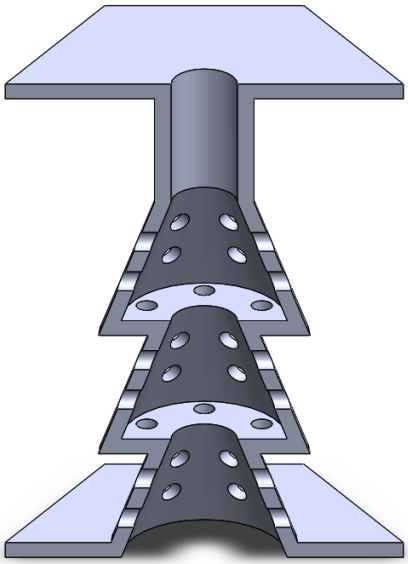

Figure 2-54 - MIMO - Base Feature AMM Cell - CAD

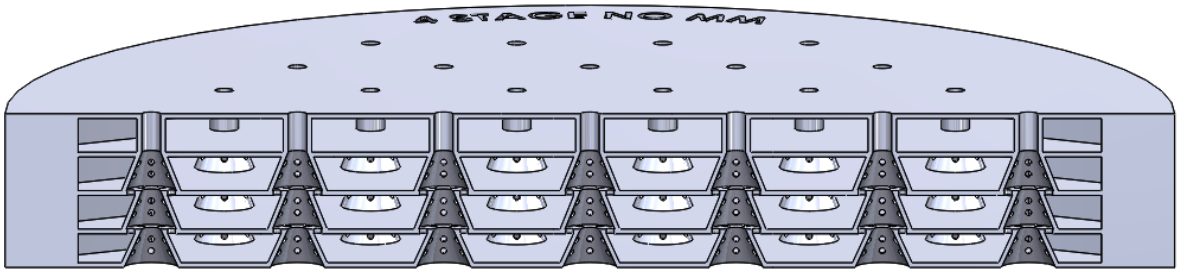

Figure 2-55 - MIMO - Base Feature AMM Panel - CAD - Vertical Cross-Section View

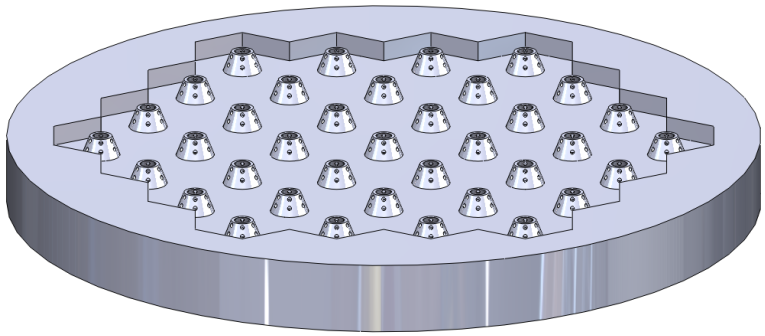

Figure 2-56 - MIMO - Base Feature AMM Panel - CAD - Horizontal Cross-Section View

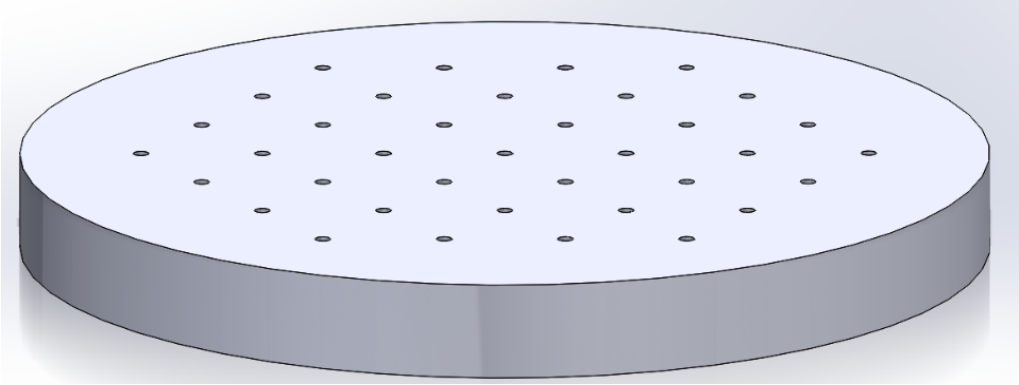

Figure 2-57 - MIMO - Base Feature AMM Panel - CAD

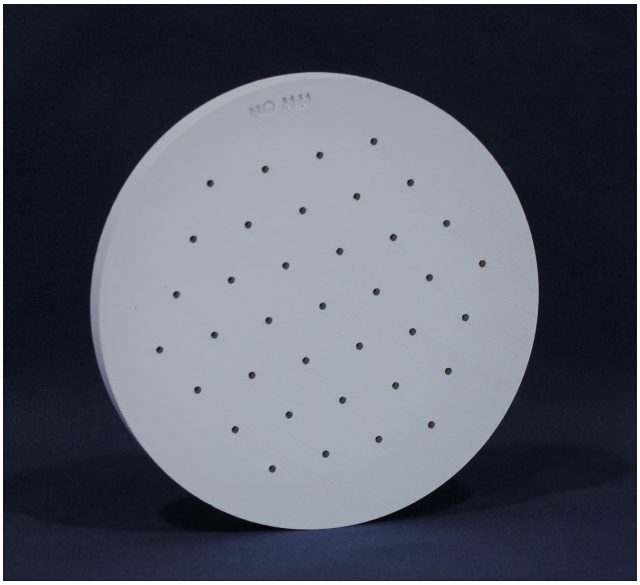

Figure 2-58 - MIMO - Base Feature AMM Panel - Prototype - Forward View

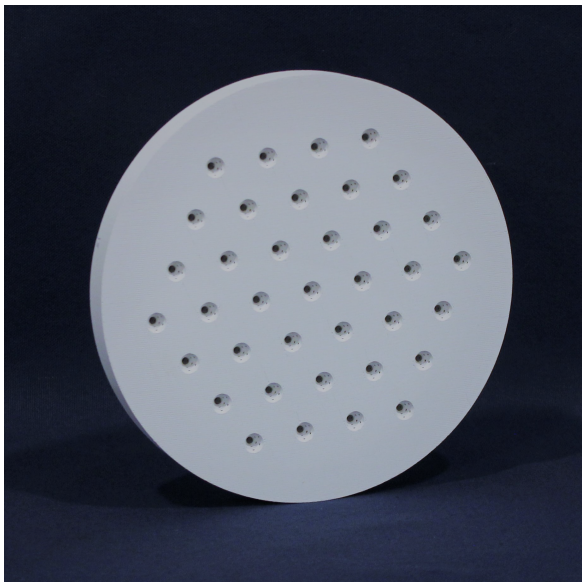

Figure 2-59 - MIMO - Base Feature AMM Panel - Prototype - Aft View

2.6.3 Large Cavity Acoustic Metamaterials

The first interconnected cavity AMM design utilized the enclosure walls as a base for the AMM interconnected cavity design. In the area between the nozzle and the enclosure walls, a bisecting wall from the base of the nozzle to the top of the stage was added. The top of the bisecting wall intersected with the upper hexagonal corners of the cell. In order to design the bisecting wall to connect a circle with a hexagon, the bisecting wall was swept around the base of the nozzle. This design results in the wall being disconnected from the entire upper perimeter of the cavity, but the entire bisecting wall is connected to the outer cell walls. This bisecting wall divided the stage cavity into an inner and outer section, resulting in 2 cavities surrounding the nozzle in each stage. Six perforations were made in the bisecting wall to connect the inner and outer cavities. Six perforations were added to each stage division wall, connecting the outer cavity to the subsequent stage's internal cavity. The APs of each nozzle were connected to the subsequent stage's internal cavity, allowing the stages to be connected by the nozzles and the inner cavities. The outer cell walls were modified to have perforations to connect the cell to

adjacent cells. The perforations connected each outer cavity to the adjacent cell's outer cavity. Each stage of the hexagonal cell contained 6 perforations with 1 perforation per side of the hexagon. The Large Cavity AMM included the COOP.

The dimensions are shown in Table 2-4. Figure 2-60 shows a vertical cross-sectional view from the cell CAD model and Figure 2-61 shows a horizontal cross-section from the cell CAD model. Figure 2-62 shows an isometric view from the cell CAD model. Figure 2-63 shows a vertical cross-sectional view from the panel CAD model. Figure 2-64 shows a horizontal cross-sectional view from the panel CAD model. Figure 2-65 shows an isometric view from the CAD panel model. Figure 2-66 shows the forward and aft view of finished prototype. Due to the COOP, the forward and aft views are identical.

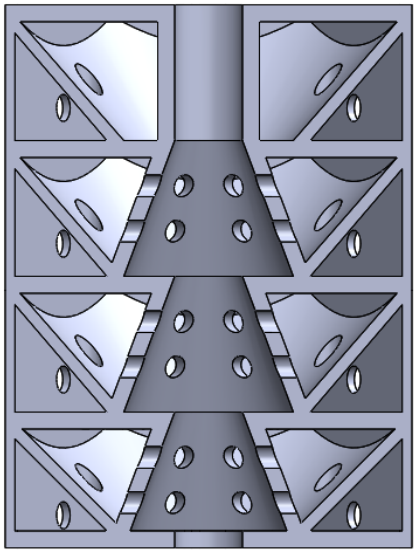

Figure 2-60 - MIMO - Large Cavity AMM Cell - CAD - Vertical Cross-Section View

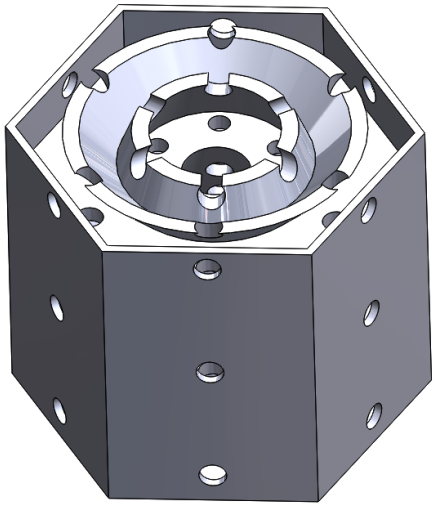

Figure 2-61 - MIMO - Large Cavity AMM Cell - CAD - Horizontal Cross-Section View

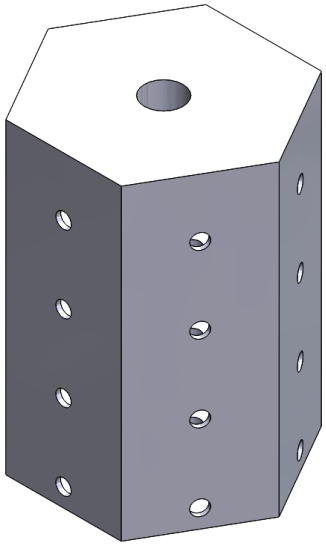

Figure 2-62 - MIMO - Large Cavity AMM Cell - CAD

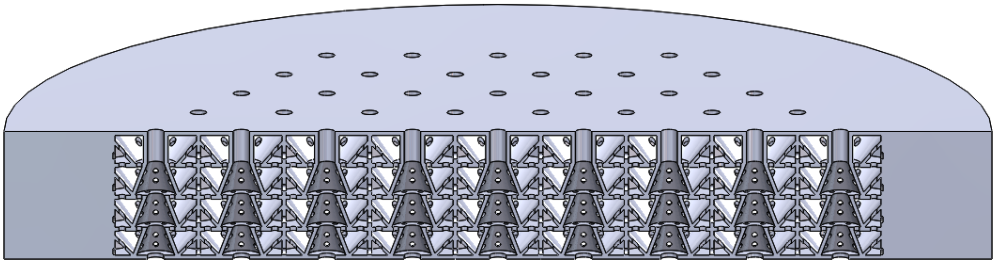

Figure 2-63 - MIMO - Large Cavity AMM Panel - CAD - Vertical Cross-Section View

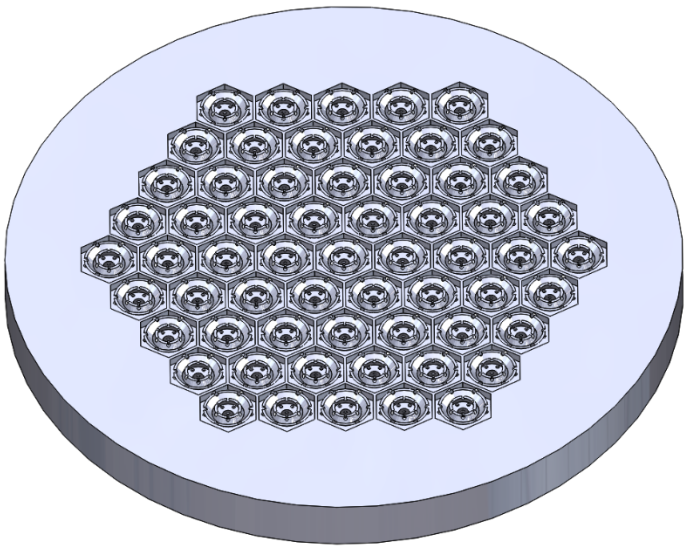

Figure 2-64 - MIMO - Large Cavity AMM Panel - CAD - Horizontal Cross-Section View

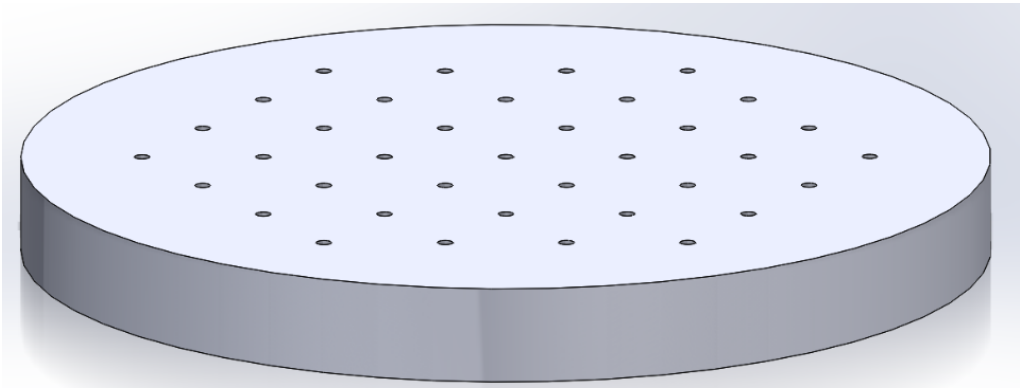

Figure 2-65 - MIMO - Large Cavity AMM Panel - CAD

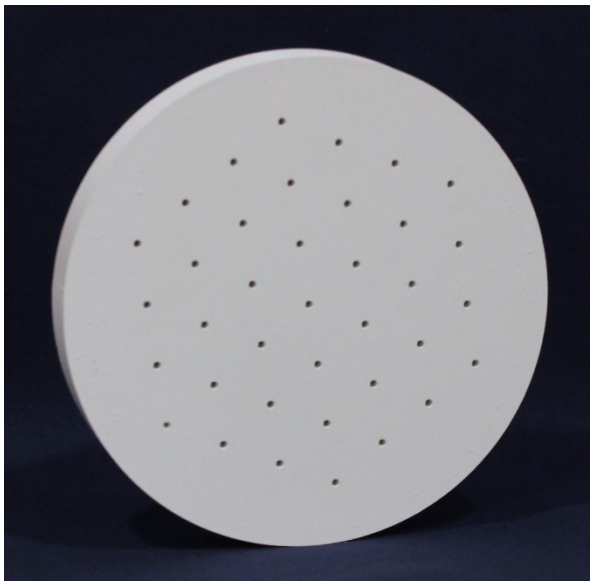

Figure 2-66 - MIMO - Large Cavity AMM Panel - Prototype

2.6.4 Small Cavity Acoustic Metamaterials

The Small Cavity AMM added structure to the design of the Large Cavity AMM and does contain the COOP. In each stage, 6 vertical walls were added to connect the nozzle's outer cell walls with each hexagonal corner of the cell. These vertical walls divided each stage's inner and outer cavities into 6 sections, for a total of 12 interconnected cavities per stage. Perforations in the vertical walls were added to connect each inner stage to the adjacent inner stage. Identical perforations were made in order to connect the outer cavities.

The dimensions are shown in Table 2-4. Figure 2-67 shows a vertical cross-sectional view from the cell CAD model and Figure 2-68 shows a horizontal cross-sectional from the cell CAD model. Figure 2-69 shows an isometric view from the cell CAD model. Figure 2-70 shows a vertical cross-sectional view from the CAD model. Figure 2-71 shows a horizontal cross-sectional view from the CAD model. Figure 2-72 shows an isometric view from the CAD model. Figure 2-73

shows the forward and aft view of the finished prototype. Due to the COOP, the input and output diameters are equal, therefore the forward and aft views are identical.

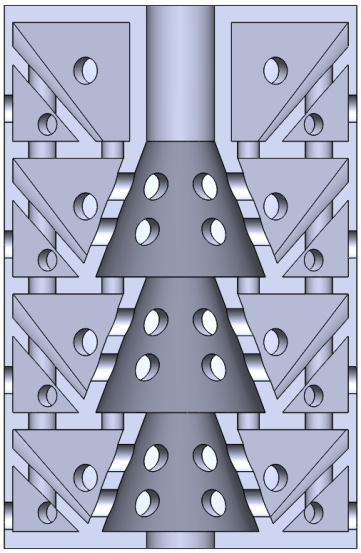

Figure 2-67 - MIMO - Small Cavity AMM Cell - CAD - Vertical Cross-Section View

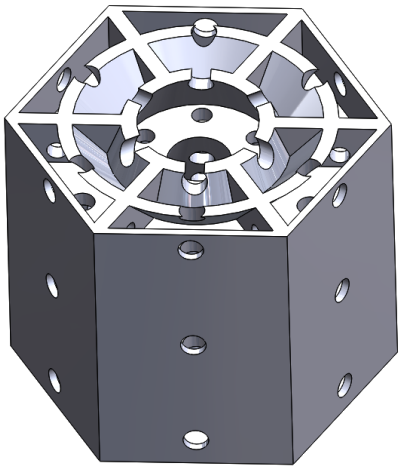

Figure 2-68 - MIMO - Small Cavity AMM Cell - CAD - Horizontal Cross-Section View

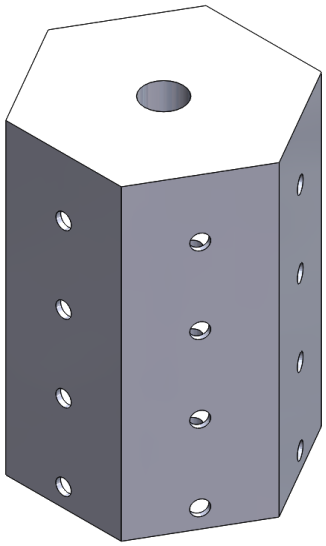

Figure 2-69 - MIMO - Small Cavity AMM Cell - CAD

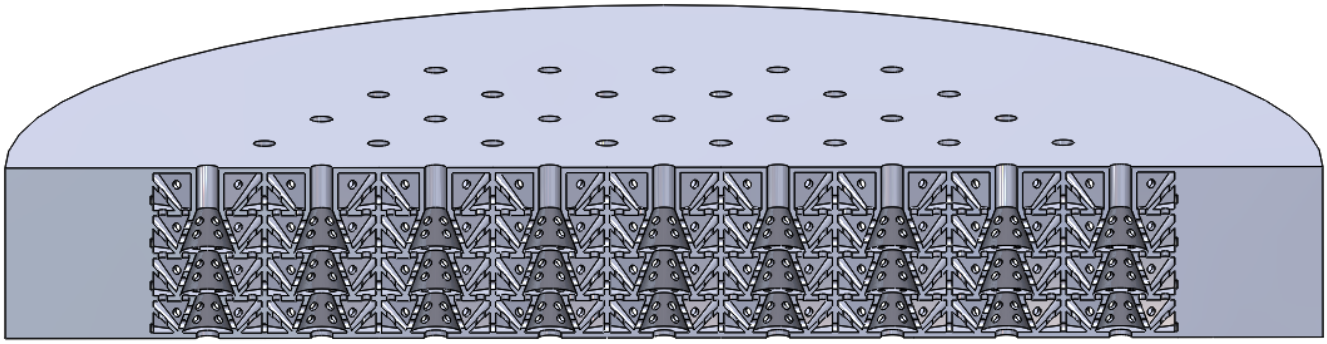

Figure 2-70 - MIMO - Small Cavity AMM Panel - CAD - Vertical Cross-Section View

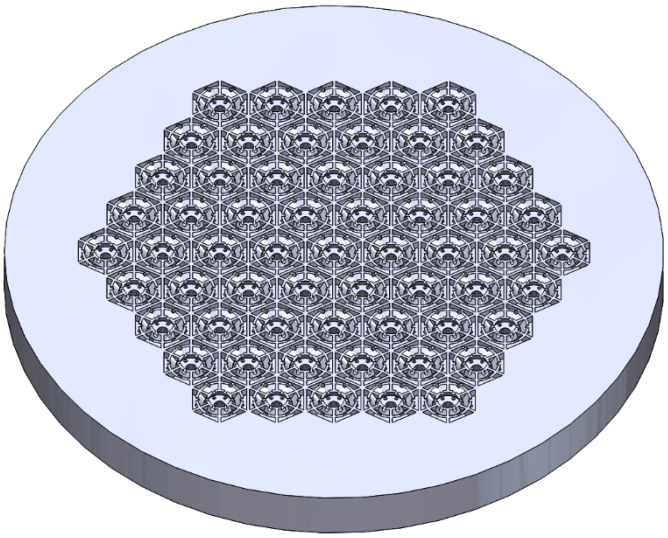

Figure 2-71 - MIMO - Small Cavity AMM Panel - CAD - Horizontal Cross-Section View

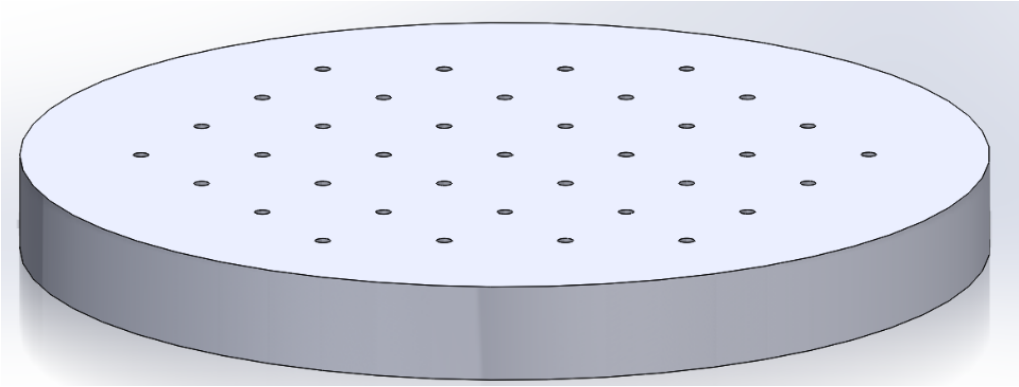

Figure 2-72 - MIMO - Small Cavity AMM Panel - CAD

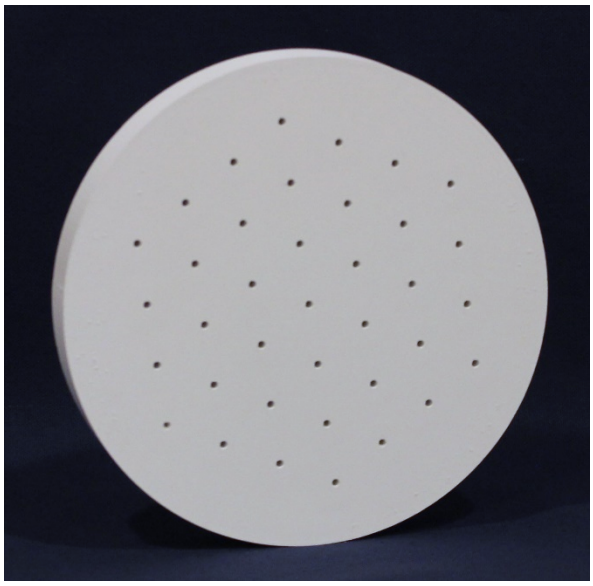

Figure 2-73 - MIMO - Small Cavity AMM Panel - Prototype

2.6.5 Infill Acoustic Metamaterials

Infill AMM consisting of a porous hexagonal material surrounded the BF AMM and replaced the outer cell walls, the stage division walls, and the interconnected cavity AMM walls. The Infill AMM BF AMM includes the COOP. Due to the nature of the additive manufacturing software, a gap of 0.01" separates the BF AMM and the Infill AMM in the CAD model. The 0.01" gap between the BF AMM and the Infill AMM does not exist in the manufactured part. The BF AMM dimensions are shown in Table 2-4. Figure 2-74 shows a vertical cross-section from the cell CAD model. The Infill AMM is shown as a solid surrounding the BF AMM. Figure 2-75 shows the porous hexagonal material that created the Infill AMM. Figure 2-76 shows an isometric view from the panel CAD model. Figure 2-77 shows the forward and aft view of the finished prototype. Due to the COOP, the forward and aft views are identical.

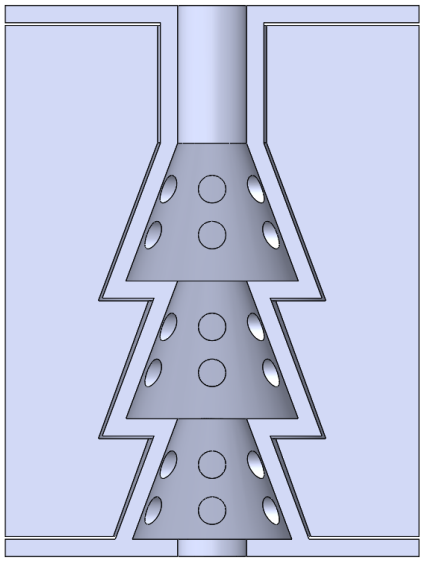

Figure 2-74 - MIMO - Infill AMM Cell - CAD - Vertical Cross-Section

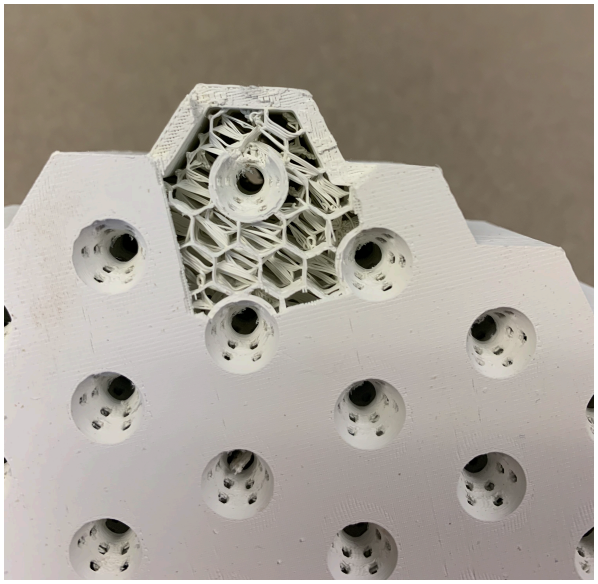

Figure 2-75 - MIMO - Infill AMM

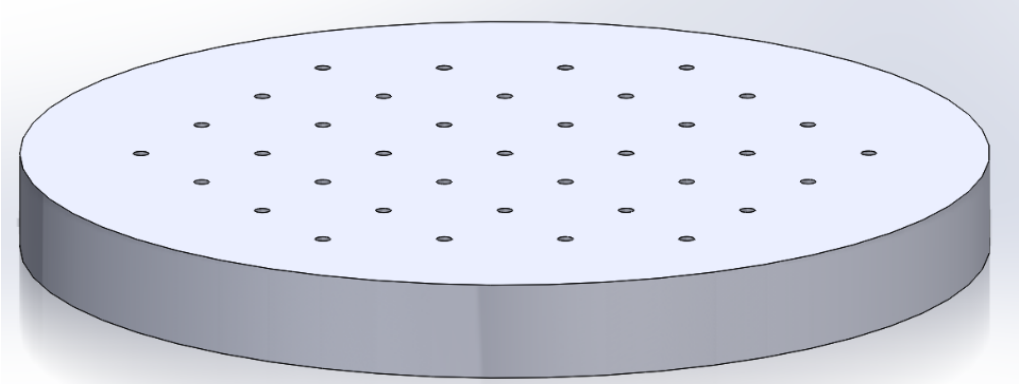

Figure 2-76 - MIMO - Infill AMM Panel - CAD

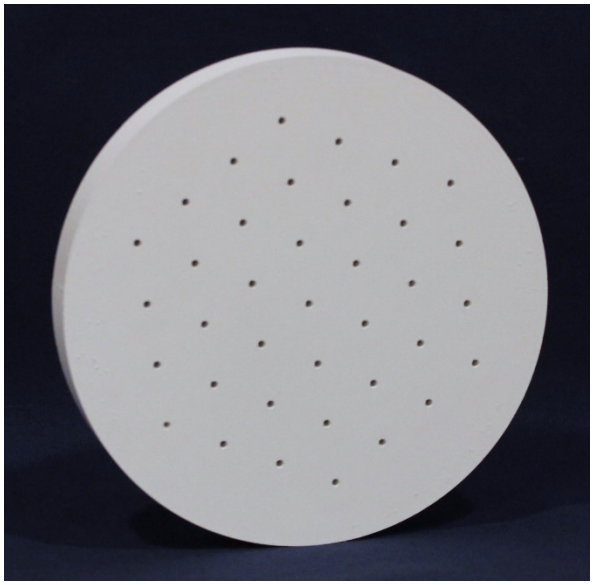

Figure 2-77 - MIMO - Infill AMM Panel - Prototype

2.7 Acoustic Metamaterial Sphere Design

The final phase of the research focused on taking the results from section 3.6.6 and modifying the cell for use in a spherical design. The Small Cavity AMM was the top performing MIMO design. The modified Small Cavity AMM design retained the dimensions from Table 2-4 but incorporated curvature to support a spherical design. The AMM Sphere had an inner radius of 6” and an outer radius of 7”, therefore the AMM Sphere maintained the 1” thickness from the panel prototypes.

The AMM Sphere consisted of 2 sections each consisting of 115 cells. The AMM Sphere Top has grooves to ensure a solid fit onto the AMM Sphere Base. The AMM Sphere Base has a perforated platform for instrumentation mounting in order to verify the performance of the system. Both parts contain a groove for instrumentation cabling. Additionally, a test stand was constructed.

A sphere cannot consist entirely of hexagons. Some cells would need to be pentagons in order to fully encapsulate the interior cavity. Due to this constraint, each cell is surrounded by a minimal amount of empty space. In addition, manufacturing required the empty space around the cells in order to prevent the build from collapsing during manufacturing due to excess heat.

Figure 2-78 shows a vertical cross-sectional view from the cell CAD model. Figure 2-79 shows a vertical cross-section from the AMM Sphere Top CAD model. Figure 2-80 shows the top view from the AMM Sphere Top CAD model and Figure 2-81 shows the bottom view from the AMM Sphere Top CAD model. Figure 2-82 shows the top view from the AMM Sphere Top finished prototype. Figure 2-83 shows the bottom view from the AMM Sphere Top finished prototype. Figure 2-84 shows a vertical cross-sectional view from the AMM Sphere Base CAD model. Figure 2-85 shows a top view from the AMM Sphere Base CAD model and Figure 2-86 shows the bottom view from the AMM Sphere Base CAD model. Figure 2-87 shows the top view from the AMM Sphere Base and Figure 2-88 shows the bottom view from the AMM Sphere Base. Figure 2-89 shows the assembled AMM Sphere CAD model. Figure 2-90 shows a vertical cross-sectional view from the assembled AMM Sphere CAD model. Figure 2-91 and Figure 2-92 shows isometric and forward views of the finished, assembled prototype and stand, respectively.

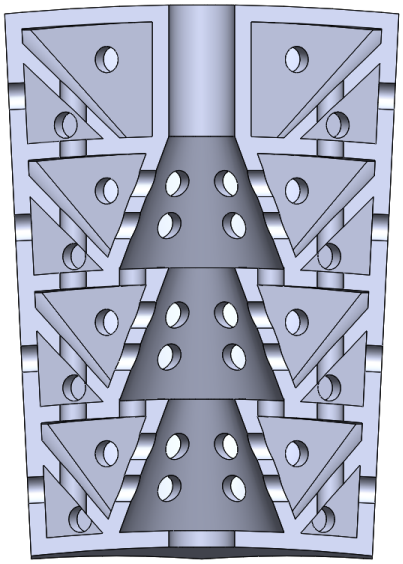

Figure 2-78 - AMM Sphere - Cell - CAD - Vertical Cross-Section View

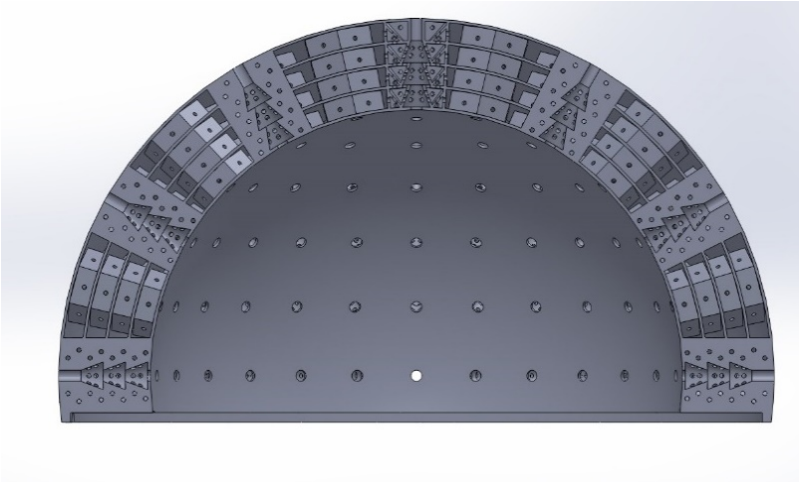

Figure 2-79 - AMM Sphere - Top - CAD - Vertical Cross-Section View

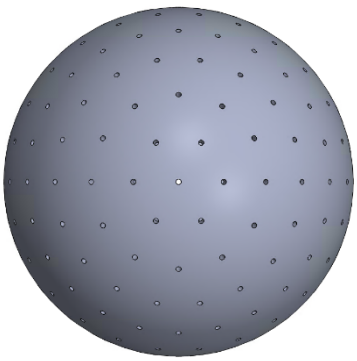

Figure 2-80 - AMM Sphere - Top - CAD - Top View

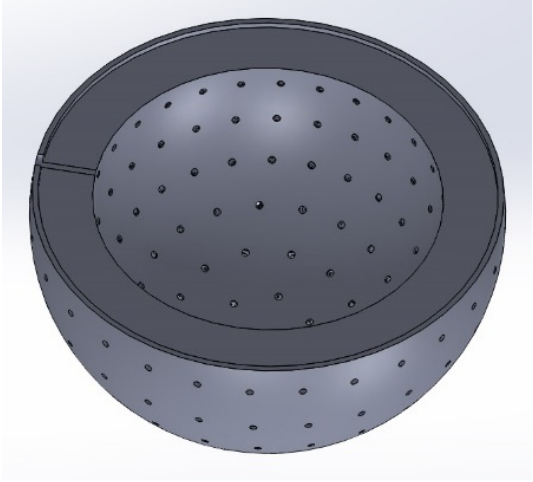

Figure 2-81 - AMM Sphere - Top - CAD - Bottom View

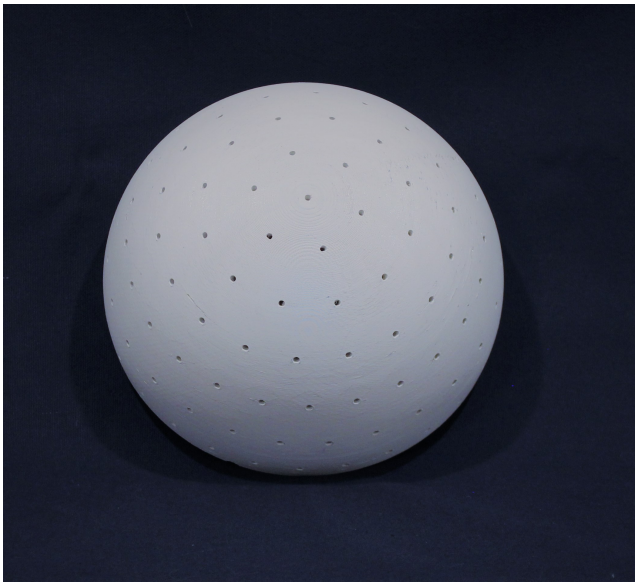

Figure 2-82 - AMM Sphere - Top - Prototype - Top View

Figure 2-83 - AMM Sphere - Top - Prototype - Bottom View

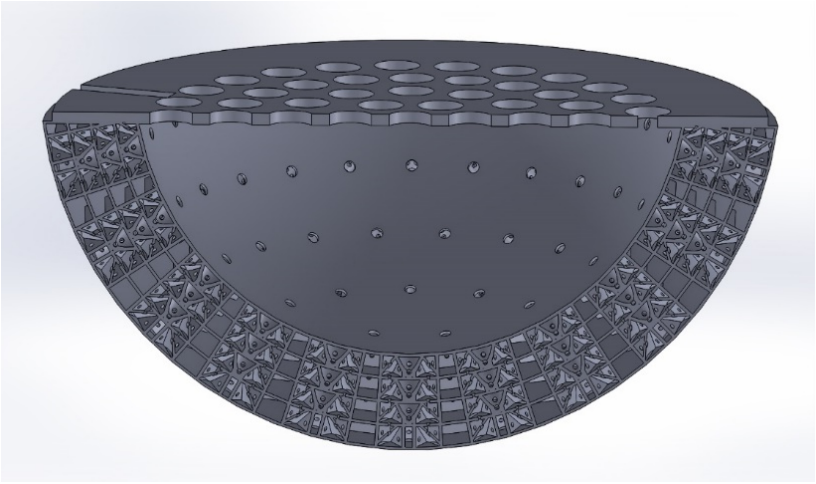

Figure 2-84 - AMM Sphere - Base - CAD - Vertical Cross-Section View

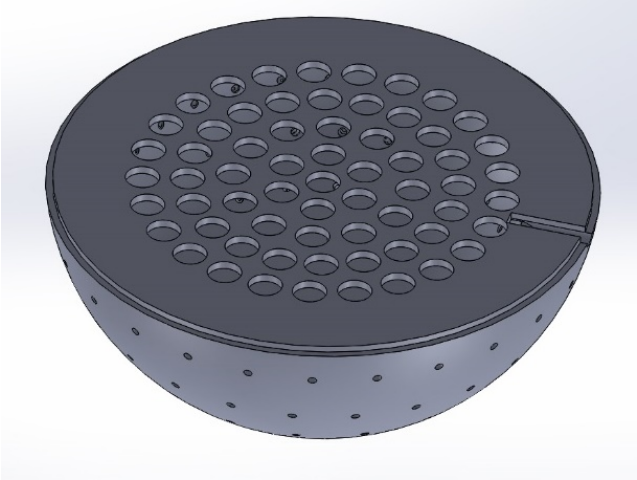

Figure 2-85 - AMM Sphere - Base - CAD - Top View

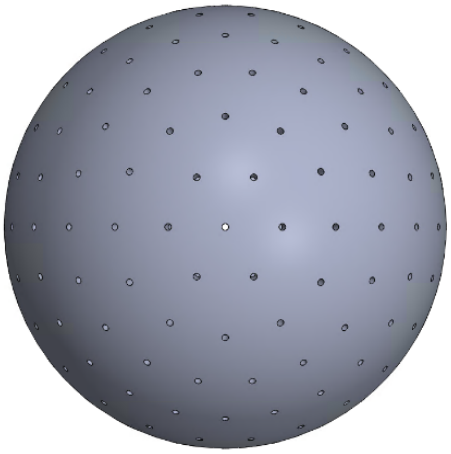

Figure 2-86 - AMM Sphere - Base - CAD - Bottom View

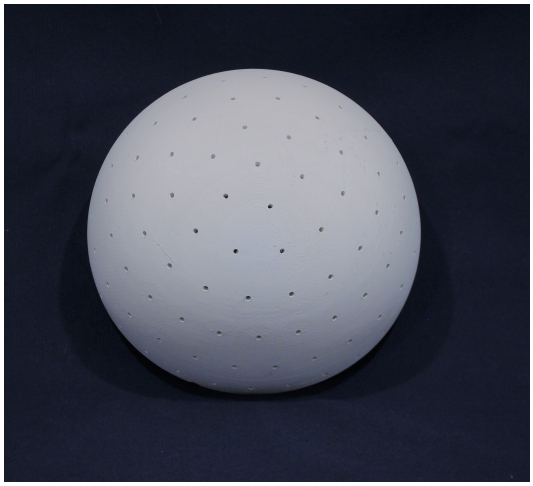

Figure 2-87 - AMM Sphere - Base - Prototype - Top View

Figure 2-88 - AMM Sphere - Base - Prototype - Bottom View

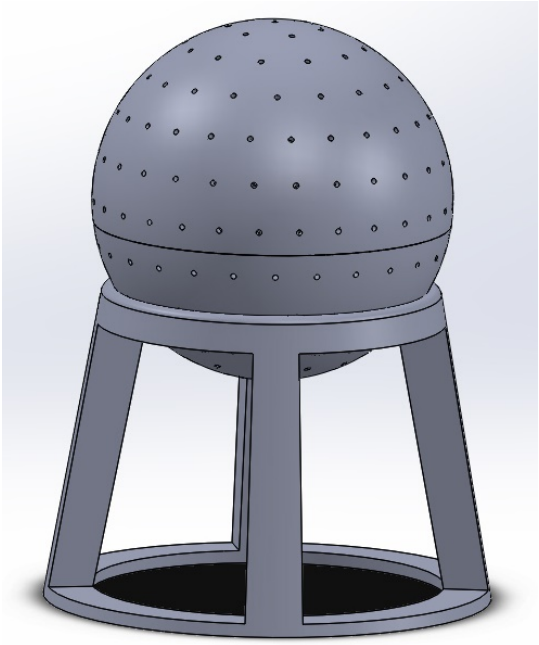

Figure 2-89 - Assembled AMM Sphere - CAD

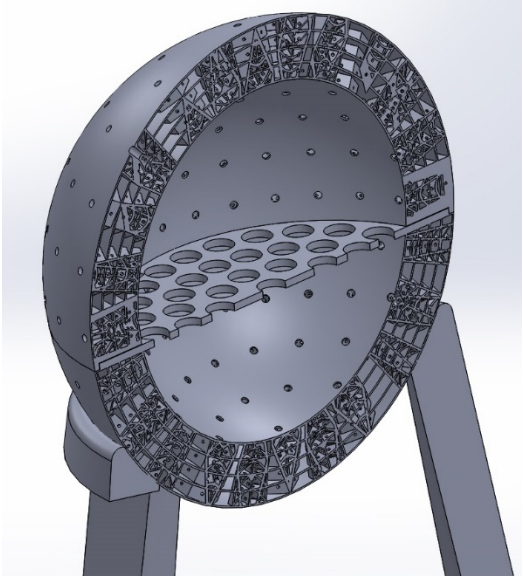

Figure 2-90 - Assembled AMM Sphere - CAD - Vertical Cross-Section View

Figure 2-91 - Assembled AMM Sphere - Prototype - Isometric View

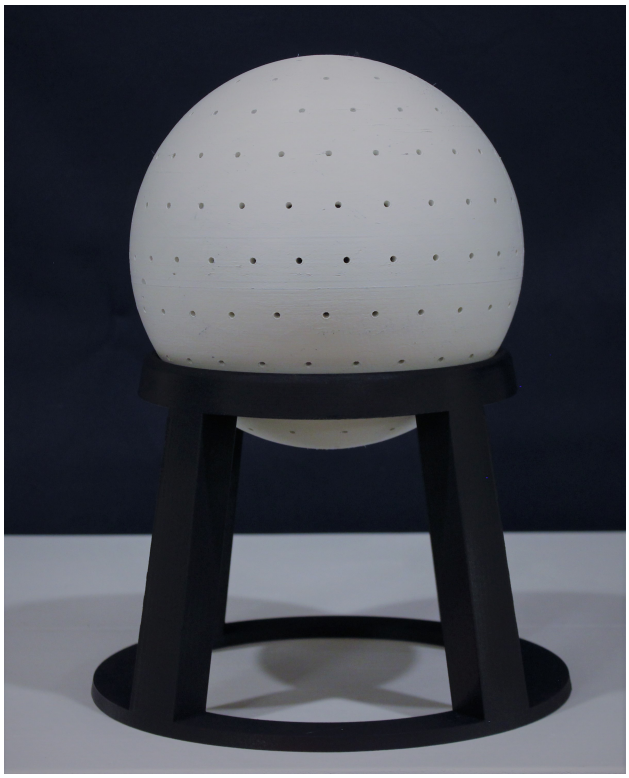

Figure 2-92 - Assembled AMM Sphere - Prototype - Forward View

2.8 Prototypes Summary

Beginning the design phase with a simple SISO system then adding complexity allowed an optimal SISO configuration to be determined. Building on the SISO BF AMM design allowed the modular stage, cell, and panel designs to emerge. Consequently, the requirement of a modular, configurable system was met.

In order to meet the compact footprint requirement, the cell of the BF AMM was downsized. This modular, compact cell was the basis for the design of the MIMO AMM configurations. The development and experimental testing of the MIMO prototypes allowed the optimal AMM design to be selected and provided the basis for the spherical cell design. The AMM Sphere met the final design requirement of omnidirectionally.

Chapter 3: Experimental Test

"All life is an experiment. The more experiments you make the better."

-Ralph Waldo Emerson [37]

As discussed in chapters 1 and 2, experimental testing was crucial to the design process by providing a metric to compare features and evaluate designs so that the best configuration progressed into the next phase of the research. The testing is grouped into 3 categories: SISO, MIMO, and AMM Sphere. Test setups were designed to allow for repeatability, test article interchangeability, and consistency across the phases of the research.

Experimental test data was processed in such a way that one can easily determine performance across the entire acoustic spectrum. Processing the data into graphs of Fast Fourier Transforms (FFTs), spectrograms, time histories, and TL allow the reader to see the same data in multiple formats. Additionally, tabular data to compare TL for multiple bandwidths is presented. The bandwidths presented are 20 Hz to 5 kHz, 5 kHz to 10 kHz, 10 kHz to 15 kHz, 15 kHz to 20 kHz, and 20 Hz to 20 kHz.

3.1 Test Equipment

The data was collected using a DEWEsoft Sirius Mini Data Acquisition (DAQ) System. The 4 channel DAQ was connected to a laptop via 2 USB ports, one for power to the DAQ and the other for data collection. Two channels were used during testing, one for the input microphone and the other for the output microphone. PicoCoulomB (PCB) Piezotronics model 130F20 microphones were used for testing. The microphones were equipped with Transducer Electronic

Data Sheet (TEDS). Therefore, the DAQ calculated the sound pressure in Pascals using the measured voltage and the microphone sensitivity. In order to avoid any aliasing issues, the data was sampled at 100 kHz. Figure 3-1 shows the DAQ and laptop setup as well as the amplifier for the speaker. Figure 3-2 shows the DEWEsoft DAQ and Figure 3-3 shows the PCB microphone.

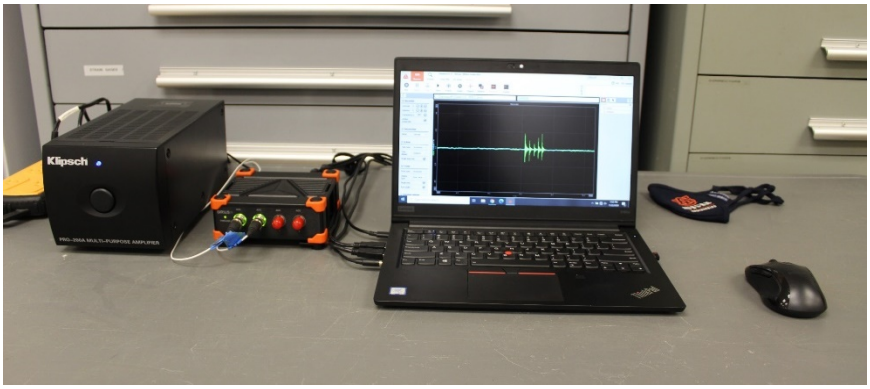

Figure 3-1 - Data Acquisition System Setup

Figure 3-2 - DEWEsoft Data Acquisition Hardware [38]

Figure 3-3 - Microphone - PCB [39]

The input sound was generated by a Klipsch RF-7 III speaker and a Klipsch RC-64 III speaker. The combination of multiple types of speakers was able to generate noise across the entire spectrum while maintaining a large overall sound pressure level (SPL). Figure 3-4 and Figure 3-5 show the speakers. The speakers were controlled by a Klipsch PRO-200A amplifier shown in Figure 3-6.

Figure 3-4 - Test Speaker - Klipsch RF-7 III [40]

Figure 3-5 - Test Speaker - Klipsch RC-64 III [41]

Figure 3-6 - Test Speaker Amplifier - Klipsch PRO-200A [42]

In order to create the test setups described in section 3.4, acoustic insulation was required. Owens Corning 703 Rigid Fiberglass with a 4” thickness was used. Due to the number of test configurations, the test article and setup required a significant amount of handling. Since the fiberglass in the acoustic insulation is a skin irritant, cotton covers were manufactured for personal protective equipment (PPE). Figure 3-7 shows 4” sheets of the acoustic insulation.

Figure 3-7 - Owens Corning 703 Rigid Fiberglass [43]

3.2 Test Input

To provide input noise that was consistent across the acoustic spectrum, Gaussian white noise (GWN) was used. Using MATLAB code, 10 seconds of GWN was generated and converted in to a *.wav audio file. In order to verify the audio file, the GWN was plotted in the time domain, as a spectrogram, and as FFT data. The verified sound file graphs are shown in Figure 3-8. The code used to generate and verify the GWN is available in Appendix A-5.

In order to validate performance of the test equipment, a recording of the input sound without any test articles or setup was created. The same graphs used to verify the audio file were used to evaluate test equipment performance. The graphs are shown in Figure 3-9 and the MATLAB code is shown in Appendix A-6.

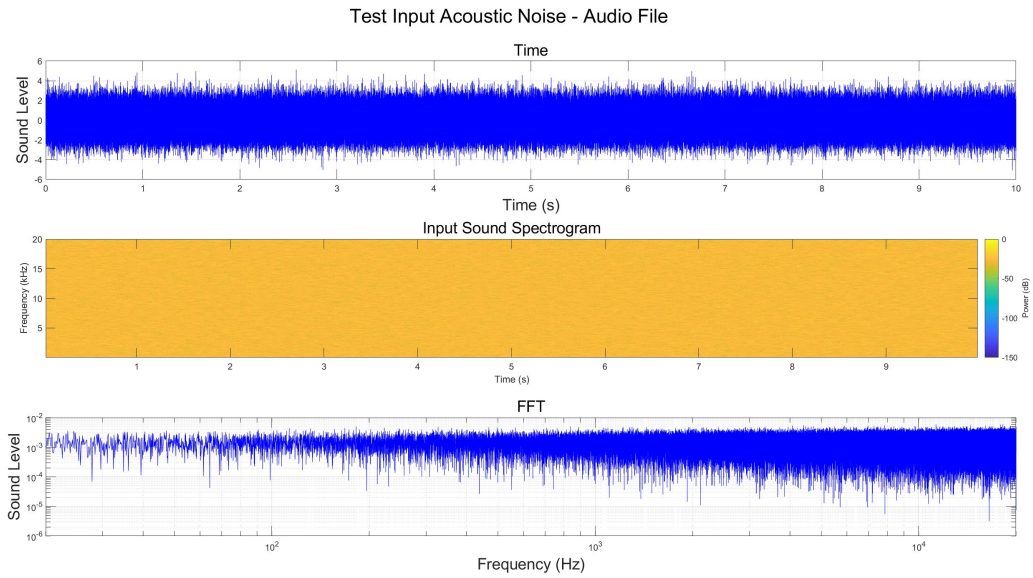

Figure 3-8 - White Noise - Audio File Verification

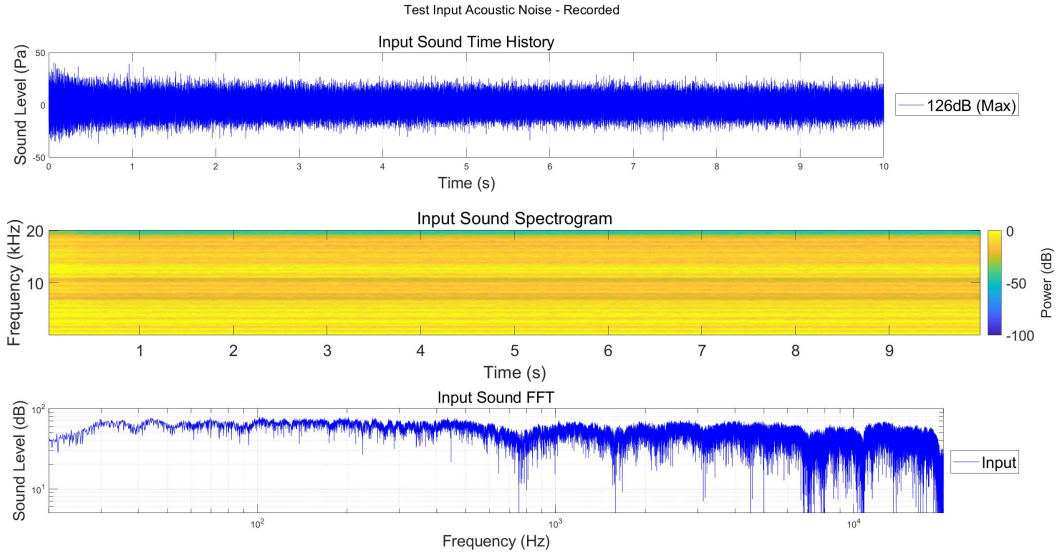

Figure 3-9 - White Noise - Input Sound Verification

3.3 Experimental Test Data Processing

All of the experimental test data presented in this dissertation is presented in the same format with the same limits on the axis. The data is presented in a 3x2 matrix. Within the composite data plot, position (1,1) is the input noise time history, position (1,2) is the output

noise time history, position (2,1) is the input noise spectrogram, position (2,2) is the output noise spectrogram, position (3,1) consists of the input and output noise FFTs, and position (3,2) is the transmission loss of the system. In position (3,1), the input data FFT data is always presented in blue and the output data FFT data is always presented in red. Experimental test configurations are compared by using TL plots. The TL was calculated using equations 1.6 and 1.7. The MATLAB script used to process and plot the time data is available in Appendix A-7.

3.4 Description of SISO and MIMO Test Setup

For the fundamental feature SISO testing, a wooden anechoic box was built. The box contained 2 internal sections. The first section housed the test article and the second section contained instrumentation and insulation. Surrounding the test article, acoustic insulation described in section 3.1 was used to surround the test article. In order to reduce test setup time, the insulation was configured into 2 pieces. In the instrumentation section of the test box, the acoustic insulation was configured so that the only sound that could reach the microphone had to come through the test article. Additionally, there was empty space surrounding the instrumentation to ensure that the acoustic insulation did not affect experimental test results. A microphone stand was affixed to insulation to ensure the location within the box was consistent.

The box contained grooves in order for the test article to be easily interchangeable. The flanges on each end of the SISO prototypes described in section 2.2 fit into the grooves. In the grooves above the test article, wooden inserts were added in order to completely isolate the sections of the test box. Once the test article and instrumentation were installed in the box and the acoustic insulation was in place, the lid to the box was latched shut. The input microphone

was placed on a stand near the input of the test article. The speakers were located approximately 3 feet from the test box.

Figure 3-10 shows the test box without all of the insulation installed. The input microphone is shown on the left, in the middle is the test article chamber with the test article shown in white, and on the right the microphone is shown surrounded by acoustic insulation. Figure 3-11 shows the test box with all of the insulation installed. Figure 3-12 shows an overview of the test box and speaker location. Figure 3-13 shows the input side of the test article and the input microphone on the Forward of the test box.

The figures shown below have 4 microphones in the test setup. In order to validate the equations derived in sections 1.3.3 and 1.3.4, 2 microphones a known distance apart were required. The 2 microphones allowed for measurements of the input and output sound velocity. The microphones were mounted to a fixture with nylon inserts between the microphones. In addition, the fixture geometry was known and placed directly on the test box. Consequently, the distance between the microphone and the input and output planes was known. For the results presented in section 3.4, only the microphones closest to the test article were used.

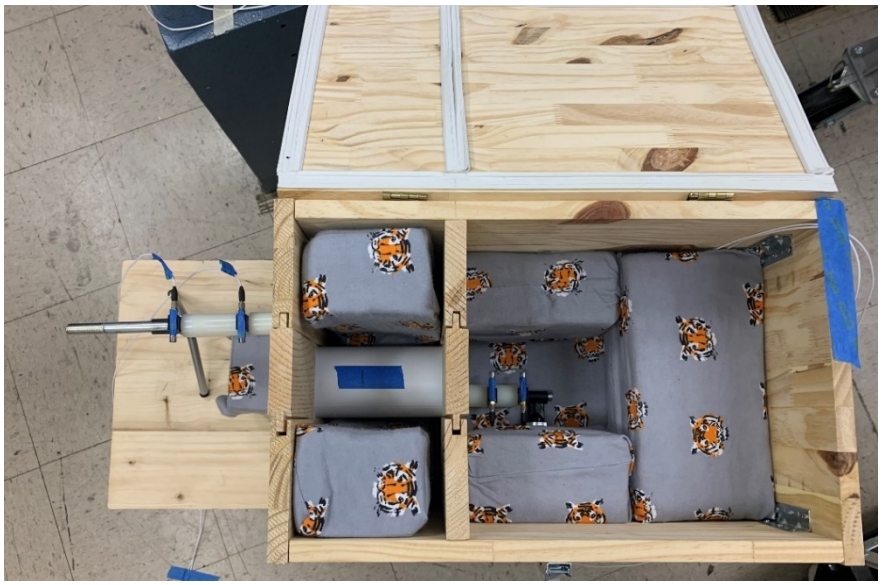

Figure 3-10 - SISO - Test Box - Inner Box without Insulation View

Figure 3-11 - SISO - Test Box - Inner Box with Insulation View

Figure 3-12 - SISO - Test Setup - Speakers and Test Box

Figure 3-13 - SISO - Test Setup - Test Box - Forward View

The remaining SISO testing and the MIMO testing was set up similarly to the fundamental feature SISO testing. A wooden anechoic box was built. The forward of the test box and the rear

panel support contained a 7” diameter hole with 7.5” diameter countersink, which was 0.375” deep. This allowed the test article to be installed between the forward of the test box and the support wall. Since the MIMO testing required numerous sized prototypes ranging from 8” to 3/4 of an inch in thickness, the rear panel support wall was created to be movable. Consequently, this required the acoustic insulation to be modular. This modularity of the acoustic insulation ensured that the rear panel support had adequate contact with the test article and that the instrumentation chamber was acoustically isolated. Figure 3-14 and Figure 3-15 show test articles of different sizes and the associated configurations of the modular acoustic insulation. Figure 3-14 shows a larger test article in white. Figure 3-15 shows the setup for a 3/4” thick test article. Consequently, the test article is not visible in the fixture, but the additional acoustic insulation is installed.

The rear section of the box contained insulation and instrumentation. Like the SISO test box, the acoustic insulation was configured so that the sound that could only reach the microphone through the test article. Additionally, there was empty space surrounding the instrumentation to ensure that the acoustic insulation did not muffle or affect the test results. The microphone was affixed to the insulation to ensure the location within the box was consistent. The location of the microphone was fixed with respect to the rear panel support wall. This ensured that the output microphone location was consistent for all sizes of MIMO test articles. The input microphone was placed on a clamped mount near the input of the test article. The speakers were located approximately 3 feet from the test box.

Figure 3-16 shows the output instrumentation within the test box and without all of the insulation installed. Figure 3-17 shows an overview of the test box and speaker location. Figure

3-18 shows the input of the test article and the input microphone on the forward end of the test box.

Figure 3-14 - MIMO Test Box - Inner Box with Larger Prototype

Figure 3-15 - MIMO Test Box - Inner Box with Smaller Prototype

Figure 3-16 - MIMO Test Box - Inner Box Instrumentation

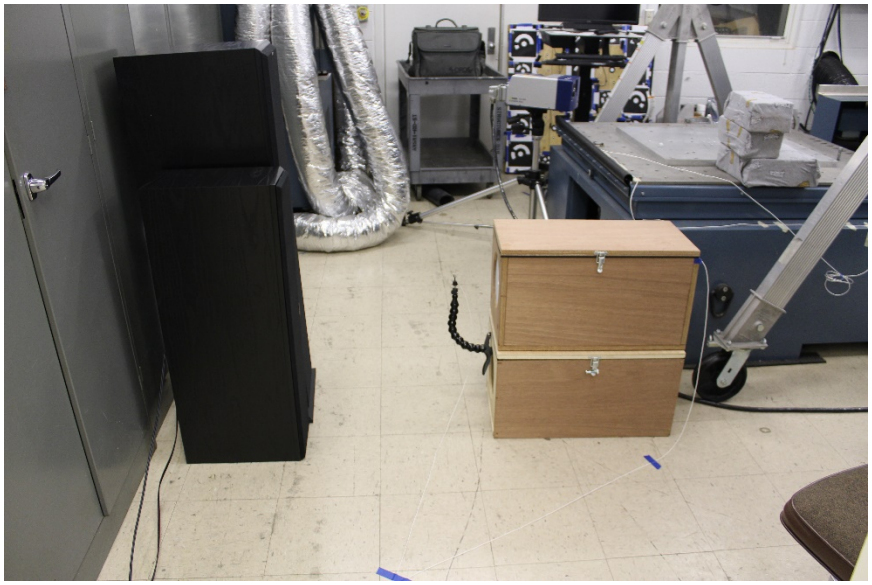

Figure 3-17 - MIMO Test Setup - Speakers and Test Box

Figure 3-18 - MIMO Test Setup - Test Box Overview

3.5 Single Input Single Output Systems

3.5.1 Single Input Single Output Fundamental Features Systems

The test articles described in section 2.2 were tested and evaluated for acoustic performance. The results of this testing allowed the BF AMM configuration to be identified. Testing results, comparison plots, and summary for the fundamental features SISO prototypes are available in section 3.5.1.9.

3.5.1.1 Effects of a Straight Pipe on Output Sound

Experimental testing results for the SP established a baseline for comparison of the prototypes. The time domain data decreased from 126 dB to 119 dB. From 600 Hz to 1 kHz, the acoustic output was amplified. Across the 20 Hz to 20 kHz bandwidth, the average transmission loss (TL_{avg}) equaled 4.8 dB. Figure 3-19 shows the input and output time history, spectrograms,

and FFTs as well as the TL across the acoustic spectrum. Table 3-1 details the TL_{avg} in the 20 Hz to 5 kHz, 5 kHz to 10 kHz, 10 kHz to 15 kHz, 15 kHz to 20 kHz, and 20 Hz to 20 kHz bandwidths.

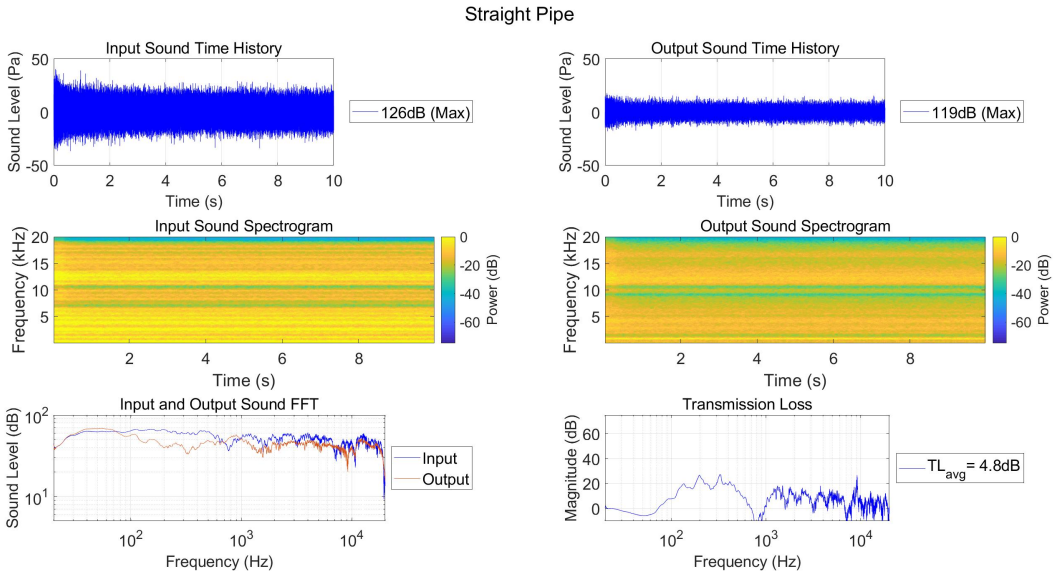

Figure 3-19 - SISO - Straight Pipe - Test Results

Average Transmission Loss (dB)					
Configuration	20 Hz - 5 kHz	5 kHz - 10 kHz	10 kHz - 15 kHz	15 kHz - 20 kHz	20 Hz - 20 kHz
SP	8.5	5.8	2.5	2.6	4.8

Table 3-1 - SISO - Straight Pipe - Average Transmission Loss

3.5.1.2 Effects of a Straight Pipe with Radial Perforations on Output Sound

Experimental testing results for the SP with RP indicated poor performance across the acoustic bandwidth. The time domain data decreased from 127 dB to 118 dB. The SP with RP contained amplified output from approximately 6 kHz to 7 kHz. Spectral gaps begin to appear at approximately 8 kHz to 10 kHz and 17 kHz to 20 kHz. Across the 20 Hz to 20 kHz bandwidth, the TL_{avg} equaled 5.6 dB. Figure 3-20 shows the input and output time history, spectrograms, and

FFTs as well as the TL across the acoustic spectrum. Table 3-2 details the TL_{avg} in the 20 Hz to 5 kHz, 5 kHz to 10 kHz, 10 kHz to 15 kHz, 15 kHz to 20 kHz, and 20 Hz to 20 kHz bandwidths.

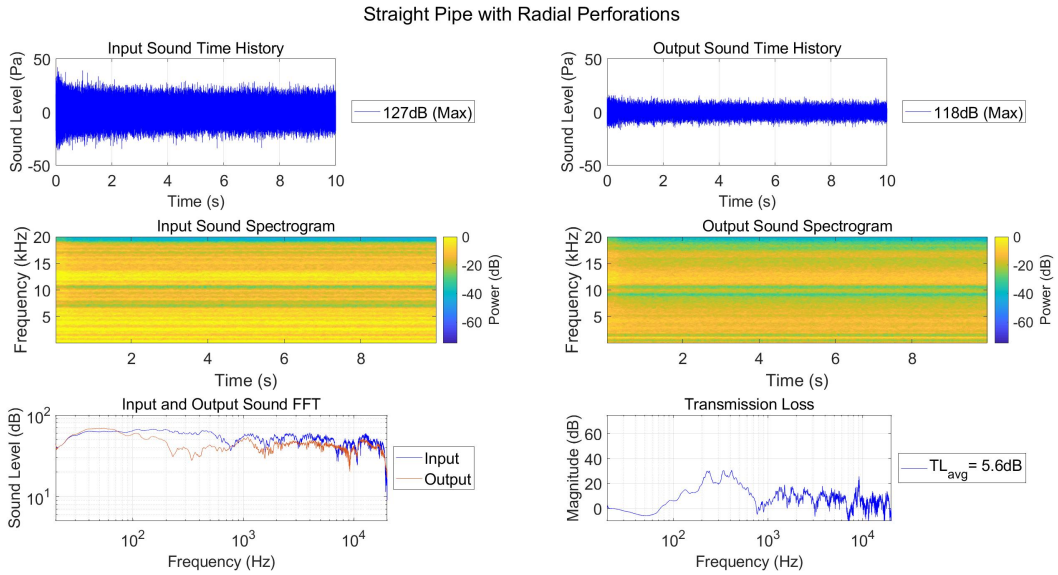

Figure 3-20 - SISO - Straight Pipe with Radial Perforations - Test Results

Average Transmission Loss (dB)					
Configuration	20 Hz - 5 kHz	5 kHz - 10 kHz	10 kHz - 15 kHz	15 kHz - 20 kHz	20 Hz - 20 kHz
SP with RP	9.6	6.0	3.2	3.5	5.6

Table 3-2 - SISO - Straight Pipe with Radial Perforations - Average Transmission Loss

3.5.1.3 Effects of a Nozzle on Output Sound

Experimental testing results for the nozzle indicated improved performance across the acoustic bandwidth. The configuration was tested in both the converging and diverging configurations. The time domain data decreased from 126 dB to 116 dB and 115 dB for the converging and diverging configurations, respectively. Both configurations show an increase in

width and in the number of spectral gaps from approximately 5 kHz to 10 kHz, 15 kHz to 16 kHz, and above 17 kHz. Both configurations show a slight increased output at approximately 1 kHz.

Across the 20 Hz to 20 kHz bandwidth, the TL_{avg} for the converging configuration equaled 9.3 dB while the diverging configuration equaled 13 dB. Figure 3-21 and Figure 3-22 show the input and output time history, spectrograms, and FFT as well as the TL across the acoustic spectrum for the converging and diverging configurations, respectively. Figure 3-23 shows a comparison plot of TL_{avg} for the converging and diverging configurations. The diverging configuration outperformed the converging configuration across the acoustic spectrum. However, the performance of both configurations is comparable. Table 3-3 details the TL_{avg} in the 20 Hz to 5 kHz, 5 kHz to 10 kHz, 10 kHz to 15 kHz, 15 kHz to 20 kHz, and 20 Hz to 20 kHz bandwidths for both configurations.

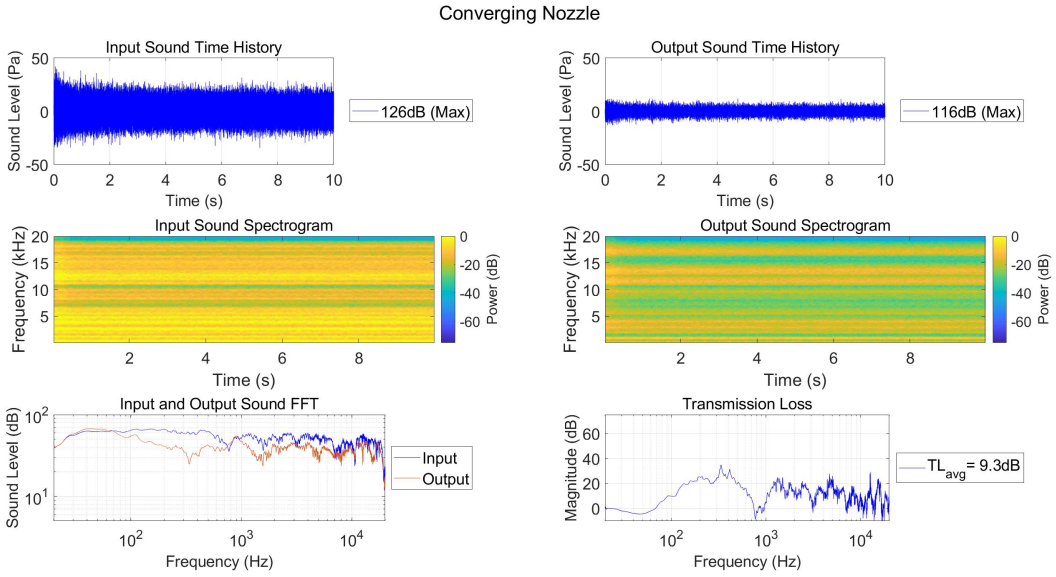

Figure 3-21 - SISO - Converging Nozzle - Test Results

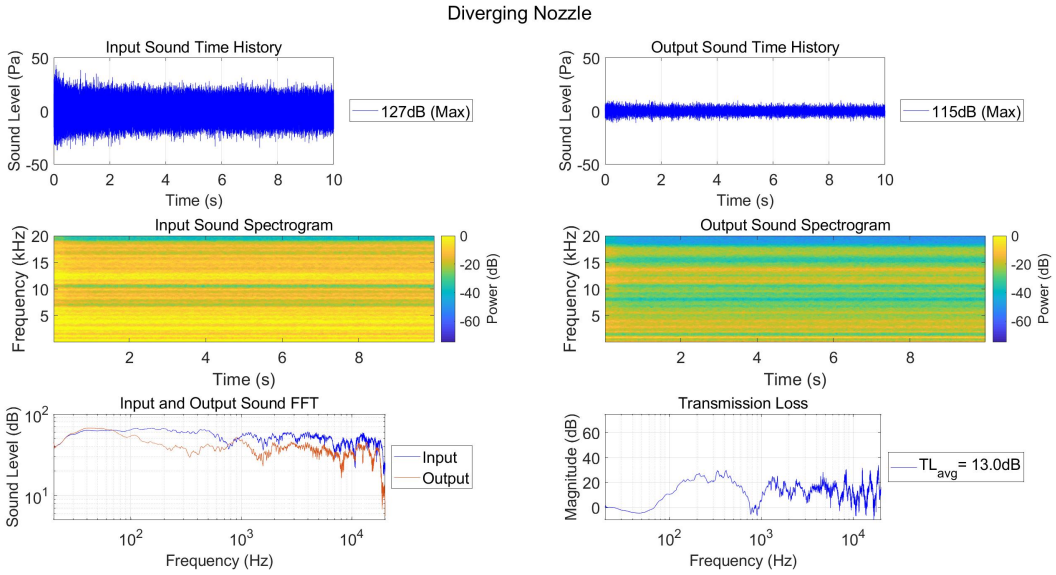

Figure 3-22 - SISO - Diverging Nozzle - Test Results

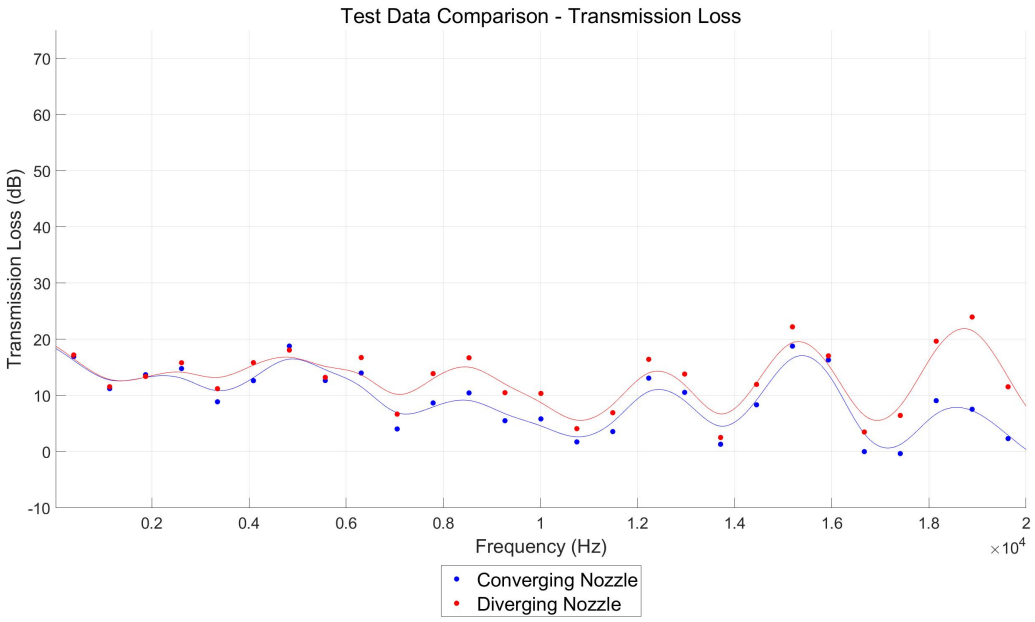

Figure 3-23 - SISO - Effects of Nozzle Direction - Transmission Loss Comparison

Average Transmission Loss (dB)					
Configuration	20 Hz - 5 kHz	5 kHz - 10 kHz	10 kHz - 15 kHz	15 kHz - 20 kHz	20 Hz - 20 kHz
CN	13.7	9.4	6.6	7.4	9.3
DN	14.7	13.0	9.5	14.8	13.0

Table 3-3 - SISO - Effects of Nozzle Direction - Average Transmission Loss

3.5.1.4 Effects of a Nozzle with Radial Perforations on Output Sound

Experimental testing results for the nozzle with RP indicated a promising performance across the acoustic bandwidth. The configuration was tested in both the converging and diverging configurations. The time domain data decreased from 126 dB to 115 dB and 114 dB for the converging and diverging configurations, respectively. Both configurations show a number

of spectral gaps scattered across the 5 kHz to 20 kHz spectrum. The amplified output previously seen at approximately 1 kHz was mitigated.

Across the 20 Hz to 20 kHz bandwidth, the TL_{avg} for the converging configuration equaled 10.5 dB while the diverging configuration equaled 14.7 dB. Figure 3-24 and Figure 3-25 show the input and output time history, spectrograms, and FFT as well as the TL across the acoustic spectrum for the converging and diverging configurations, respectively. Figure 3-26 shows a comparison plot of TL_{avg} for the converging and diverging configurations. The diverging configuration outperformed the converging configuration across the acoustic spectrum. However, the configurations are comparable in performance. Table 3-4 details the TL_{avg} in the 20 Hz to 5 kHz, 5 kHz to 10 kHz, 10 kHz to 15 kHz, 15 kHz to 20 kHz, and 20 Hz to 20 kHz bandwidths for both configurations.

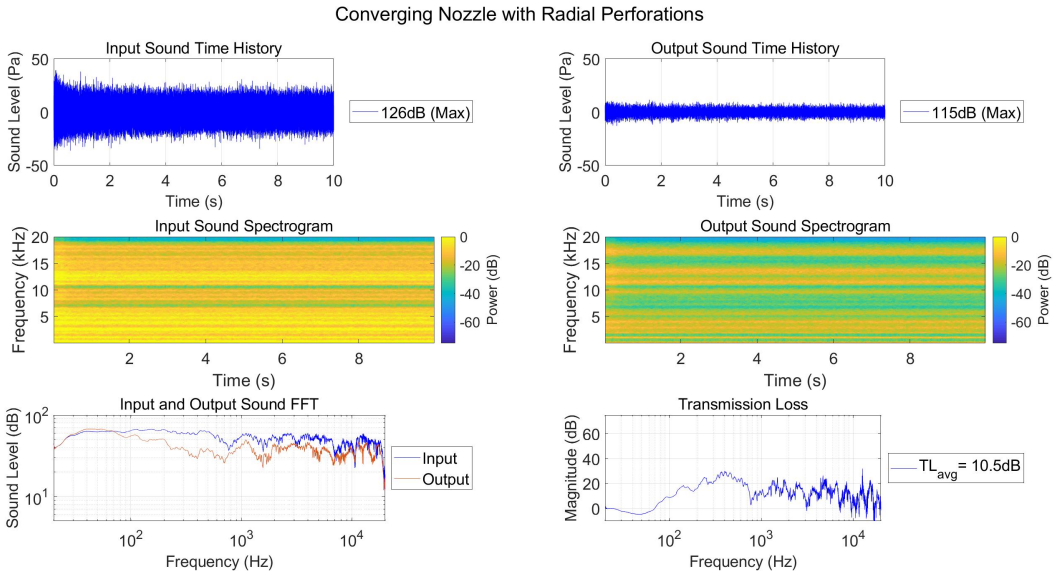

Figure 3-24 - SISO - Converging Nozzle with Radial Perforations - Test Results

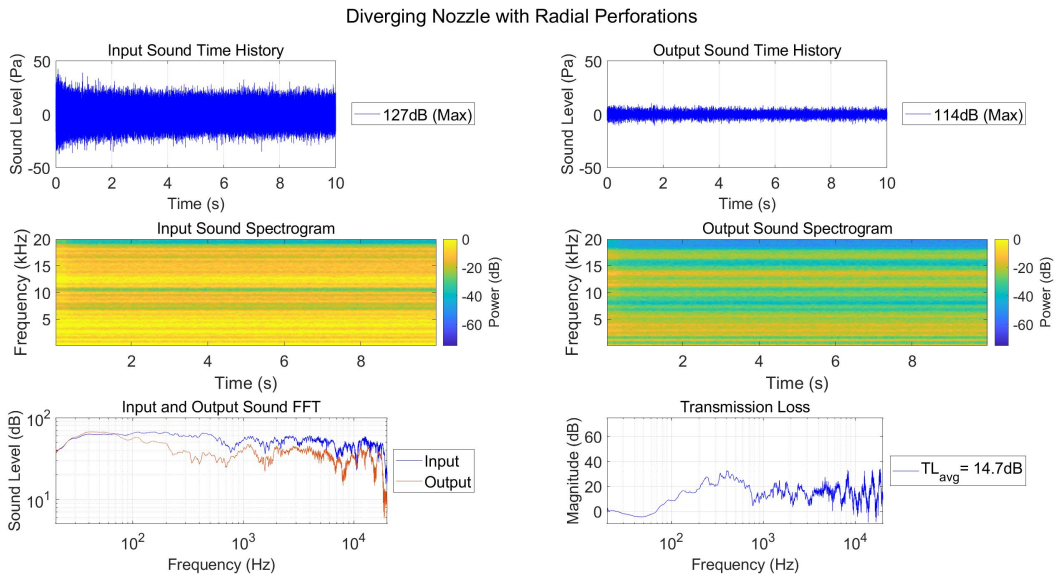

Figure 3-25 - SISO - Diverging Nozzle with Radial Perforations - Test Results

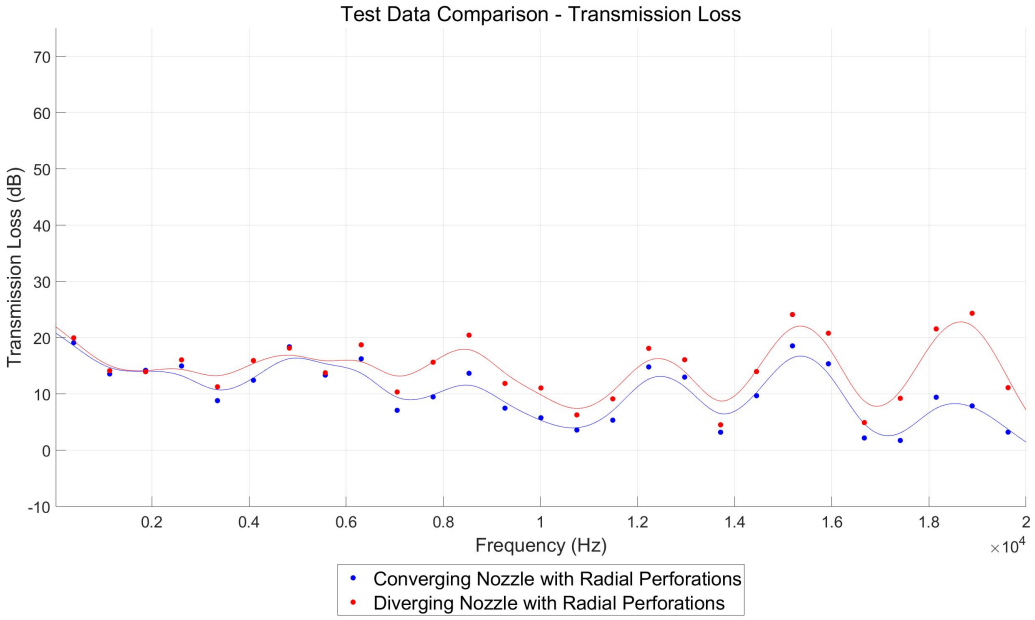

Figure 3-26 - SISO - Effects of a Nozzle with Radial Perforations - Transmission Loss Comparison

Average Transmission Loss (dB)					
Configuration	20 Hz - 5 kHz	5 kHz - 10 kHz	10 kHz - 15 kHz	15 kHz - 20 kHz	20 Hz - 20 kHz
CN with RP	14.4	11.1	8.3	8.1	10.5
DN with RP	15.6	15.1	11.4	16.5	14.7

Table 3-4 - SISO - Effects of a Nozzle with Radial Perforations - Average Loss Comparison

3.5.1.5 Effects of a Series of Nozzles on Output Sound

Experimental testing results for the SCN/SDN prototypes drastically improved performance across the acoustic bandwidth. The configuration was tested in both the converging and diverging configurations. The time domain data decreased from 126 dB to 113 dB and 112 dB for the converging and diverging configurations, respectively. Both configurations show a significant number of spectral gaps. The spectral gaps have ranges spanning several kilohertz. This is especially evident due to a spectral gap that spans from 5 kHz to 9 kHz. The performance in the 10 kHz to the 20 kHz range is exceptionally promising.

Across the 20 Hz to 20 kHz bandwidth, the TL_{avg} for the converging configuration equaled 20 dB while the diverging configuration equaled 23.4 dB. Figure 3-27 and Figure 3-28 show the input and output time history, spectrograms, and FFT as well as the TL across the acoustic spectrum for the converging and diverging configurations, respectively. Figure 3-29 shows a comparison plot of TL_{avg} for the converging and diverging configurations. The diverging configuration outperformed the converging configuration across most of the acoustic spectrum, but the performance of the configurations is comparable. Table 3-5 details the TL_{avg} in the 20 Hz

to 5 kHz, 5 kHz to 10 kHz, 10 kHz to 15 kHz, 15 kHz to 20 kHz, and 20 Hz to 20 kHz bandwidths for both configurations.

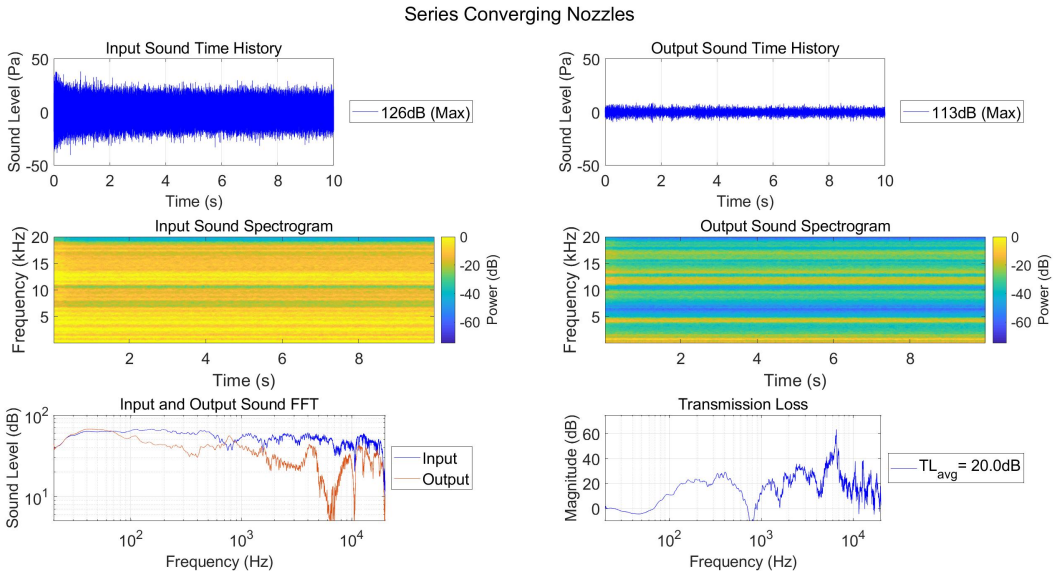

Figure 3-27 - SISO - Series of Converging Nozzles - Test Results

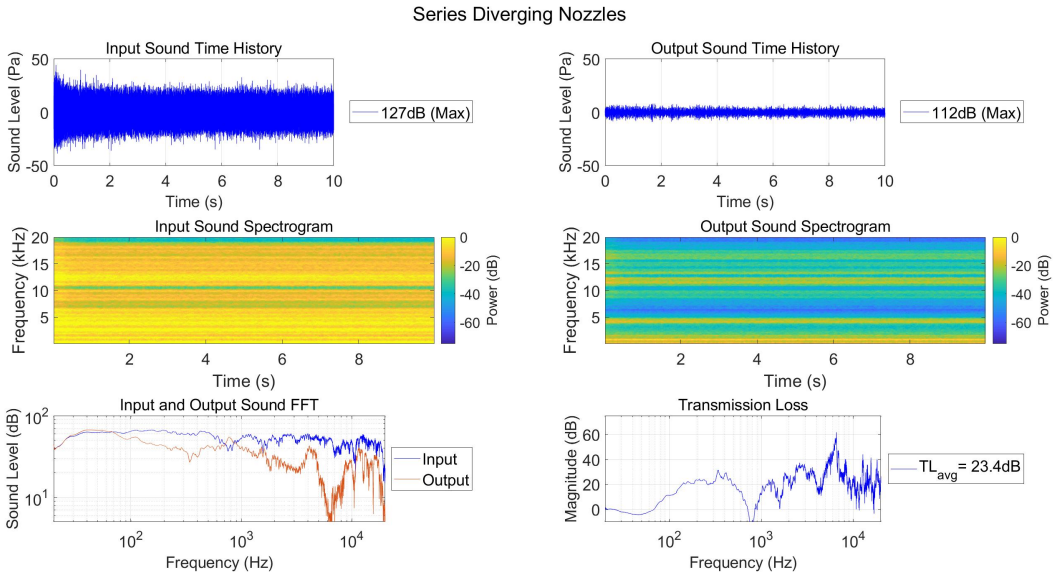

Figure 3-28 - SISO - Series of Diverging Nozzles - Test Results

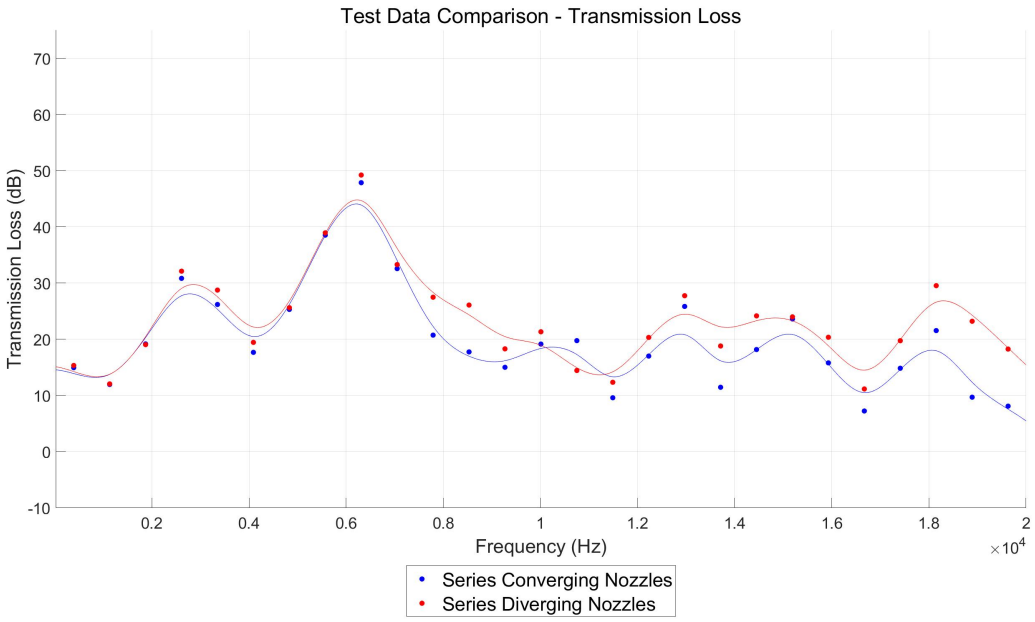

Figure 3-29 - SISO - Effects of a Series of Nozzles - Transmission Loss Comparison

Average Transmission Loss (dB)					
Configuration	20 Hz - 5 kHz	5 kHz - 10 kHz	10 kHz - 15 kHz	15 kHz - 20 kHz	20 Hz - 20 kHz
SCN	20.4	28.0	17.7	14.0	20.0
SDN	21.3	31.4	19.9	20.9	23.4

Table 3-5 - SISO - Effects of a Series of Nozzles - Average Transmission Loss

3.5.1.6 Effects of a Series of Nozzles with Radial Perforations on Output Sound

Experimental testing results for the SCN/SDN with RP showed exceptional performance across the acoustic bandwidth. The configuration was tested in both the converging and diverging configurations. The time domain data decreased from 126 dB to 113 dB and 112 dB for the converging and diverging configurations, respectively. Both configurations show a number of wide spectral gaps across the entire bandwidth. The spectral gaps are beginning to overlap.

From 5.5 kHz to 8.5 kHz, the transmitted sound is essentially zero for both configurations. Performance in the 10 kHz to the 20 kHz bandwidth is exceptional.

Across the 20 Hz to 20 kHz bandwidth, the TL_{avg} for the converging configuration equaled 22.9 dB while the diverging configuration equaled 26.3 dB. Figure 3-30 and Figure 3-31 show the input and output time history, spectrograms, and FFT as well as the TL across the acoustic spectrum for the converging and diverging configurations, respectively. Figure 3-32 shows a comparison plot of TL_{avg} for the converging and diverging configurations. The diverging configuration outperformed the converging configuration across most of the acoustic spectrum, but the performance of the configurations is comparable. Table 3-6 details the TL_{avg} in the 20 Hz to 5 kHz, 5 kHz to 10 kHz, 10 kHz to 15 kHz, 15 kHz to 20 kHz, and 20 Hz to 20 kHz bandwidths for both configurations.

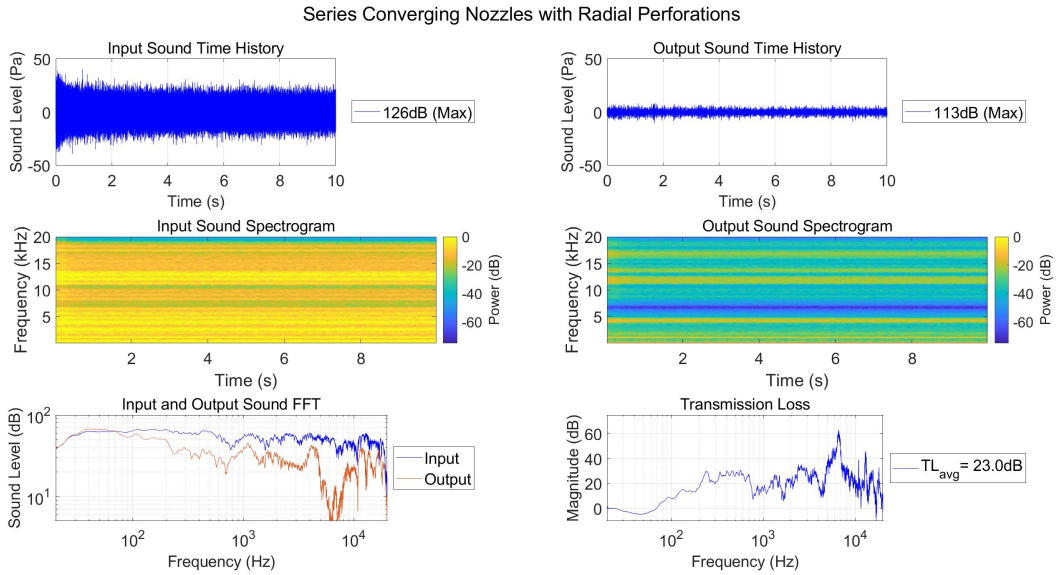

Figure 3-30 - SISO - Series of Converging Nozzles with Radial Perforations - Test Results

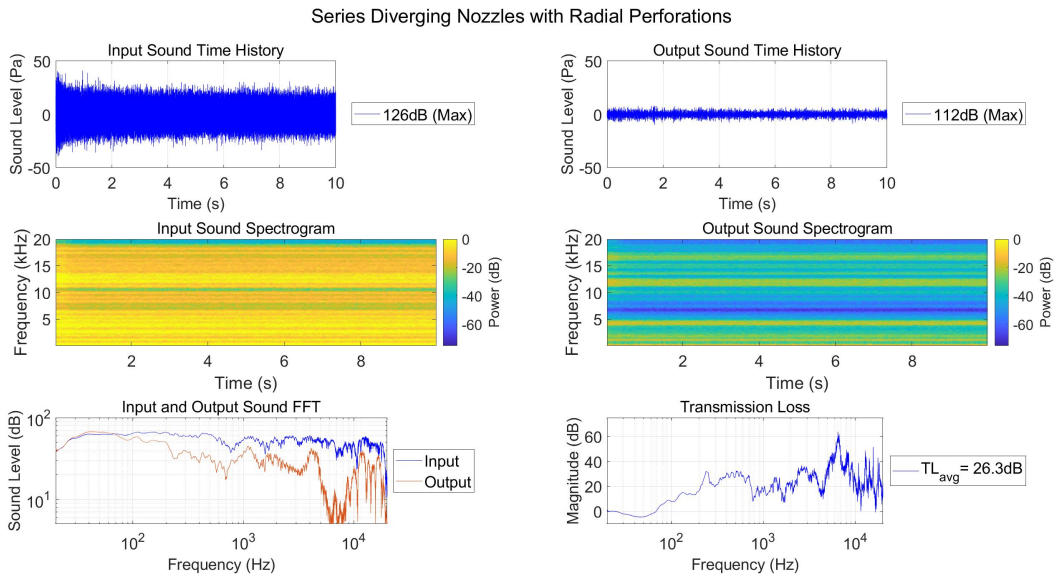

Figure 3-31 - SISO - Series of Diverging Nozzles with Radial Perforations - Test Results

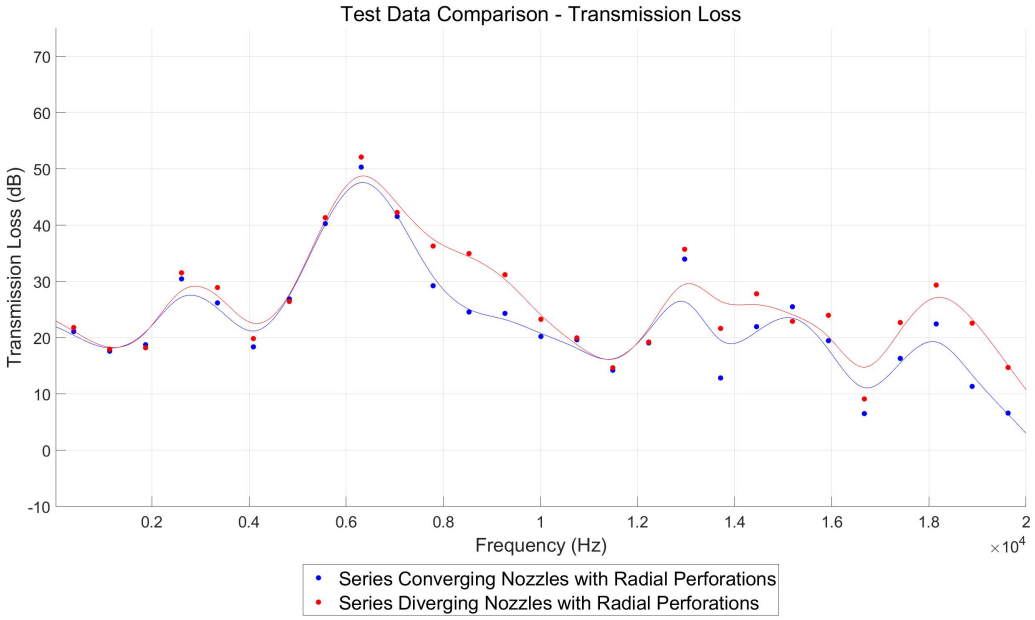

Figure 3-32 - SISO - Effects of Series of Nozzles with Radial Perforations - Transmission Loss Comparison

Average Transmission Loss (dB)					
Configuration	20 Hz - 5 kHz	5 kHz - 10 kHz	10 kHz - 15 kHz	15 kHz - 20 kHz	20 Hz - 20 kHz
SCN with RP	22.3	34.2	20.3	15.0	23.0
SDN with RP	23.2	38.5	22.9	20.7	26.3

Table 3-6 - SISO - Effects of Series of Nozzles with Radial Perforations - Average Transmission Loss

3.5.1.7 Effects of a Series of Nozzles with Radial and Axial Perforations on Output Sound

Experimental testing results for the SCN/SDN with RAP showed exceptional performance across the acoustic bandwidth. The configuration was tested in both the converging and diverging configurations. The time domain data decreased from 126 dB to 112 dB for the both configurations. Both configurations show a number of wide spectral gaps across the entire bandwidth. The spectral gaps are beginning to overlap. From 5.5 kHz to 8.5 kHz, the transmitted sound is essentially zero for both configurations. Performance in the 10 kHz to the 20 kHz bandwidth is exceptional.

Across the 20 Hz to 20 kHz bandwidth, the TL_{avg} for the converging configuration equaled 23.5 dB while the diverging configuration equaled 26.9 dB. Figure 3-33 and Figure 3-34 show the input and output time history, spectrograms, and FFT as well as the TL across the acoustic spectrum for the converging and diverging configurations, respectively. Figure 3-35 shows a comparison plot of TL_{avg} for the converging and diverging configurations. The diverging configuration outperformed the converging configuration across most of the acoustic spectrum, but the performance of both configurations is comparable. Table 3-7 details the TL_{avg} in the 20

Hz to 5 kHz, 5 kHz to 10 kHz, 10 kHz to 15 kHz, 15 kHz to 20 kHz, and 20 Hz to 20 kHz bandwidths for both configurations.

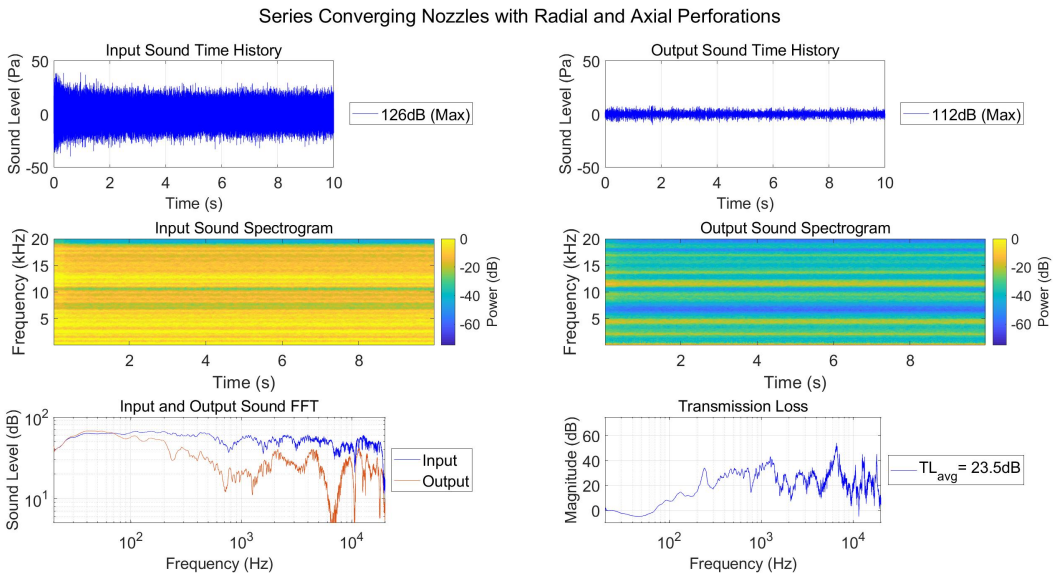

Figure 3-33 - SISO - Series of Converging Nozzles with Radial and Axial Perforations - Test Results

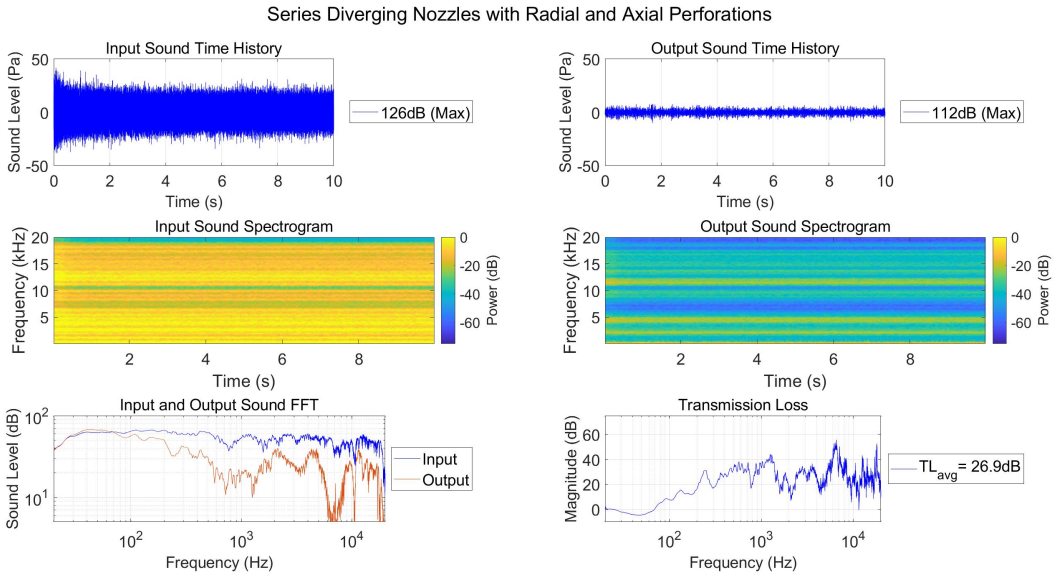

Figure 3-34 - SISO - Series of Diverging Nozzles with Radial and Axial Perforations - Test Results

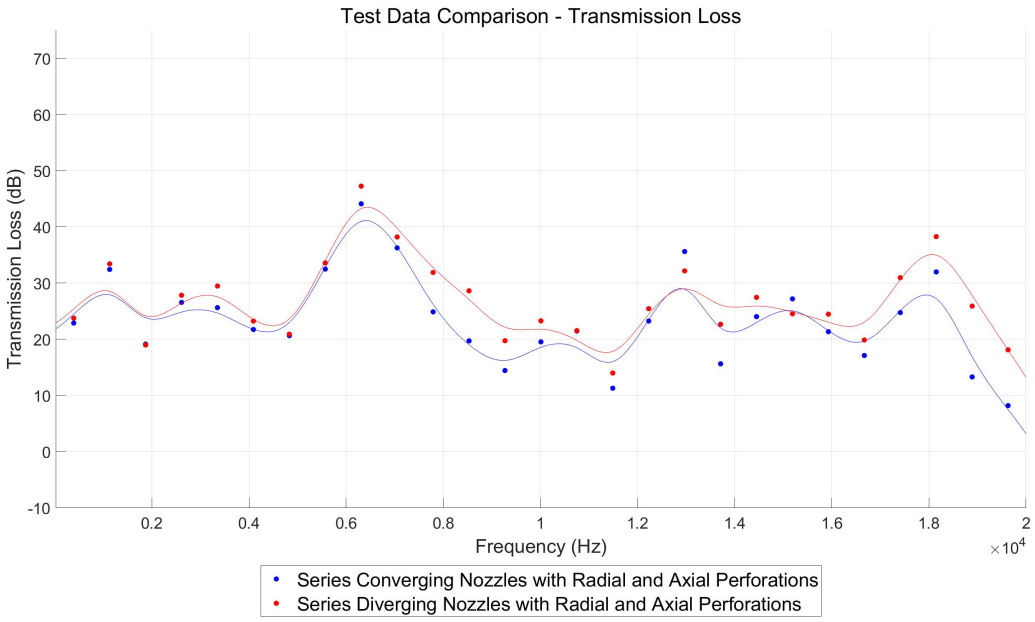

Figure 3-35 - SISO - Effects of Series of Nozzles with Radial and Axial Perforations - Transmission Loss Comparison

Average Transmission Loss (dB)					
Configuration	20 Hz - 5 kHz	5 kHz - 10 kHz	10 kHz - 15 kHz	15 kHz - 20 kHz	20 Hz - 20 kHz
SCN with RAP	24.1	27.7	22.1	20.3	23.5
SDN with RAP	25.4	32.1	23.8	26.1	26.9

Table 3-7 - SISO - Effects of Series of Nozzles with Radial and Axial Perforations - Average Transmission Loss

3.5.1.8 Effects of a Series of Nozzles with Radial and Axial Perforations and a Constricted Opening at the Output Plane on Output Sound

Experimental testing results for the SDN with RAP and a COOP showed remarkable performance across the acoustic bandwidth. The configuration was tested only in the diverging configuration. The time domain data decreased from 126 dB to 111 dB. The configuration shows

a substantial increase in the performance of the spectral gaps as well as the overlap in the spectral gaps.

Across the 20 Hz to 20 kHz bandwidth, the TL_{avg} equaled 33.9 dB. Figure 3-36 shows the input and output time history, spectrograms, and FFT as well as the TL across the acoustic spectrum. The output spectrogram and output FFT show tremendous acoustic mitigation in most of the acoustic bandwidth. Table 3-8 details the TL_{avg} in the 20 Hz to 5 kHz, 5 kHz to 10 kHz, 10 kHz to 15 kHz, 15 kHz to 20 kHz, and 20 Hz to 20 kHz bandwidths for both configurations.

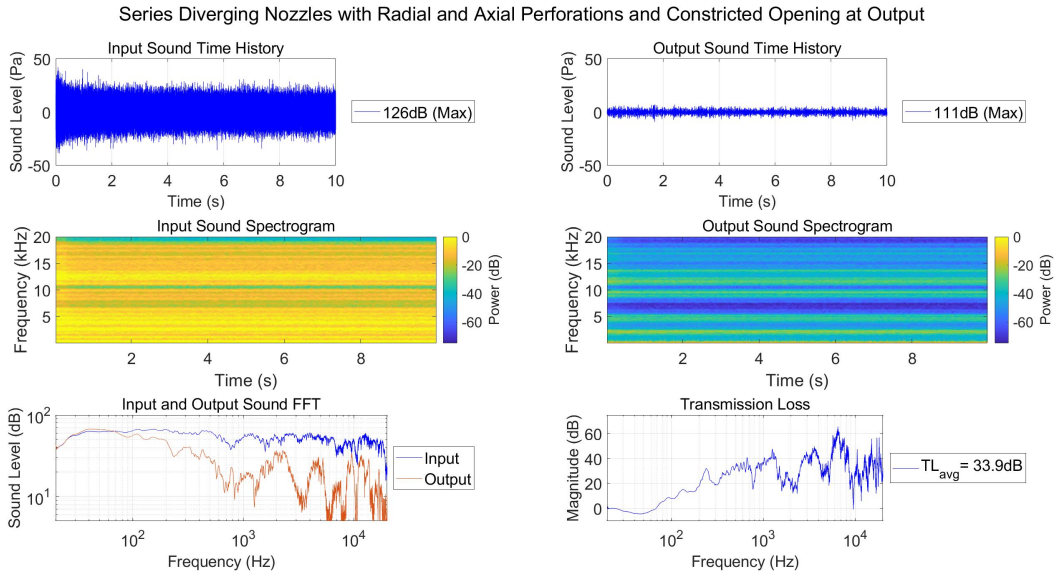

Figure 3-36 - SISO - Series of Diverging Nozzles with Radial and Axial Perforations and a Constricted Opening at the Output Plane - Test Results

	Average Transmission Loss (dB)				
Configuration	20 Hz - 5 kHz	5 kHz - 10 kHz	10 kHz - 15 kHz	15 kHz - 20 kHz	20 Hz - 20 kHz
SDN with RAP and a COOP	31.9	39.2	30.3	34.3	33.9

Table 3-8 - SISO - Series of Diverging Nozzles with Radial and Axial Perforations and a Constricted Opening at the Output Plane - Average Transmission Loss

3.5.1.9 Single Input Single Output Fundamental Features Systems Experimental Testing Summary

Sections 3.5.1.3 through 3.5.1.8 discuss the comparison of each prototype in the converging and diverging configurations. The results for each section show that both configurations had comparable results, with the diverging configuration performing slightly better than the converging configuration. In order to compare the results, the prototypes will be shown first with in the converging configurations, and then in the diverging configurations. The converging configurations will be compared with the SP and the SP with RP. Subsequently, the same comparison will be made with the diverging configurations.

Figure 3-37 shows the TL for converging configurations as well as the SP and SP with RP. The SP, SP with RP, CN, and the CN with RP all perform moderately the same across the spectrum. Between 11 kHz and 17 kHz, the CN and CN with RP show larger values of TL. Once the configurations included nozzles placed in series, a large spectral gap appeared as well as an increase in TL from 5 kHz to 8 kHz. The trends of the configurations placed in series follow the shape seen with the nozzle configurations, but have much higher amplitudes.

Table 3-9 shows the comparison in a tabular form. Across each bandwidth, the results improve with the design complexity. The SCN with RAP and COOP is the top performer for the converging configurations as shown in both Figure 3-37 and Table 3-9.

Figure 3-38 shows the TL for diverging configurations as well as the SP and SP with RP. The DN and the DN with RP all perform moderately the same across the spectrum but have increased performance below 10 kHz. As with the converging nozzles, once the configurations

include nozzles placed in series, spectral gaps appear. Above 14 kHz, the TL of the SDN with RAP and COOP becomes noticeably higher than the rest of the configurations.

Table 3-10 shows the comparison in a tabular form. Across each bandwidth, the results improve with the design complexity. The SDN with RAP and COOP is the top performer for the converging configurations as shown in both Figure 3-38 and Table 3-10.

With the results from Figure 3-37, Figure 3-38, Table 3-9, Table 3-10 and section 3.5.1.8, the BF AMM will be configured as a SDN with RAP and COOP.

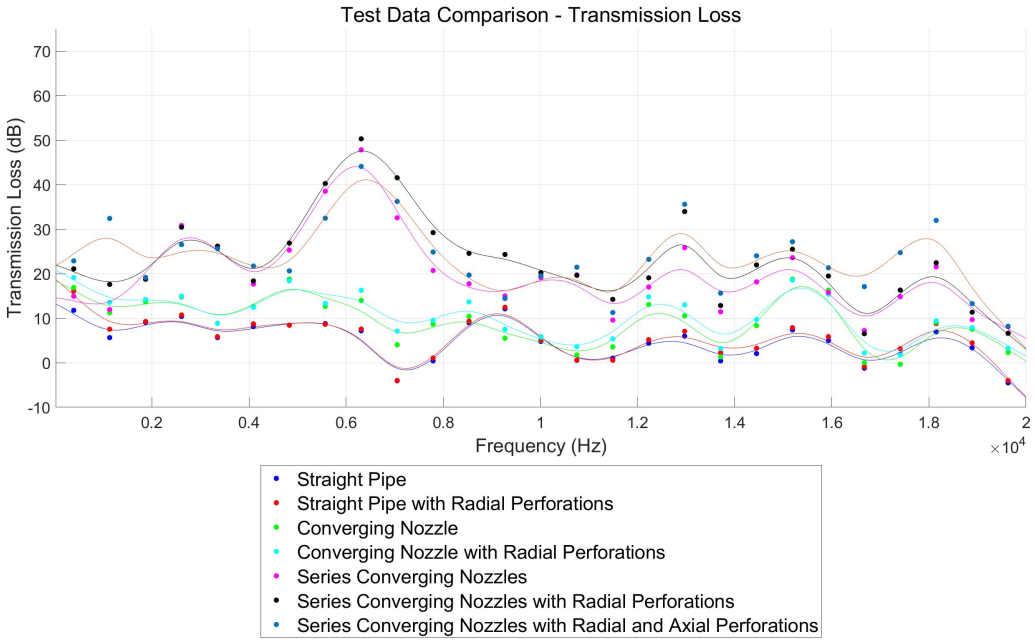

Figure 3-37 - SISO - Fundamental Features - Converging Configurations - Transmission Loss Comparison

Average Transmission Loss (dB)					
Configuration	20 Hz - 5 kHz	5 kHz - 10 kHz	10 kHz - 15 kHz	15 kHz - 20 kHz	20 Hz - 20 kHz
SP	8.5	5.8	2.5	2.6	4.8
SP with RP	9.6	6.0	3.2	3.5	5.6
CN	13.7	9.4	6.6	7.4	9.3
CN with RP	14.4	11.1	8.3	8.1	10.5
SCN	20.4	28.0	17.7	14.0	20.0
SCN with RP	22.3	34.2	20.3	15.1	23.0
SCN with RAP	24.1	27.7	22.1	20.3	23.5

Table 3-9 - SISO - Converging Configurations - Average Transmission Loss

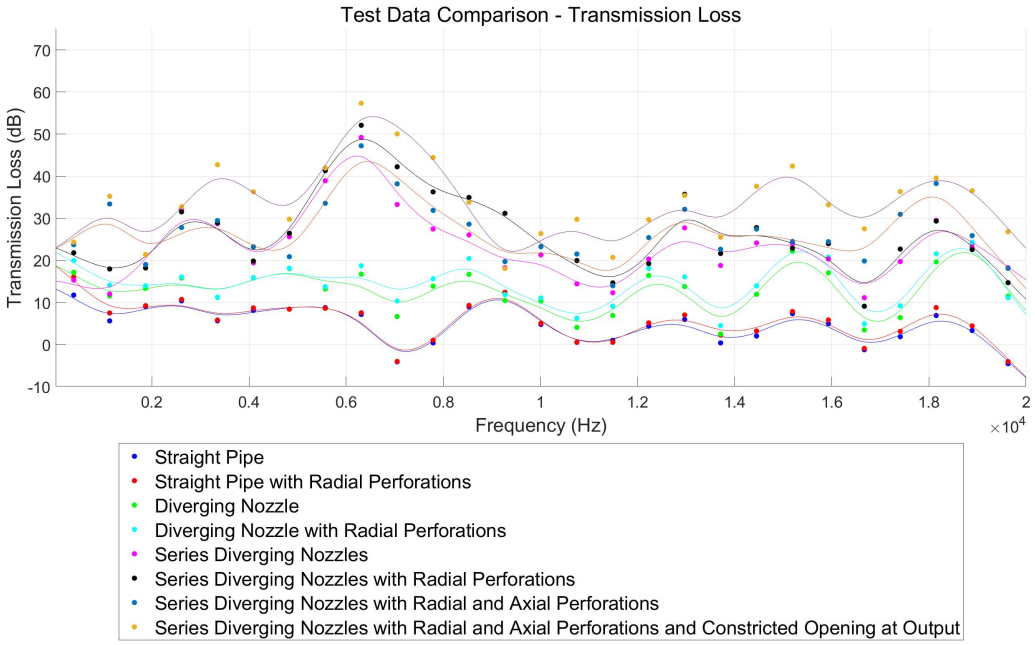

Figure 3-38 - SISO - Fundamental Features - Diverging Configurations - Transmission Loss Comparison

Average Transmission Loss (dB)					
Configuration	20 Hz - 5 kHz	5 kHz - 10 kHz	10 kHz - 15 kHz	15 kHz - 20 kHz	20 Hz - 20 kHz
SP	8.5	5.8	2.5	2.6	4.8
SP with RP	9.6	6.0	3.2	3.5	5.6
DN	14.7	13.1	9.5	14.8	13.0
DN with RP	15.6	15.1	11.4	16.5	14.7
SDN	21.3	31.4	19.9	20.9	23.4
SDN with RP	23.2	38.5	22.9	20.7	26.3
SDN with RAP	25.4	32.1	23.8	26.1	26.9
SDN with RAP and COOP	31.9	39.2	30.3	34.3	33.9

Table 3-10 - SISO - Diverging Configurations - Average Transmission Loss

3.5.2 Enclosing of the Single Input Single Output Systems

The test articles described in section 2.3 were tested and evaluated for acoustic performance. The results of this testing allowed the effectiveness of the enclosure around the BF AMM to be quantified. Experimental testing results, comparison plots, and summary for the enclosure testing is available in section 3.5.2.3. Experimental testing was conducted in the converging and diverging configurations. The converging section will be discussed followed by the diverging section. The prototypes discussed in this section do not include the COOP.

3.5.2.1 Base Feature Acoustic Metamaterial in the Converging Configuration

Experimental testing results for the BF AMM with and without an enclosure showed improved performance with the enclosure. The time domain data decreased from 126 dB to 112 dB and 113 dB for the BF AMM and the enclosed BF AMM, respectively. The enclosure provided improved performance in the acoustic bandwidth from 11 kHz to 20 kHz.

Across the 20 Hz to 20 kHz bandwidth, the TL_{avg} equaled 23.5 dB and 25.0 dB, for the BF AMM and the enclosed BF AMM, respectively. Figure 3-39 and Figure 3-40 show the input and output time history, spectrograms, and FFT as well as the TL across the acoustic spectrum for the BF AMM and the enclosed BF AMM, respectively. Figure 3-41 shows a comparison plot of TL_{avg} for both configurations. Table 3-11 details the TL_{avg} in the 20 Hz to 5 kHz, 5 kHz to 10 kHz, 10 kHz to 15 kHz, 15 kHz to 20 kHz, and 20 Hz to 20 kHz bandwidths for both configurations. Improvement in high frequency performance is clearly seen with the enclosed configuration.

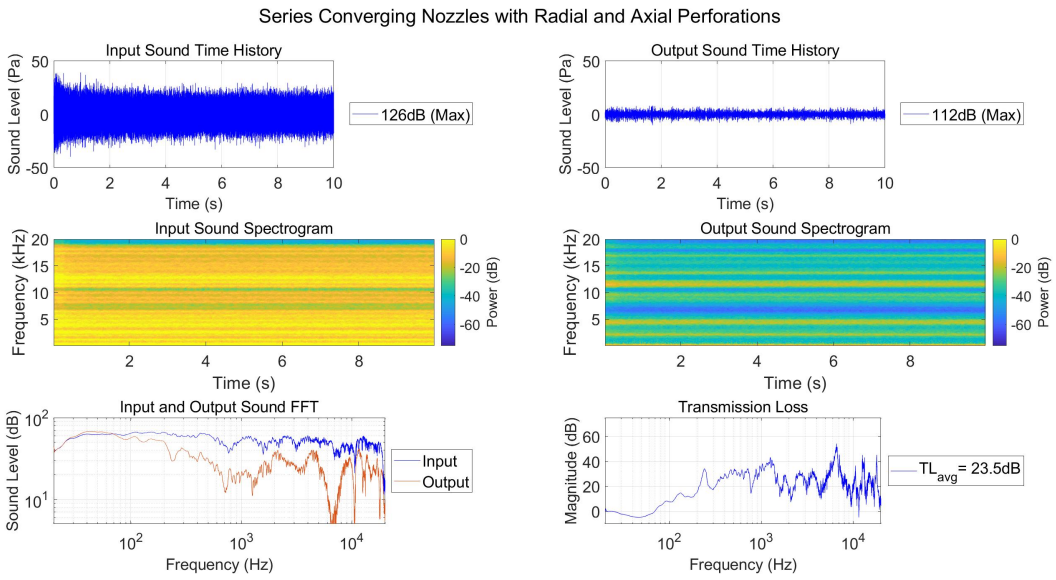

Figure 3-39 - SISO - Series of Converging Nozzles with Radial and Axial Perforations - Test Results

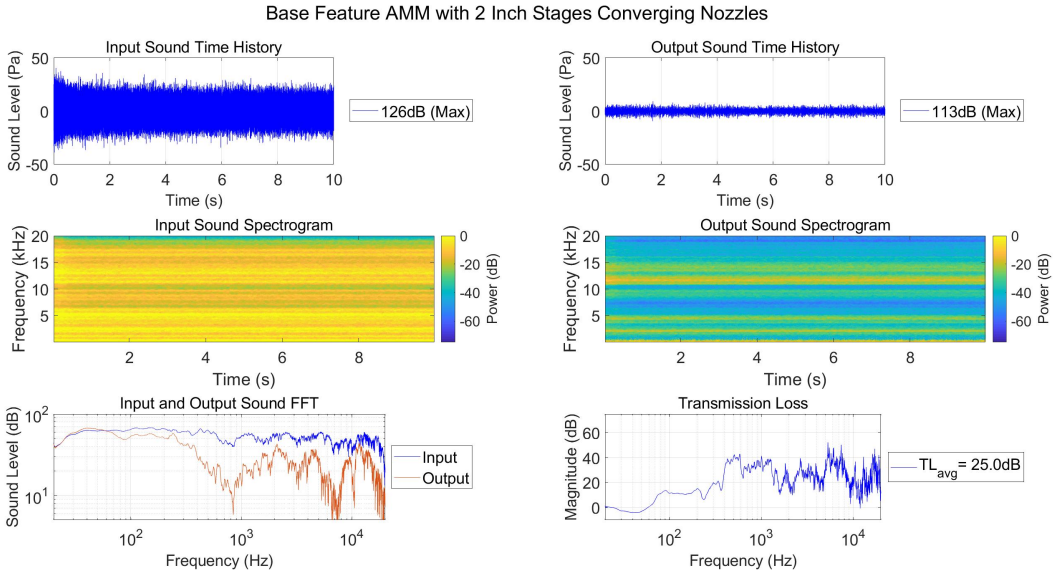

Figure 3-40 - SISO - Enclosed Series of Converging Nozzles - Test Results

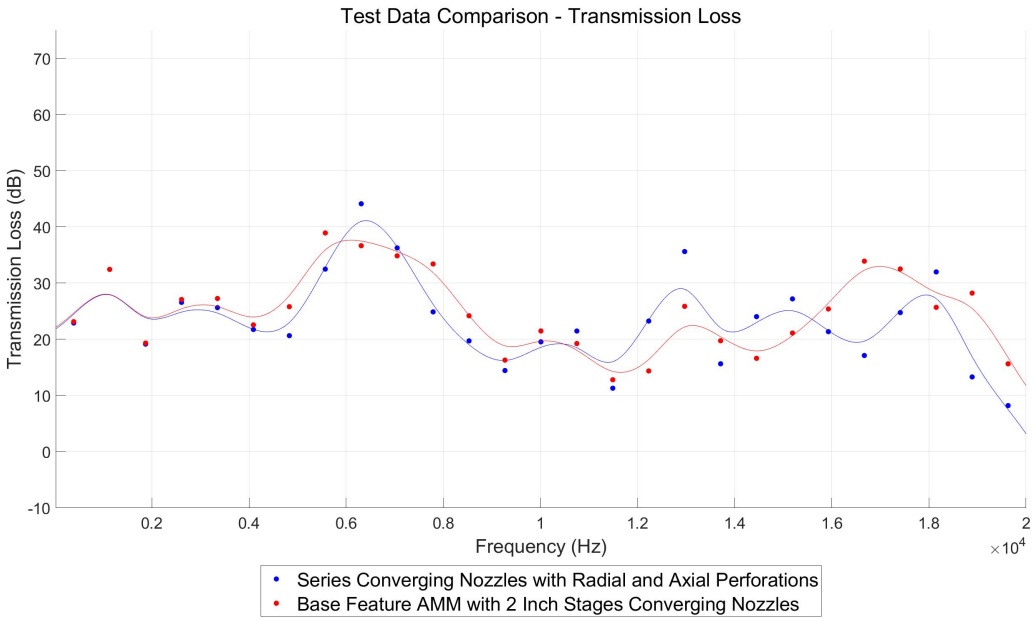

Figure 3-41 - SISO - Effects of Enclosures on Series of Converging Nozzles - Transmission Loss Comparison

Average Transmission Loss (dB)					
Configuration	20 Hz - 5 kHz	5 kHz - 10 kHz	10 kHz - 15 kHz	15 kHz - 20 kHz	20 Hz - 20 kHz
SCN with RAP	20.4	28.0	17.7	14.0	20.0
Enclosed SCN with RAP	25.1	30.0	18.4	26.4	25.0

Table 3-11 - SISO -Effects of Enclosures on Series of Converging Nozzles - Average Transmission Loss

3.5.2.2 Base Feature Acoustic Metamaterial in the Diverging Configuration

Experimental testing results for the diverging configuration of BF AMM and the enclosed BF AMM indicated that the enclosure improved performance across the acoustic spectrum. The time domain data decreased from 126 dB to 112 dB for the BF AMM and to 111 dB for the enclosed BF AMM, respectively.

Across the 20 Hz to 20 kHz bandwidth, the TL_{avg} equaled 26.9 dB and 28.1 dB, for the BF AMM and the enclosed BF AMM, respectively. Figure 3-42 and Figure 3-43 show the input and output time history, spectrograms, and FFT as well as the TL across the acoustic spectrum for the BF AMM and the enclosed BF AMM, respectively. Figure 3-44 shows a comparison plot of TL_{avg} for both configurations. Table 3-12 details the TL_{avg} in the 20 Hz to 5 kHz, 5 kHz to 10 kHz, 10 kHz to 15 kHz, 15 kHz to 20 kHz, and 20 Hz to 20 kHz bandwidths for both configurations. Above 10 kHz, the enclosure improved the performance considerably.

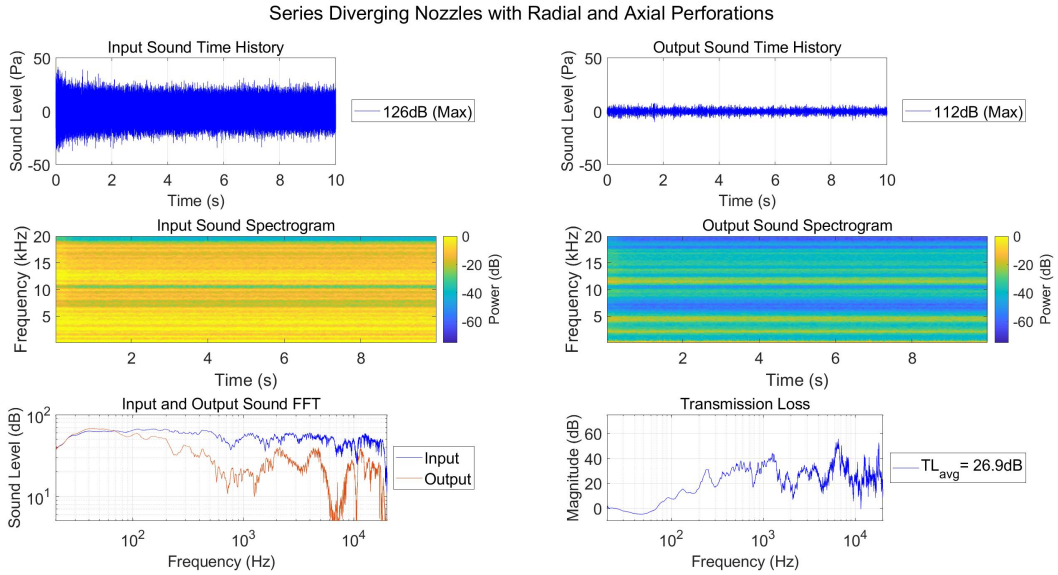

Figure 3-42 - SISO - Series of Diverging Nozzles with Radial and Axial Perforations - Test Results

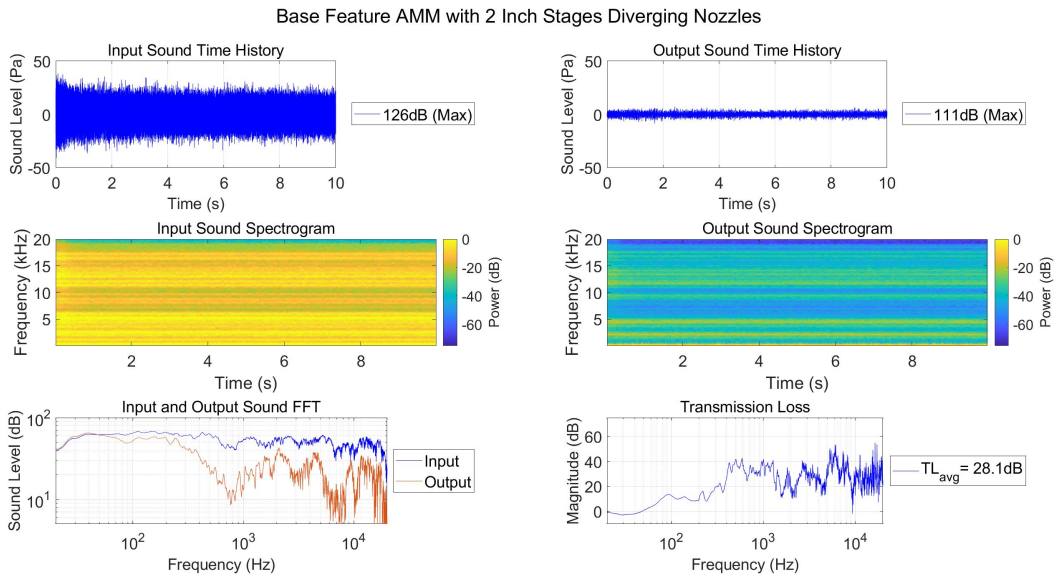

Figure 3-43 - SISO - Enclosed Series of Diverging Nozzles with Radial and Axial Perforations - Test Results

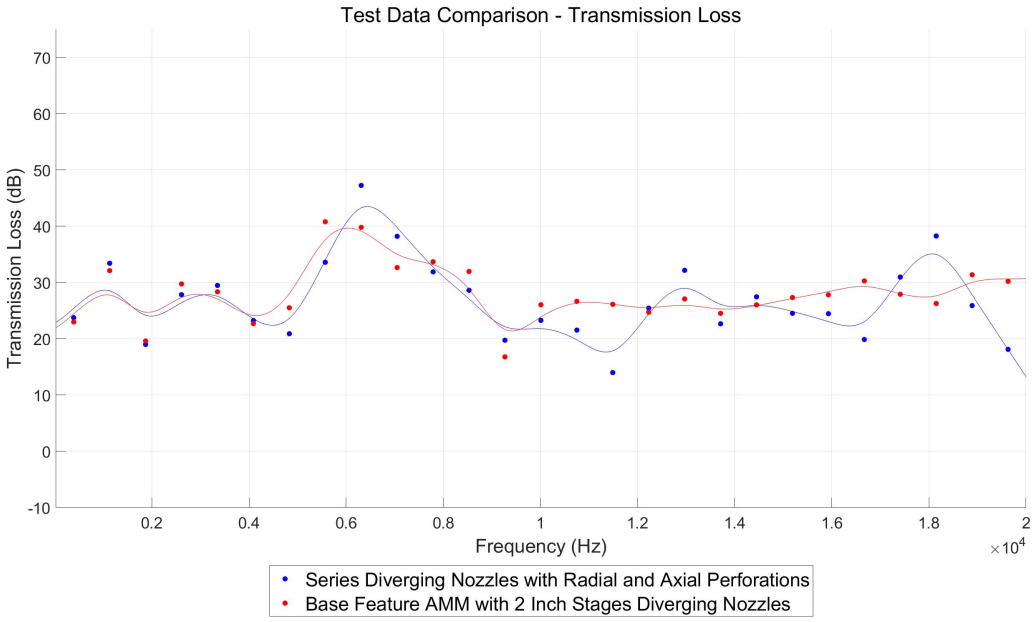

Figure 3-44 - SISO - Effects of Enclosures on Series of Diverging Nozzles - Transmission Loss Comparison

Average Transmission Loss (dB)					
Configuration	20 Hz - 5 kHz	5 kHz - 10 kHz	10 kHz - 15 kHz	15 kHz - 20 kHz	20 Hz - 20 kHz
SDN with RAP	25.4	32.1	23.8	26.1	26.9
Enclosed SDN with RAP	25.6	32.0	25.9	28.9	28.1

Table 3-12 - SISO - Effects of Enclosures on Series of Diverging Nozzles - Average Transmission Loss

3.5.2.3 Enclosing of the Single Input Single Output Systems Experimental Testing Summary

The enclosure improved performance in both the converging and diverging configurations. Particularly, the bandwidth from 15 kHz to 20 kHz and above 10 kHz for the converging and diverging configurations, respectively, saw a significant increase in performance. These results show that the enclosure was effective in acoustic mitigation; therefore, the feature was included in subsequent testing.

3.5.3 Single Input Single Output Downsizing

The test articles described in section 2.4 were tested and evaluated for acoustic performance. The results of this testing allowed for the evaluation of the performance of the BF AMM at decreased sizes. The results will be shown for each of the four sizes of BF AMM. Experimental testing results, comparison plots, and summary for the downsizing testing is available in section 3.5.3.5. It is to be noted that these prototypes had already been built when the notion of the COOP was conceived. Consequently, this configuration does not have the feature.

3.5.3.1 Configurations with a Two Inch Stage Length

Experimental testing results for the 2" stage length established the baseline for the downsizing prototypes. The configuration was tested in both the converging and diverging configurations. Test results were consistent from results seen with the enclosed BF AMM discussed in section 3.5.2. The time domain data decreased from 126 dB to 113 dB and to 111 dB for the converging and diverging configurations respectively.

Across the 20 Hz to 20 kHz bandwidth, the TL_{avg} equaled 23.3 dB and 28.1 dB, for the converging and diverging configurations respectively. Figure 3-45 and Figure 3-46 show the input and output time history, spectrograms, and FFT as well as the TL across the acoustic spectrum for the converging and diverging configurations respectively. Figure 3-47 shows a comparison plot of TL_{avg} for both configurations. The diverging configuration outperformed the converging configuration across most of the acoustic spectrum. From 10 kHz to 20 kHz, the enclosure improves the performance consistently. Table 3-13 details the TL_{avg} in the 20 Hz to 5 kHz, 5 kHz to 10 kHz, 10 kHz to 15 kHz, 15 kHz to 20 kHz, and 20 Hz to 20 kHz bandwidths for both configurations.

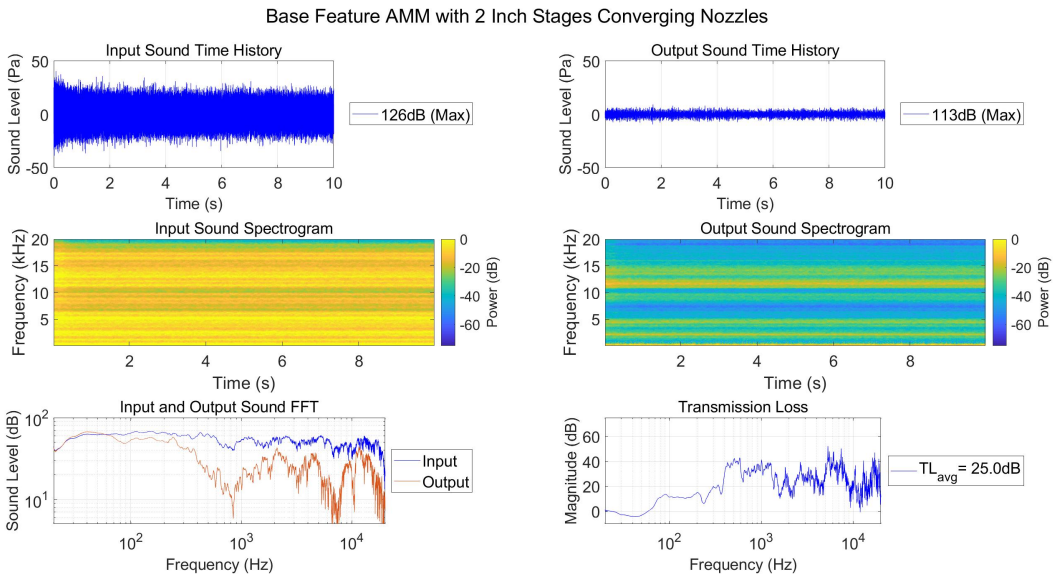

Figure 3-45 - SISO - Base Feature AMM with Two Inch Stages - Converging Configuration - Test Results

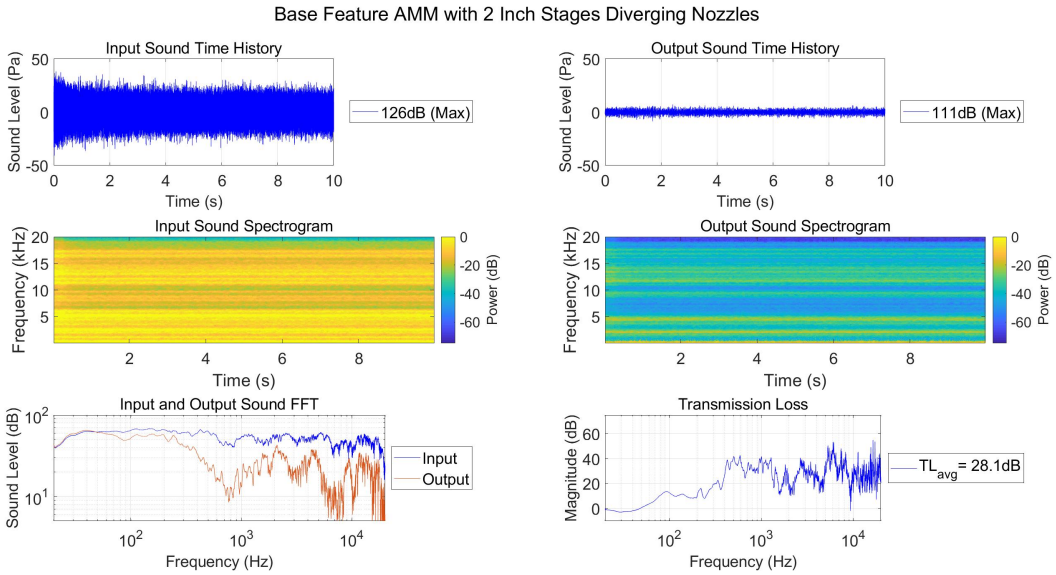

Figure 3-46- SISO - Base Feature AMM with Two Inch Stages - Diverging Configuration - Test Results

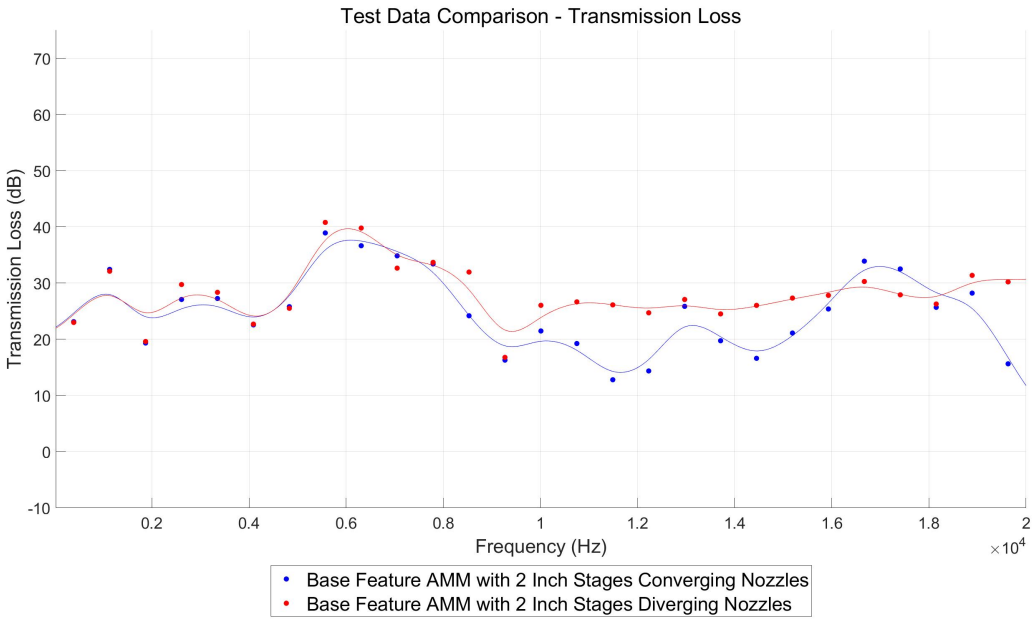

Figure 3-47 - SISO - Base Feature AMM with Two Inch Stages - Transmission Loss Comparison

	Average Transmission Loss (dB)				
Configuration	20 Hz - 5 kHz	5 kHz - 10 kHz	10 kHz - 15 kHz	15 kHz - 20 kHz	20 Hz - 20 kHz
BF AMM with 2 Inch Stages - Converging	25.1	30.0	18.4	26.4	25.0
BF AMM with 2 Inch Stages - Diverging	25.6	32.0	25.9	28.9	28.1

Table 3-13 - SISO - Base Feature AMM with Two Inch Stages - Average Transmission Loss

3.5.3.2 Configurations with a One Inch Stage Length

Experimental testing results for the 1" stage length proved that performance was not adversely effected. The configuration was tested in both the converging and diverging configurations. The time domain data decreased from 126 dB to 111 dB for both configurations.

Across the 20 Hz to 20 kHz bandwidth, the TL_{avg} equaled 29.2 dB and 29.9 dB, for the converging and diverging configurations respectively. Figure 3-48 and Figure 3-49 show the input

and output time history, spectrograms, and FFT as well as the TL across the acoustic spectrum for the converging and diverging configurations respectively. Figure 3-50 shows a comparison plot of TL_{avg} for both configurations. The performance of both configurations was comparable. Table 3-14 details the TL_{avg} in the 20 Hz to 5 kHz, 5 kHz to 10 kHz, 10 kHz to 15 kHz, 15 kHz to 20 kHz, and 20 Hz to 20 kHz bandwidths for both configurations.

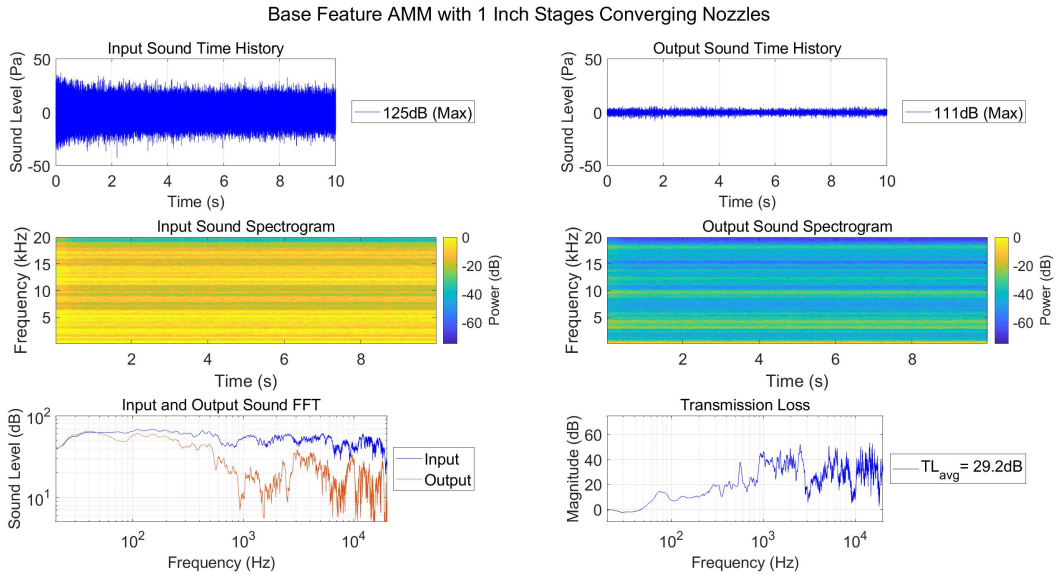

Figure 3-48 - SISO - Base Feature AMM with One Inch Stages - Converging Configuration - Test Results

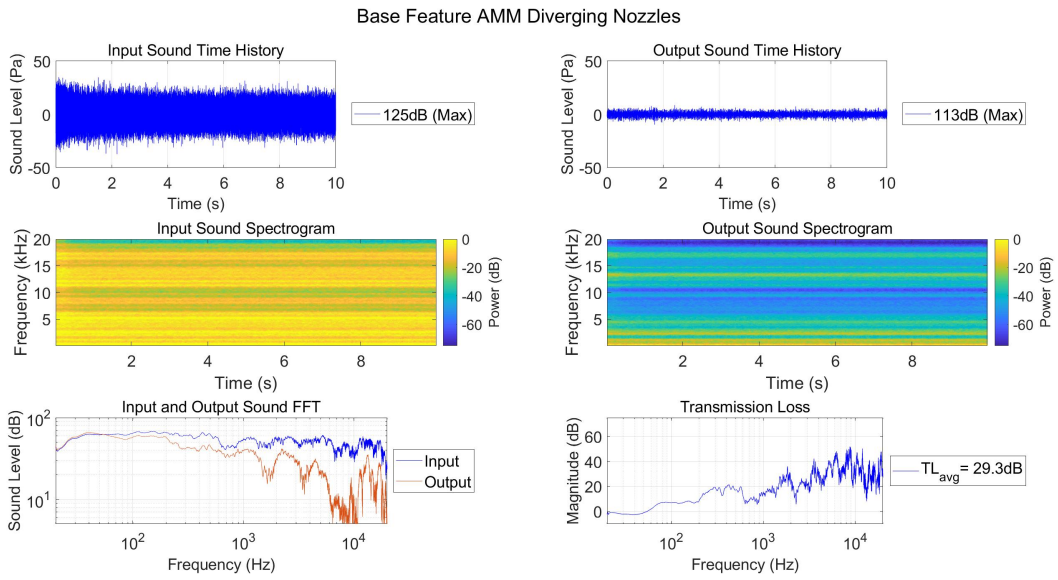

Figure 3-49 - SISO - Base Feature AMM with One Inch Stages - Diverging Configuration - Test Results

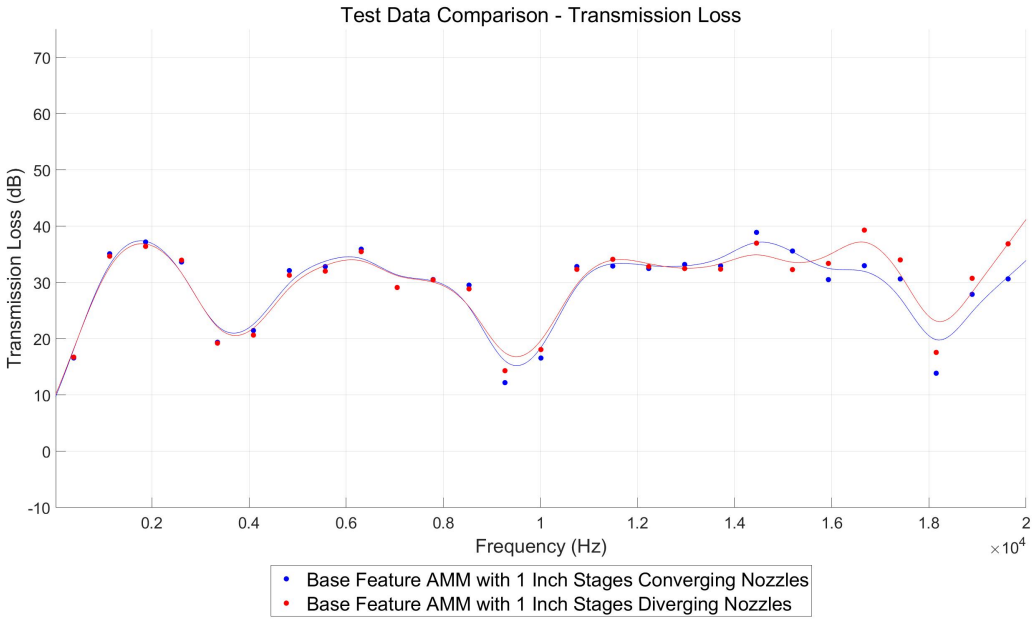

Figure 3-50 - SISO - Base Feature AMM with One Inch Stages - Transmission Loss Comparison

Average Transmission Loss (dB)					
Configuration	20 Hz - 5 kHz	5 kHz - 10 kHz	10 kHz - 15 kHz	15 kHz - 20 kHz	20 Hz - 20 kHz
BF AMM with 1 Inch Stages - Converging	27.5	27.6	32.6	28.9	29.2
BF AMM with 1 Inch Stages - Diverging	27.1	27.8	32.7	31.9	29.9

Table 3-14 - SISO - Base Feature AMM with One Inch Stages - Average Transmission

3.5.3.3 Configurations with a Half Inch Stage Length

Experimental testing results for the 1/2" stage length proved that performance was not adversely effected. The configuration was tested in both the converging and diverging configurations. The time domain data decreased from 125 dB to 107 dB and to 108 dB for the converging and diverging configurations respectively. These configurations decreased the output SPL in the time domain more than the previous configurations.

Across the 20 Hz to 20 kHz bandwidth, the TL_{avg} equaled 31.8 dB and 32.0 dB, for the converging and diverging configurations respectively. Figure 3-51 and Figure 3-52 show the input and output time history, spectrograms, and FFT as well as the TL across the acoustic spectrum for the converging and diverging configurations respectively. Figure 3-53 shows a comparison plot of TL_{avg} for both configurations. The performance for both configurations is comparable. Table 3-15 details the TL_{avg} in the 20 Hz to 5 kHz, 5 kHz to 10 kHz, 10 kHz to 15 kHz, 15 kHz to 20 kHz, and 20 Hz to 20 kHz bandwidths for both configurations.

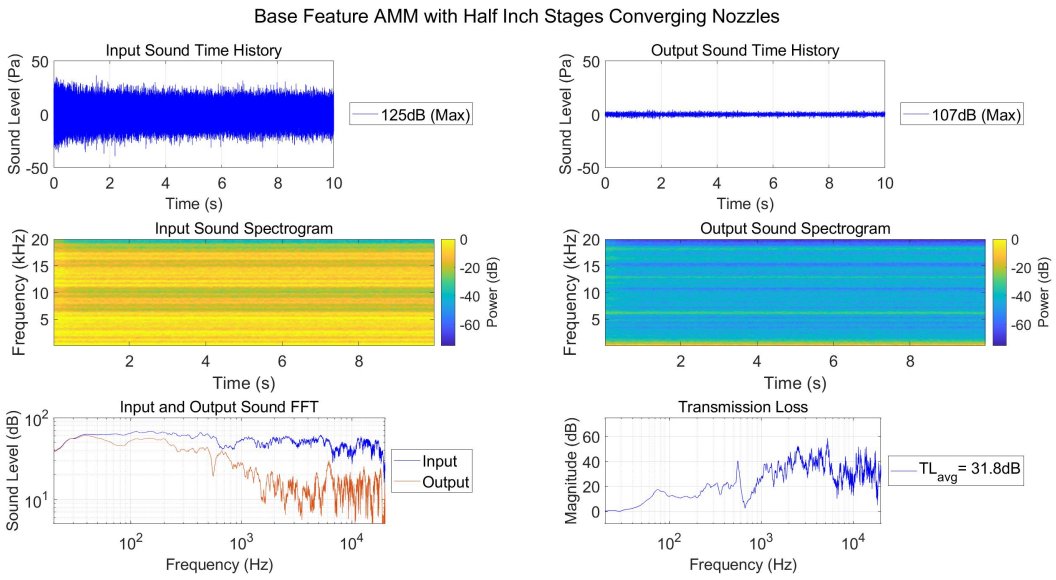

Figure 3-51 - SISO - Base Feature AMM with Half Inch Stages - Converging Configuration - Test Results

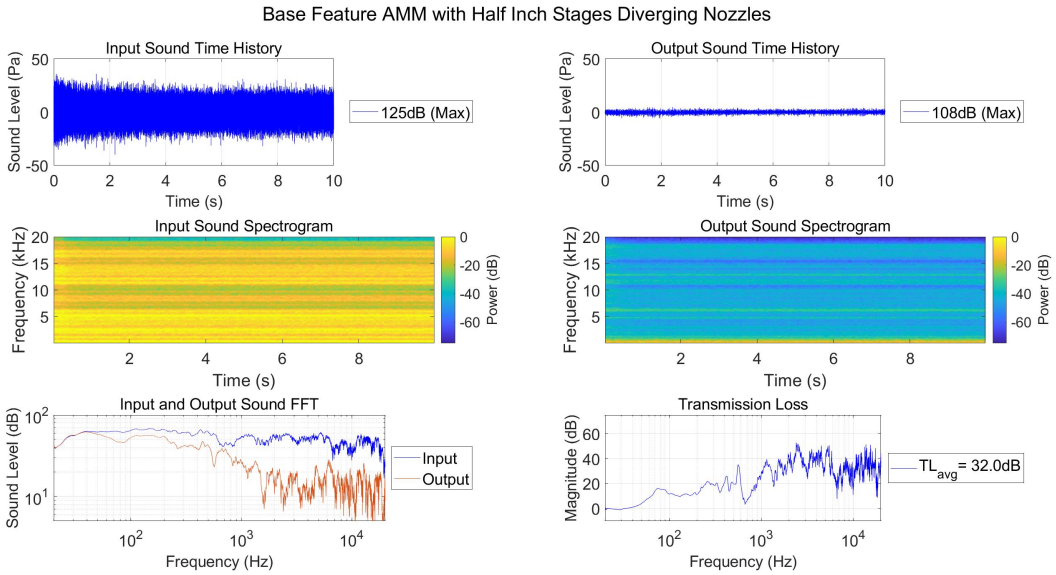

Figure 3-52 - SISO - Base Feature AMM with Half Inch Stages - Diverging Configuration - Test Results

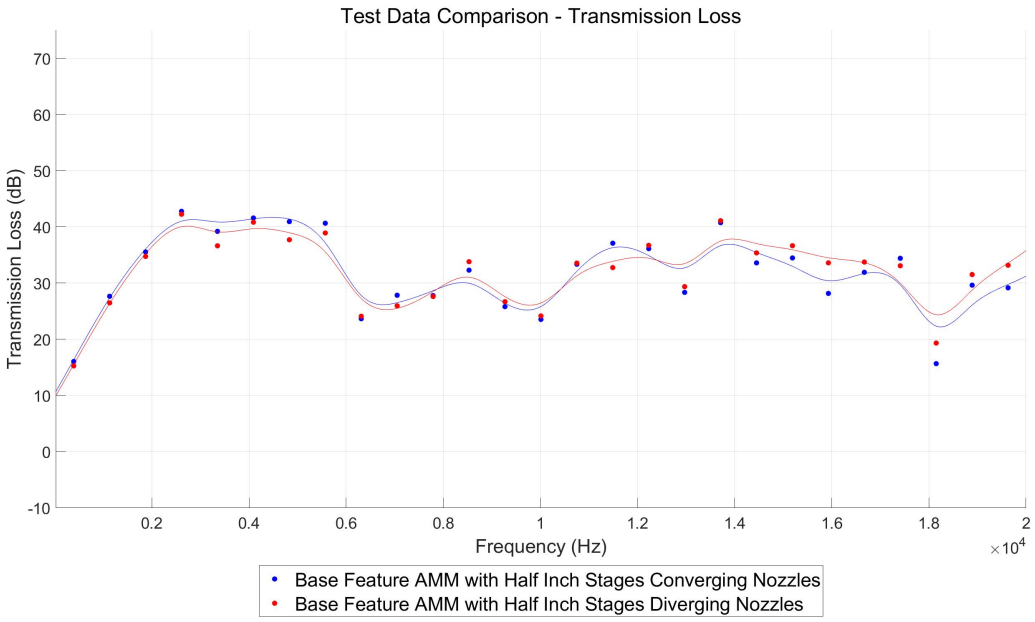

Figure 3-53 - SISO - Base Feature AMM with Half Inch Stages - Transmission Loss Comparison

	Average Transmission Loss (dB)				
Configuration	20 Hz - 5 kHz	5 kHz - 10 kHz	10 kHz - 15 kHz	15 kHz - 20 kHz	20 Hz - 20 kHz
BF AMM with Half Inch Stages - Converging	34.3	30.0	33.9	28.9	31.8
BF AMM with Half Inch Stages - Diverging	33.0	29.7	34.0	31.5	32.0

Table 3-15 - SISO - Base Feature AMM with Half Inch Stages - Average Transmission Loss

3.5.3.4 Configurations with a Quarter Inch Stage Length

Experimental testing results for the 1/4" stage length proved that performance was not adversely effected. The configuration was tested in both the converging and diverging configurations. The time domain data decreased from 126 dB to 109 dB and to 107 dB for the converging and diverging configurations respectively.

Across the 20 Hz to 20 kHz bandwidth, the TL_{avg} equaled 28.7 dB and 28.6 dB, for the converging and diverging configurations respectively. Figure 3-54 and Figure 3-55 show the input and output time history, spectrograms, and FFT as well as the TL across the acoustic spectrum for the converging and diverging configurations respectively. Figure 3-56 shows a comparison plot of TL_{avg} for both configurations. The difference in performance between the configurations is essentially negligible. Table 3-16 details the TL_{avg} in the 20 Hz to 5 kHz, 5 kHz to 10 kHz, 10 kHz to 15 kHz, 15 kHz to 20 kHz, and 20 Hz to 20 kHz bandwidths for both configurations.

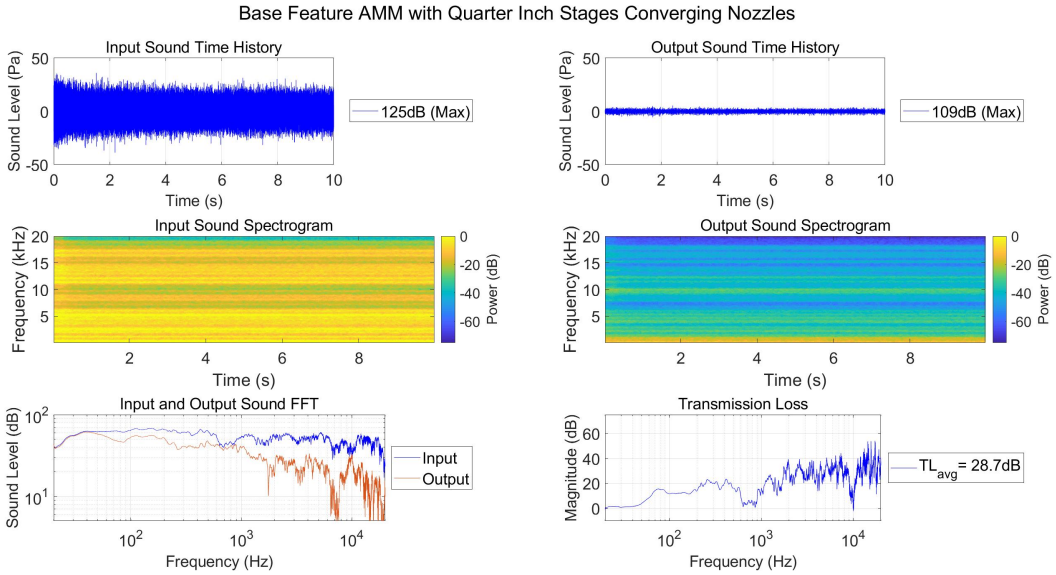

Figure 3-54 - SISO - Base Feature AMM with Quarter Inch Stages - Converging Configuration - Test Results

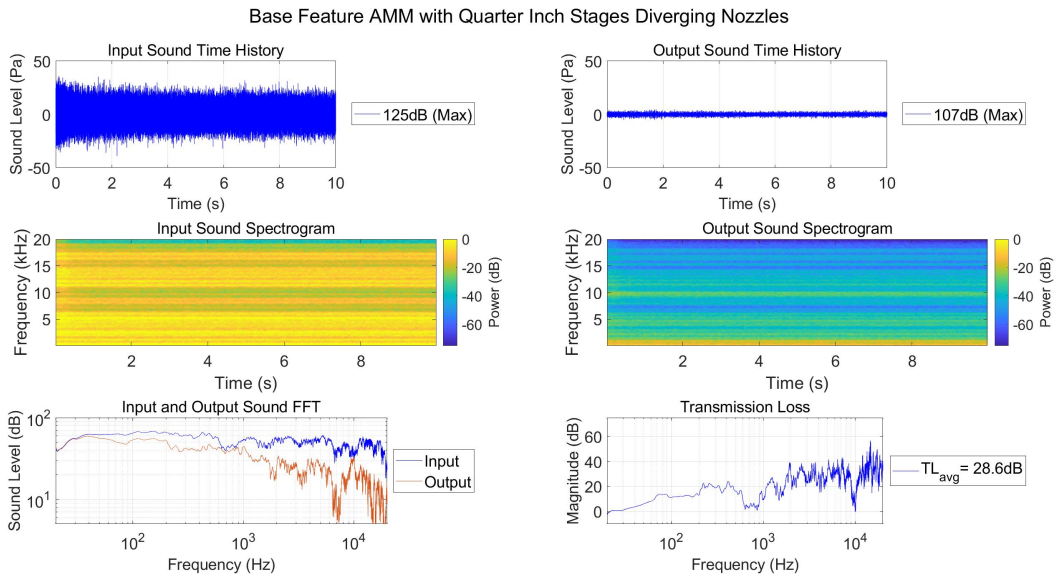

Figure 3-55 -SISO - Base Feature AMM with Quarter Inch Stages - Diverging Configuration - Test Results

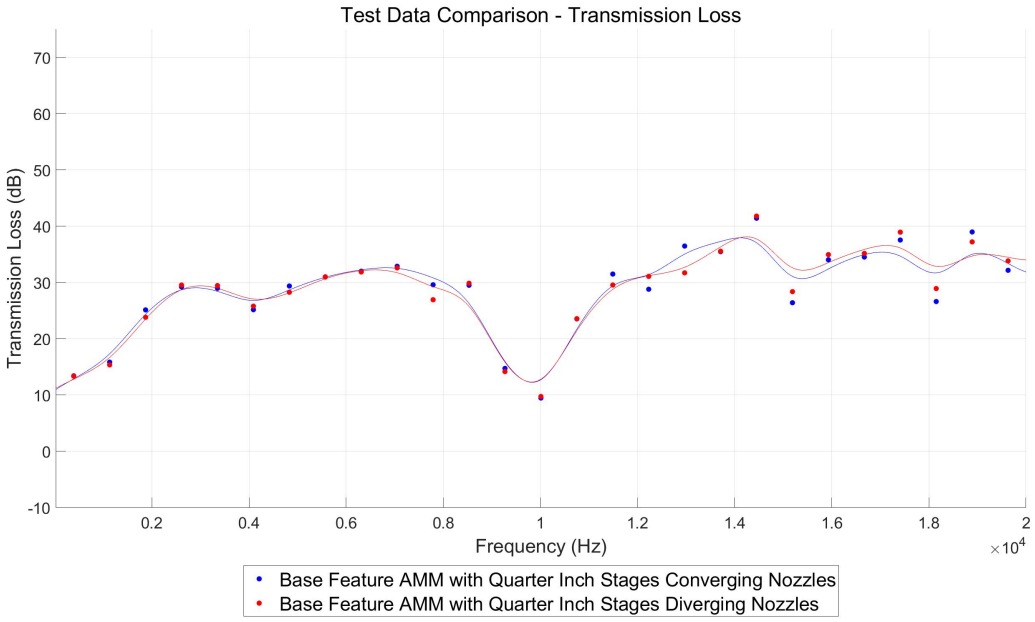

Figure 3-56 - SISO - Base Feature AMM with Quarter Inch Stages - Transmission Loss Comparison

Average Transmission Loss (dB)					
Configuration	20 Hz - 5 kHz	5 kHz - 10 kHz	10 kHz - 15 kHz	15 kHz - 20 kHz	20 Hz - 20 kHz
BF AMM with Quarter Inch Stages - Converging	23.4	27.2	31.1	32.9	28.7
BF AMM with Quarter Inch Stages - Diverging	23.2	26.7	30.8	33.8	28.6

Table 3-16 - SISO - Base Feature AMM with Quarter Inch Stages - Average Transmission Loss

3.5.3.5 Single Input Single Output Systems Downsizing Experimental Testing Summary

Sections 3.5.3.1 through 3.5.3.4 discuss the comparison of each prototype in the converging and diverging configurations. The results for each section show that both configurations had comparable results, with the diverging configuration performing slightly better than the converging configuration. The experimental testing data will be shown first with the converging configurations then with the diverging configurations.

Figure 3-57 shows the TL for converging configurations. Across a majority of the acoustic spectrum, the smaller stage configurations had a better performance than the 2” stage configurations. The 1/2” and 1/4” configurations showed very comparable performance across the spectrum. Overall, the 1”, 1/2”, and 1/4” had comparable performance. Table 3-17 shows the comparison in a tabular form.

Figure 3-58 shows the TL for diverging configurations. The 4 configurations show similar performance across the acoustic spectrum. Table 3-18 shows the comparison in a tabular form.

Experimental testing for both converging and diverging configurations show that overall performance is not negatively impacted by downsizing the prototypes.

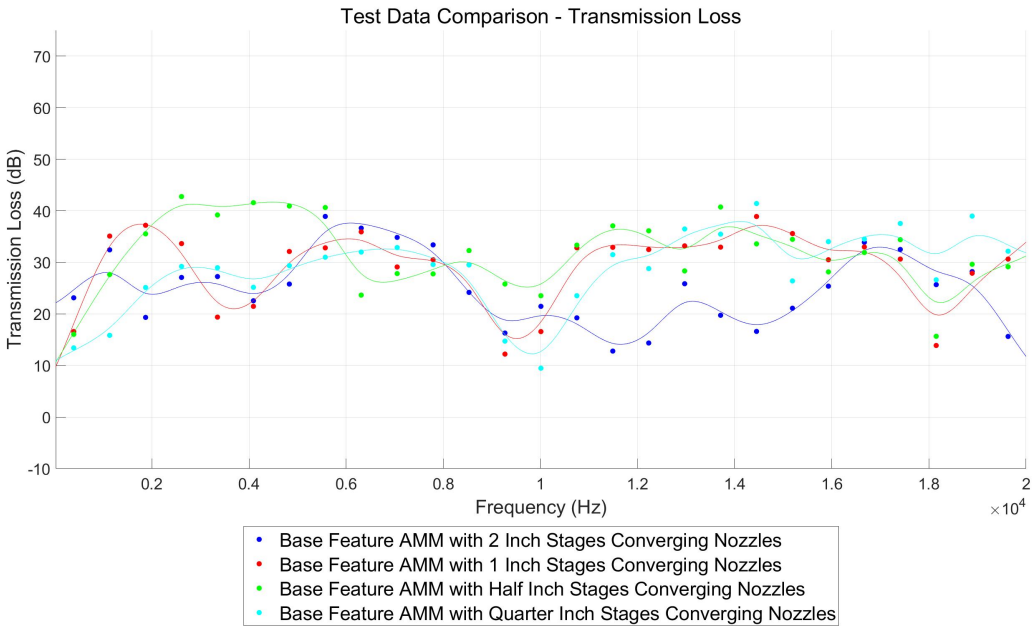

Figure 3-57 - SISO - Effects of Downsizing - Converging Configuration - Transmission Loss Comparison

Average Transmission Loss (dB)					
Configuration	20 Hz - 5 kHz	5 kHz - 10 kHz	10 kHz - 15 kHz	15 kHz - 20 kHz	20 Hz - 20 kHz
BF AMM with 2 Inch Stages - Converging	25.1	30.0	18.4	26.4	25.0
BF AMM with 1 Inch Stages - Converging	27.5	27.6	32.6	28.9	29.2
BF AMM with Half Inch Stages - Converging	34.3	30.0	33.9	28.9	31.8
BF AMM with Quarter Inch Stages - Converging	23.4	27.2	31.1	32.9	28.7

Table 3-17 - SISO - Effects of Downsizing - Converging Configuration - Transmission Loss Comparison

Figure 3-58 - SISO - Effects of Downsizing - Diverging Configuration - Transmission Loss Comparison

Average Transmission Loss (dB)					
Configuration	20 Hz - 5 kHz	5 kHz - 10 kHz	10 kHz - 15 kHz	15 kHz - 20 kHz	20 Hz - 20 kHz
BF AMM with 2 Inch Stages - Diverging	25.6	32.0	25.9	28.9	28.1
BF AMM with 1 Inch Stages - Diverging	27.1	27.8	32.7	31.9	29.9
BF AMM with Half Inch Stages - Diverging	33.0	29.7	34.0	31.5	32.0
BF AMM with Quarter Inch Stages - Diverging	23.2	26.7	30.8	33.8	28.6

Table 3-18 - SISO - Effects of Downsizing - Diverging Configuration - Transmission Loss Comparison

3.5.4 Single Input Single Output Additional Stage

The test articles described in section 2.5 were tested and evaluated for acoustic performance. The results of this testing allowed for the evaluation of the four stage BF AMM configuration against the 3-stage BF AMM configuration. It is to be noted that these prototypes had already been built when the notion of the COOP was conceived. Consequently, this configuration does not have the feature.

Experimental testing results for the 4-stage BF AMM with a 1/4" stage length proved that performance was improved over the 3-stage configuration. The configuration was tested in only the diverging configuration. The time domain data decreased from 125 dB to 107 dB for both the 3- and 4-stage configurations.

Across the 20 Hz to 20 kHz bandwidth, the TL_{avg} equaled 26.6 dB and 33.7 dB for the 3- and 4-stage configurations, respectively. Figure 3-59 and Figure 3-60 show the input and output time history, spectrograms, and FFT as well as the TL across the acoustic spectrum for the 3- and 4-stage configurations respectively. Figure 3-61 shows a comparison plot of TL_{avg} for both configurations. The majority of the improvement is seen from below 12 kHz. Table 3-19 details the TL_{avg} in the 20 Hz to 5 kHz, 5 kHz to 10 kHz, 10 kHz to 15 kHz, 15 kHz to 20 kHz, and 20 Hz to 20 kHz bandwidths for both configurations.

Figure 3-61 shows a comparison plot between the configurations. Below 14 kHz, the fourth stage provides a substantial amount of acoustic mitigation. Table 3-19 shows the data in tabular form. In the 10 kHz to 15 kHz bandwidth, the additional stage provided additional

acoustic mitigation. These results show that the additional stage was effective in acoustic mitigation. Therefore, the feature will be included in subsequent testing.

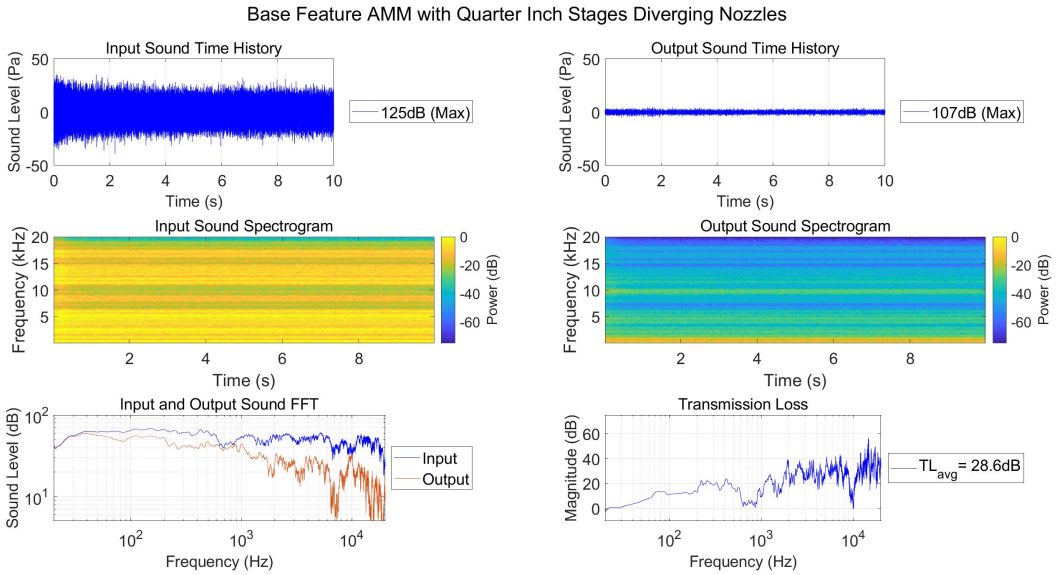

Figure 3-59 - SISO - Base Feature AMM with Quarter Inch Stages - Diverging Configuration - Test Results

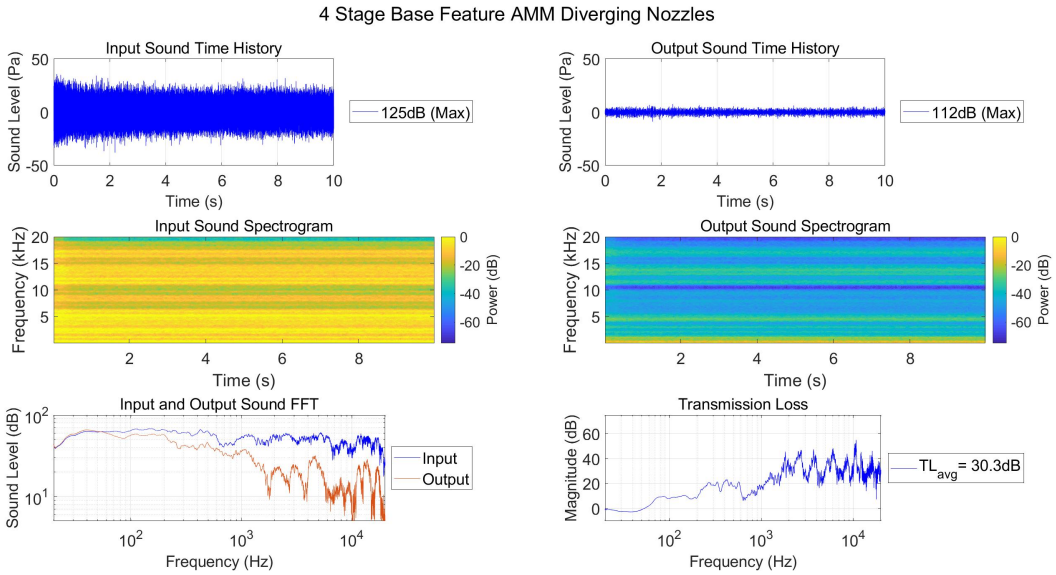

Figure 3-60 - SISO - Base Feature AMM with Quarter Inch Stages - Four Stage Diverging Configuration - Test Results

Figure 3-61 - SISO - Base Feature AMM with Quarter Inch Stages - Additional Stage - Transmission Loss Comparison

	Average Transmission Loss (dB)				
Configuration	20 Hz - 5 kHz	5 kHz - 10 kHz	10 kHz - 15 kHz	15 kHz - 20 kHz	20 Hz - 20 kHz
BF AMM with Quarter Inch Stages - Diverging	23.2	26.7	30.8	33.8	28.6
BF AMM with 4 Stages and Quarter Inch Stages - Diverging	29.2	35.4	35.3	35.0	33.7

Table 3-19 - SISO - Base Feature AMM with Quarter Inch Stages - Additional Stage - Average Transmission Loss

3.5.5 Single Input Single Output Experimental Testing Summary

Experimental testing outlined in 3.5.1 proved the acoustic mitigation of several features could be combined in order to see a substantial amount of acoustic mitigation. The first big improvement was seen when the nozzles were placed in series. Significantly broader bandgaps

were then seen. The addition of the perforations in both the radial and axial direction as well as the COOP significantly improved the performance.

Further improvement in the design came from enclosing the BF AMM as outlined in section 3.5.2. The downsizing of the prototypes outlined in section 3.5.3 proved that scaling the system down in size did not affect performance. The testing outlined in section 3.5.4 proved the additional stage was beneficial to acoustic mitigation above 10 kHz. Overall, the addition of all the features improved the acoustic TL from 4.8 dB to 33.9 dB. A comparison plot of the TL from the SP to the BF AMM is shown in Figure 3-62. Tabular data is shown in Table 3-20.

All of these features became incorporated into the BF AMM design. An enclosed cell, with 4 one-quarter inch long stages configured with a SDN with RAP and a COOP was chosen as the base design moving forward into the MIMO phase of testing and design. This configuration will henceforth be referred to as the BF AMM.

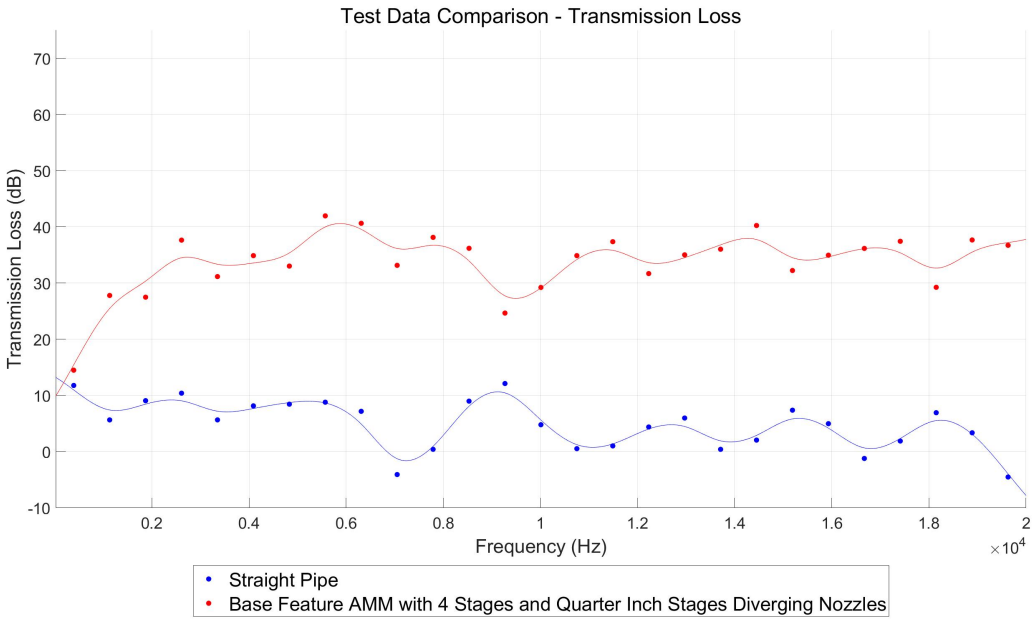

Figure 3-62 - Straight Pipe and Base Feature AMM - Transmission Loss Comparison

	Average Transmission Loss (dB)				
Configuration	20 Hz - 5 kHz	5 kHz - 10 kHz	10 kHz - 15 kHz	15 kHz - 20 kHz	20 Hz - 20 kHz
SP	8.5	5.8	2.5	2.6	4.8
BF AMM with 4 Stages and Quarter Inch Stages - Diverging	29.2	35.4	35.3	35.0	33.7

Table 3-20 - SISO - Straight Pipe and Base Feature AMM - Average Transmission Loss

3.6 Multiple Input Multiple Output Systems

3.6.1 Effects of a Straight Pipe on Output Sound

Experimental testing results for the SP panel provided a baseline of performance across the acoustic bandwidth. The time domain data decreased from 126 dB to 116 dB. The configuration showed improvement from the SISO SP test results. This can be attributed to the

size difference of the prototypes. The smaller size of the MIMO SP allowed for more of the acoustic spectrum to be larger than the prototype. This is most noticeable around 10 kHz.

Across the 20 Hz to 20 kHz bandwidth, the TL_{avg} equaled 16.4 dB. Figure 3-63 shows the input and output time history, spectrograms, and FFT as well as the TL across the acoustic spectrum. The output spectrogram and output FFT show poor performance in the 10 kHz to 20 kHz bandwidth. Table 3-21 details the TL_{avg} in the 20 Hz to 5 kHz, 5 kHz to 10 kHz, 10 kHz to 15 kHz, 15 kHz to 20 kHz, and 20 Hz to 20 kHz bandwidths for both configurations.

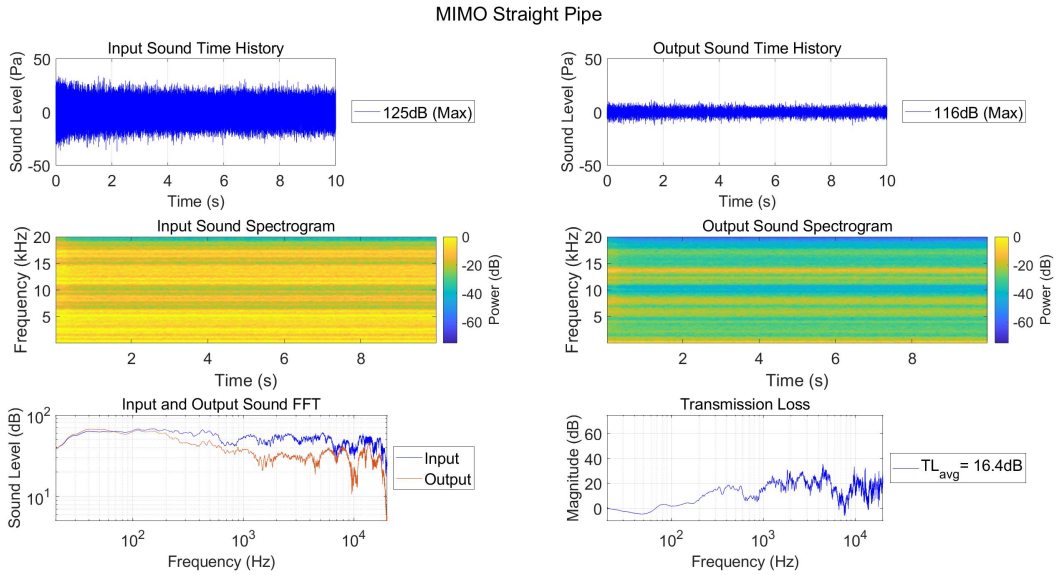

Figure 3-63 - MIMO - Straight Pipe - Test Results

Average Transmission Loss (dB)					
Configuration	20 Hz - 5 kHz	5 kHz - 10 kHz	10 kHz - 15 kHz	15 kHz - 20 kHz	20 Hz - 20 kHz
MIMO SP	19.8	12.5	15.7	17.6	16.4

Table 3-21 - MIMO - Straight Pipe - Average Transmission Loss

3.6.2 Effects of a Base Feature Acoustic Metamaterial on Output Sound

Experimental testing for the BF AMM was performed in the converging and diverging configurations for the 3-stage prototype and in the diverging configuration for the 4-stage prototype. The time domain data decreased from 126 dB to 112 dB, 113 dB, and 112 dB for the converging, diverging, and 4-stage configurations, respectively. It is to be noted that these prototypes had already been built when the notion of the COOP was conceived. Consequently, this configuration does not have the feature.

The BF AMM MIMO configurations performed remarkably well. There was an almost complete mitigation of acoustic noise from 5 kHz - 10 kHz and there was substantial acoustic mitigation from 10 kHz to 20 kHz as well. Across the 20 Hz to 20 kHz bandwidth, the TL_{avg} equaled 29.6 dB, 29.3 dB, and 30.3 dB for the converging, diverging, and 4-stage configurations, respectively. Figure 3-64, Figure 3-65, and Figure 3-66 show the input and output time history, spectrograms, and FFT as well as the TL across the acoustic spectrum, for the converging, diverging, and 4-stage configurations, respectively. The 4-stage configuration outperformed in frequencies less than 400 Hz. The spectrogram and FFTs for all configurations show an almost complete mitigation of acoustic noise above 5 kHz, but the 4-stage configuration showed an almost complete mitigation of acoustic noise above 2 kHz. Figure 3-67 shows a comparison plot for all of the configurations. Table 3-22 details the TL_{avg} in the 20 Hz to 5 kHz, 5 kHz to 10 kHz, 10 kHz to 15 kHz, 15 kHz to 20 kHz, and 20 Hz to 20 kHz bandwidths for both configurations.

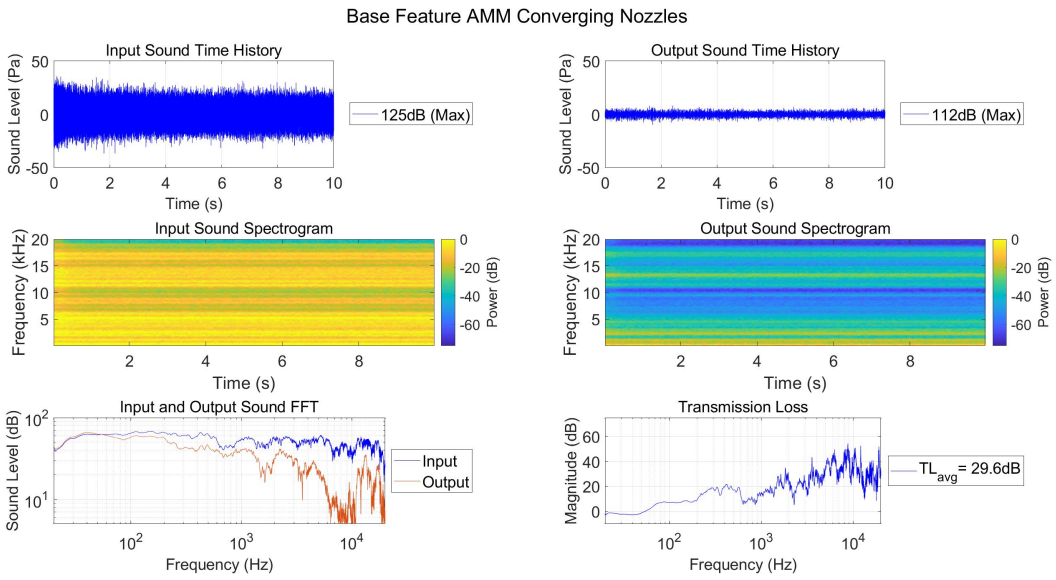

Figure 3-64 - MIMO - Base Feature AMM - Converging Configuration - Test Results

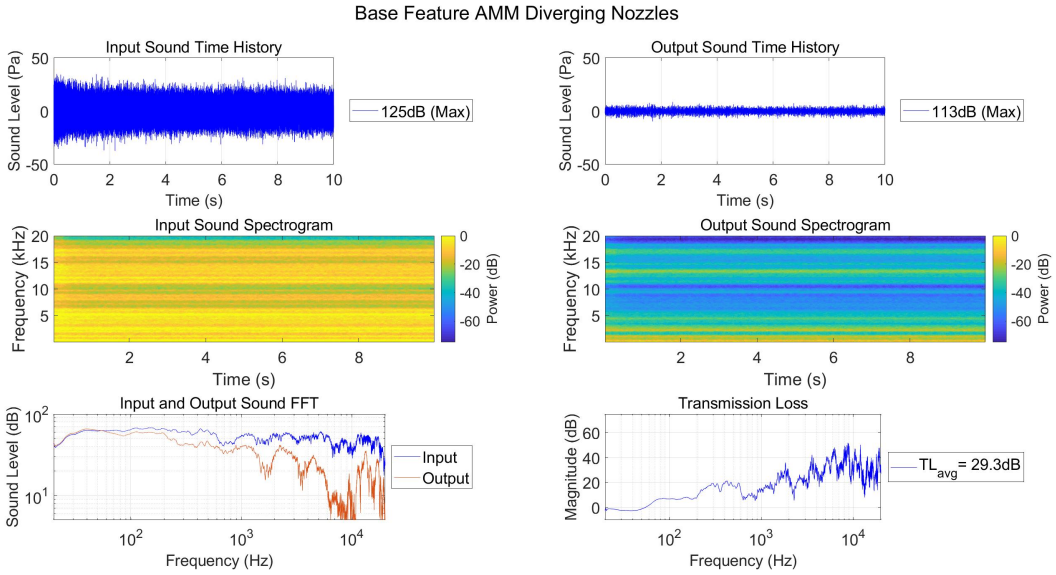

Figure 3-65 - MIMO - Base Feature AMM - Diverging Configuration - Test Results

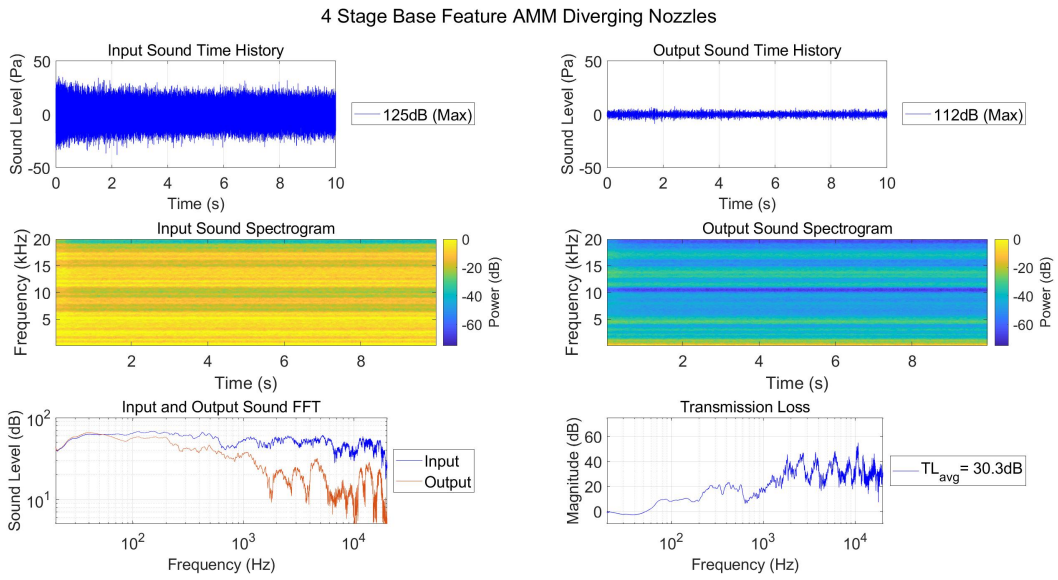

Figure 3-66 - MIMO - Base Feature AMM - Four Stage Diverging Configuration - Test Results

Figure 3-67 - MIMO - Base Feature AMM - Transmission Loss Comparison

Average Transmission Loss (dB)					
Configuration	20 Hz - 5 kHz	5 kHz - 10 kHz	10 kHz - 15 kHz	15 kHz - 20 kHz	20 Hz - 20 kHz
BF AMM - Converging	21.3	37.0	30.1	29.9	29.6
BF AMM - Diverging	21.6	35.9	29.6	30.2	29.4
4-stage BF AMM - Diverging	27.1	32.5	31.8	29.9	30.3

Table 3-22 - MIMO - Base Feature AMM - Transmission Loss Comparison

3.6.3 Effects of a Large Cavity Acoustic Metamaterials on Output Sound

Experimental testing for the Large Cavity AMM was performed in the converging and diverging configurations for the 3-stage prototype and in the diverging configuration for the 4-stage prototype. The time domain data decreased from 126 dB to 114 dB, 115 dB, and 112 dB for the converging, diverging, and 4-stage configurations, respectively. The Large Cavity AMM panel showed improved performance across the acoustic bandwidth. The addition of outer cell walls, stage division walls, and a diagonal wall in the Large Cavity AMM panel considerably improved the performance. The output sound above 5 kHz is in the noise floor for all configurations.

Across the 20 Hz to 20 kHz bandwidth, the TL_{avg} equaled 124 dB to 25.4 dB, 24.6 dB, and 33.3 dB for the converging, diverging, and 4-stage configurations, respectively. Figure 3-68, Figure 3-69, and Figure 3-70 show the input and output time history, spectrograms, and FFT. In addition, it shows the TL across the acoustic spectrum, for the converging, diverging, and 4-stage configurations, respectively. Across most of the acoustic spectrum, the 4-stage configuration outperformed the 3-stage configurations. Above 17 kHz, the performance between the

configurations is comparable. The spectrogram and FFTs for all configurations show an almost complete mitigation of acoustic noise above 5 kHz, but the 4-stage configuration shows an almost complete mitigation of acoustic noise above 2 kHz. Figure 3-71 shows a comparison plot for all of the configurations. Table 3-23 details the TL_{avg} in the 20 Hz to 5 kHz, 5 kHz to 10 kHz, 10 kHz to 15 kHz, 15 kHz to 20 kHz, and 20 Hz to 20 kHz bandwidths for both configurations.

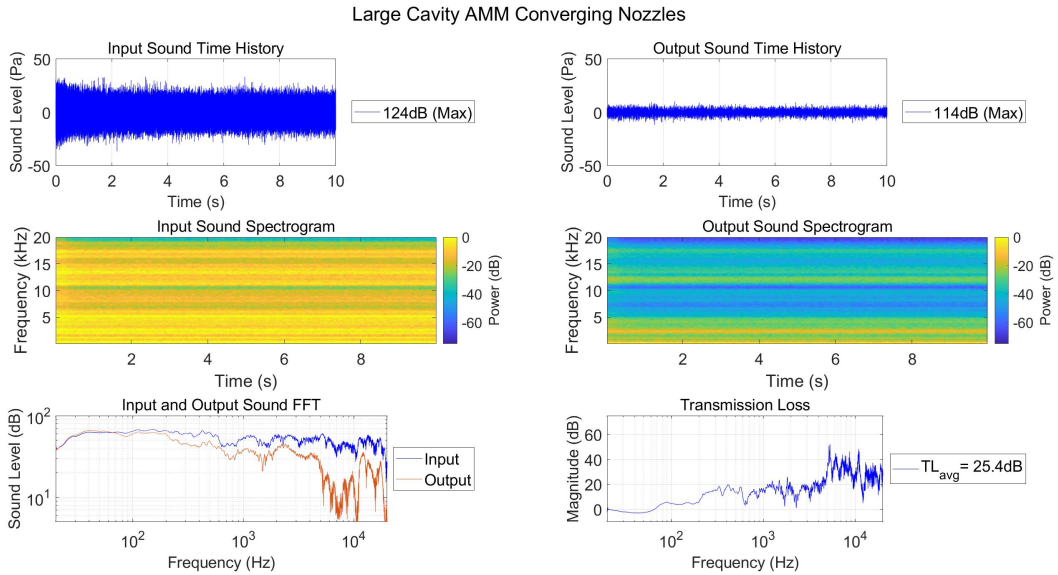

Figure 3-68 - MIMO Large Cavity AMM - Converging Configuration - Test Results

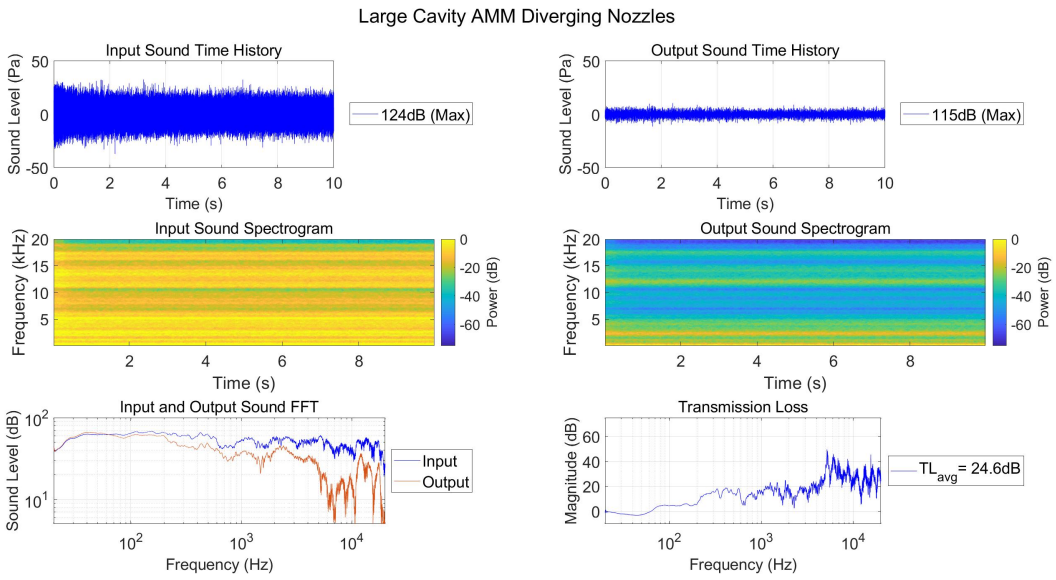

Figure 3-69 - MIMO Large Cavity AMM - Diverging Configuration - Test Results

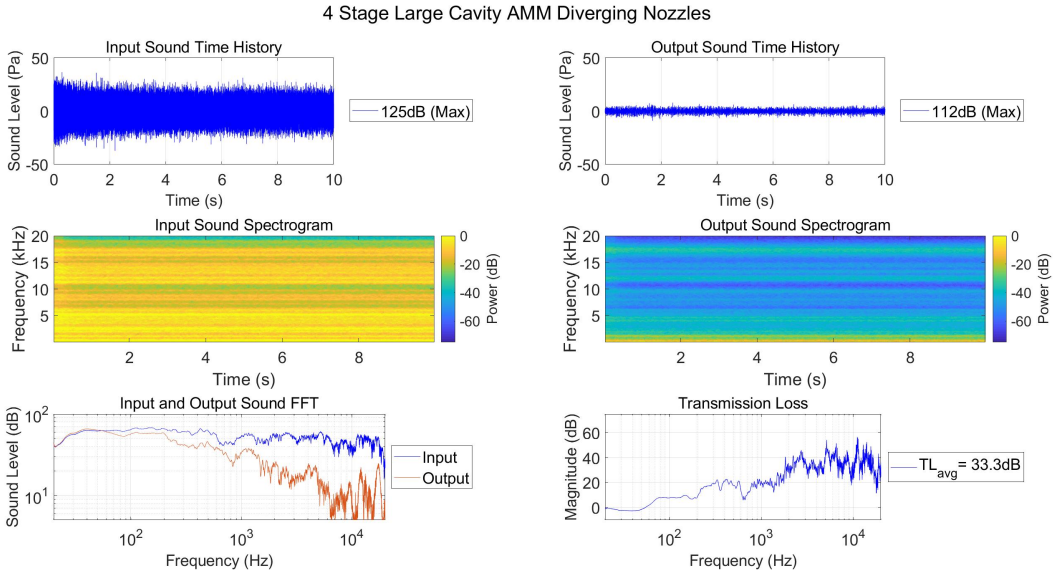

Figure 3-70 - MIMO Large Cavity AMM - 4-stage Diverging Configuration - Test Results

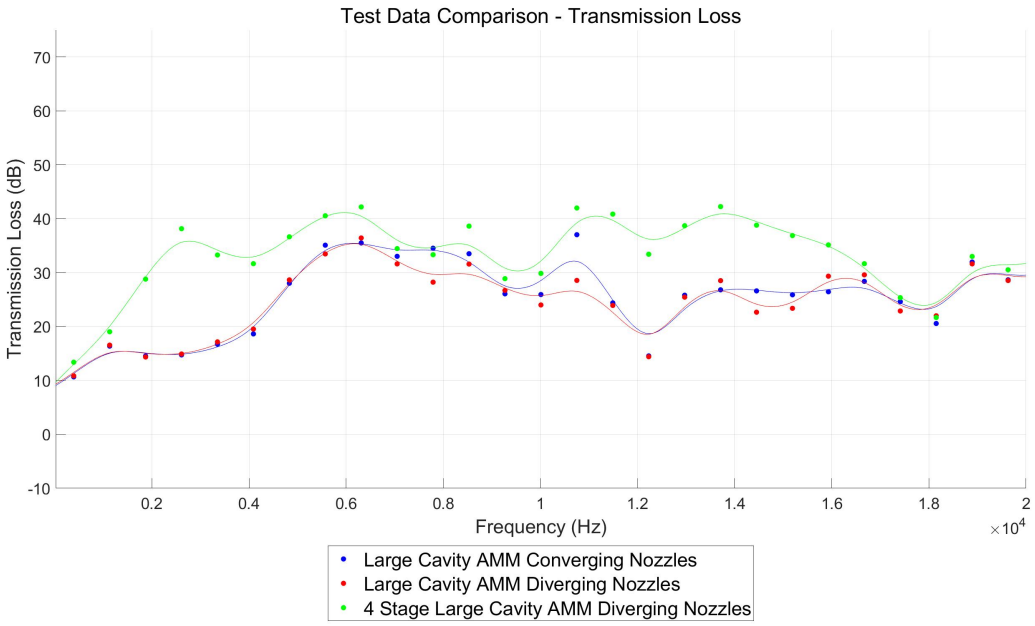

Figure 3-71 - MIMO - Large Cavity AMM - Transmission Loss Comparison

Average Transmission Loss (dB)					
Configuration	20 Hz - 5 kHz	5 kHz - 10 kHz	10 kHz - 15 kHz	15 kHz - 20 kHz	20 Hz - 20 kHz
Large Cavity AMM - Converging	16.3	32.6	26.1	26.6	25.4
Large Cavity AMM - Diverging	16.6	31.1	23.9	26.9	24.6
4-stage Large Cavity AMM - Diverging	28.1	36.1	38.6	30.4	33.3

Table 3-23 - MIMO - Large Cavity AMM - Average Transmission Loss

3.6.4 Effects of a Small Cavity Acoustic Metamaterials on Output Sound

Experimental testing for the Small Cavity AMM was performed in the converging and diverging configurations for the 3-stage prototype and in the diverging configuration for the 4-stage prototype. The time domain data decreased from 126 dB to 114 dB, 115 dB, and 112 dB for the converging, diverging, and 4-stage configurations, respectively. Further dividing the Large

Cavity AMM cavities with the addition of the walls from the corners to the nozzle in the Small Cavity AMM panel drastically enhanced performance in the 15 kHz - 20 kHz range.

Across the 20 Hz to 20 kHz bandwidth, the TL_{avg} equaled 25.4 dB, 24.6 dB, and 33.3 dB for the converging, diverging, and 4-stage configurations, respectively. Figure 3-72, Figure 3-73, and Figure 3-74 show the input and output time history, spectrograms, and FFT as well as the TL across the acoustic spectrum. Figure 3-72, Figure 3-73, and Figure 3-74 show the converging, diverging, and 4-stage configurations, respectively. The spectrogram and FFTs for all configurations show an almost complete mitigation of acoustic noise above 5 kHz, but the 4-stage configuration shows an almost complete mitigation of acoustic noise above 2 kHz. Figure 3-75 shows a comparison plot for all of the configurations. The 4-stage configuration clearly provides substantially more acoustic mitigation across the entire acoustic spectrum than the 3-stage configurations. Table 3-24 details the TL_{avg} in the 20 Hz to 5 kHz, 5 kHz to 10 kHz, 10 kHz to 15 kHz, 15 kHz to 20 kHz, and 20 Hz to 20 kHz bandwidths for both configurations.

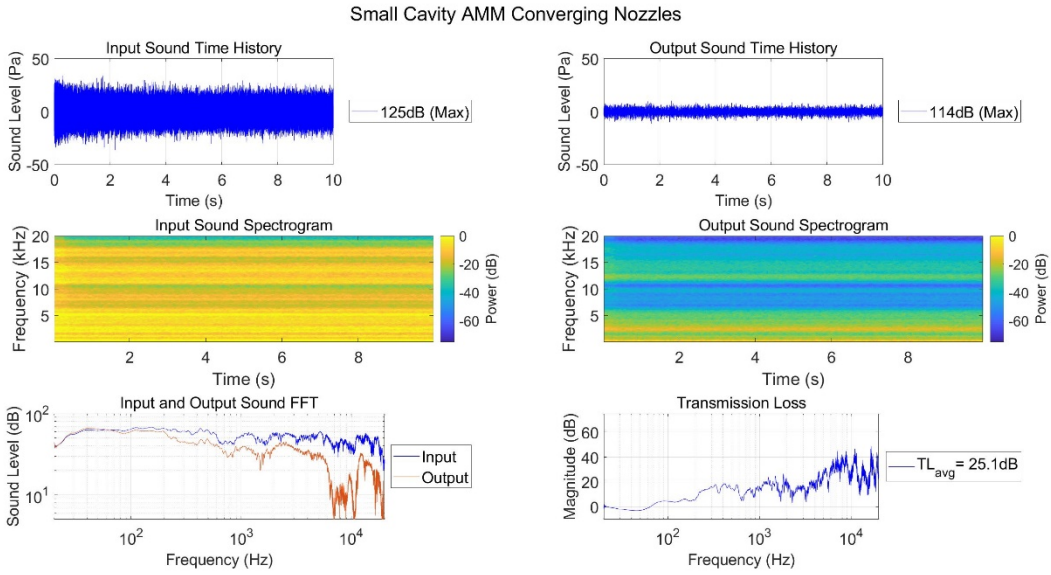

Figure 3-72 - MIMO Small Cavity AMM - Converging Configuration - Test Results

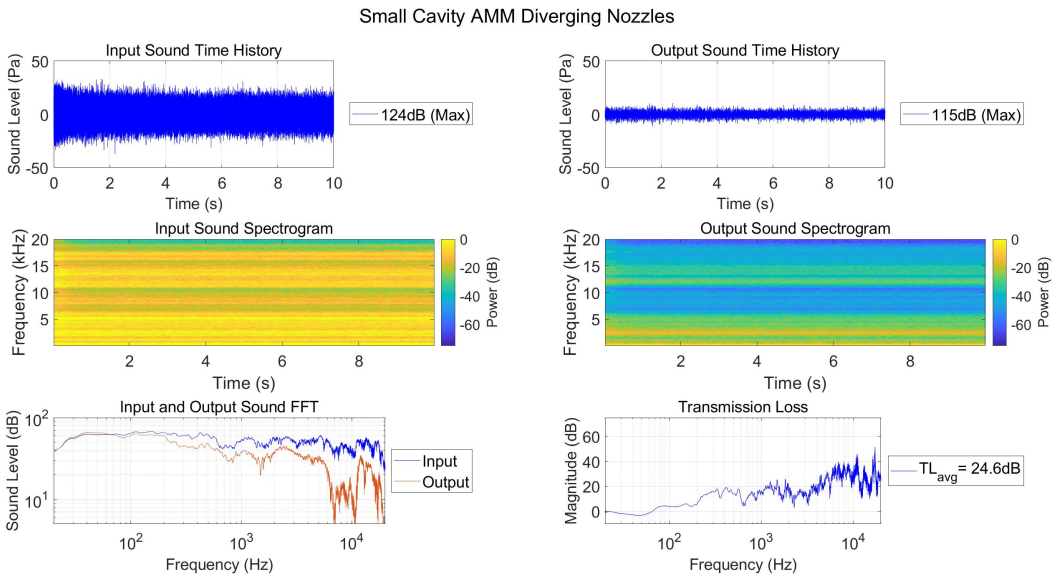

Figure 3-73 - MIMO Small Cavity AMM - Diverging Configuration - Test Results

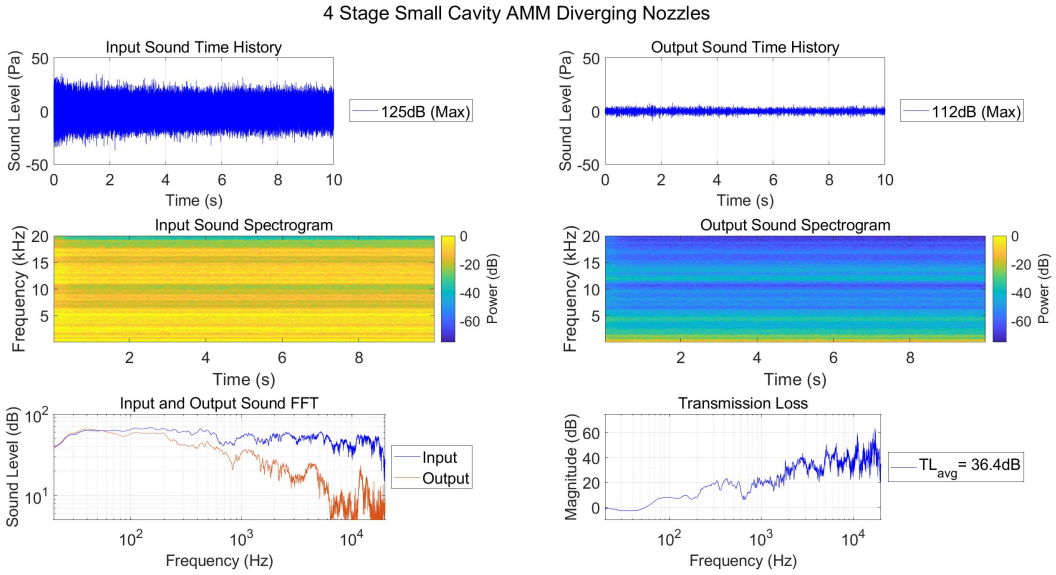

Figure 3-74 - MIMO Small Cavity AMM - Four Stage Diverging Configuration - Test Results

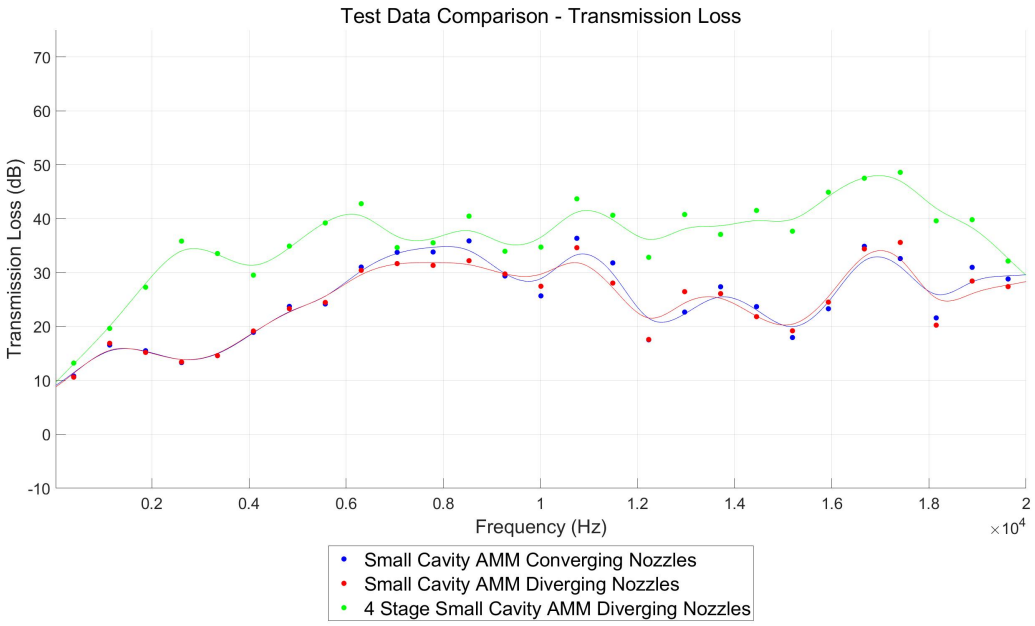

Figure 3-75 - MIMO - Small Cavity AMM - Transmission Loss Comparison

Average Transmission Loss (dB)					
Configuration	20 Hz - 5 kHz	5 kHz - 10 kHz	10 kHz - 15 kHz	15 kHz - 20 kHz	20 Hz - 20 kHz
Small Cavity AMM - Converging	15.8	30.7	26.4	27.4	25.1
Small Cavity AMM - Diverging	15.7	29.6	25.7	27.4	24.6
4-stage Small Cavity AMM - Diverging	27.1	37.7	39.1	41.5	36.4

Table 3-24 - MIMO - Small Cavity AMM - Average Transmission Loss

3.6.5 Effects of Infill Acoustic Metamaterials on Output Sound

Experimental testing for the Infill AMM was performed in the converging and diverging configurations for the 3-stage prototype and in the diverging configuration for the 4-stage prototype. The time domain data decreased from 125 dB to 115 dB, 115 dB, and 112 dB for the converging, diverging, and 4-stage configurations, respectively.

The Infill AMM panel had exceptional performance across the entire acoustic bandwidth. Across the 20 Hz to 20 kHz bandwidth, the TL_{avg} equaled 24.2 dB, 23.3 dB, and 33.8 dB for the converging, diverging, and 4-stage configurations, respectively. Figure 3-76, Figure 3-77, and Figure 3-78 show the input and output time history, spectrograms, and FFT as well as the TL across the acoustic spectrum. Figure 3-76, Figure 3-77, and Figure 3-78 show the converging, diverging, and 4-stage configurations, respectively. All configurations provided exceptional acoustic mitigation above 3 kHz. Figure 3-79 shows a comparison plot for all of the configurations. The 4-stage configuration provides more acoustic mitigation across the entire acoustic spectrum than the 3-stage configurations. Table 3-25 details the TL_{avg} in the 20 Hz to 5 kHz, 5 kHz to 10 kHz, 10 kHz to 15 kHz, 15 kHz to 20 kHz, and 20 Hz to 20 kHz bandwidths for both configurations.

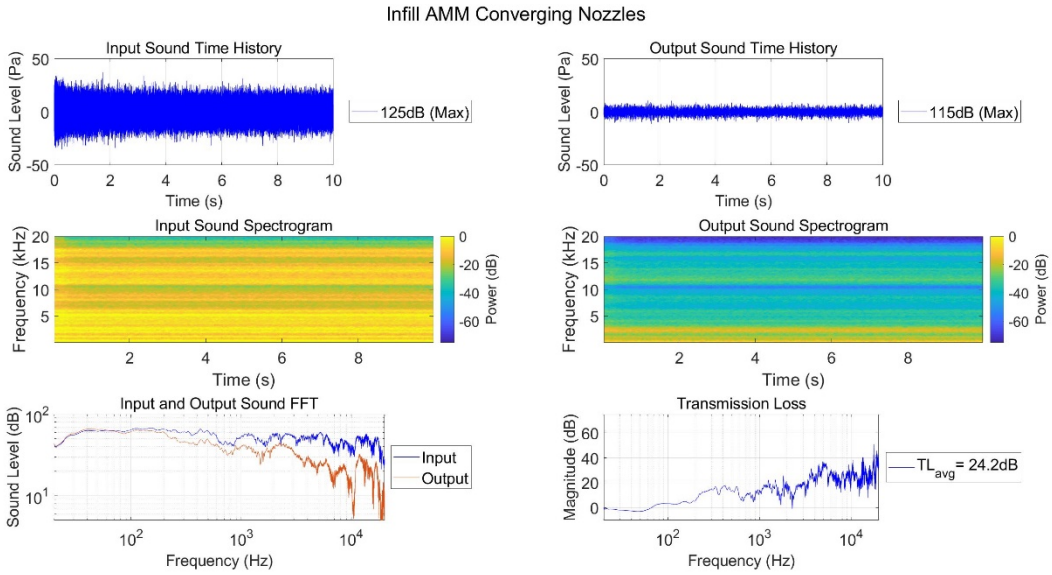

Figure 3-76 - MIMO - Infill AMM - Converging Configuration - Test Results

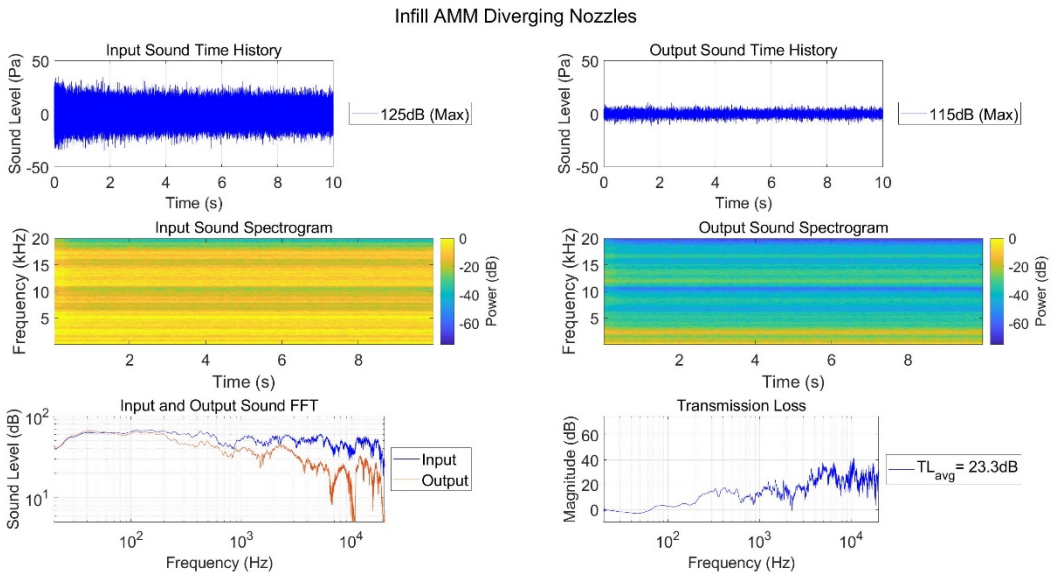

Figure 3-77 - MIMO - Infill AMM - Diverging Configuration - Test Results

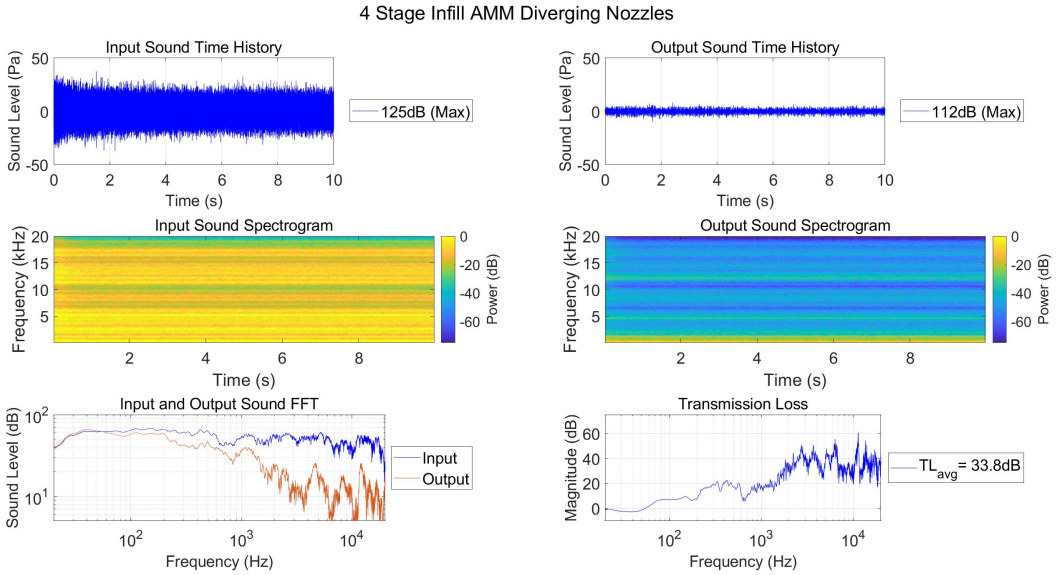

Figure 3-78 - MIMO - Infill AMM - Four Stage Diverging Configuration - Test Results

Figure 3-79 - MIMO - Infill AMM - Transmission Loss Comparison

Average Transmission Loss (dB)					
Configuration	20 Hz - 5 kHz	5 kHz - 10 kHz	10 kHz - 15 kHz	15 kHz - 20 kHz	20 Hz - 20 kHz
Infill AMM - Converging	17.9	24.7	25.3	28.8	24.2
Infill AMM - Diverging	17.7	25.4	25.6	24.6	23.3
4-stage Infill AMM - Diverging	29.8	34.5	36.6	34.2	33.8

Table 3-25 - MIMO - Infill AMM - Average Transmission Loss

3.6.6 Multiple Input Multiple Output Experimental Testing Comparison and Summary

All of the MIMO AMM configurations performed exceptionally well, especially in the 2 kHz to 20 kHz range. Figure 3-80 compares the all of the MIMO AMM prototypes in the converging configuration and Figure 3-81 makes the comparison in the diverging configuration. The converging and diverging nozzle configurations for each configuration of MIMO AMM

performed comparably. Substantial acoustic mitigation is seen in all 3-stage configurations from 2 kHz to 20 kHz. Table 3-26 and Table 3-27 show the tabular data of the converging and diverging configurations, respectively.

When comparing the 4-stage MIMO AMM prototypes, the Small Cavity AMM has a much higher TL than the other configurations from 15 kHz to 19 kHz. The spectrogram and FFTs for all MIMO AMM configurations show an almost complete mitigation of acoustic noise above 2 kHz. The comparison plots for the 4-stage MIMO configurations are shown in Figure 3-82 and the tabular data is presented in Table 3-28. The comparison plots as well as the tabular data show that the 4-stage Small Cavity AMM MIMO configuration is the preeminent prototype. This design was used as the basis for the AMM Sphere design.

Figure 3-80 - MIMO - Converging Configurations - Transmission Loss Comparison

Average Transmission Loss (dB)					
Configuration	20 Hz - 5 kHz	5 kHz - 10 kHz	10 kHz - 15 kHz	15 kHz - 20 kHz	20 Hz - 20 kHz
MIMO SP	19.8	12.5	15.7	17.6	16.4
BF AMM - Converging	21.3	37.0	30.1	29.9	29.6
Large Cavity AMM - Converging	16.3	32.6	26.1	26.6	25.4
Small Cavity AMM - Converging	15.8	30.7	26.4	27.4	25.1
Infill AMM - Converging	17.9	24.7	25.3	28.8	24.2

Table 3-26 - MIMO - Converging Configurations - Average Transmission Loss

Figure 3-81 - MIMO - Diverging Configurations - Transmission Loss Comparison

Average Transmission Loss (dB)					
Configuration	20 Hz - 5 kHz	5 kHz - 10 kHz	10 kHz - 15 kHz	15 kHz - 20 kHz	20 Hz - 20 kHz
MIMO SP	19.8	12.5	15.7	17.6	16.4
BF AMM - Diverging	21.6	35.9	29.6	30.2	29.4
Large Cavity AMM - Diverging	16.6	31.1	23.9	26.9	24.6
Small Cavity AMM - Diverging	15.7	29.6	25.7	27.4	24.6
Infill AMM - Diverging	17.7	25.4	25.6	24.6	23.3

Table 3-27 - MIMO - Diverging Configurations - Average Transmission Loss

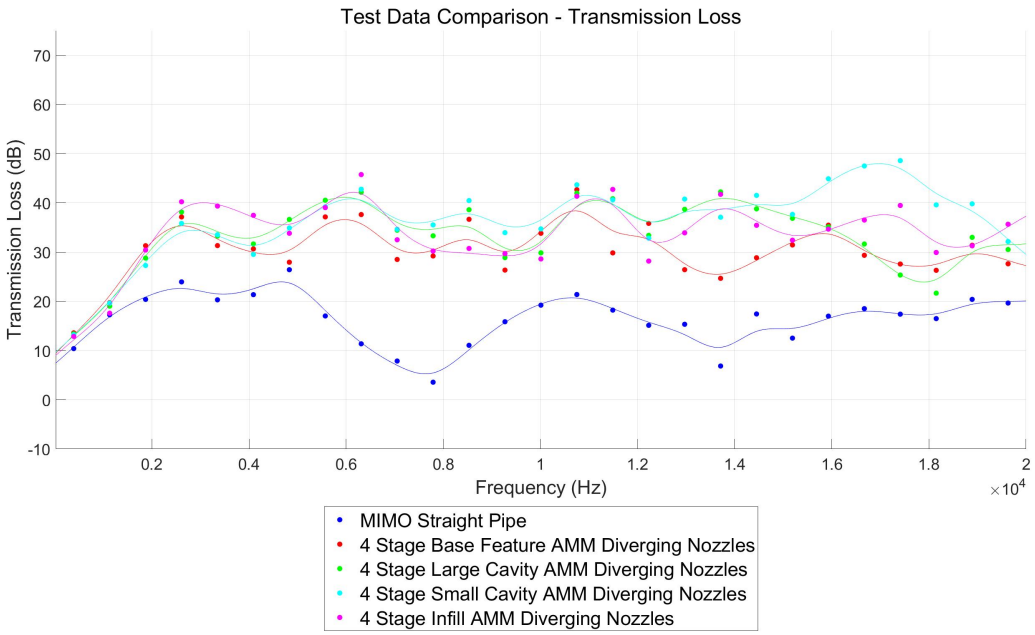

Figure 3-82 - MIMO - Four Stage Diverging Configurations - Transmission Loss Comparison

Average Transmission Loss (dB)					
Configuration	20 Hz - 5 kHz	5 kHz - 10 kHz	10 kHz - 15 kHz	15 kHz - 20 kHz	20 Hz - 20 kHz
MIMO SP	19.8	12.5	15.7	17.6	16.4
4-stage BF AMM - Diverging	27.1	32.5	31.8	29.9	30.3
4-stage Large Cavity AMM - Diverging	28.1	36.1	38.6	30.4	33.3
4-stage Small Cavity AMM - Diverging	27.1	37.7	39.1	41.5	36.4
4-stage Infill AMM - Diverging	29.8	34.5	36.6	34.2	33.8

Table 3-28 - MIMO - Four Stage Diverging Configurations - Average Transmission Loss

3.7 Acoustic Metamaterial Sphere Experimental Testing

3.7.1 Description of AMM Sphere Test Setup

The test setup was much simpler for the AMM Sphere testing. The AMM Sphere was simply placed on the test stand. Instrumentation was attached to the perforated platform on the AMM Sphere base and the cabling was run through a rubber gasket located between the AMM Sphere top and AMM Sphere base. Details are shown in Figure 3-83, Figure 3-84, and Figure 3-85. The input microphone was mounted to a stand fixed near the base of the test stand. Figure 3-86 shows the assembled AMM Sphere, test stand, and input microphone.

The AMM Sphere was tested in 4 test setup configurations: nominal distance, close distance, extended distance, and between two sound sources. The first 3 test setup configurations varied distances between the speakers and the test article. The fourth test setup configuration placed the AMM Sphere directly between the 2 test speakers. The approximate distance between the AMM Sphere and the speakers is detailed in Table 3-29. Dimensions are in feet. Overall views of each test setup configuration are shown in Figure 3-87, Figure 3-88, Figure 3-89, and Figure 3-90.

In each test setup configuration, 2 configurations that varied the AMM Sphere orientation were tested. The first configuration, referred to as the joint horizontal configuration, consisted of the interface between the AMM Sphere base and the AMM Sphere top orientated in the horizontal plane. The second AMM Sphere configuration, referred to as the joint vertical configuration, consisted of the interface between the AMM Sphere base and the AMM Sphere top orientated in the vertical plane.

Test Configuration	Approximate Distance from Speaker (ft.)
Nominal Distance	5
Close Distance	2.5
Extended Distance	7.5
Between Sound Sources	1

Table 3-29 - AMM Sphere - Test Configurations

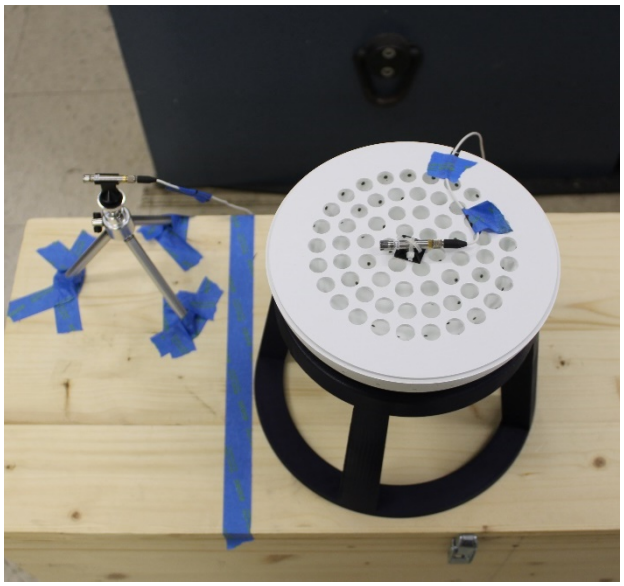

Figure 3-83 - AMM Sphere - Test Setup - Inner AMM Sphere View - Top View

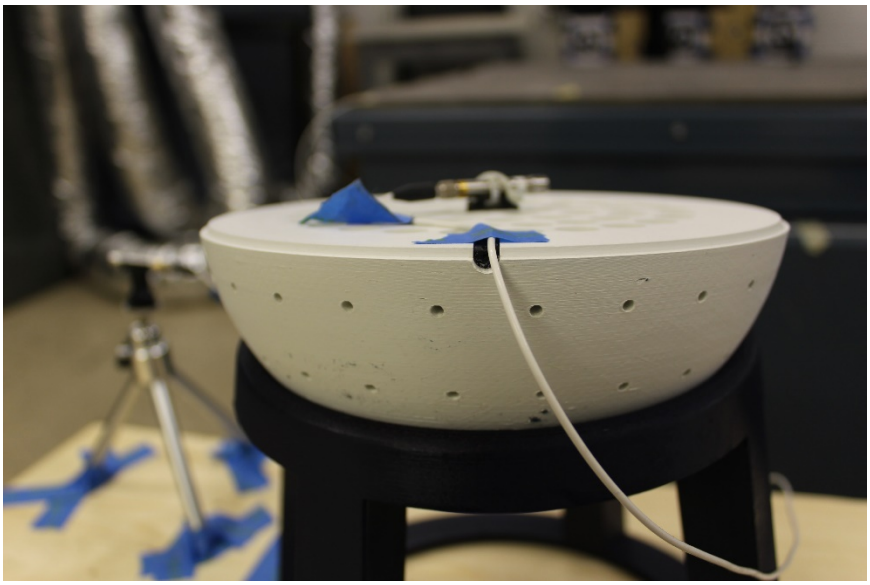

Figure 3-84 - AMM Sphere - Test Setup - Inner AMM Sphere View - Side View

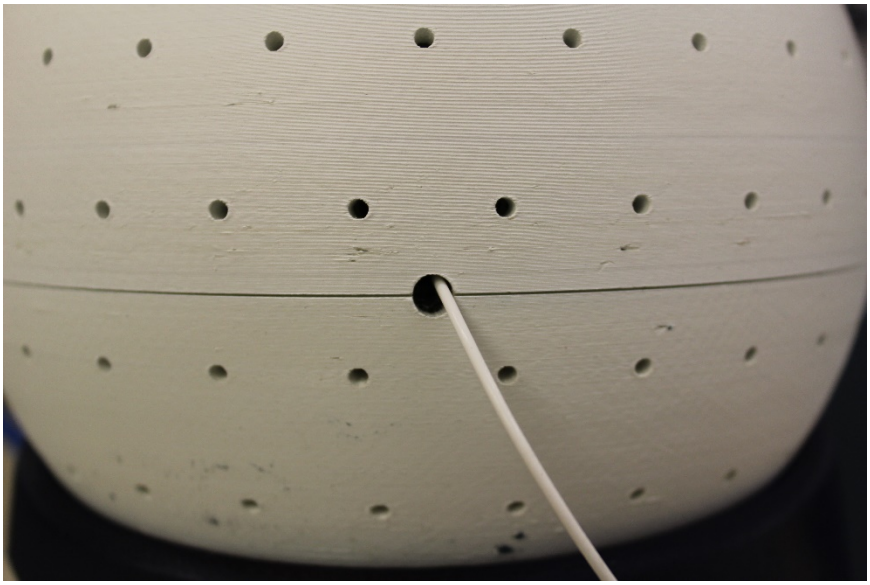

Figure 3-85 - AMM Sphere - Test Setup - Cabling Hole

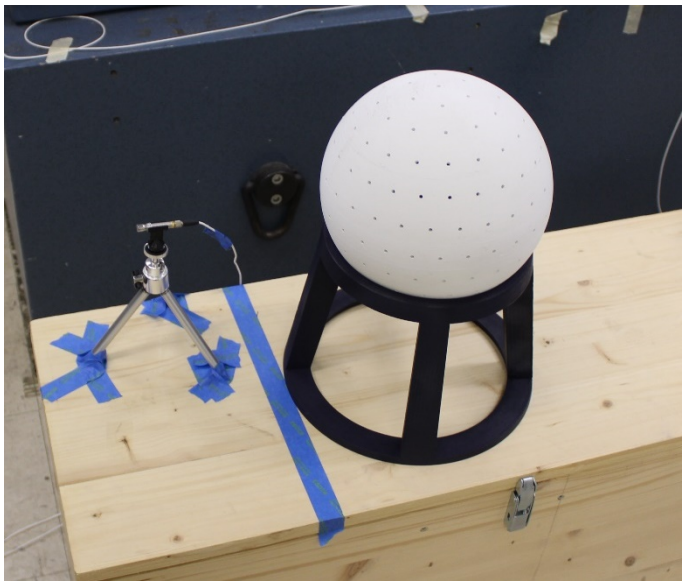

Figure 3-86 - AMM Sphere - Test Setup

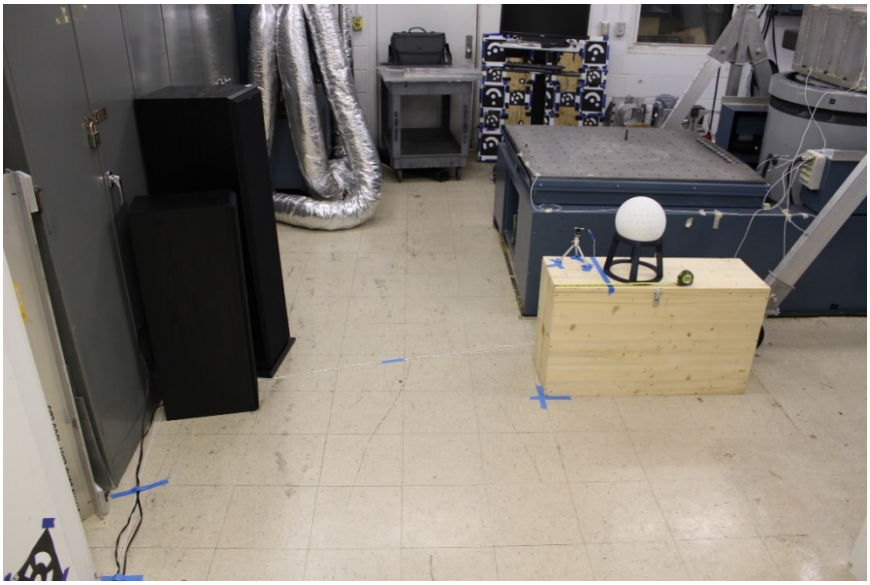

Figure 3-87 - AMM Sphere - Test Setup - Nominal Distance

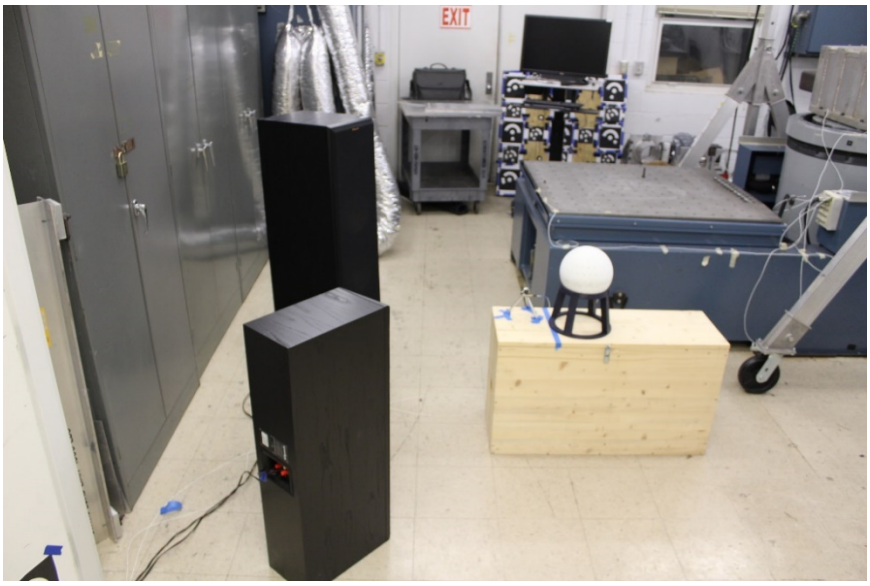

Figure 3-88 - AMM Sphere - Test Setup - Close Distance

Figure 3-89 - AMM Sphere - Test Setup - Extended Distance

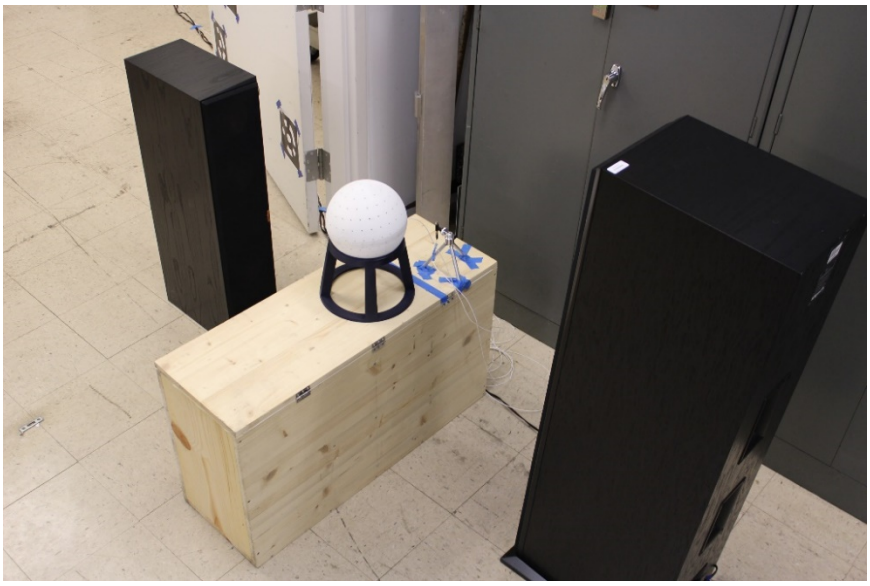

Figure 3-90 - AMM Sphere - Test Setup - Between Multiple Sound Sources

3.7.2 Acoustic Metamaterial Sphere Experimental Testing at a Nominal Distance

Experimental testing for the AMM Sphere at a nominal distance was performed in 2 configurations. The first configuration, referred to as the joint horizontal configuration, consisted of the interface between the AMM Sphere base and the AMM Sphere top in the horizontal plane. The second configuration, referred to as the joint vertical configuration, consisted of the interface between the AMM Sphere base and the AMM Sphere top in the vertical plane.

The time domain data decreased from 125 dB to 119 dB for both configurations. Across the 20 Hz to 20 kHz bandwidth, the TL_{avg} equaled 29.9 dB and 28.3 dB for the joint vertical and joint horizontal configurations, respectively. Figure 3-91 and Figure 3-92 show the input and output time history, spectrograms, and FFT as well as the TL across the acoustic spectrum, for joint vertical and joint horizontal configurations, respectively. Above 2 kHz, the transmitted acoustic noise is in the noise floor. Figure 3-93 shows a comparison plot for all of the configurations. Both configurations performed similarly across the acoustic spectrum. Table

3-30 details the TL_{avg} in the 20 Hz to 5 kHz, 5 kHz to 10 kHz, 10 kHz to 15 kHz, 15 kHz to 20 kHz, and 20 Hz to 20 kHz bandwidths for both configurations.

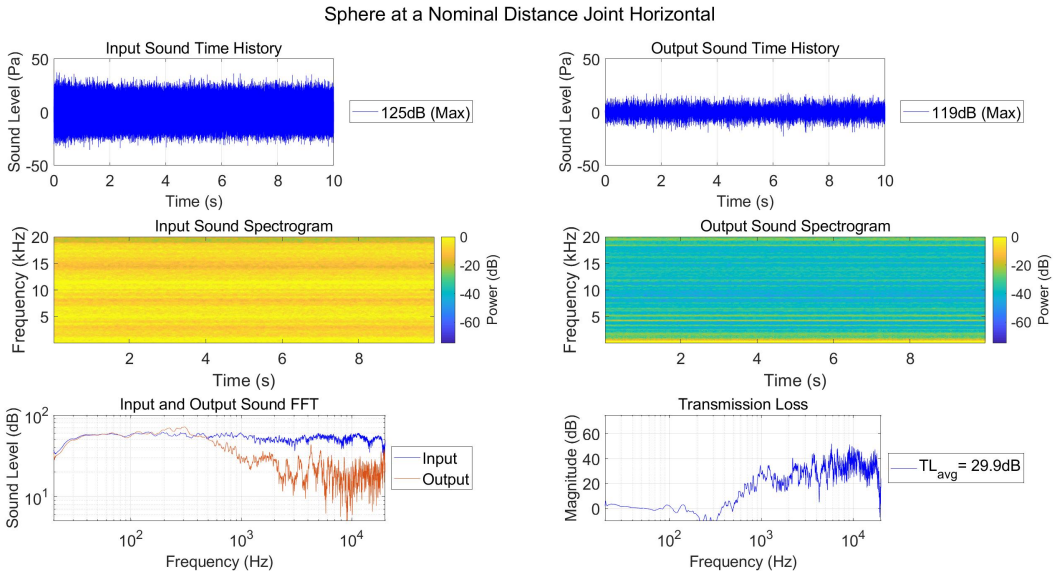

Figure 3-91 - AMM Sphere - Test - Nominal Distance - Joint Horizontal - Test Results

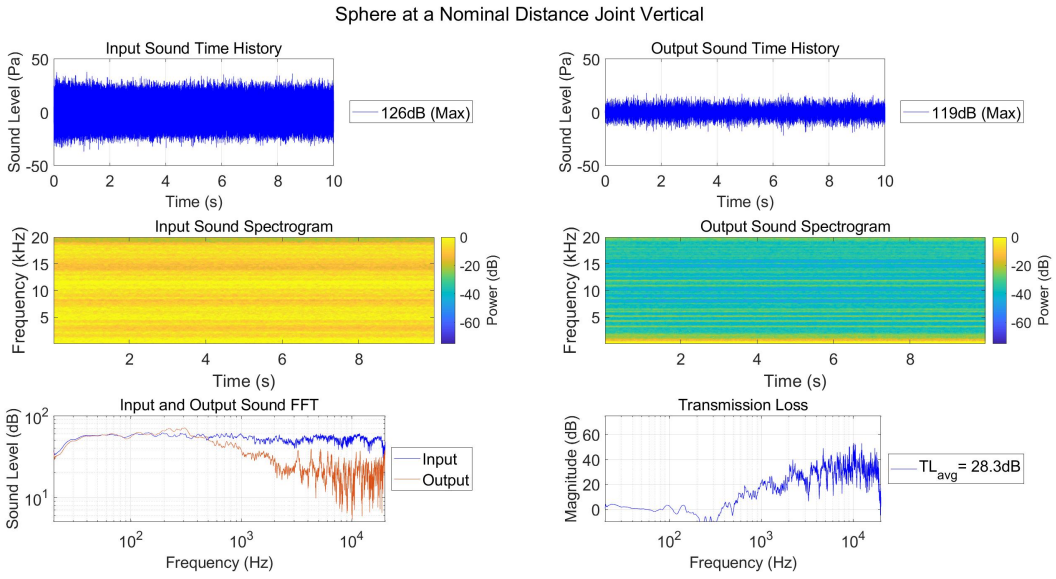

Figure 3-92 - AMM Sphere - Test - Nominal Distance - Joint Vertical - Test Results

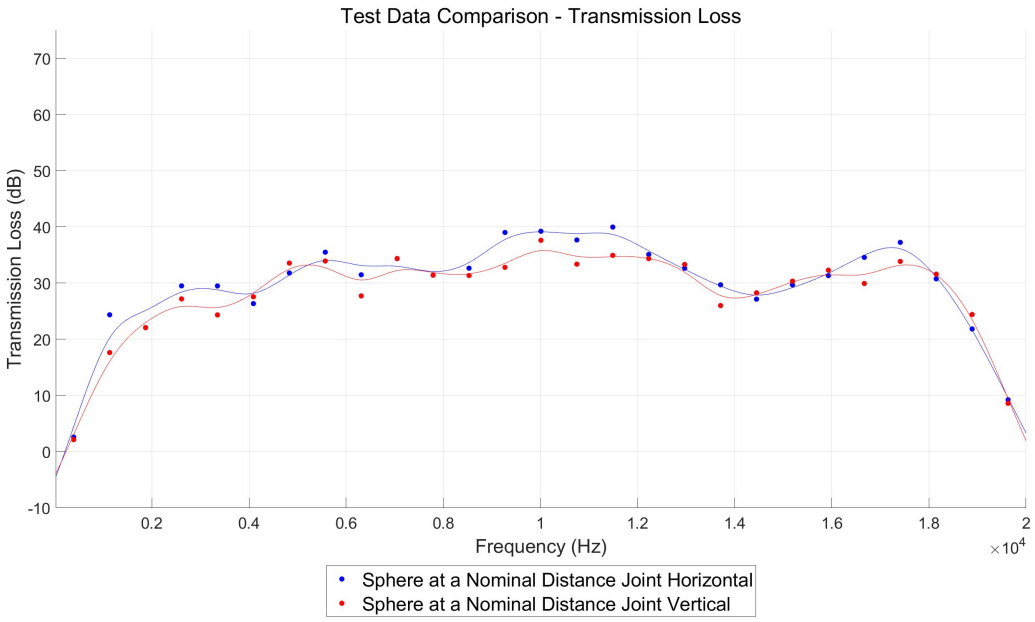

Figure 3-93 - AMM Sphere - Test - Nominal Distance - Transmission Loss Comparison

	Average Transmission Loss (dB)				
Configuration	20 Hz - 5 kHz	5 kHz - 10 kHz	10 kHz - 15 kHz	15 kHz - 20 kHz	20 Hz - 20 kHz
AMM Sphere at a Nominal Distance Joint Horizontal	23.7	34.2	34.0	27.7	29.9
AMM Sphere at a Nominal Distance Joint Vertical	21.9	32.0	32.2	27.2	28.3

Table 3-30 - AMM Sphere - Test - Nominal Distance - Average Transmission Loss

3.7.3 Acoustic Metamaterial Sphere Experimental Testing at a Close Distance

Experimental testing for the AMM Sphere at a close distance was performed in 2 configurations. The first configuration, referred to as the joint horizontal configuration, consisted of the interface between the AMM Sphere base and the AMM Sphere top being placed in the horizontal plane. The second configuration, referred to as the joint vertical configuration,

consisted of the interface between the AMM Sphere base and the AMM Sphere top placed in the vertical plane.

The time domain data decreased from 128 dB to 120 dB and 121 dB for the joint vertical and joint horizontal configurations, respectively. Across the 20 Hz to 20 kHz bandwidth, the TL_{avg} equaled 28.3 dB and 28.8 dB for the joint vertical and joint horizontal configurations, respectively. Figure 3-94 and Figure 3-95 show the input and output time history, spectrograms, and FFT as well as the TL across the acoustic spectrum. Figure 3-94 and Figure 3-95 show the joint vertical and joint horizontal configurations, respectively. Above 2 kHz, the transmitted acoustic noise is in the noise floor. Figure 3-96 shows a comparison plot for all of the configurations. Both configurations performed similarly across the acoustic spectrum. Table 3-31 details the TL_{avg} in the 20 Hz to 5 kHz, 5 kHz to 10 kHz, 10 kHz to 15 kHz, 15 kHz to 20 kHz, and 20 Hz to 20 kHz bandwidths for both configurations.

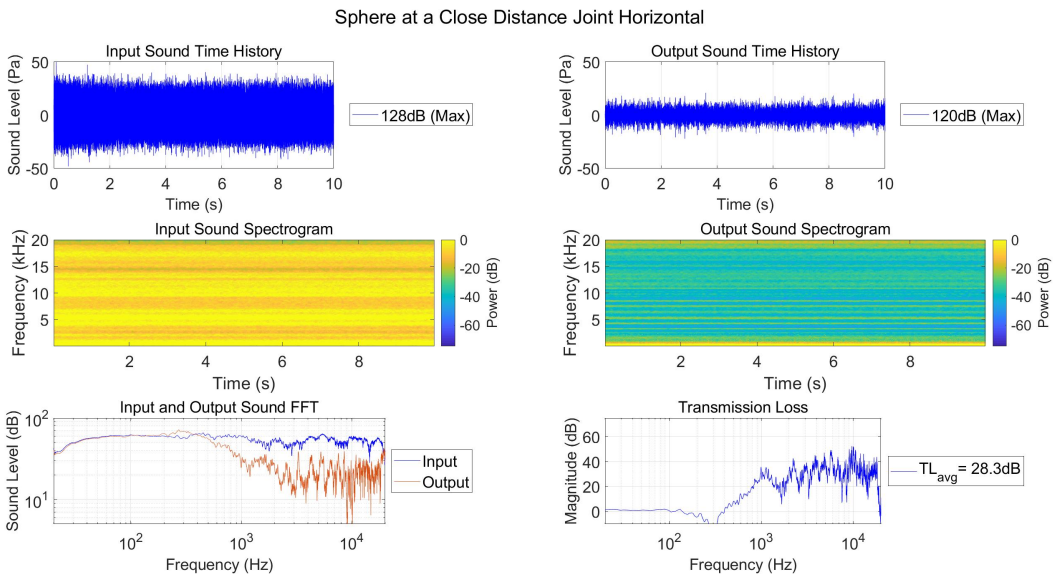

Figure 3-94 - AMM Sphere - Test - Close Distance - Joint Horizontal - Test Results

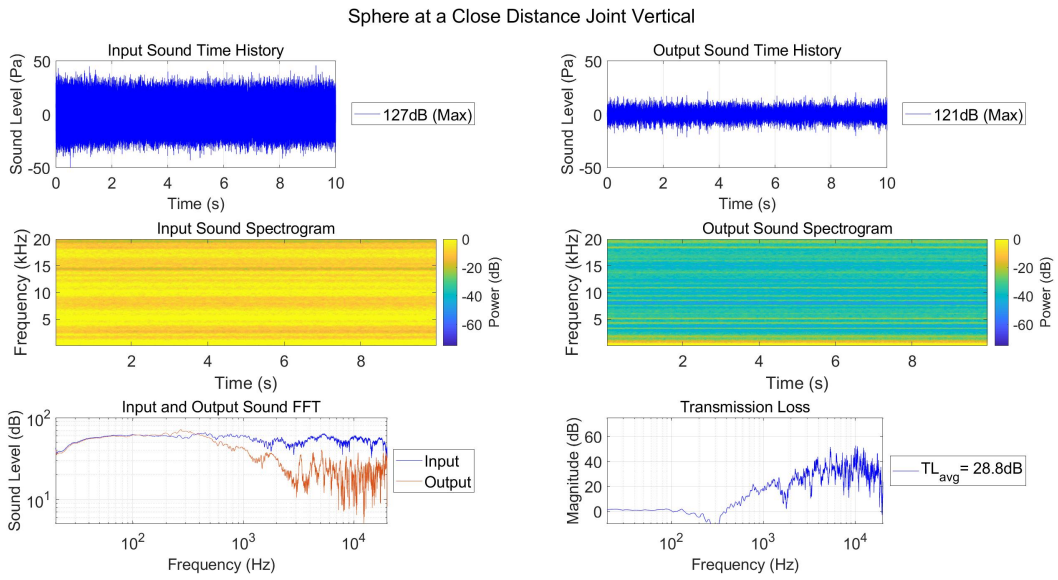

Figure 3-95 - AMM Sphere - Test - Close Distance - Joint Vertical - Test Results

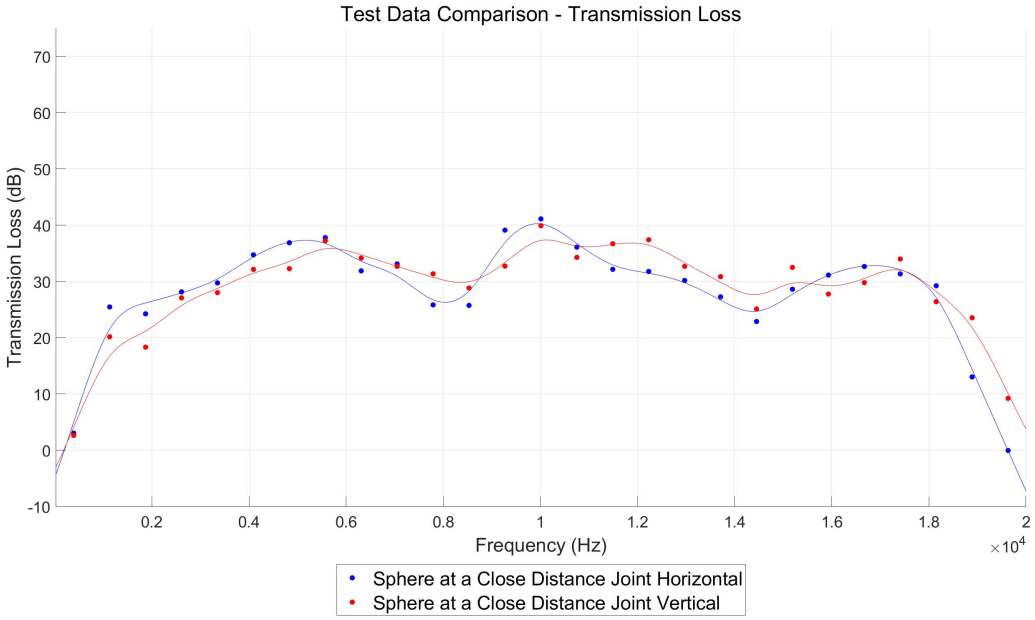

Figure 3-96 - AMM Sphere - Test - Close Distance - Transmission Loss Comparison

Average Transmission Loss (dB)					
Configuration	20 Hz - 5 kHz	5 kHz - 10 kHz	10 kHz - 15 kHz	15 kHz - 20 kHz	20 Hz - 20 kHz
AMM Sphere at a Close Distance Joint Horizontal	25.8	33.0	30.9	23.5	28.3
AMM Sphere at a Close Distance Joint Vertical	22.9	33.0	33.4	26.0	28.8

Table 3-31 - AMM Sphere - Test - Close Distance - Average Transmission Loss

3.7.4 Acoustic Metamaterial Sphere Experimental Testing at an Extended Distance

Experimental testing for the AMM Sphere at an extended distance was performed in 2 configurations. The first configuration, referred to as the joint horizontal configuration, consisted of the interface between the AMM Sphere base and the AMM Sphere top being placed in the horizontal plane. The second configuration, referred to as the joint vertical configuration, consisted of the interface between the AMM Sphere base and the AMM Sphere top placed in the vertical plane.

The time domain data decreased from 124 dB to 118 dB and 119 dB for the joint vertical and joint horizontal configurations, respectively. Across the 20 Hz to 20 kHz bandwidth, the TL_{avg} equaled 28.4 dB and 27.0 dB for the joint vertical and joint horizontal configurations, respectively. Figure 3-97 and Figure 3-98 show the input and output time history, spectrograms, and FFT as well as the TL across the acoustic spectrum, for joint vertical and joint horizontal configurations, respectively. Above 2 kHz, the transmitted acoustic noise is in the noise floor. Figure 3-99 shows a comparison plot for all of the configurations. Both configurations performed similarly across the acoustic spectrum. Table 3-32 details the TL_{avg} in the 20 Hz to 5 kHz, 5 kHz to 10 kHz, 10 kHz to 15 kHz, 15 kHz to 20 kHz, and 20 Hz to 20 kHz bandwidths for both configurations.

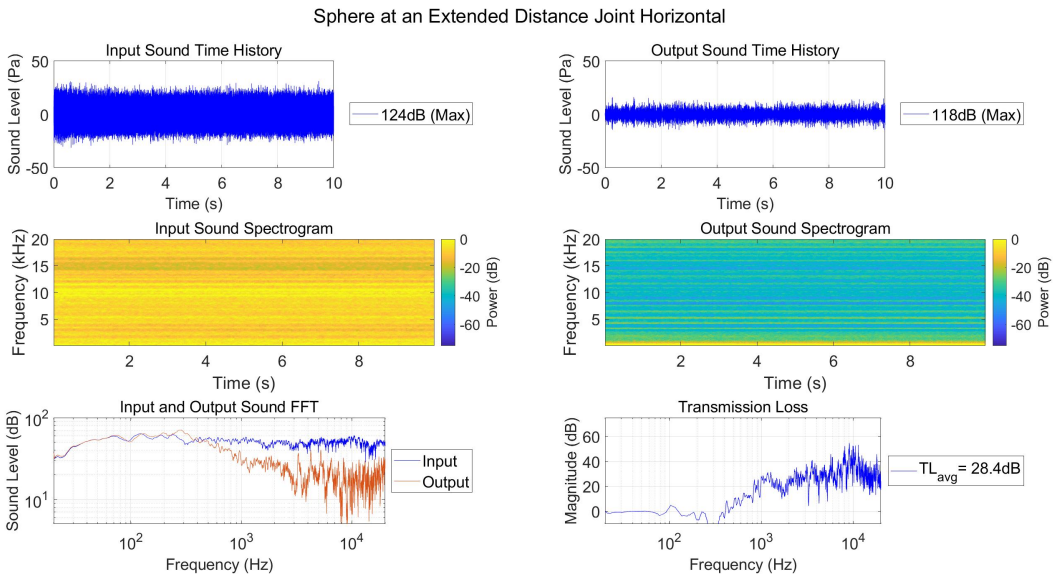

Figure 3-97 - AMM Sphere - Test - Extended Distance - Joint Horizontal - Test Results

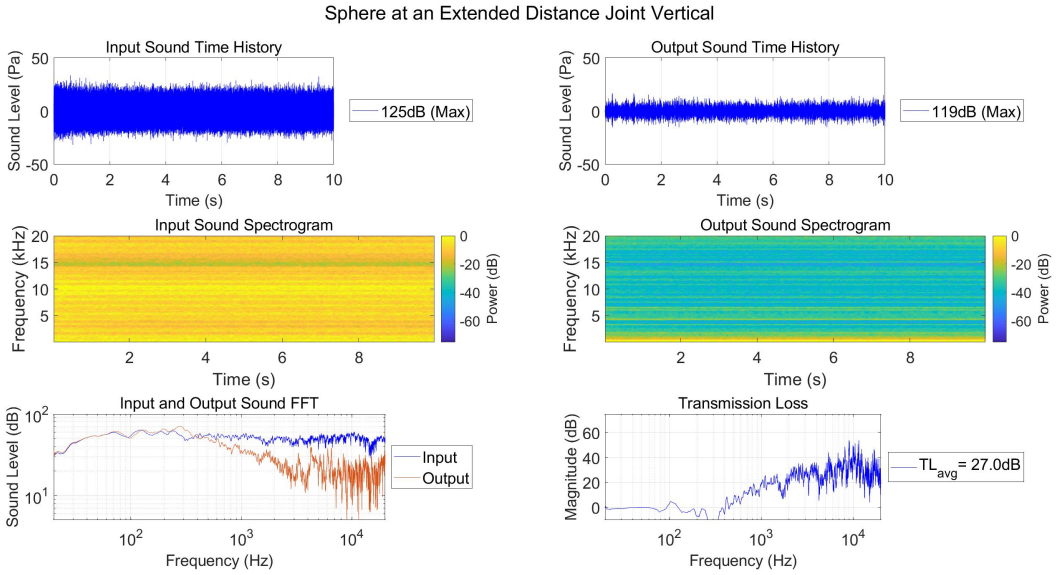

Figure 3-98 - AMM Sphere - Test - Extended Distance - Joint Vertical - Test Results

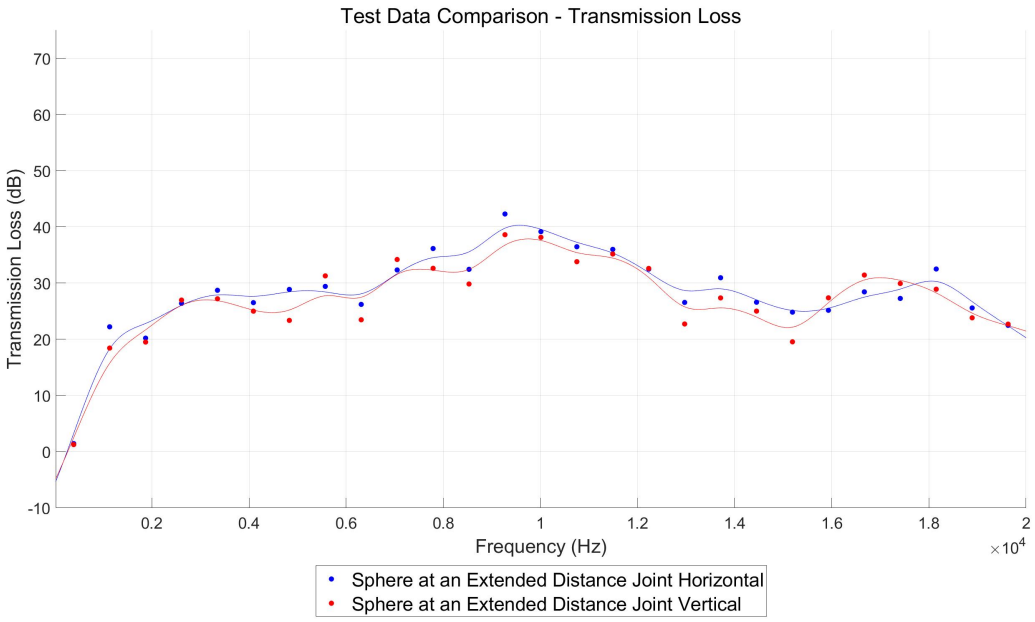

Figure 3-99 - AMM Sphere - Test - Extended Distance - Transmission Loss Comparison

	Average Transmission Loss (dB)				
Configuration	20 Hz - 5 kHz	5 kHz - 10 kHz	10 kHz - 15 kHz	15 kHz - 20 kHz	20 Hz - 20 kHz
AMM Sphere at an Extended Distance Joint Horizontal	21.9	33.3	31.9	26.6	28.4
AMM Sphere at an Extended Distance Joint Vertical	20.1	31.7	30.0	26.4	27.0

Table 3-32 - AMM Sphere - Test - Extended Distance - Average Transmission Loss

3.7.5 Acoustic Metamaterial Sphere Experimental Testing between Multiple Sound Sources

Experimental testing for the AMM Sphere between multiple sound sources was performed in 2 configurations. The first configuration, referred to as the joint horizontal configuration, consisted of the interface between the AMM Sphere base and the AMM Sphere top being placed in the horizontal plane. The second configuration, referred to as the joint

vertical configuration, consisted of the interface between the AMM Sphere base and the AMM Sphere top placed in the vertical plane.

The time domain data decreased from 127 dB to 123 dB for both configurations. Across the 20 Hz to 20 kHz bandwidth, the TL_{avg} equaled 26.5 dB and 24.5 dB for the joint vertical and joint horizontal configurations, respectively. Figure 3-100 and Figure 3-101 show the input and output time history, spectrograms, and FFT as well as the TL across the acoustic spectrum, for joint vertical and joint horizontal configurations, respectively. From 2 kHz to 19 kHz, the transmitted acoustic noise is in the noise floor. Figure 3-102 shows a comparison plot for all of the configurations. Both configurations performed similarly across the acoustic spectrum. Table 3-33 details the TL_{avg} in the 20 Hz to 5 kHz, 5 kHz to 10 kHz, 10 kHz to 15 kHz, 15 kHz to 20 kHz, and 20 Hz to 20 kHz bandwidths for both configurations.

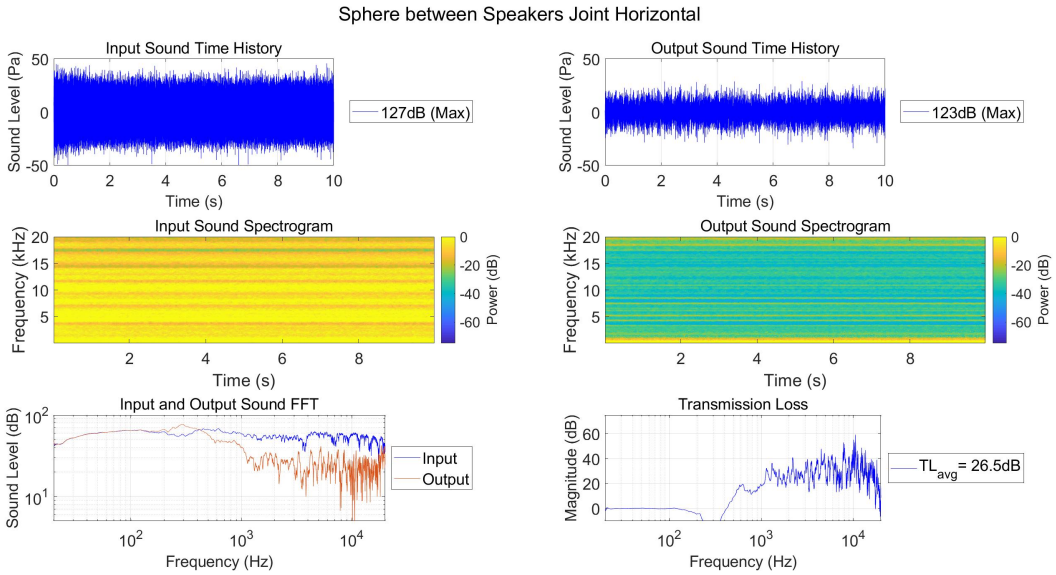

Figure 3-100 - AMM Sphere - Test - Between Multiple Sound Sources - Joint Horizontal - Test Results

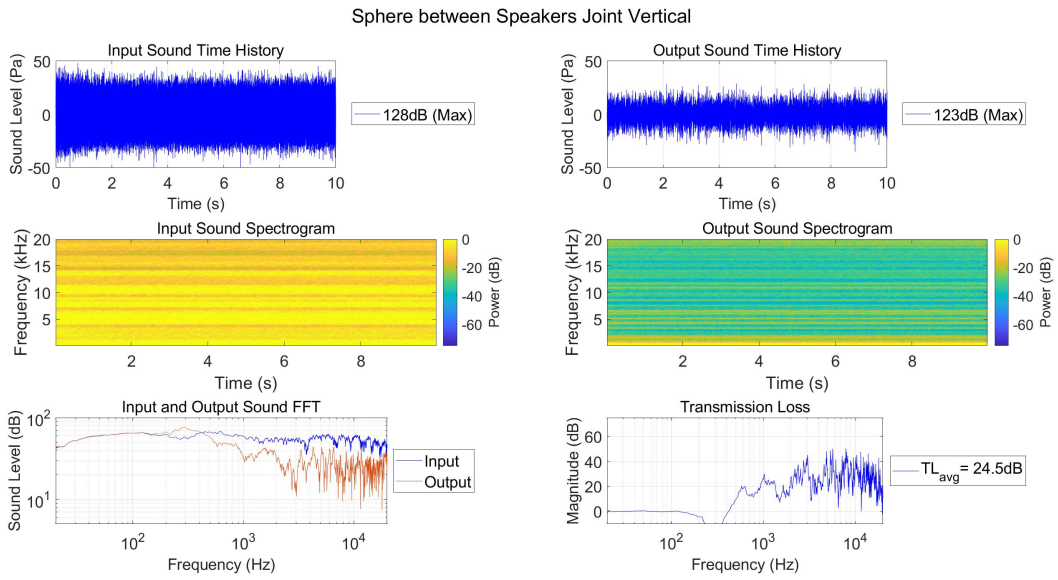

Figure 3-101 - AMM Sphere - Test - Between Multiple Sound Sources - Joint Vertical - Test Results

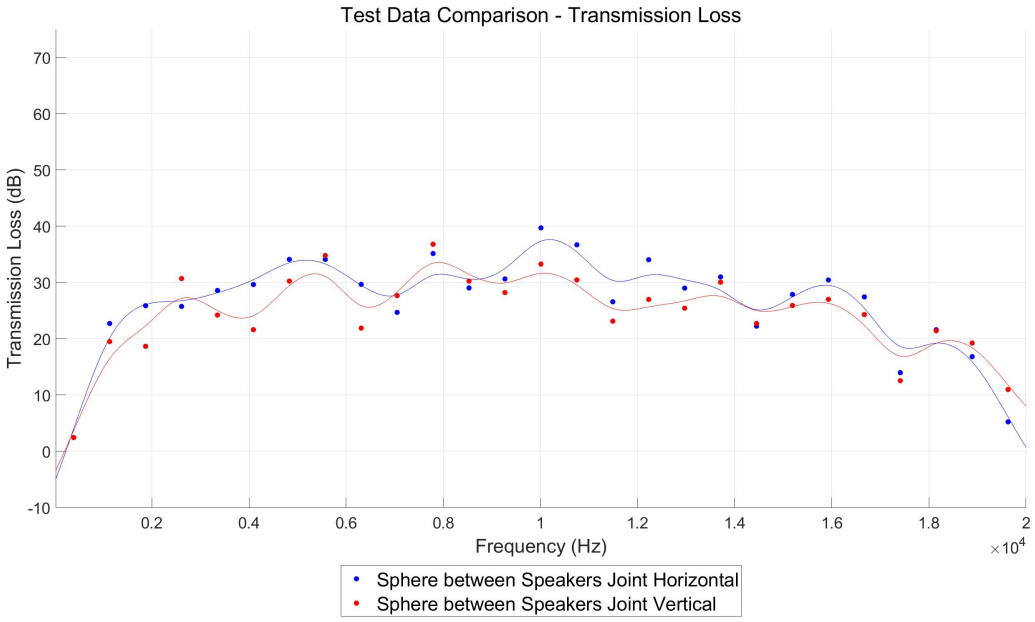

Figure 3-102 - AMM Sphere - Test - Between Multiple Sound Sources - Transmission Loss Comparison

Average Transmission Loss (dB)					
Configuration	20 Hz - 5 kHz	5 kHz - 10 kHz	10 kHz - 15 kHz	15 kHz - 20 kHz	20 Hz - 20 kHz
AMM Sphere between Speakers Joint Horizontal	24.2	30.8	30.6	20.4	26.5
AMM Sphere between Speakers Joint Vertical	21.1	29.5	27.1	20.1	24.5

Table 3-33 - AMM Sphere - Test - Between Multiple Sound Sources - Average Transmission Loss

3.7.6 Acoustic Metamaterial Sphere Experimental Testing Comparison and Summary

Since the AMM Sphere is affectionately known as the Death Star, a quote from Star Wars: Episode IV - Return of the Jedi nicely sums up the overall performance.

"That things operational!"

- Lando Calrissian [44]

All of the AMM Sphere test configurations performed exceptionally well, especially in the 2 kHz to 20 kHz range. Figure 3-103 shows a comparison of all of the test configurations in the joint horizontal configuration. Figure 3-104 shows a comparison of all of the test configurations in the joint vertical configuration. Both figures show minimal variability between the different test setups. The comparison data is presented in Table 3-34 and Table 3-35 for joint horizontal and joint vertical test configurations, respectively. The data for all test configurations and all joint orientations yielded similar results - near total acoustic mitigation from 2 kHz to 20 kHz. This consistency in testing verifies that the design has met the goal of omnidirectionally. Additionally, the design has shown to be effective with multiple sound sources.

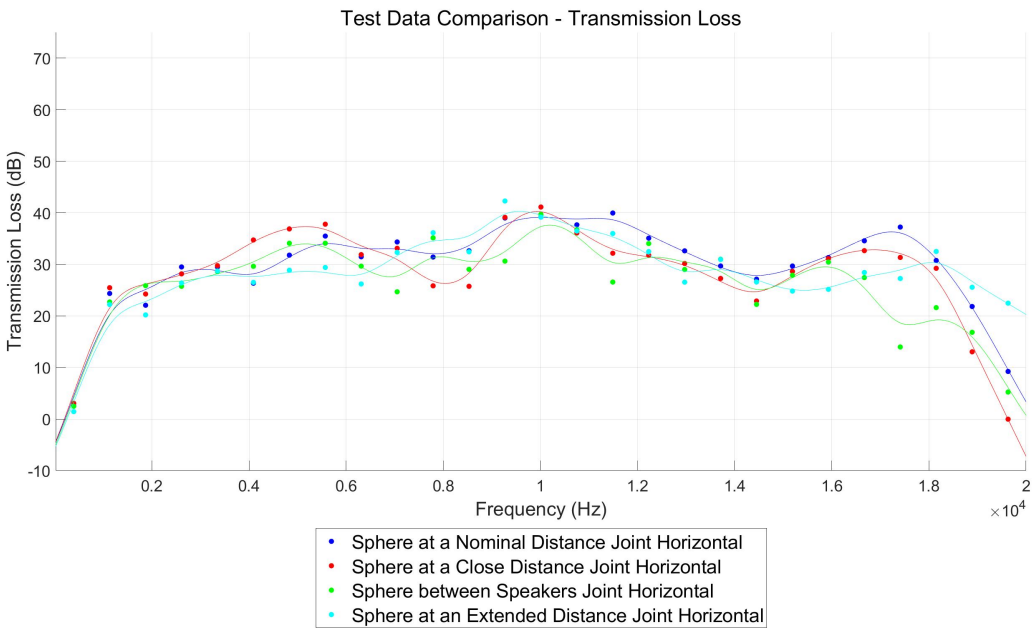

Figure 3-103 - AMM Sphere - Test - Joint Horizontal - Transmission Loss Comparison

Average Transmission Loss (dB)					
Configuration	20 Hz - 5 kHz	5 kHz - 10 kHz	10 kHz - 15 kHz	15 kHz - 20 kHz	20 Hz - 20 kHz
AMM Sphere at a Nominal Distance Joint Horizontal	23.7	34.2	34.0	27.7	29.9
AMM Sphere at a Close Distance Joint Horizontal	25.8	33.0	30.9	23.5	28.3
AMM Sphere between Speakers Joint Horizontal	24.2	30.8	30.6	20.4	26.5
AMM Sphere at an Extended Distance Joint Horizontal	21.9	33.3	31.9	26.6	28.4

Table 3-34 - AMM Sphere - Test - Joint Horizontal - Average Transmission Loss

Figure 3-104 - AMM Sphere - Test - Joint Vertical - Transmission Loss Comparison

Average Transmission Loss (dB)					
Configuration	20 Hz - 5 kHz	5 kHz - 10 kHz	10 kHz - 15 kHz	15 kHz - 20 kHz	20 Hz - 20 kHz
AMM Sphere at a Nominal Distance Joint Vertical	21.9	32.0	32.2	27.2	28.3
AMM Sphere at a Close Distance Joint Vertical	22.9	33.0	33.4	26.0	28.8
AMM Sphere between Speakers Joint Vertical	21.1	29.5	27.1	20.1	24.5
AMM Sphere at an Extended Distance Joint Vertical	20.1	31.7	30.0	26.4	27.0

Table 3-35 - AMM Sphere - Test - Joint Vertical - Average Transmission Loss

3.8 Experimental Testing Summary

The fundamental feature SISO experimental testing provided the data required in order to determine effective features and allowed for a quantitative evaluation of said features. The testing proved that the configuration of a Series of Diverging Nozzles with Radial and Axial Perforations with a Constricted Opening at the Output Plane was effective in the mitigation of high frequency acoustic noise. This configuration became the BF AMM.

The next phase of the SISO testing enclosed the BF AMM configuration. This enclosure was crucial in ensuring that the design meets the requirement of configurability as well as providing a structure for the interconnected cavity AMM. Experimental testing not only proved that the enclosure could be incorporated into the design, but the enclosure enhanced performance as well. Supplementary testing confirmed that the BF AMM could be downsized into a compact system. Experimental testing demonstrated that a 3/4" structure could mitigate acoustic noise as well as a 6” structure. The additional stage feature was tested and found to further enhance performance. The SISO testing concluded that the optimal design to use in MIMO testing was the 4-stage BF AMM with quarter inch stages.

MIMO testing consisted of evaluating types of AMM against a control. Experimental testing concluded that all variations of AMM were very effective at acoustic mitigation from 2 kHz to 20 kHz, but the 4-stage Small Cavity AMM was the best choice for incorporation into the AMM Sphere.

The AMM Sphere test configurations all performed exceptionally well, especially in the 2 kHz to 20 kHz range. Experimental testing showed minimal variability in results between test

setups and test asset orientation. Additionally, testing proved the design was functional with multiple sound sources.

Additionally, all of the configurations were tested in the CN and DN configurations with similar results. This is indicative of the structure having the functionality of keeping sound in as well as keeping sound out.

Chapter 4: Acoustic Simulation

"The good news about computers is that they do what you tell them to do.

The bad news is they do what you tell them to do."

-Ted Nelson [45]

The numerical results outlined in section 1.3 demonstrated the need for acoustic simulation software. MSC ACTRAN was chosen to perform the analysis. As discussed in section 1.4, not all test configurations were analyzed. Acoustic simulations were performed on 9 SISO configurations and 4 MIMO configurations. When the performance of the prototypes was determined as discussed in chapter 3, it became apparent that not all configurations required analysis. For example, not all of the downsizing prototypes required analysis. Performing analysis on each of the downsizing prototypes would not yield valuable data or insight and would be time and cost adverse. The SISO configurations simulated were the SP, SP with RP, CN, DN, DN with RP, SDN, SDN with RP, SDN with RAP, and SDN with RAP and COOP. The MIMO configurations simulated were the SP, BF AMM, Large Cavity AMM, and the Small Cavity AMM.

The MIMO acoustic simulations were performed just like the SISO acoustic simulations. By determining the performance of a cell, the performance of the panel was determined. The acoustic properties do not change with added surface area due to additional cells placed in a parallel configuration. This is the same principle as characterizing foam. Once the properties of a foam with a certain thickness are determined, adding surface area to the foam does not change the acoustic performance with respect to thickness. Additionally, the MIMO acoustic simulations do not account for the cells being interconnected. The initial simulation runs showed good

correlation with experimental test results. Additionally, in order to perform an analysis on the entire panel would have been extremely difficult computationally.

The acoustic simulation does not include any structural deflection or vibration. The walls are considered smooth and perfectly reflecting. These factors certainly contribute to some of the deviations seen in the experimental test results as compared to the acoustic simulation data outlined in chapter 5.

4.1 Methodology

The solid models created during the design phase were the basis for the acoustic simulation models. In Solidworks, the prototype models were used to create a mold of the inner cavities and acoustic control volume. Hemispheres were added to each input and output surface. The hemispheres allow MSC ACTRAN to apply boundary conditions as outlined in section 4.1.2. Once the internal cavity model was created, the geometry was exported as a Parasolid (*.x_t) file and imported into MSC.PATRAN for mesh creation. MSC ACTRAN does not have strong meshing tools, so the mesh was generated with PATRAN and exported as a bulk data input file (*.bdf). Details about the mesh creation and mesh size are available in section 4.1.1. Once the meshed internal geometry was imported into MSC ACTRAN, the acoustic simulation was setup as detailed in section 4.1.2.

4.1.1 Meshing

"Results eventually reach a point at which a finer mesh no longer yields an appreciable difference. This type of convergence study helps generate accurate solutions with meshes that are sufficiently dense and yet not overly demanding of computer resources."

-Bob Williams [46]

The mesh size for the models needed to be sufficiently small to capture an acoustic wave at 20 kHz. To capture a sine wave, a minimum of 6 elements are needed, as shown in Figure 4-1. The blue curve represents the sine wave and the red lines represent the mesh elements. The 6 elements can replicate the general shape of the wave. Using the equations listed in Table 1-3 and the constants listed in Table 1-1, the wavelength for a 20 kHz wave is determined as follows:

$$\lambda = \frac{c}{f} = \frac{343m/s}{20000Hz} = 0.0172m \qquad 4.1$$

Dividing the wavelength by 6 yields a mesh size of 0.00285 m or 0.112 inches. The maximum element size used in the acoustic simulations was 0.1 inches.

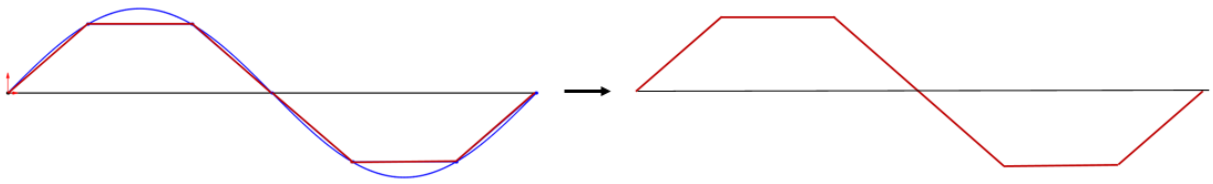

Figure 4-1 - Acoustic Wavelength and Mesh Size Comparison

The mesh was created using a combination of surface and solid meshes. In order to easily define different domains to be used in MSC ACTRAN, the surface meshes were created using

different materials. There were no differences in any of the mesh elements except the property identification (PID) number associated with each material. This method allowed the elements to be grouped by location, such as input surface or output surface.

The surface meshes consisted of triangle 3 (Tria3) elements and the solid meshes consisted of tetrahedron 4 (Tet4) elements. Figure 4-2 shows the MSC.PATRAN surface element settings used and Figure 4-3 shows the surface element materials. Figure 4-4 shows the MSC.PATRAN solid element settings used and Figure 4-5 shows the solid element material.

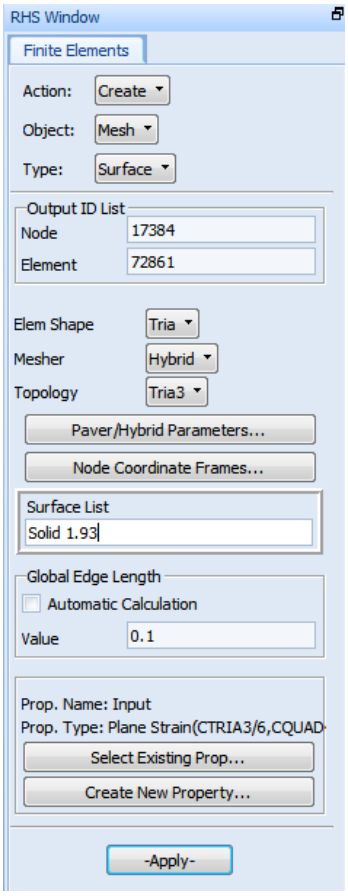

Figure 4-2 - MSC.PATRAN Surface Elements Settings

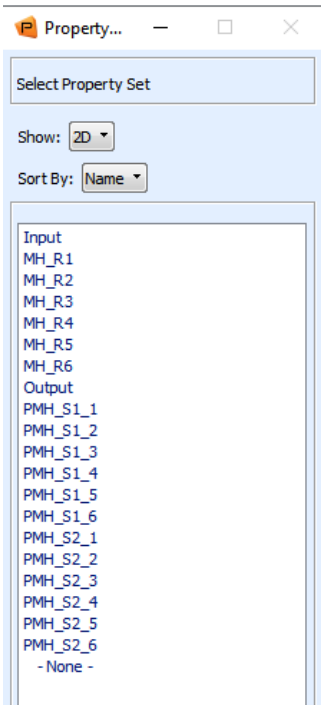

Figure 4-3 - MSC.PATRAN Surface Elements Materials

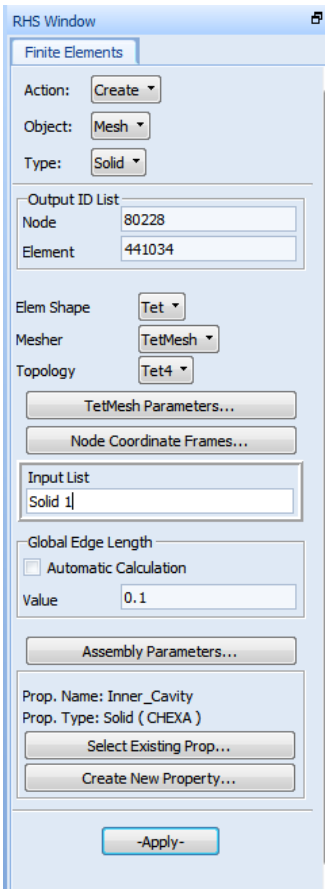

Figure 4-4 - MSC.PATRAN Solid Elements Settings

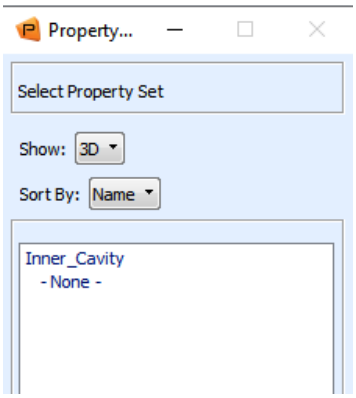

Figure 4-5 - MSC.PATRAN Solid Elements Materials

4.1.2 MSC ACTRAN

The meshed models were imported into MSC ACTRAN. The assignment of different surface materials within the mesh allowed for the domains to easily be created. The domains are a set of finite elements with common PID numbers. The domains were used to assign Infinite Fluid Components (IFCs), Finite Fluid Components, and Diffused Sound Fields throughout the model. IFCs, Finite Fluid Components, and Diffused Sound Fields are discussed in sections 4.1.2.1 through 4.1.2.3.

Once the domains were created, then the fluid material was added to the model. Air at ambient and standard atmospheric conditions was used. During this step, the damping properties for air were added. The damping value was 1%, which was input as 0.01 in the acoustic simulation models. [23] Figure 4-6 shows the fluid material window and associated settings and properties.

The base for the physical properties of the model is the Direct Frequency Response Solver. In this window, the frequency array is set. MSC ACTRAN solves the model in the frequency domain; therefore, the frequency array needs to be defined. In this dissertation, the array was

defined from 20 Hz to 20 kHz with a 10 Hz step size. Figure 4-7 shows the Direct Frequency Response Solver window.

MSC ACTRAN uses linear solvers. For the acoustic simulations discussed in this dissertation, a MultiFrontal Massively Parallel Solver (MUMPS) was used. This direct algebraic linear solver was chosen for its robustness as well as it being a relatively fast solver. With 1999 frequency iterations per simulation model, the speed of the solver was a significant consideration. At each iteration, the simulation created a large matrix of the system of equations. The MUMPS solver performs a Gaussian factorization to divide the matrix into 3 multifrontal components: a lower triangular matrix, a matrix diagonal consisting of ones and an upper triangular matrix. The solutions to the triangular matrices are then obtained and processed to determine the overall solution. [47] [48]

The Direct Frequency Response Solver consisted of subsections for IFCs, finite fluid components, sound fields, and virtual instrumentation. These subsections with the exception of the virtual instrumentation are discussed in sections 4.1.2.1 through 4.1.2.3.

The virtual instrumentation consisted of 2 virtual microphones: an input and an output microphone. The microphones were added to the PostProcessing subsection of the Analysis Block as Field Points. Each microphone was located within the Finite Fluid Component and aligned in the x-axis with the center of the SP or the nozzles. For the SISO acoustic simulations, the virtual microphones were located 2 inches from the input and output planes. For the MIMO acoustic simulations, the virtual microphones were located 0.2 inches from the input and output planes.

Due to the Diffused Sound Field, discussed in section 4.1.2.3, 15 total simulation runs per model were conducted. The data generated by the acoustic simulations consisted of a series of input and output FFTs. The multiple simulation runs allowed for the generation of solution statistics. The simulation data is presented as a mean TL plot with 1 standard deviation boundaries. Due to the nature of the Diffused Sound Field, the SPLs for the acoustic simulation runs are not comparable to the SPLs for the experimental testing. Only the TL data is presented in this chapter and comparison with FFTs would not yield usable data. The data was post-processed using a MATLAB script presented in Appendix A-8. The TL was calculated using equations 1.6 and 1.7. Additionally, the data is presented in 5 bandwidths of the acoustic spectrum: 20 Hz to 5 kHz, 5 kHz to 10 kHz, 10 kHz to 15 kHz, 15 kHz to 20 kHz, and 20 Hz to 20 kHz.

The acoustic simulation models were designed to have the same input, output, and internal cavity domains. The internal cavity domain geometry changes with each model but MSC ACTRAN has the capability to utilize identical Analysis Blocks despite the change in system geometry. The differences between the Analysis Blocks for each simulation model were dependent on the number of radial and axial perforations within the AMM. Additional perforations required additional IFCs to be added in the model. All of the acoustic simulations discussed in this dissertation have identical settings within the Analysis Block with the exception of the number of IFC. The configurations discussed in section 4.2 and section 4.3 show the Analysis Block components in the model setup window.

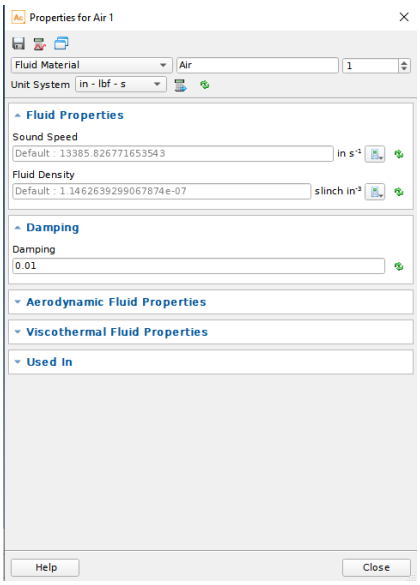

Figure 4-6 - MSC ACTRAN Fluid Material Settings

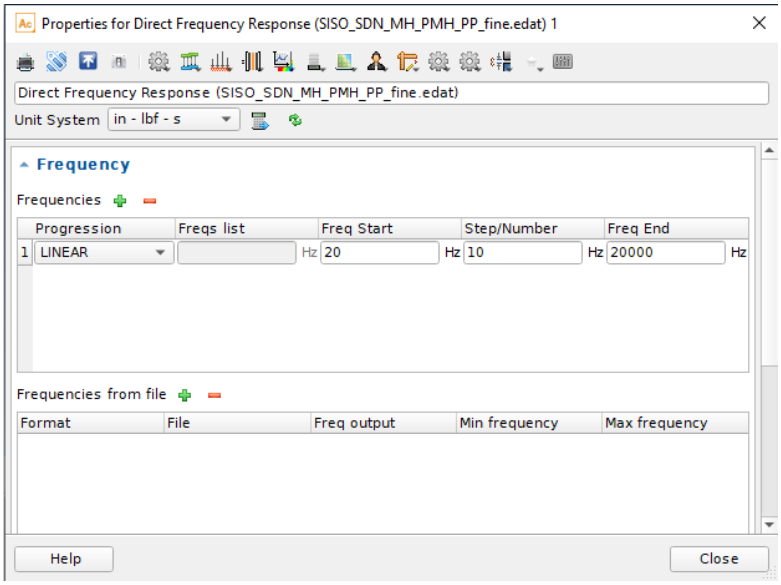

Figure 4-7 - MSC ACTRAN Direct Frequency Response Solver Settings

4.1.2.1 Finite Fluid Component

The Finite Fluid Component defines the acoustic simulation model working area as well as boundary layers within that working space. The finite elements of the Finite Fluid must be solid elements. Within this space, acoustic waves are unbounded to allow for reflection,

interaction, and interference. The walls within the Finite Fluid are modeled to be rigid and perfectly reflecting.

In this dissertation, the Finite Fluid Component was specified as a Visco-Thermal Fluid. This allowed the simulation to account for energy losses within the system due to viscosity and thermal effects. Within a small space such as an AMM cavity, the boundary layer can encompass the entire working area, so the viscous effects were needed to model the system. The boundary layer was calculated using the "Distance-Based Linearized Navier-Stokes-Fourier" (DBLNSF) method. DBLNSF allows the model to operate within arbitrary geometries with no fluid flow throughout the system. The thermal and viscous fields are approximated using an estimation of a wall distance field based on the continuity, momentum, energy, and wave equations. [47] The Finite Fluid Component settings are shown in Figure 4-8.

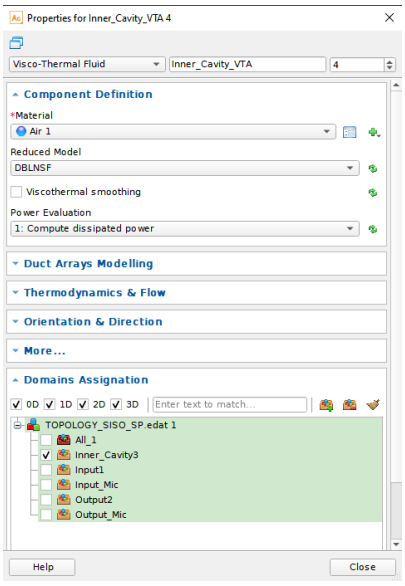

Figure 4-8 - MSC ACTRAN Visco-Thermal Fluid Settings

4.1.2.2 Infinite Fluid Components

The acoustic simulation model cannot encompass the entire region of space in which the system operates. IFCs allow the simulation to model unbounded acoustic domains. Surface elements were used to create the interface between the unbounded acoustic domains and the Finite Fluid Components. The IFCs are infinitely long, so no sound reflection is introduced back into the simulation. To avoid simulation errors, the IFCs must be applied to a non-planar surface. [47] The IFCs component settings are shown in Figure 4-9. An example depiction of an Infinite Fluid component is shown in Figure 4-10. A single row RP within the model can be modeled as one IFC. The rows of RP are aligned on the x-axis and directed outward, so the y- and z-coordinates were set to zero. Consequently, a single row of RP shared an origin allowing the row of RP to become one IFCs component. Figure 4-11 and Figure 4-12 show an example of a RP IFC. The AP aligned on the x-axis, but not on the y- and z-axes. Consequently, each AP required an individual IFC.

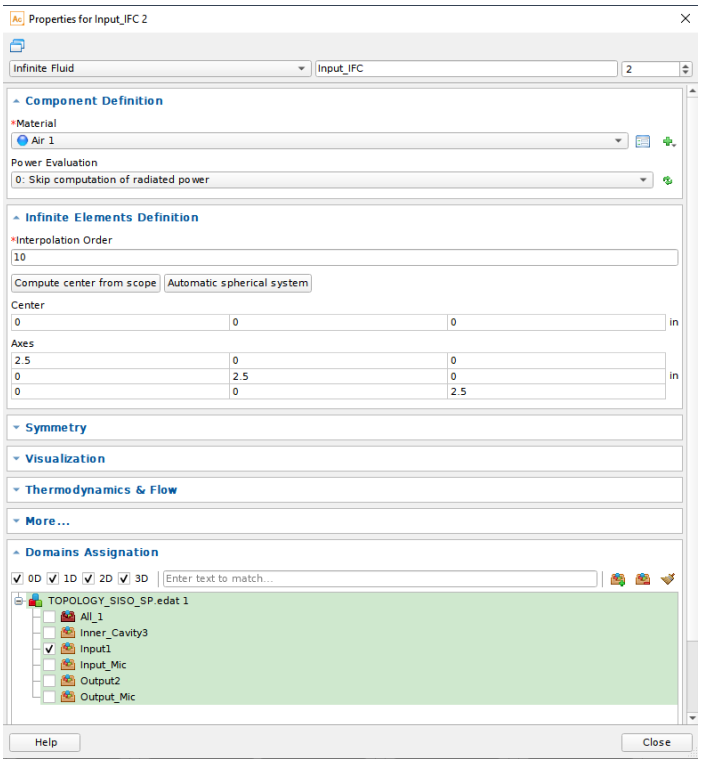

Figure 4-9 - MSC ACTRAN Infinite Fluid Component Settings

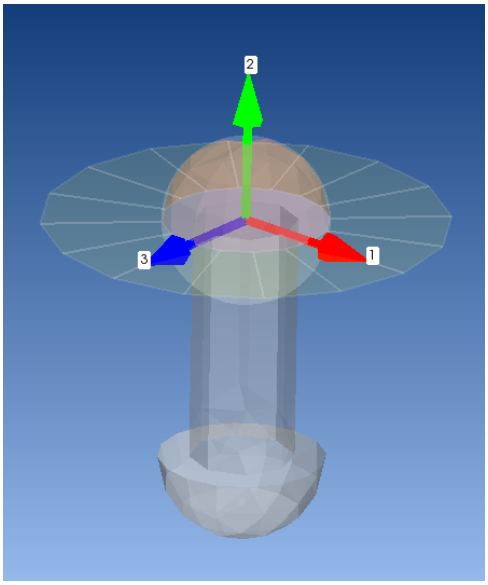

Figure 4-10 - MSC ACTRAN Infinite Fluid Component Example

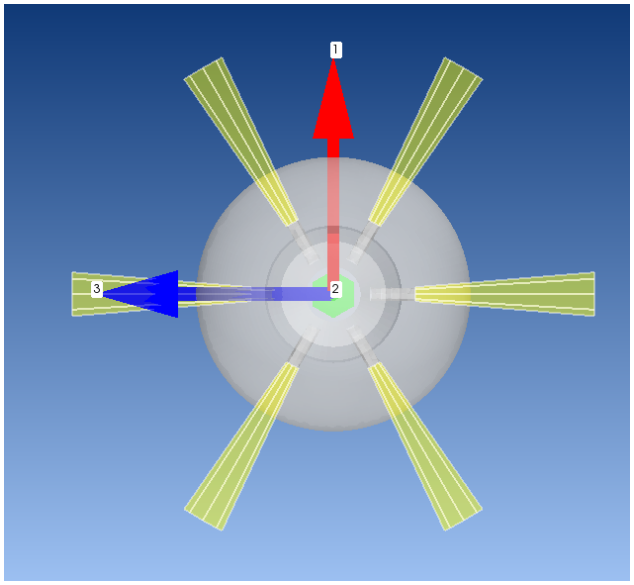

Figure 4-11 - MSC ACTRAN Infinite Fluid Component - Radial Perforation Example - Top View

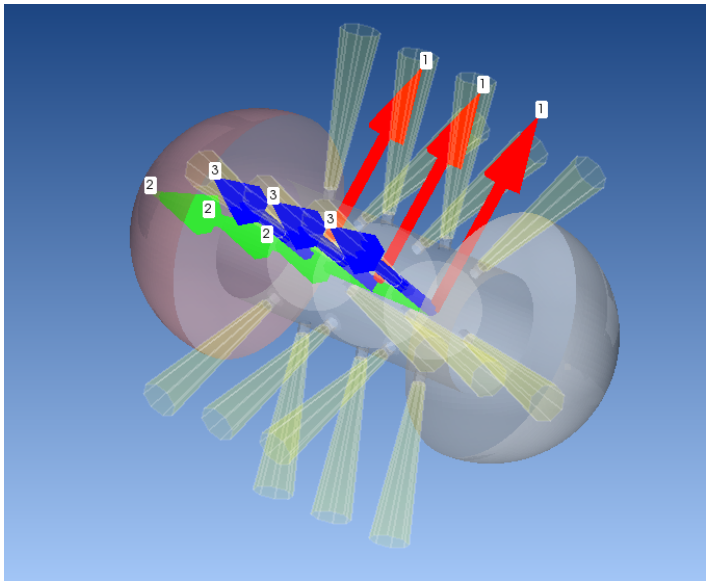

Figure 4-12 - MSC ACTRAN Infinite Fluid Component - Radial Perforation Example - Isometric View

4.1.2.3 Diffused Sound Field

A Diffused Sound Field is an applied boundary condition that was used to provide the input noise into the acoustic simulations. A Diffused Sound Field mimics an array of sound sources to allow for a sound field where the time average of the sound pressure and acoustic energy is uniform in any direction. This uniformity allows the simulation to replicate a

reverberant acoustic chamber. [49] The sound sources are applied to a non-planar surface domain. The input hemispherical surface domain was used as the application surface throughout this dissertation. The configuration window for a Diffused Sound Field is shown in Figure 4-13.

In order to configure the Diffused Sound Field several parameters must be defined. A reference power spectral density (PSD) value is used to define the amount of power input into the simulation. The intention of the acoustic simulations was to characterize the system, not to determine performance under specific conditions. Therefore, the PSD value was arbitrary. Consequently, the input and output FFTs of the acoustic simulation will not compare to the input and output FFTs of the experimental testing. In order to compare the simulation and experimental results, the TL of the system is used. Consequently, the data presented in this chapter will only consist of TL plots. The PSD value was set as 50 $slinch^2/in^2s^4$ for each frequency iteration. Since the models were designed using imperial units, the acoustic simulations were performed with imperial units.

To define the Diffused Sound Field array, several parameters are used. These parameters are the Maximum Incidence Angle, the Number of Parallels, origin, radius, and Pole Direction. Figure 4-14 shows a schematic of the Diffused Sound Field with regards to the origin, radius, and Pole Direction. For all of the acoustic simulation models, the origin is the center of the input hemispherical region located at (0,0,0). The radius is distance between the origin and the array of sound sources. In order to have fully a developed input sound field, a large radius is required. All of the simulation models used a radius of 675 inches, which is the approximate wavelength of a 20 Hz acoustic wave.

The Pole Direction defines the direction of the array with regards to the application surface. The Pole Direction is normal to the application surface. [47] All of the models were designed to have the input located at (0,0,0) with the positive x-axis direction defined from the center of the input area to the center of the output area. The Pole Direction used was (0,1,0).

Maximum Incidence defines the angle of the Diffused Sound Field with respect to a normal vector of the application surface. A grazing angle is the difference between the surface normal angle and the incidence angle. If the grazing angle is zero, then the incident wave is parallel to the application surface. The intention of these acoustic simulations is to characterize the AMM prototypes not the surrounding environment. Therefore, the Maximum Incidence Angle was set at 75 degrees to eliminate grazing as well as increase computational speed. [47] [49] Figure 4-15 shows a schematic of a grazing angle.

The number of incident waves within the diffused sound field array is controlled by the Number of Parallels defined. When using a Maximum Incidence Angle, the Number of Parallels must be specified. The application surface is virtually sectioned so that each section has the same incident wave angle. Each surface section is then sectioned into subsections. Each subsection carries an incident wave. The Number of Parallels defines the number of subsections created. [49] All of the acoustic simulations performed in this dissertation used 5 as the value for the Number of Parallels.

When using the Number of Parallels parameter, MSC ACTRAN requires that the Number of Samples must be defined. In order to use a Direct Frequency Response Analysis Block, a sampling strategy must be used in order to apply a random loading condition, such as the

Diffused Sound Field. Random vibro-acoustic time histories that are stationary stochastic in nature require multiple samples, called the Number of Samples within the simulation, in order to properly characterize the behavior of the system. These samples allow for statistical data of the system to be generated. The sampling method MULTISAMPLE_ALL was used. MULTISAMPLE_ALL creates a random generator of phases and samples the phases at each frequency. [47] [49] All of the acoustic simulations performed in this dissertation used 15 as the value for the Number of Samples.

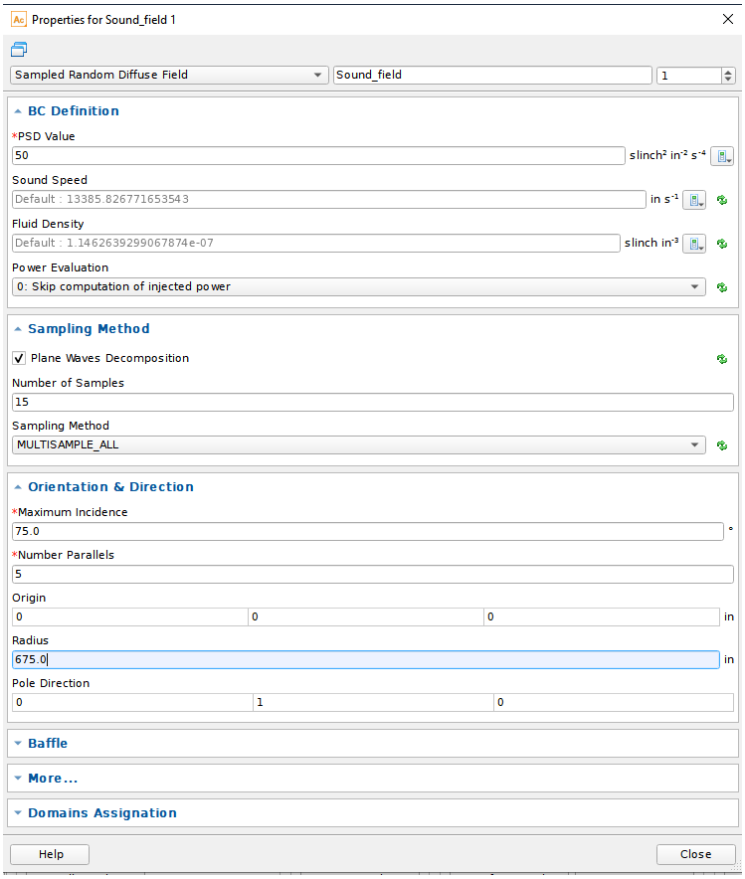

Figure 4-13 - MSC ACTRAN Diffused Sound Field Settings

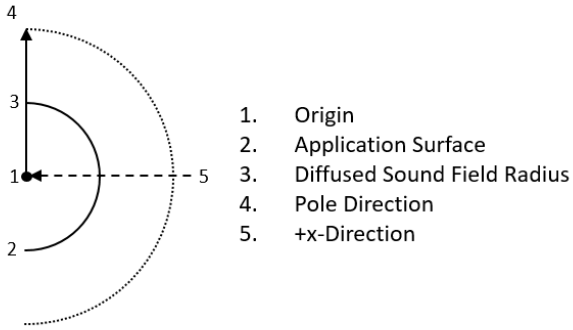

Figure 4-14 - MSC ACTRAN - Diffused Sound Field - Schematic

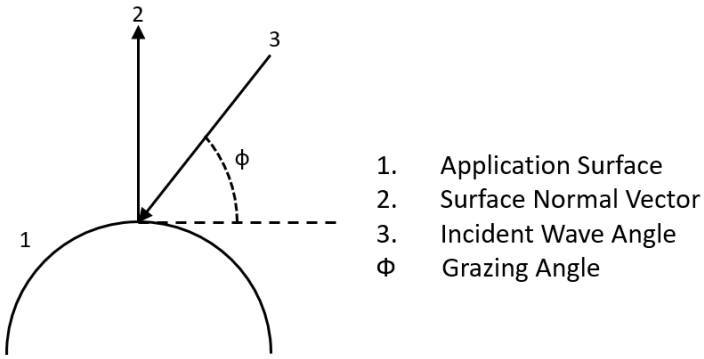

Figure 4-15 - Grazing Angle Schematic

4.2 Single Input Single Output Systems

4.2.1 Straight Pipe

The SP acoustic simulation model consisted of 3 domains. The domains consisted of the internal cavity as a Finite Fluid Component as well as the input and output domains as IFCs.

Figure 4-16 shows the internal cavity solid model developed for the simulation. Figure 4-17 shows the MSC.PATRAN mesh model. Surface elements are shown in green and solid elements are shown in pink. Figure 4-18 shows the analysis tree for the ACTRAN model as well as the imported model. Figure 4-19 shows the IFC regions for the input and output surfaces.

The TL data as defined in equations 1.6 and equation 1.7 is presented in Figure 4-20 and the corresponding tabular data is presented in Table 4-1. The data shows minimal change in the amount of TL across the acoustic spectrum.

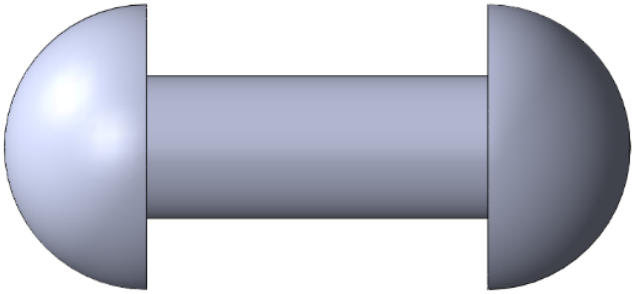

Figure 4-16 - SISO - Straight Pipe - Internal Cavity CAD

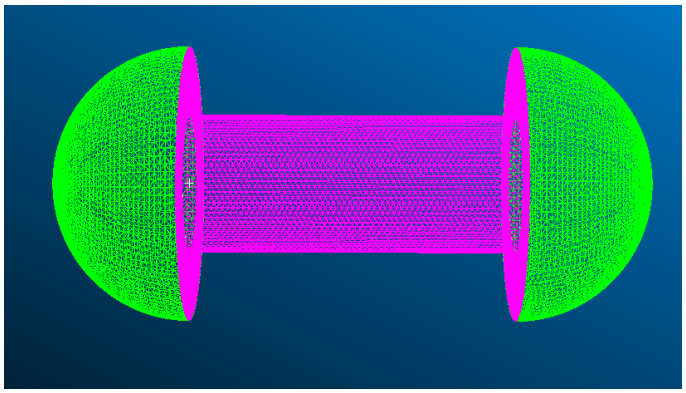

Figure 4-17 - SISO - Straight Pipe - MSC.PATRAN Mesh

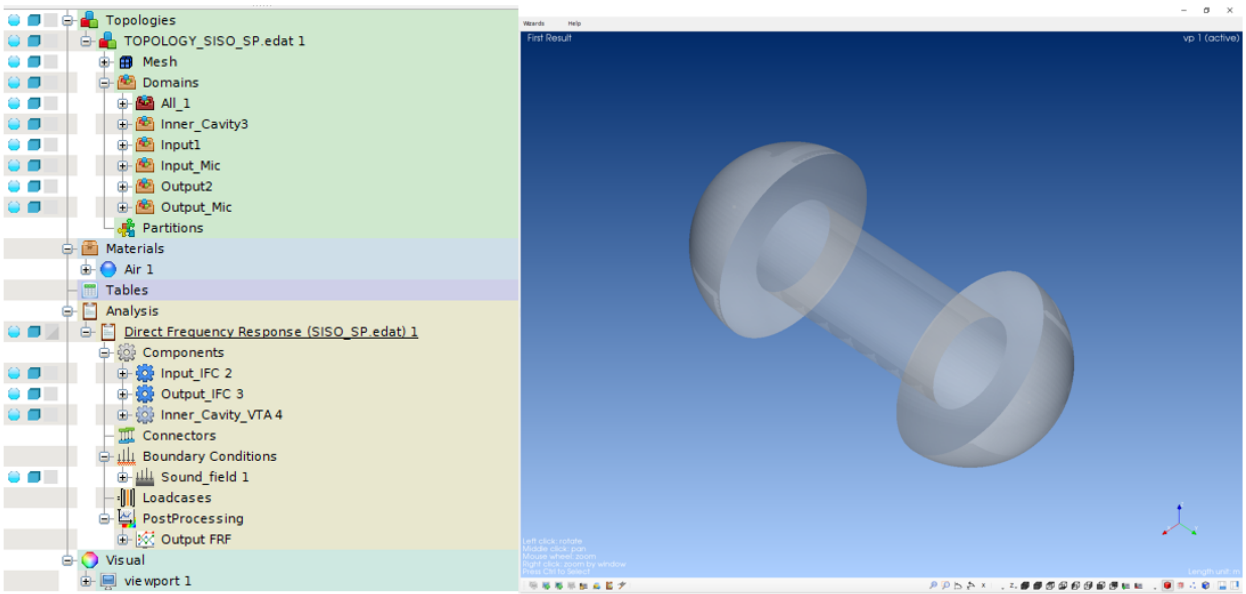

Figure 4-18 - SISO - Straight Pipe - ACTRAN Model Setup

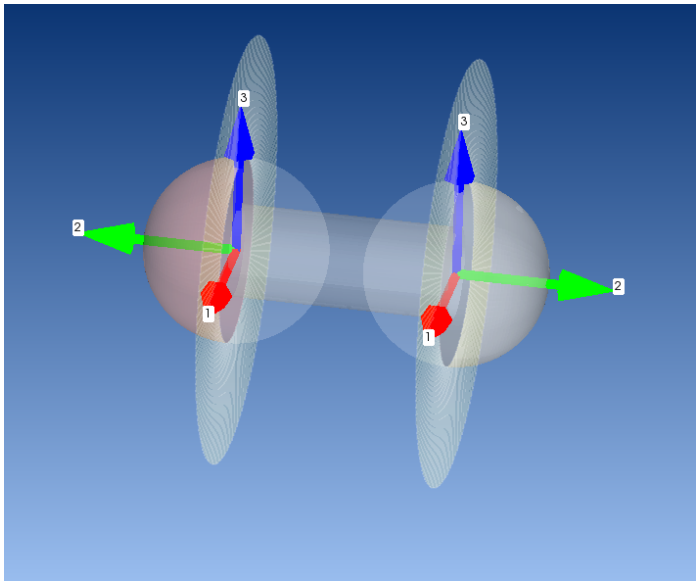

Figure 4-19 - SISO - Straight Pipe - IFC - Side View

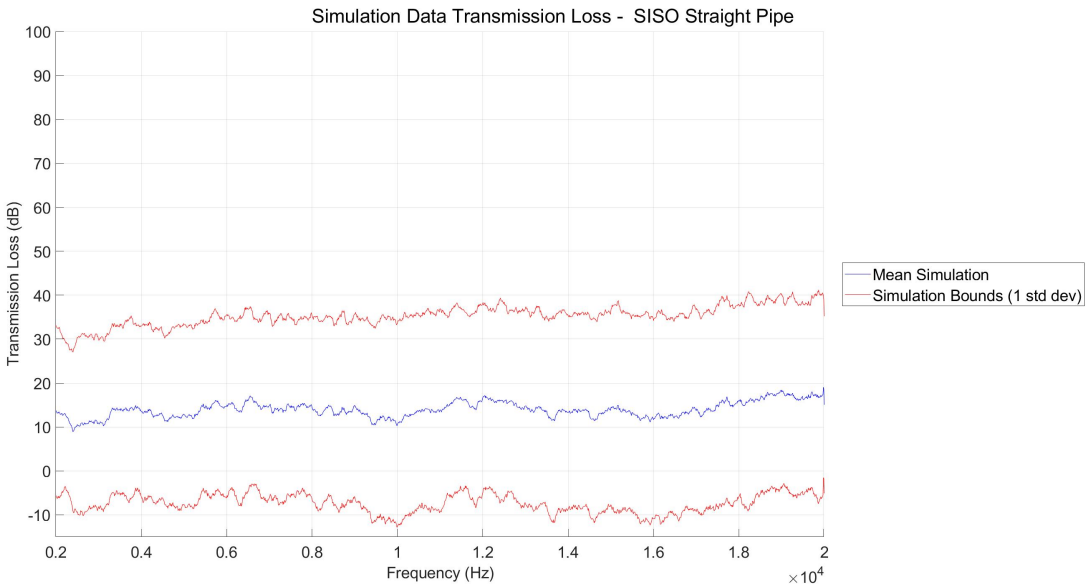

Figure 4-20 - SISO - Straight Pipe - Simulation Results

Average Transmission Loss (dB)				
20 Hz - 5 kHz	5 kHz - 10 kHz	10 kHz - 15 kHz	15 kHz - 20 kHz	20 Hz - 20 kHz
13.3	13.8	14.2	14.8	14.8

Table 4-1 - SISO - Straight Pipe - Simulation Data

4.2.2 Straight Pipe with Radial Perforations

The SP with RP acoustic simulation model consisted of 6 domains. The domains consisted of the internal cavity as a Finite Fluid Component as well as 3 rows of RP, input, and output domains as IFCs.

Figure 4-21 shows the internal cavity solid model developed for the simulation. Figure 4-22 shows the MSC.PATRAN mesh model. Surface elements are shown in green and solid elements are shown in pink. Figure 4-23 shows the analysis tree for the ACTRAN model as well

as the imported model. Figure 4-24, Figure 4-25, and Figure 4-26 show the IFC regions from the side, top, and isometric views, respectively.

The TL data is presented in Figure 4-27 and the corresponding tabular data is presented in Table 4-2. The data shows minimal change in the amount of TL across the acoustic spectrum. The overall TL_{avg} has increased from previous configurations.

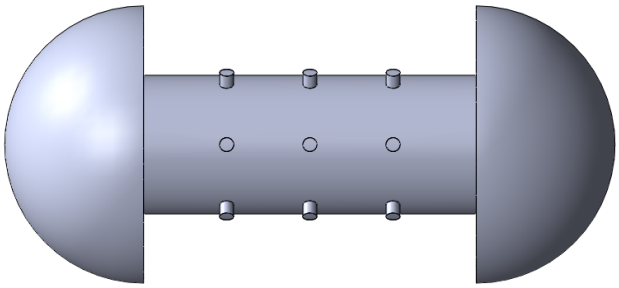

Figure 4-21 - SISO - Straight Pipe with Radial Perforations - Internal Cavity CAD

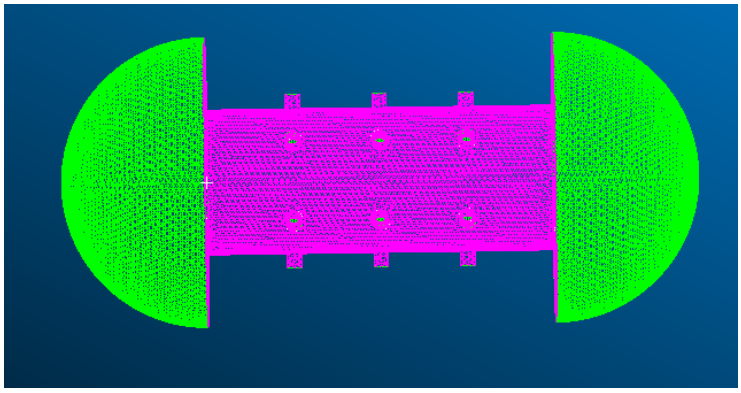

Figure 4-22 - SISO - Straight Pipe with Radial Perforations - MSC.PATRAN Mesh

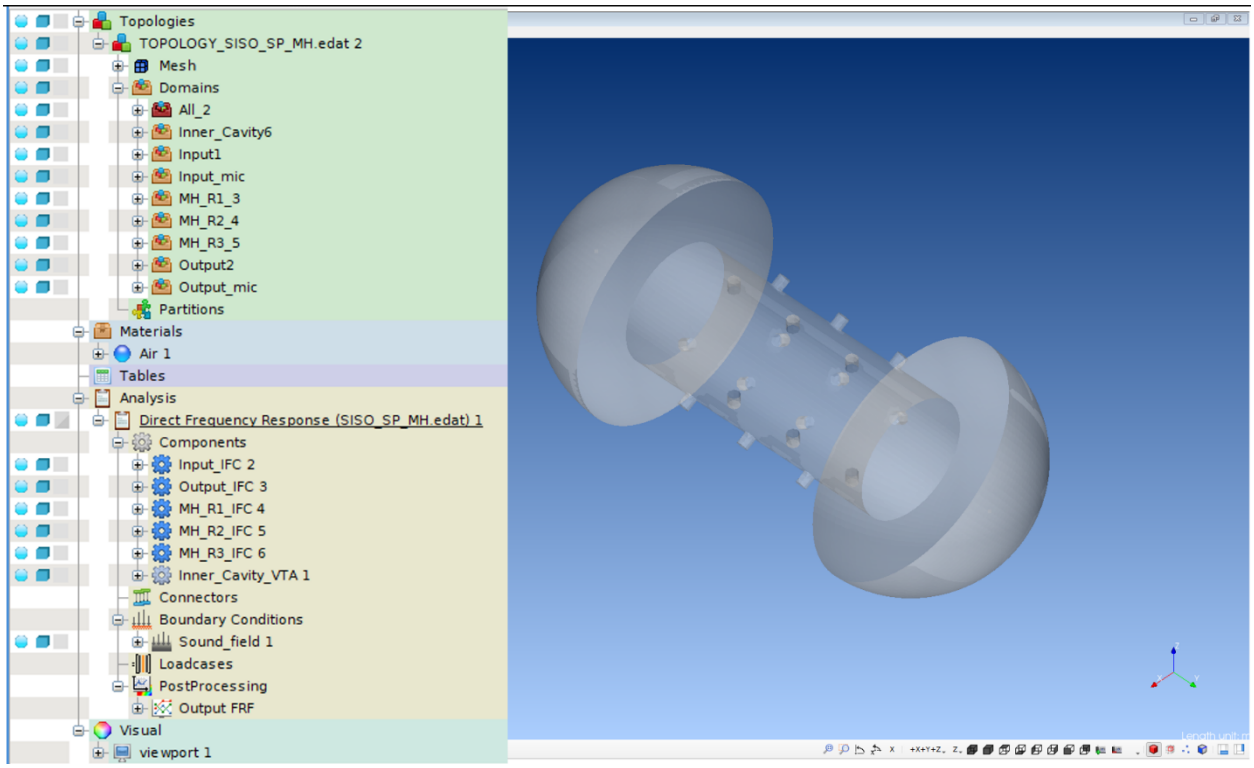

Figure 4-23 - SISO - Straight Pipe with Radial Perforations - ACTRAN Model Setup

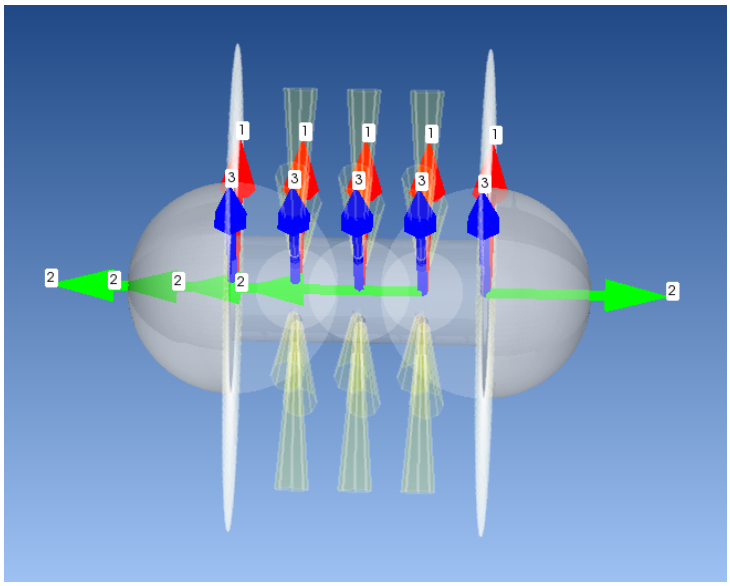

Figure 4-24 - SISO - Straight Pipe with Radial Perforations - IFC - Side View

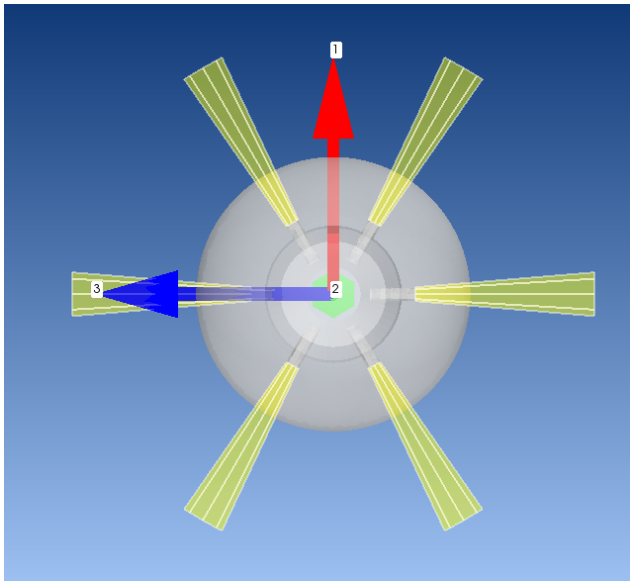

Figure 4-25 - SISO - Straight Pipe with Radial Perforations - IFC - Top View

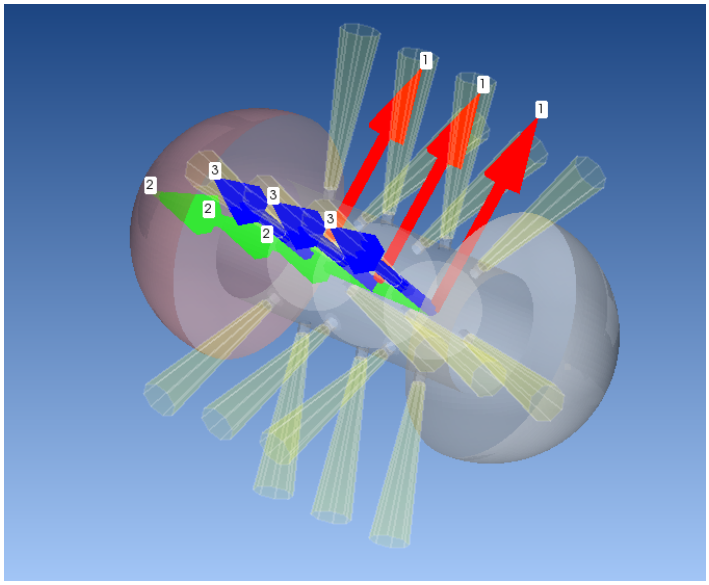

Figure 4-26 - SISO - Straight Pipe with Radial Perforations - IFC - Isometric View

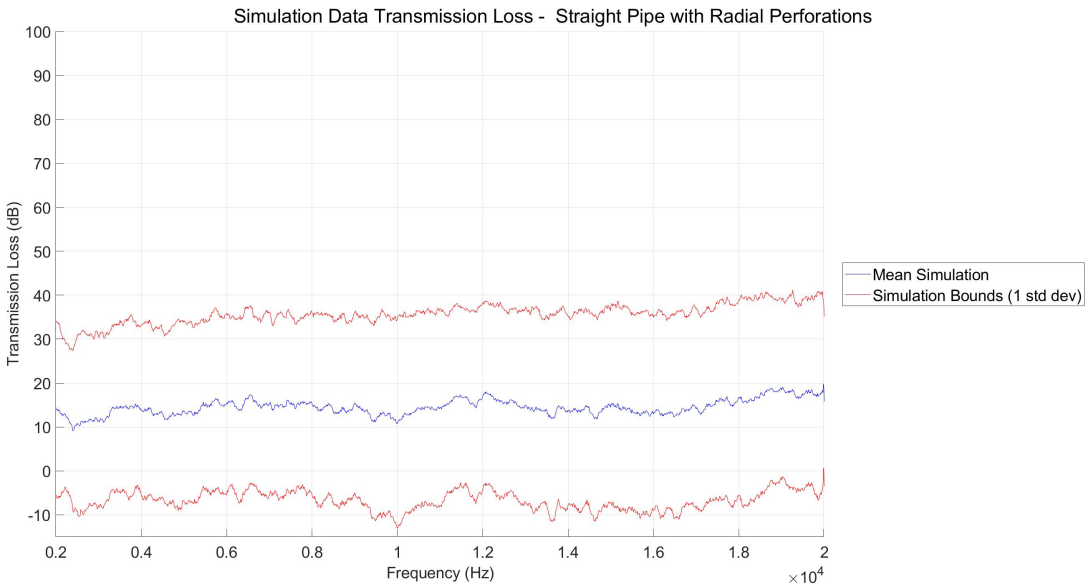

Figure 4-27 - SISO - Straight Pipe with Radial Perforations - Simulation Results

Average Transmission Loss (dB)				
20 Hz - 5 kHz	5 kHz - 10 kHz	10 kHz - 15 kHz	15 kHz - 20 kHz	20 Hz - 20 kHz
13.8	14.4	14.6	15.5	15.5

Table 4-2 - SISO - Straight Pipe with Radial Perforations - Simulation Data

4.2.3 Converging Nozzle

The CN acoustic simulation model consisted of 6 domains. The domains consisted of the internal cavity as a Finite Fluid Component as well as the input and output domains as IFCs.

Figure 4-28 shows the internal cavity solid model developed for the simulation. Figure 4-29 shows the MSC.PATRAN mesh model. Surface elements are shown in green and solid elements are shown in pink. Figure 4-30 shows the analysis tree for the ACTRAN model as well as the imported model. Figure 4-31 shows the IFC regions in an isometric view.

The TL data is presented in Figure 4-32 and the corresponding tabular data is presented in Table 4-3. The data shows minimal change in the amount of TL across the acoustic spectrum. The overall TL_{avg} has increased from previous configurations.

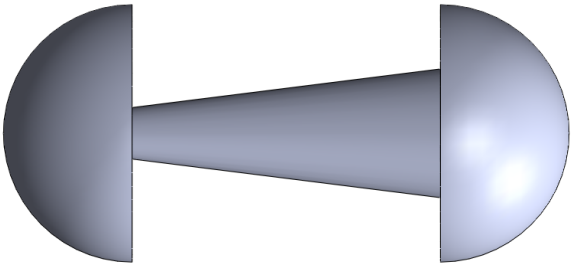

Figure 4-28 - SISO - Converging Nozzle - Internal Cavity CAD

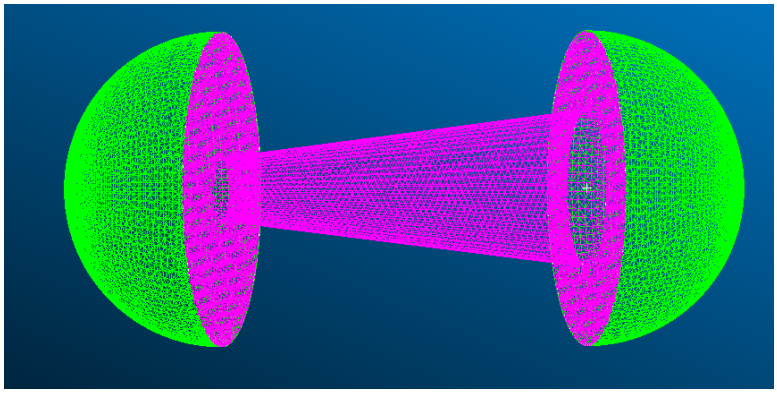

Figure 4-29 - SISO - Converging Nozzle - MSC.PATRAN Mesh

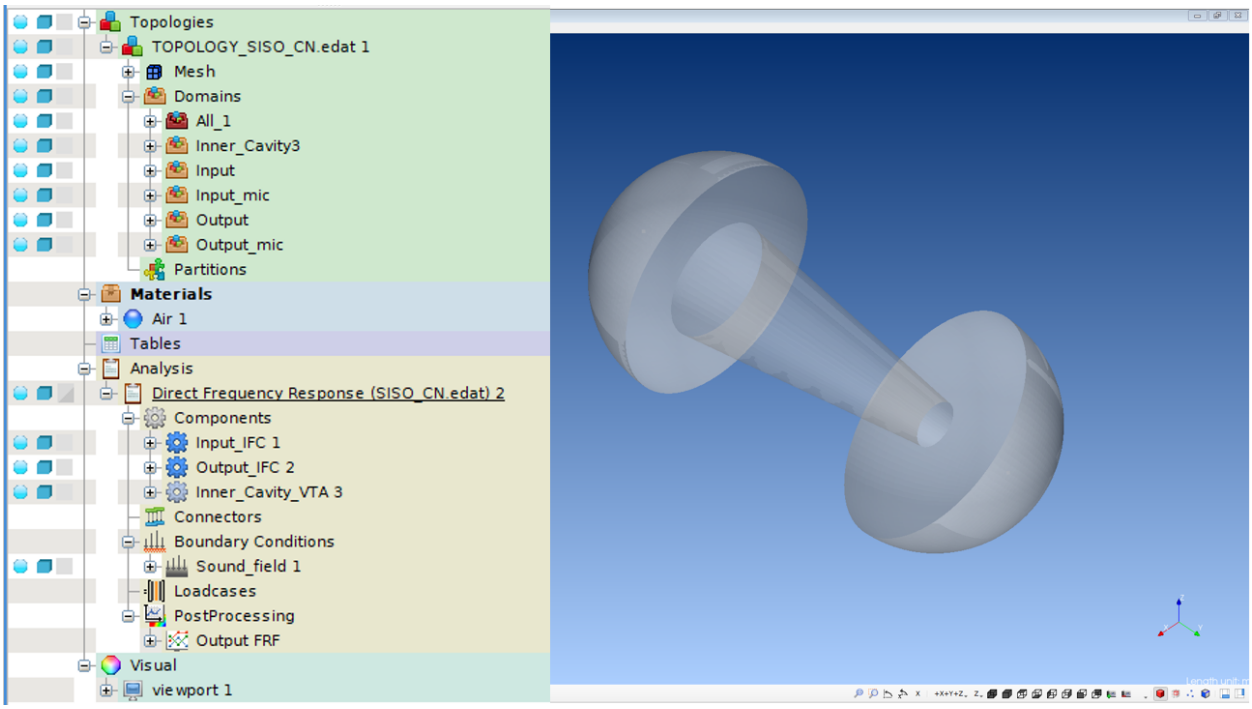

Figure 4-30 - SISO - Converging Nozzle - ACTRAN Model Setup

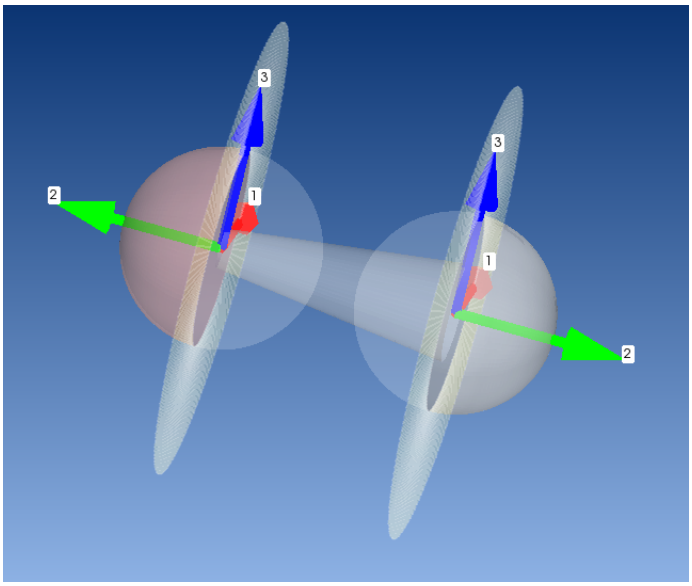

Figure 4-31 - SISO - Converging Nozzle - IFC - Isometric View

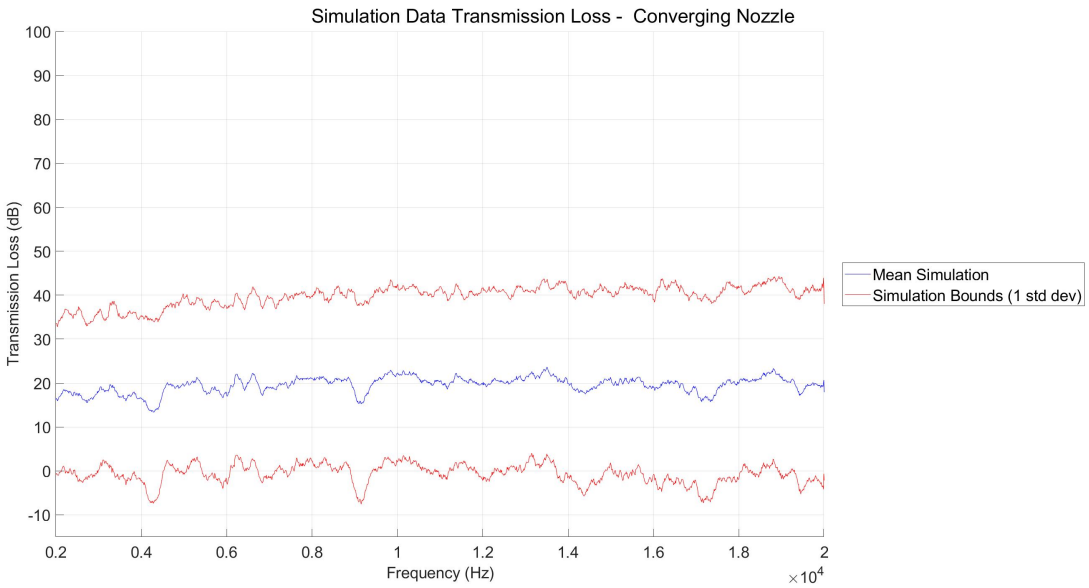

Figure 4-32 - SISO - Converging Nozzle - Simulation Results

Average Transmission Loss (dB)				
20 Hz - 5 kHz	5 kHz - 10 kHz	10 kHz - 15 kHz	15 kHz - 20 kHz	20 Hz - 20 kHz
18.3	19.8	20.5	19.7	19.7

Table 4-3 - SISO - Converging Nozzle - Simulation Data

4.2.4 Diverging Nozzle

The DN acoustic simulation model consisted of 3 domains. The domains consisted of the internal cavity as a Finite Fluid Component as well as the input and output domains as IFCs.

Figure 4-33 shows the internal cavity solid model developed for the simulation. Figure 4-34 shows the MSC.PATRAN mesh model. Surface elements are shown in green and solid elements are shown in pink. Figure 4-35 shows the analysis tree for the ACTRAN model as well as the imported model. Figure 4-36 shows the IFC regions from an isometric view.

The TL data is presented in Figure 4-37 and the corresponding tabular data is presented in Table 4-4. The data shows minimal change in the amount of TL across the acoustic spectrum. The overall TL_{avg} is comparable with the CN configuration.

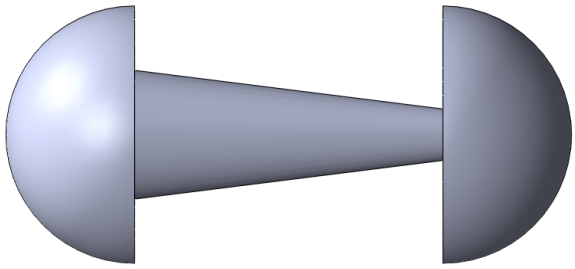

Figure 4-33 - SISO - Diverging Nozzle - Internal Cavity CAD

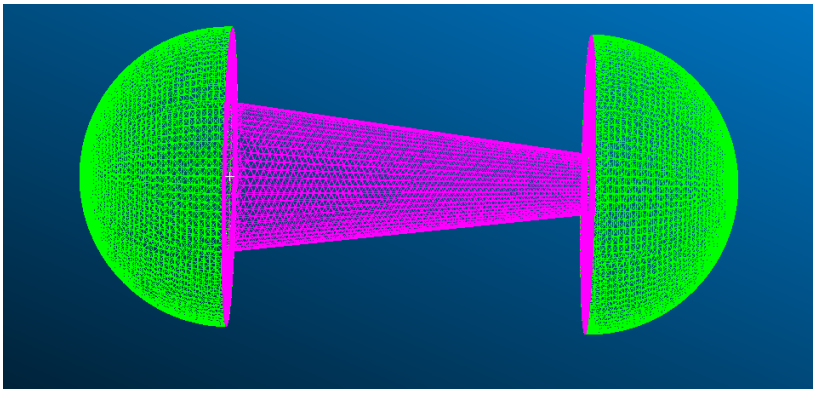

Figure 4-34 - SISO - Diverging Nozzle - MSC.PATRAN Mesh

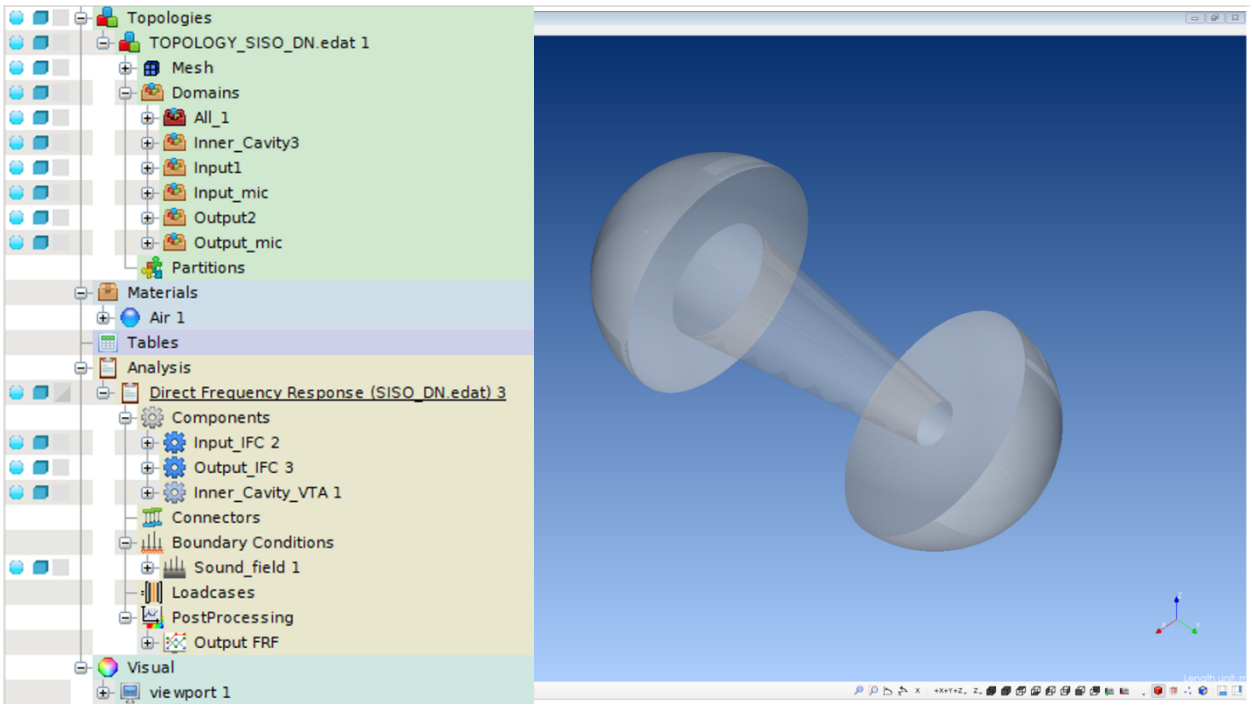

Figure 4-35 - SISO - Diverging Nozzle - ACTRAN Model Setup

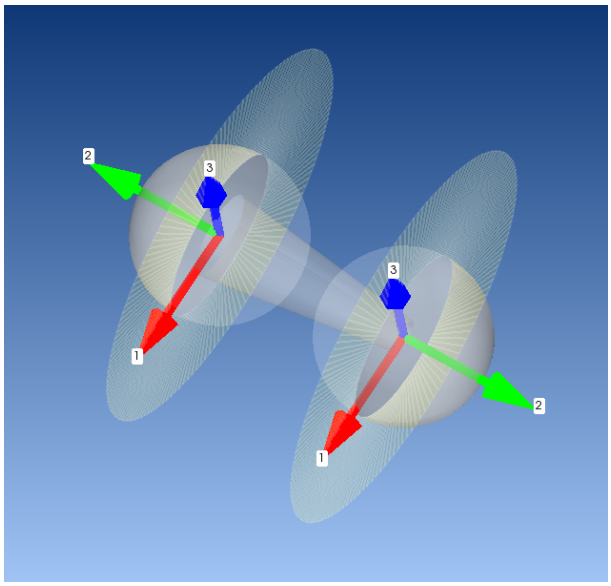

Figure 4-36 - SISO - Diverging Nozzle - IFC - Isometric View

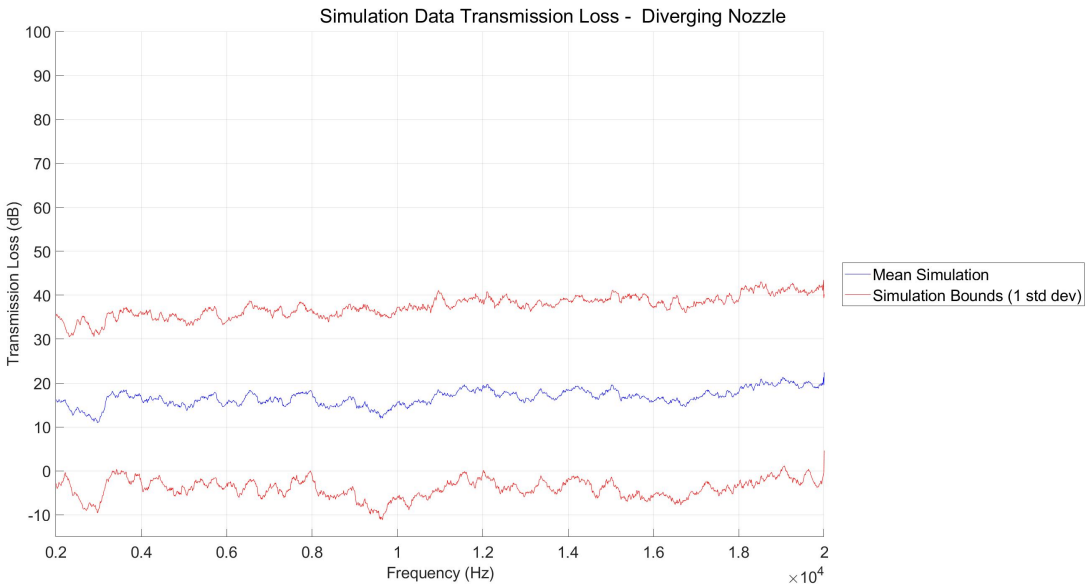

Figure 4-37 - SISO - Diverging Nozzle - Simulation Results

Average Transmission Loss (dB)				
20 Hz - 5 kHz	5 kHz - 10 kHz	10 kHz - 15 kHz	15 kHz - 20 kHz	20 Hz - 20 kHz
17.3	15.7	17.3	17.9	17.9

Table 4-4 - SISO - Diverging Nozzle - Simulation Data

4.2.5 Diverging Nozzle with Radial Perforations

The DN with RP acoustic simulation model consisted of 6 domains. The domains consisted of the internal cavity as a Finite Fluid Component as well as 3 rows of RP, input, and output domains as IFCs.

Figure 4-38 shows the internal cavity solid model developed for the simulation. Figure 4-39 shows the MSC.PATRAN mesh model. Surface elements are shown in green and solid elements are shown in pink. Figure 4-40 shows the analysis tree for the ACTRAN model as well as the imported model. Figure 4-41 shows the IFC regions for the input and output domain in an

isometric view. Figure 4-42 and Figure 4-43 show the 3 rows of RP in an isometric and top view, respectively.

The TL data is presented in Figure 4-44 and the corresponding tabular data is presented in Table 4-5. The data shows minimal change in the amount of TL across the acoustic spectrum. The overall TL_{avg} has is comparable from the previous configuration.

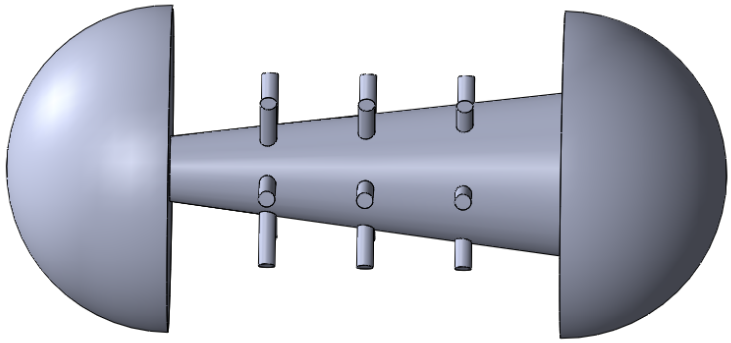

Figure 4-38 - SISO - Diverging Nozzle with Radial Perforations - Internal Cavity CAD

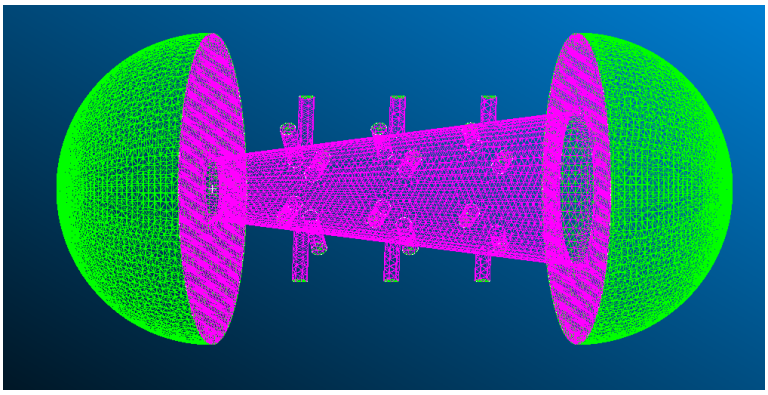

Figure 4-39 - SISO - Diverging Nozzle with Radial Perforations - MSC.PATRAN Mesh

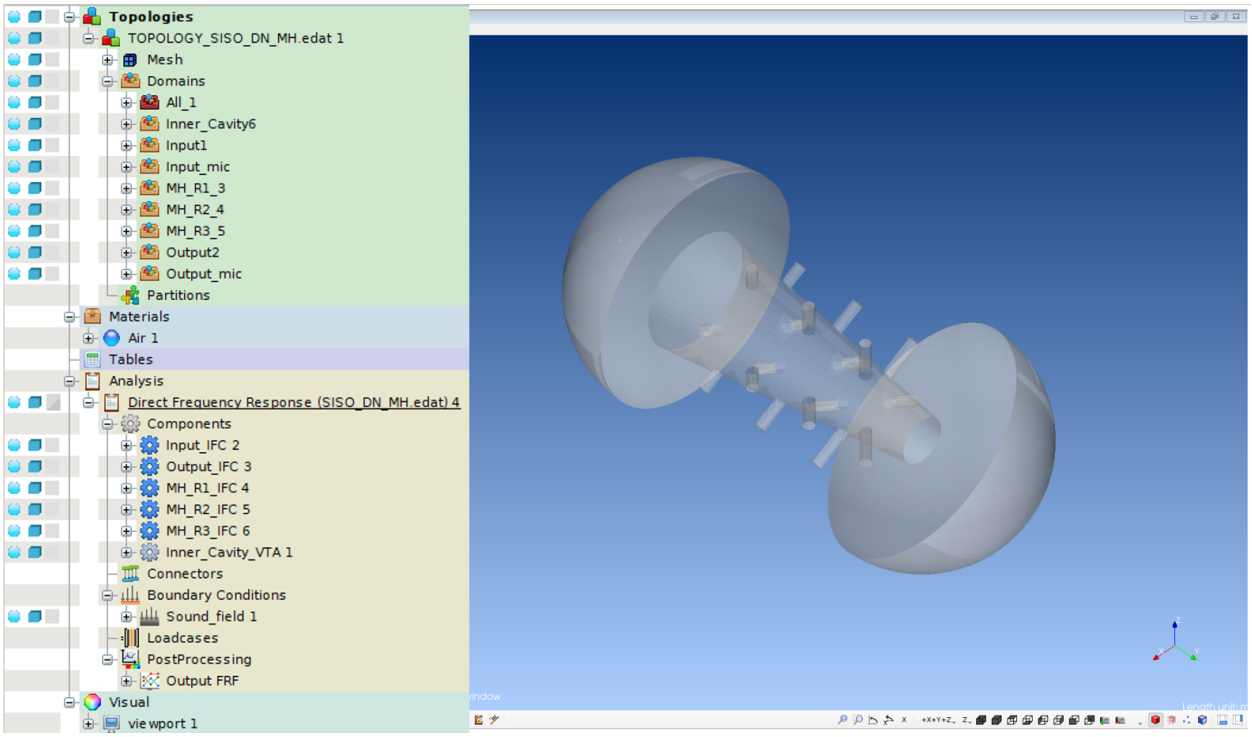

Figure 4-40 - SISO - Diverging Nozzle with Radial Perforations - ACTRAN Model Setup

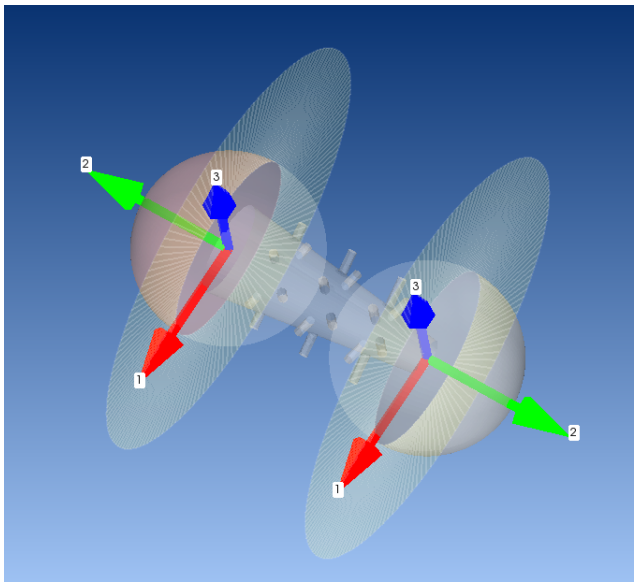

Figure 4-41 - SISO - Diverging Nozzle with Radial Perforations - Input/Output IFC - Isometric View

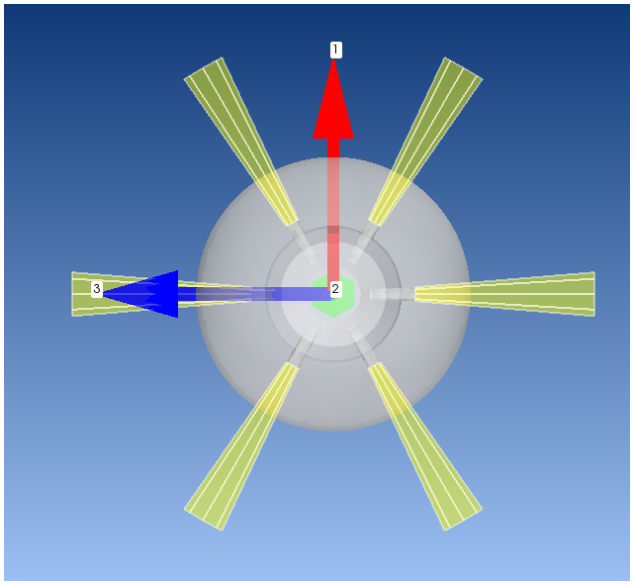

Figure 4-42 - SISO Diverging Nozzle with Radial Perforations - Perforations IFC - Top View

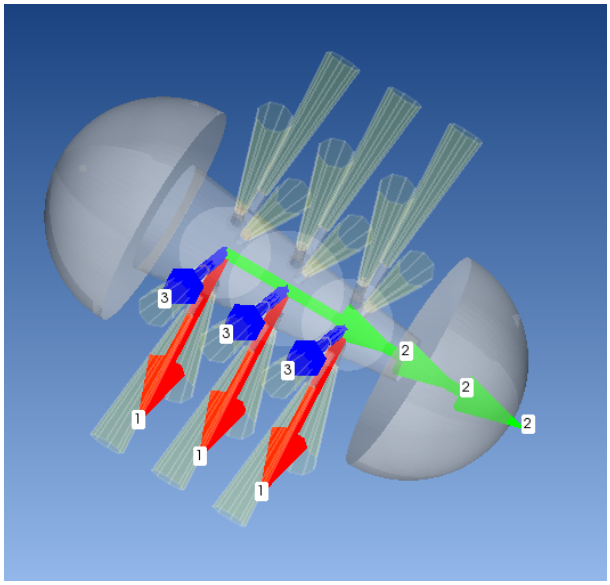

Figure 4-43 - SISO - Diverging Nozzle with Radial Perforations - Perforations IFC - Isometric View

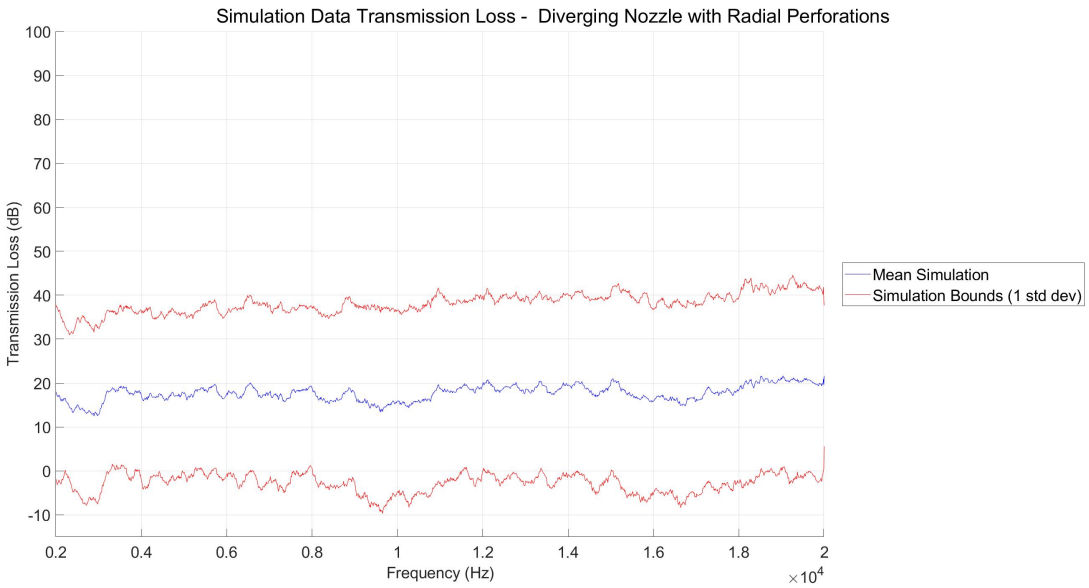

Figure 4-44 - SISO - Diverging Nozzle with Radial Perforations - Simulation Results

Average Transmission Loss (dB)				
20 Hz - 5 kHz	5 kHz - 10 kHz	10 kHz - 15 kHz	15 kHz - 20 kHz	20 Hz - 20 kHz
18.5	17.1	183	18.5	18.5

Table 4-5 - SISO - Diverging Nozzle with Radial Perforations - Simulation Data

4.2.6 Series of Diverging Nozzles

The SDN acoustic simulation model consisted of 3 domains. The domains consisted of the internal cavity as a Finite Fluid Component as well as the input and output domains as IFCs.

Figure 4-45 shows the internal cavity solid model developed for the simulation. Figure 4-46 shows the MSC.PATRAN mesh model. Surface elements are shown in green and solid elements are shown in pink. Figure 4-47 shows the analysis tree for the ACTRAN model as well as the imported model. Figure 4-48 shows the IFC regions in an isometric view.

The TL data is presented in Figure 4-49 and the corresponding tabular data is presented in Table 4-6. The data shows peaks in the TL at approximately 300 Hz, 700 Hz, and 10.5 kHz. Additional peaks with decreasing amplitudes are seen above 10.5 kHz. The peaks are indicative of band gap formation. The overall TL_{avg} has increased from previous configurations.

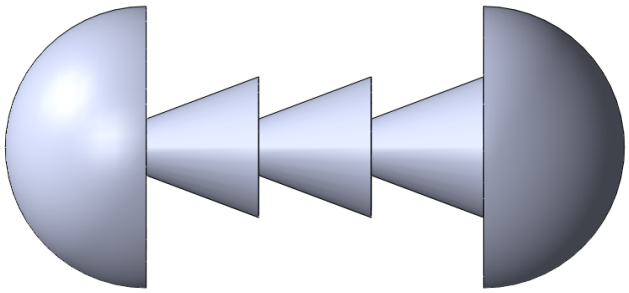

Figure 4-45 - SISO - Series of Diverging Nozzles - Internal Cavity CAD

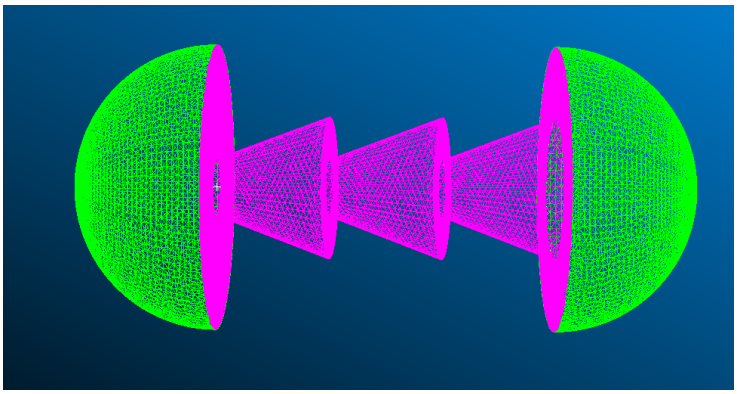

Figure 4-46 - SISO - Series of Diverging Nozzles - MSC.PATRAN Mesh

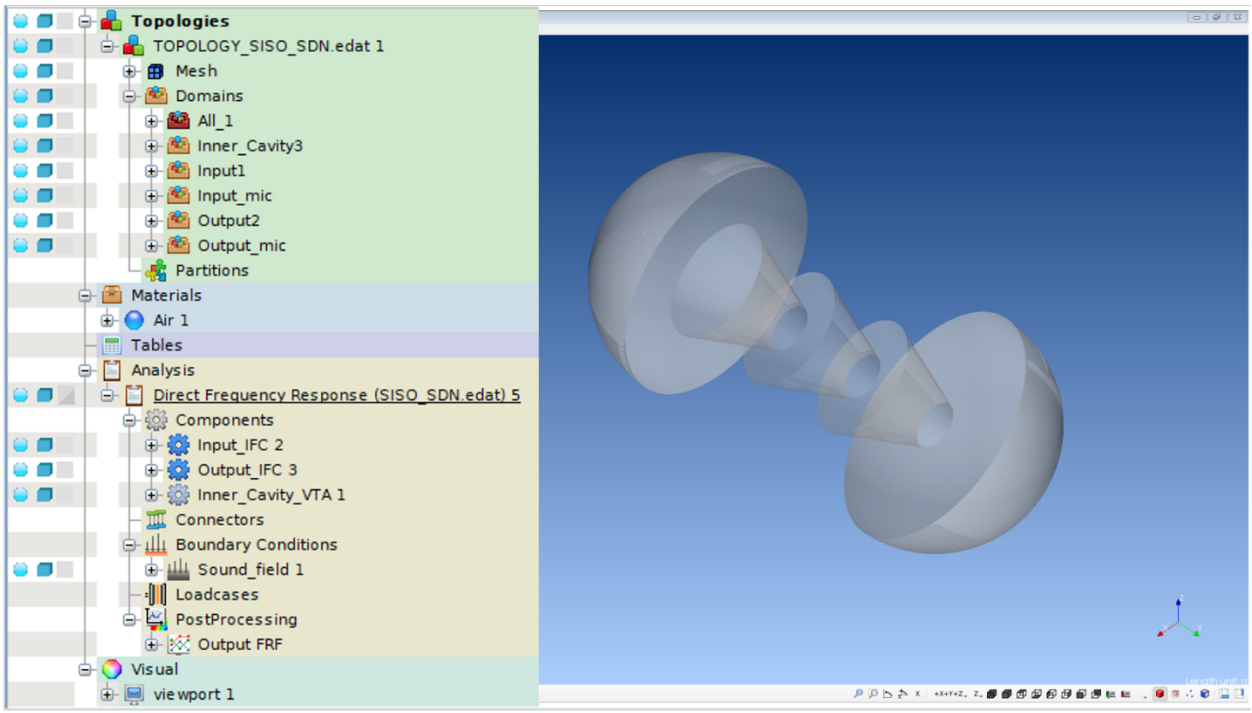

Figure 4-47 - SISO - Series of Diverging Nozzles - ACTRAN Model Setup

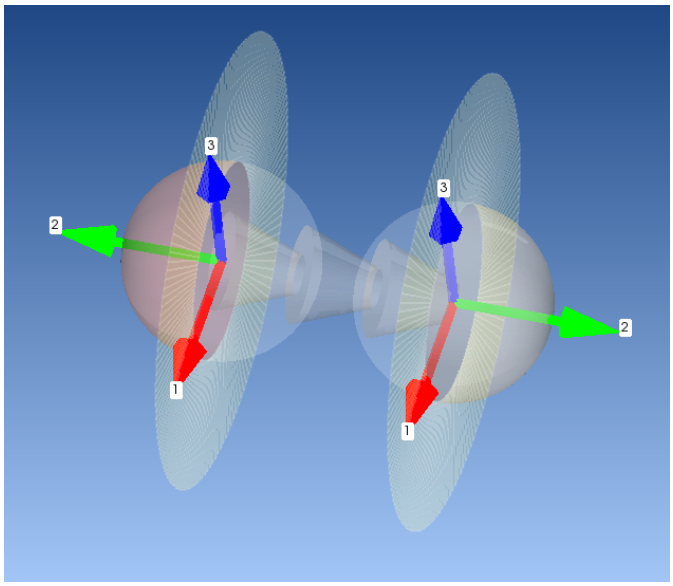

Figure 4-48 - SISO - Series of Diverging Nozzles - IFC - Isometric View

Figure 4-49 - SISO - Series of Diverging Nozzles - Simulation Results

Average Transmission Loss (dB)				
20 Hz - 5 kHz	5 kHz - 10 kHz	10 kHz - 15 kHz	15 kHz - 20 kHz	20 Hz - 20 kHz
24.2	34.3	26.9	26.1	26.1

Table 4-6 - SISO - Series of Diverging Nozzle - Simulation Data

4.2.7 Series of Diverging Nozzles with Radial Perforations

The SDN with RP acoustic simulation model consisted of 9 domains. The domains consisted of the internal cavity as a Finite Fluid Component as well as 6 rows of RP, input, and output domains as IFCs.

Figure 4-50 shows the internal cavity solid model developed for the simulation. Figure 4-51 shows the MSC.PATRAN mesh model. Surface elements are shown in green and solid elements are shown in pink. Figure 4-52 shows the analysis tree for the ACTRAN model as well as the imported model. Figure 4-53 shows an isometric view of the IFC regions for the input and

output domains. Figure 4-54 shows an isometric view of the IFC regions for the input and output domains.

The TL data is presented in Figure 4-55 and the corresponding tabular data is presented in Table 4-7. The data shows a large peak in the TL at approximately 700 Hz. Additional peaks with decreasing amplitudes are seen above 700 Hz. The overall TL_{avg} has increased from previous configurations.

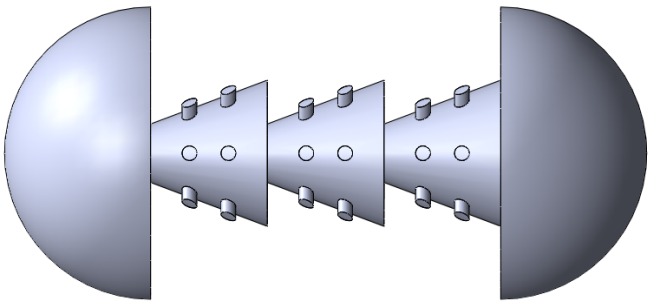

Figure 4-50 - SISO - Series of Diverging Nozzles with Radial Perforations - Internal Cavity CAD

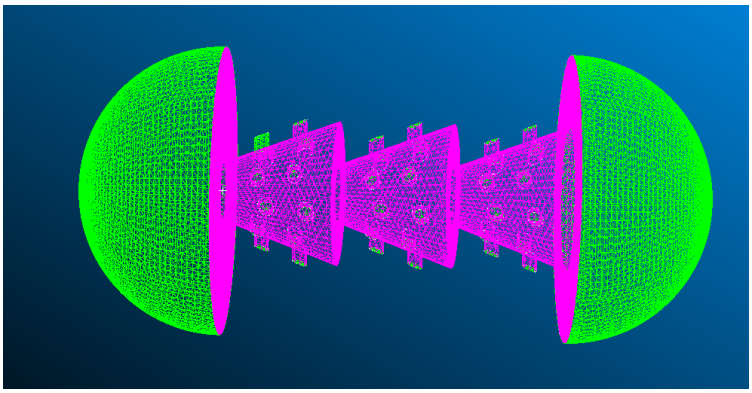

Figure 4-51 - SISO - Series of Diverging Nozzles with Radial Perforations - Mesh

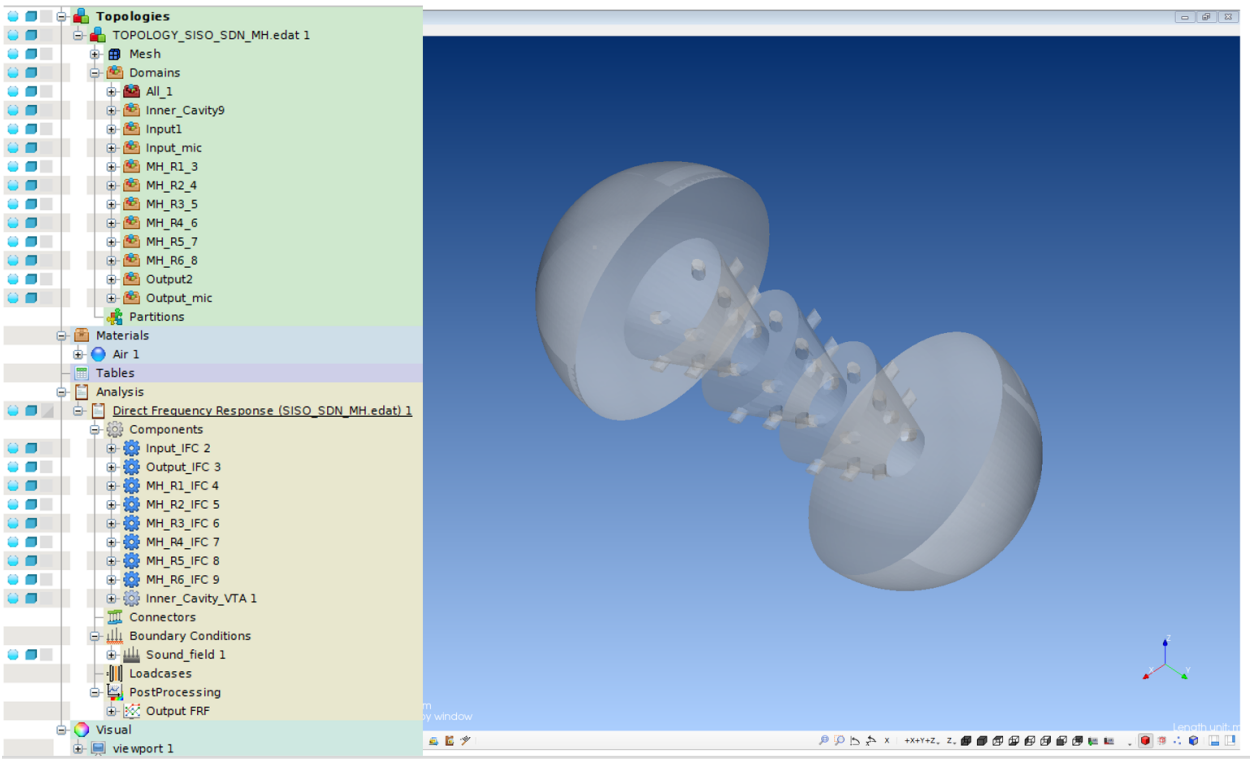

Figure 4-52 - SISO - Series of Diverging Nozzles with Radial Perforations - ACTRAN Model Setup

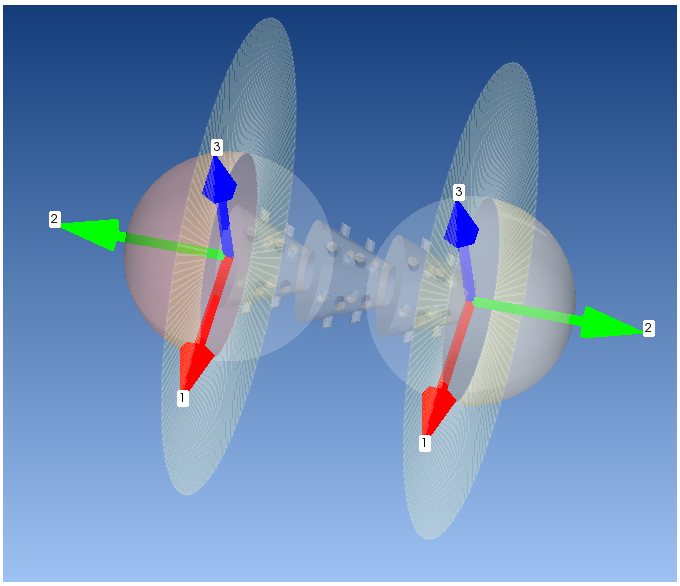

Figure 4-53 - SISO - Series of Diverging Nozzles with Radial Perforations - Input/Output IFC - Isometric View

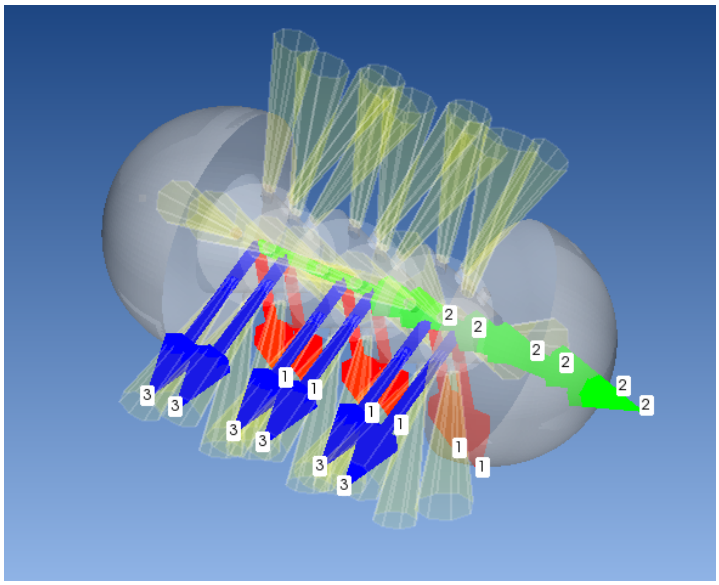

Figure 4-54 - SISO - Series of Diverging Nozzles with Radial Perforations - Perforations IFC - Isometric View

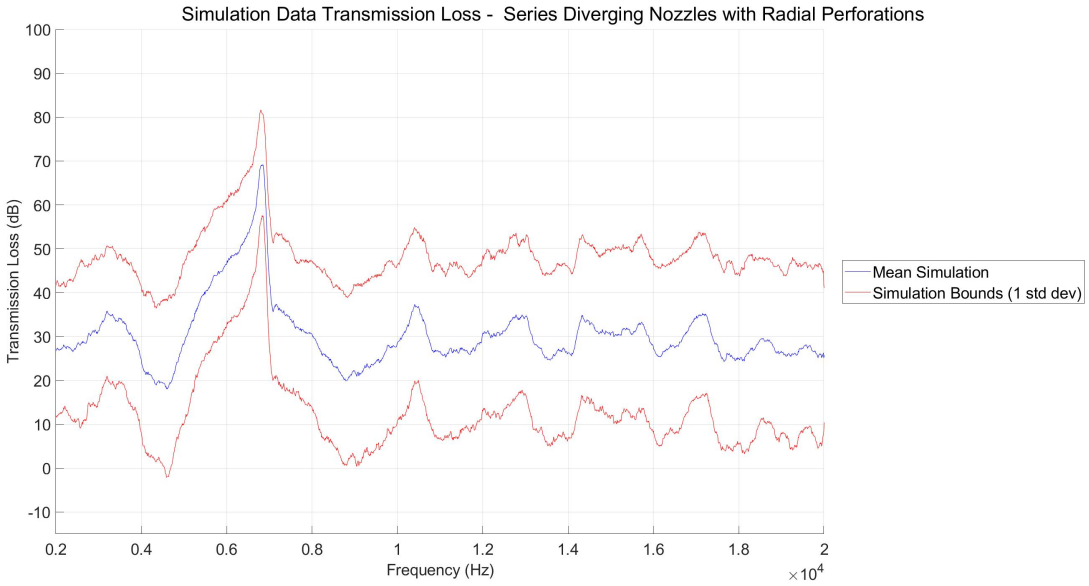

Figure 4-55 - SISO - Series of Diverging Nozzles with Radial Perforations - Simulation Results

Average Transmission Loss (dB)				
20 Hz - 5 kHz	5 kHz - 10 kHz	10 kHz - 15 kHz	15 kHz - 20 kHz	20 Hz - 20 kHz
27.2	35.3	29.8	28.5	28.5

Table 4-7 - SISO - Series of Diverging Nozzle with Radial Perforations - Simulation Data

4.2.8 Series of Diverging Nozzles with Radial and Axial Perforations

The SDN with RAP acoustic simulation model consisted of 21 domains. The domains consisted of the internal cavity as a Finite Fluid Component as well as 6 rows of RP, 6 AP for the first stage, 6 AP for the second stage, input, and output domains as IFCs.

Figure 4-56 shows the internal cavity solid model developed for the simulation. Figure 4-57 shows the MSC.PATRAN mesh model. Surface elements are shown in green and solid elements are shown in pink. Figure 4-58 shows the analysis tree for the ACTRAN model as well as the imported model. Figure 4-60 shows an isometric view of the IFC regions for the input and output domains. Figure 4-61 shows an isometric view of the IFC regions for the input and output domains. Figure 4-62 shows an isometric view of the AP domain and Figure 4-63 shows an enlarged view.

The processed TL data is presented in Figure 4-64 and the corresponding tabular data is presented in Table 4-8. The data shows peaks in the TL at approximately 300 Hz, 700 Hz, and 10.5 kHz. Additional peaks with decreasing amplitudes are seen above 10.5 kHz. The overall TL_{avg} has increased from previous configurations.

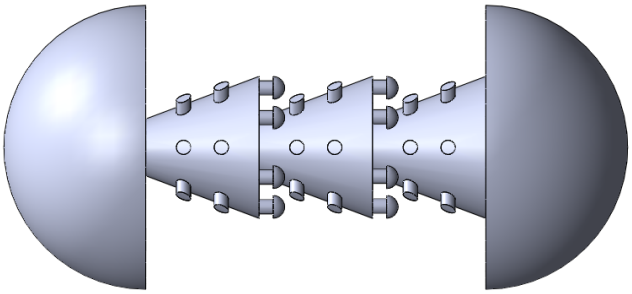

Figure 4-56 - SISO - Series of Diverging Nozzles with Radial and Axial Perforations - Internal Cavity CAD

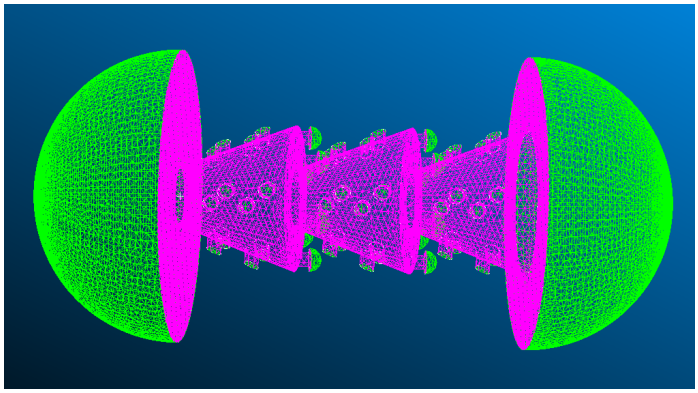

Figure 4-57 - SISO - Series of Diverging Nozzles with Radial and Axial Perforations - MSC.PATRAN Mesh

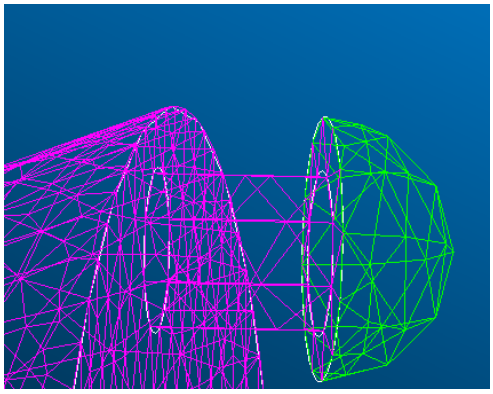

Figure 4-58 - SISO - Series of Diverging Nozzles with Radial and Axial Perforations - Axial Perforation Mesh

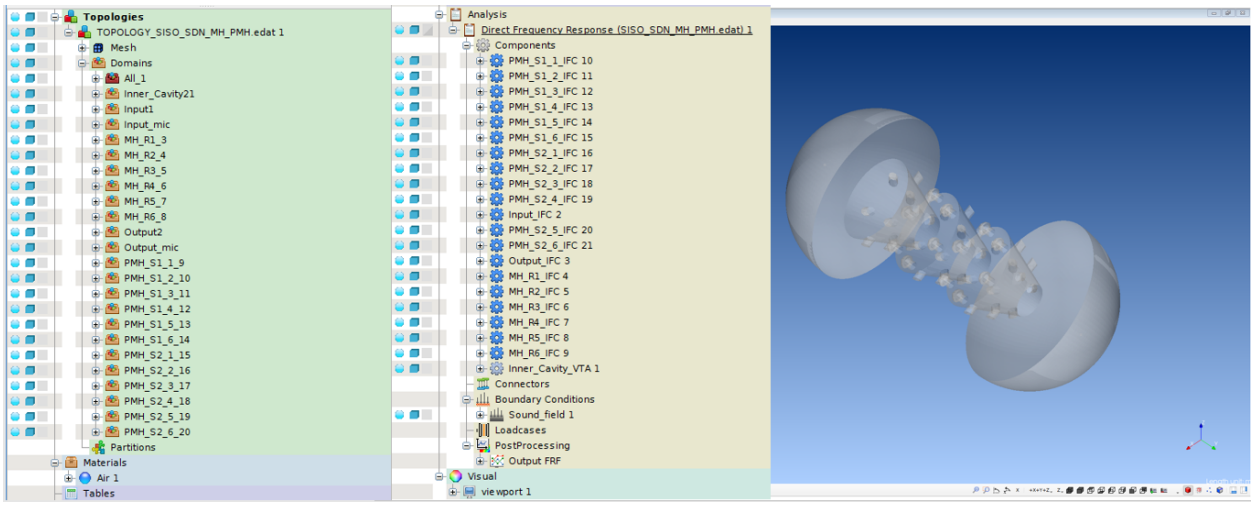

Figure 4-59 - SISO - Series of Diverging Nozzles with Radial and Axial Perforations - ACTRAN Model Setup

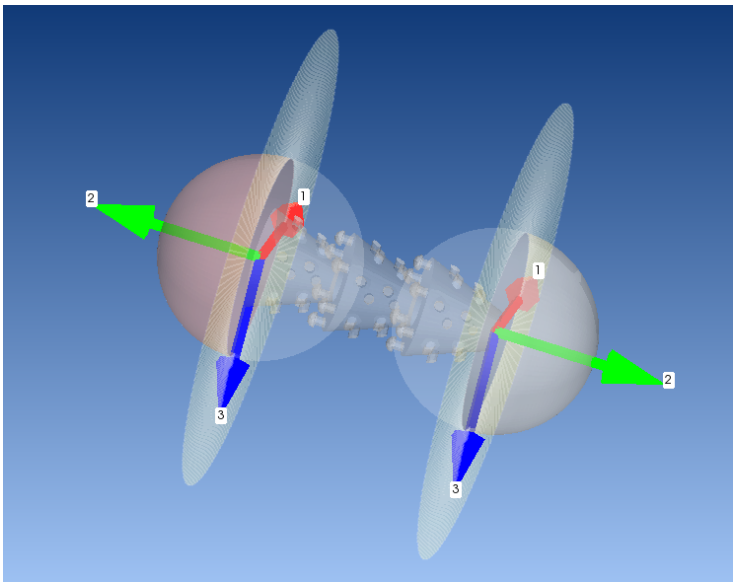

Figure 4-60 - SISO - Series of Diverging Nozzles with Radial and Axial Perforations - Input/Output IFC - Isometric View

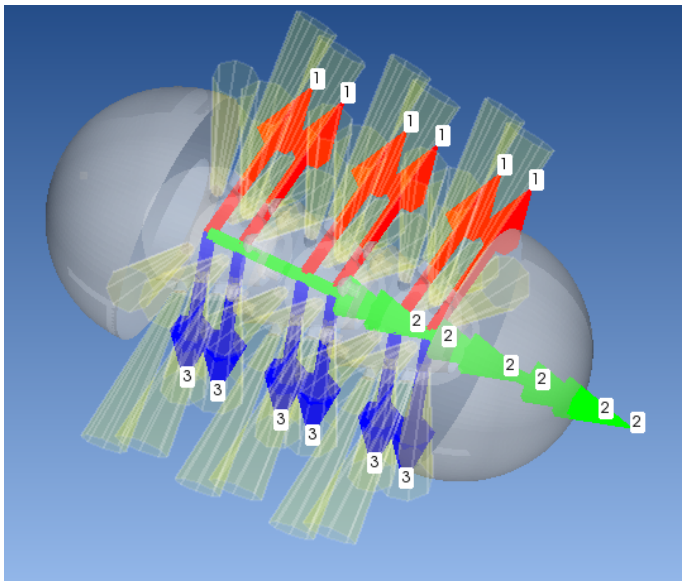

Figure 4-61 - SISO - Series of Diverging Nozzles with Radial and Axial Perforations - Radial Perforations IFC - Isometric View

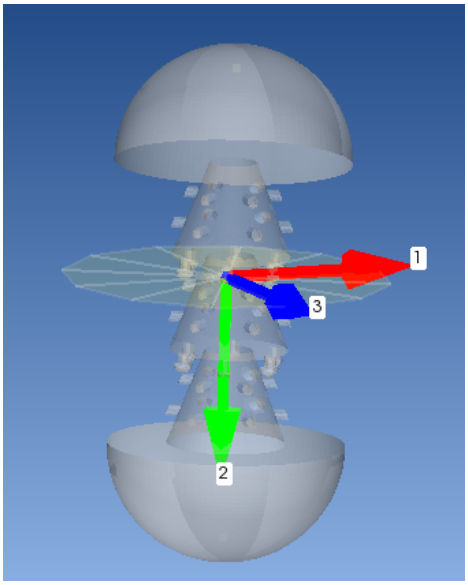

Figure 4-62 - SISO - Series of Diverging Nozzles with Radial and Axial Perforations - Axial Perforations IFC - Forward View

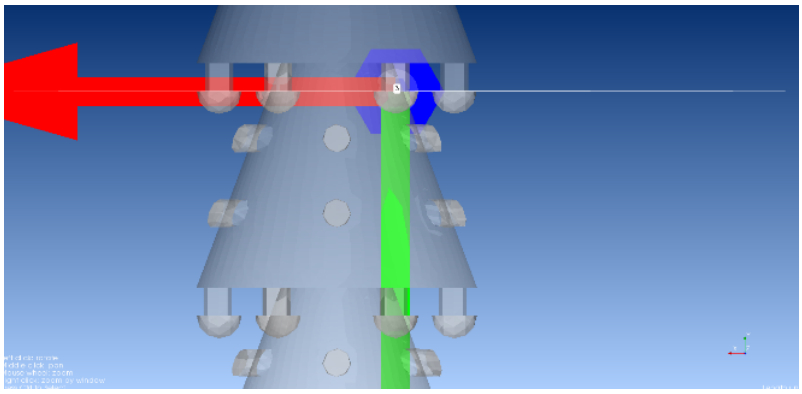

Figure 4-63 - SISO - Series of Diverging Nozzles with Radial and Axial Perforations - Axial Perforations IFC - Enlarged View

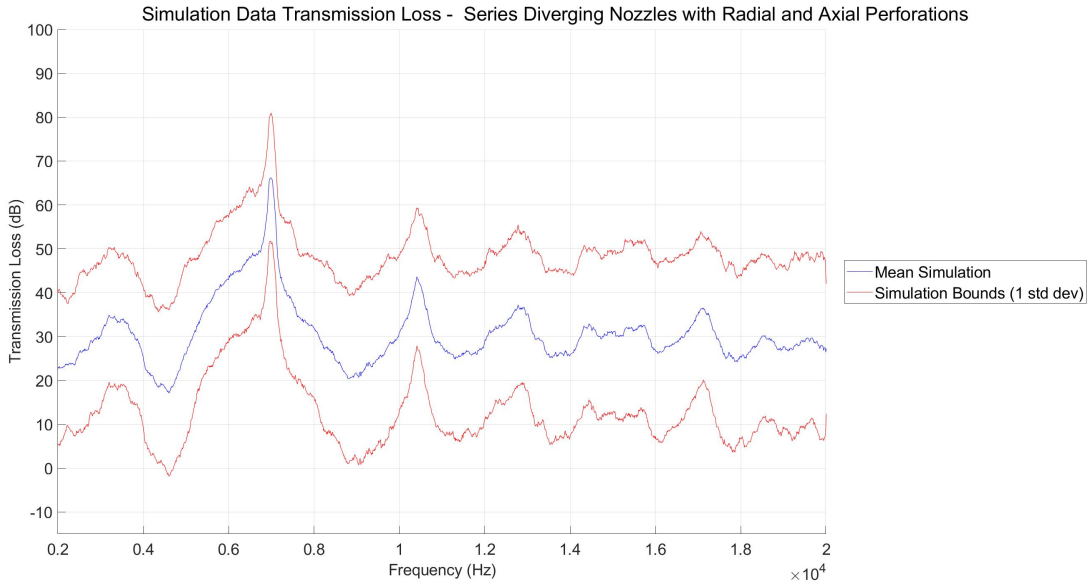

Figure 4-64 - SISO - Series of Diverging Nozzles with Radial and Axial Perforations - Simulation Results

Average Transmission Loss (dB)				
20 Hz - 5 kHz	5 kHz - 10 kHz	10 kHz - 15 kHz	15 kHz - 20 kHz	20 Hz - 20 kHz
27.7	35.2	30.5	29.2	29.2

Table 4-8 - SISO - Series of Diverging Nozzles with Radial and Axial Perforations - Simulation Data

4.2.9 Series of Diverging Nozzles with Radial and Axial Perforations and a Constricted Opening at the Output Plane

The SDN with RAP and a COOP acoustic simulation model consisted of 21 domains. The domains consisted of the internal cavity as a Finite Fluid Component as well as 6 rows of RP, 6 AP for the first stage, 6 AP for the second stage, input, and output domains as IFCs.

Figure 4-65 shows the internal cavity solid model developed for the simulation. Figure 4-66 shows the MSC.PATRAN mesh model. Surface elements are shown in green and solid elements are shown in pink. Figure 4-67 shows the analysis tree for the ACTRAN model as well as the imported model. Figure 4-68 shows an isometric view of the IFC regions for the input and output domains. Figure 4-69 shows an isometric view of the IFC regions for the input and output domains. Figure 4-70 shows an isometric view of the AP domain and Figure 4-71 shows an enlarged view.

The processed TL data is presented in Figure 4-72 and the corresponding tabular data is presented in Table 4-9. The data shows a large peak in the TL at approximately 700 Hz as well as peaks at approximately 11 kHz and 13 kHz. Additional peaks with decreasing amplitudes are seen above 13 kHz. The overall TL_{avg} has increased from previous configurations.

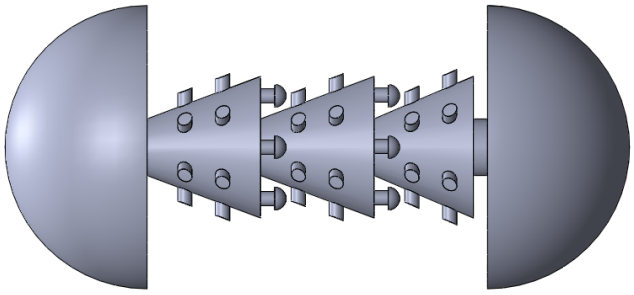

Figure 4-65 - SISO - Series of Diverging Nozzles with Radial and Axial Perforations and a Constricted Opening at the Output Plane - Internal Cavity CAD

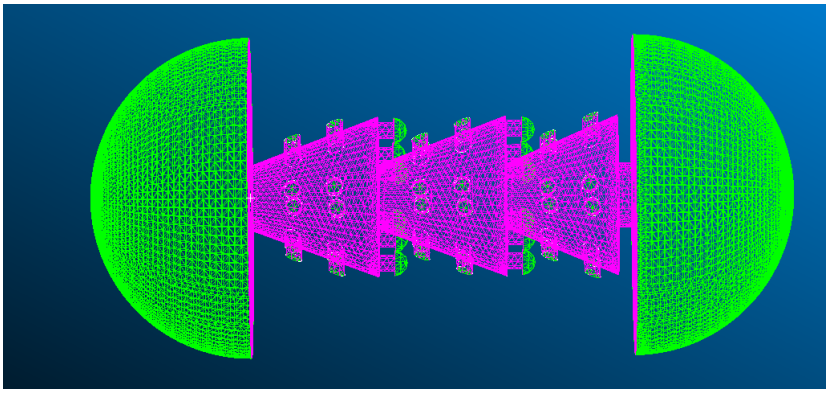

Figure 4-66 - SISO - Series of Diverging Nozzles with Radial and Axial Perforations and a Constricted Opening at the Output Plane - Mesh

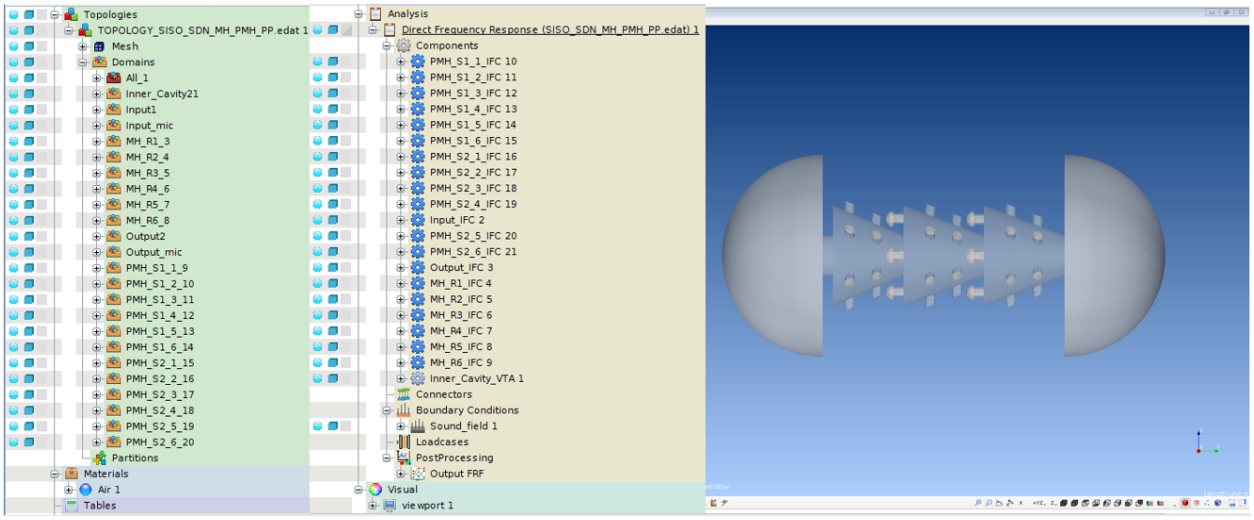

Figure 4-67 - SISO - Series of Diverging Nozzles with Radial and Axial Perforations and a Constricted Opening at the Output Plane - ACTRAN Model Setup

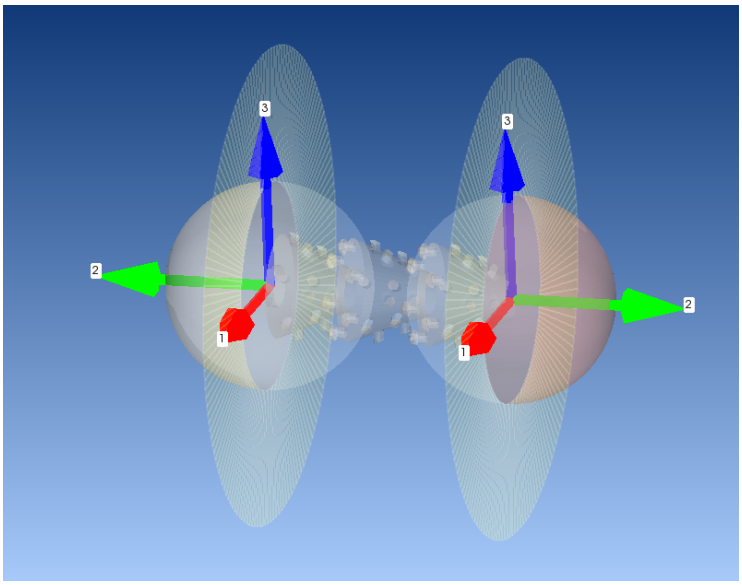

Figure 4-68 - SISO - Series of Diverging Nozzles with Radial and Axial Perforations and a Constricted Opening at the Output Plane - Input/Output IFC - Isometric View

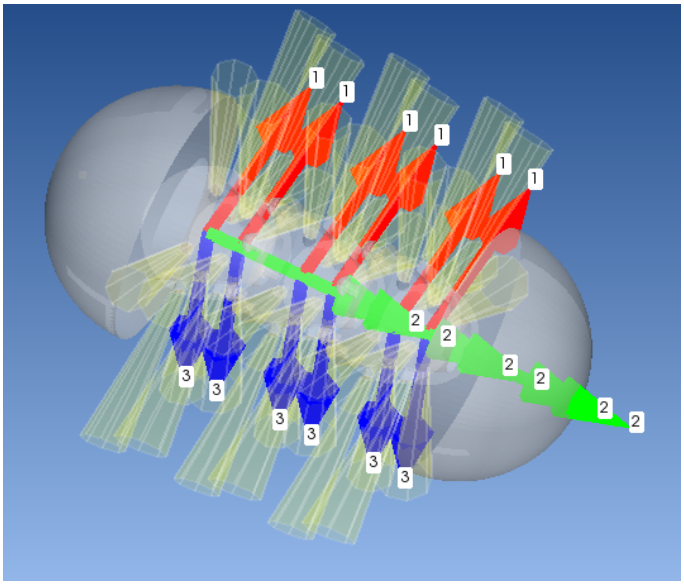

Figure 4-69 - SISO - Series of Diverging Nozzles with Radial and Axial Perforations and a Constricted Opening at the Output Plane - Radial Perforations IFC - Isometric View

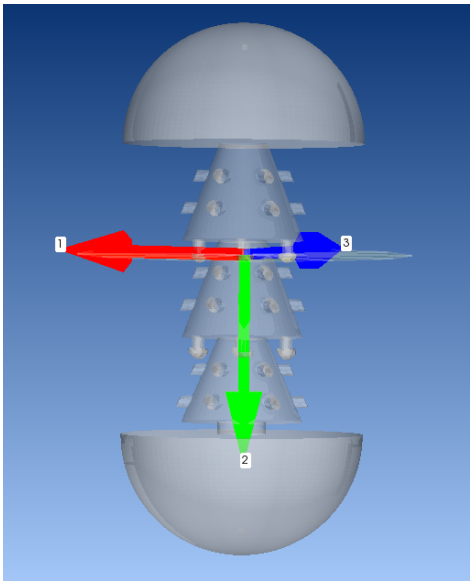

Figure 4-70 - SISO - Series of Diverging Nozzles with Radial and Axial Perforations and a Constricted Opening at the Output Plane - Axial Perforations IFC - Forward View

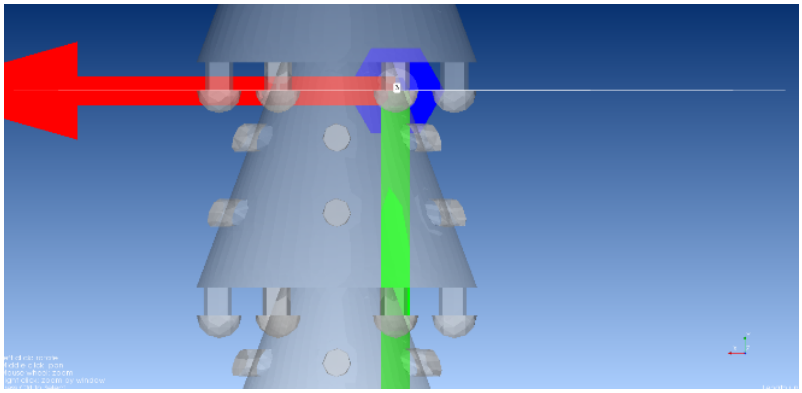

Figure 4-71 - SISO - Series of Diverging Nozzles with Radial and Axial Perforations and a Constricted Opening at the Output Plane - Axial Perforations IFC - Enlarged View

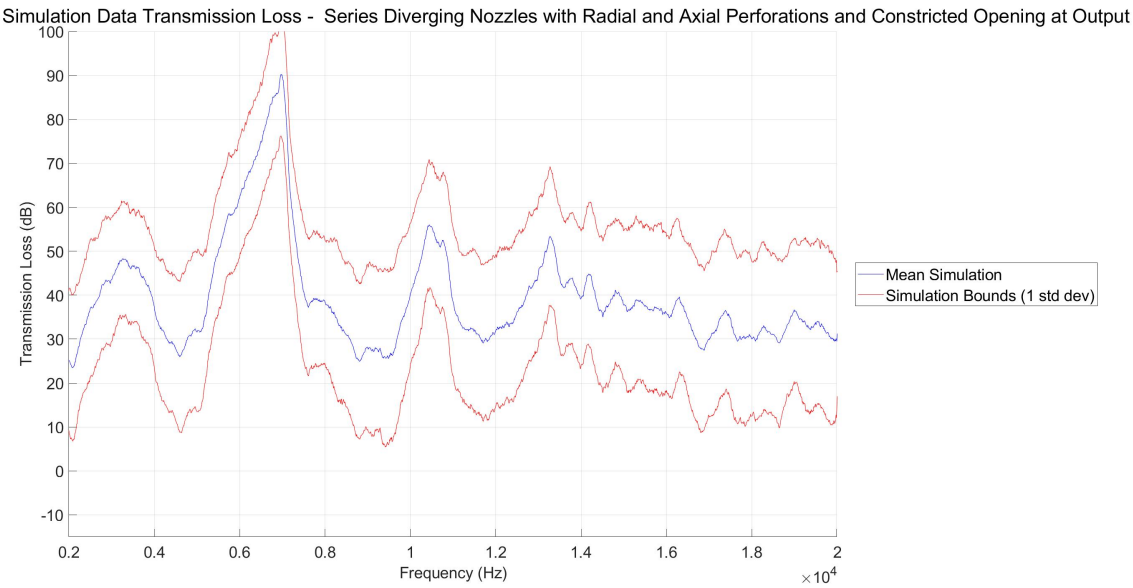

Figure 4-72 - SISO - Series of Diverging Nozzles with Radial and Axial Perforations and a Constricted Opening at the Output Plane - Simulation Results

Average Transmission Loss (dB)				
20 Hz - 5 kHz	5 kHz - 10 kHz	10 kHz - 15 kHz	15 kHz - 20 kHz	20 Hz - 20 kHz
35.1	46.9	40.7	33.5	33.5

Table 4-9 - SISO - Series of Diverging Nozzles with Radial and Axial Perforations and Constricted Opening at the Output - Simulation Data

4.3 Multiple Input Multiple Output Systems

4.3.1 Straight Pipe

The MIMO SP acoustic simulation model consisted of 3 domains. The domains consisted of the internal cavity as a Finite Fluid Component as well as the input and output domains as IFCs.

Figure 4-73 shows the internal cavity solid model developed for the simulation. Figure 4-74 shows the MSC.PATRAN mesh model. As with the SISO simulations, surface elements are shown in green and solid elements are shown in pink. Figure 4-75 shows the analysis tree for the

ACTRAN model as well as the imported model. Figure 4-76 shows the IFC regions for the input and output surfaces.

The TL data is presented in Figure 4-77 and the corresponding tabular data is presented in Table 4-10. The data shows a dip in the data at approximately 700 Hz. The amount of TL_{avg} decreases by approximately half from the lower end to the upper end of the acoustic spectrum.

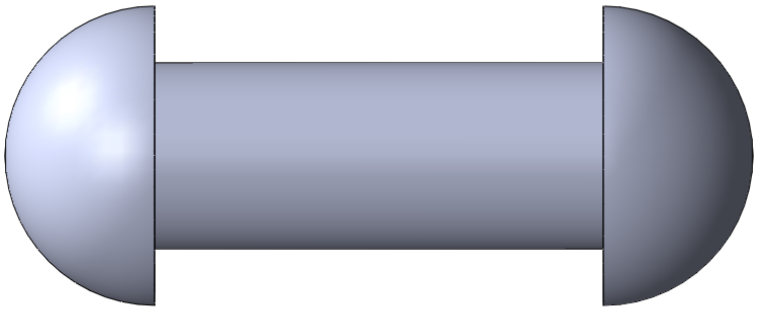

Figure 4-73 - MIMO - Straight Pipe - Internal Cavity CAD

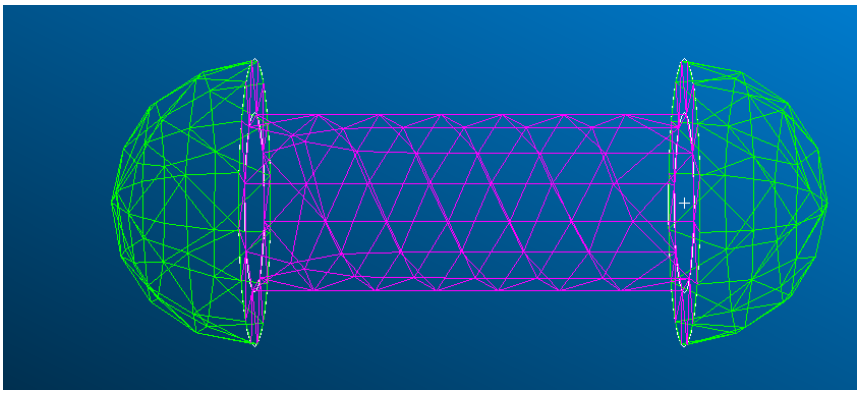

Figure 4-74 - MIMO - Straight Pipe - MSC.PATRAN Mesh

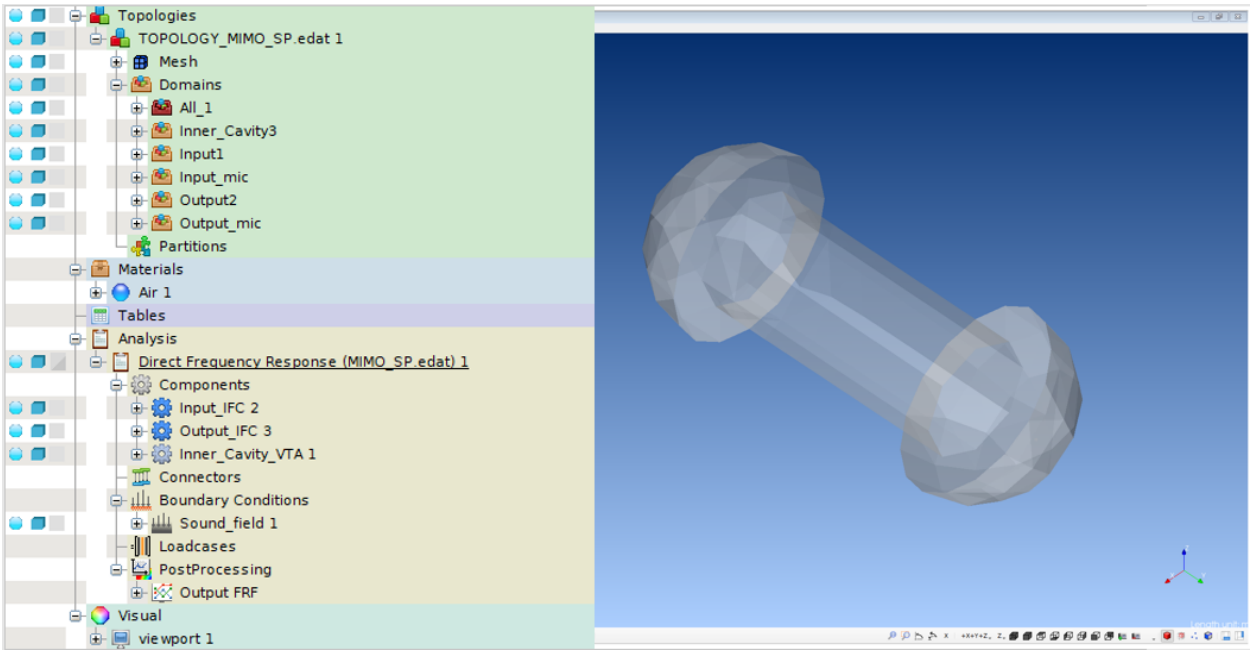

Figure 4-75 - MIMO - Straight Pipe - ACTRAN Model Setup

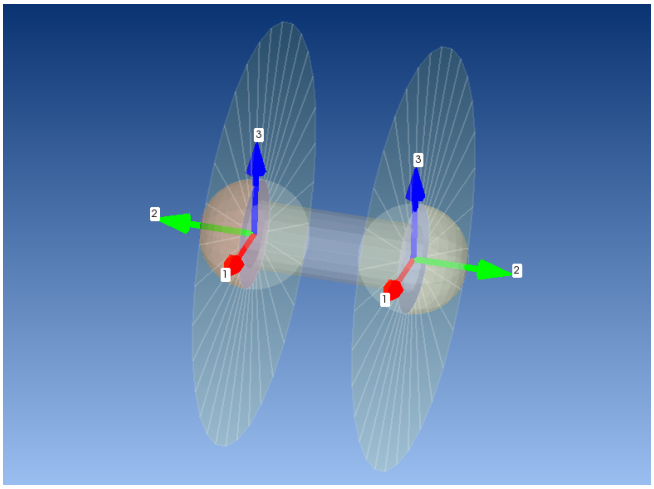

Figure 4-76 - MIMO - Straight Pipe - IFC - Side View

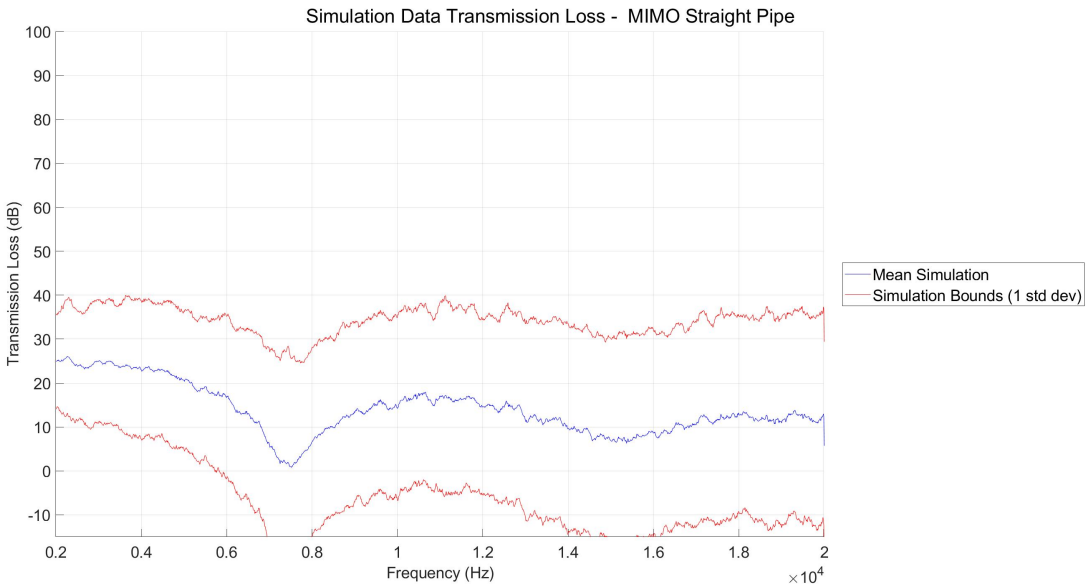

Figure 4-77 - MIMO - Straight Pipe - Simulation Results

Average Transmission Loss (dB)				
20 Hz - 5 kHz	5 kHz - 10 kHz	10 kHz - 15 kHz	15 kHz - 20 kHz	20 Hz - 20 kHz
23.5	11.7	13.4	10.6	10.6

Table 4-10 - MIMO - Straight Pipe - Simulation Data

4.3.2 Base Feature Acoustic Metamaterials

The BF AMM acoustic simulation model consisted of 21 domains. The domains consisted of the internal cavity as a Finite Fluid Component as well as 6 rows of RP, 6 AP for the first stage, 6 AP for the second stage, input, and output domains as IFCs.

Figure 4-78 shows the internal cavity solid model developed for the simulation. Figure 4-79 shows the MSC.PATRAN mesh model. Surface elements are shown in green and solid elements are shown in pink. Figure 4-80 shows the analysis tree for the ACTRAN model as well as the imported model. Figure 4-81 shows an isometric view of the IFC regions for the input and

output domains. Figure 4-82 shows an isometric view of the IFC regions for the input and output domains. Figure 4-83 shows an isometric view of the AP domain and Figure 4-84 shows an enlarged view.

The TL data is presented in Figure 4-85 and the corresponding tabular data is presented in Table 4-11. The data shows the TL increasing to a large peak at approximately 700 Hz, and then the TL slowly decreases across the remaining acoustic spectrum. The overall TL_{avg} has doubled from the previous configuration.

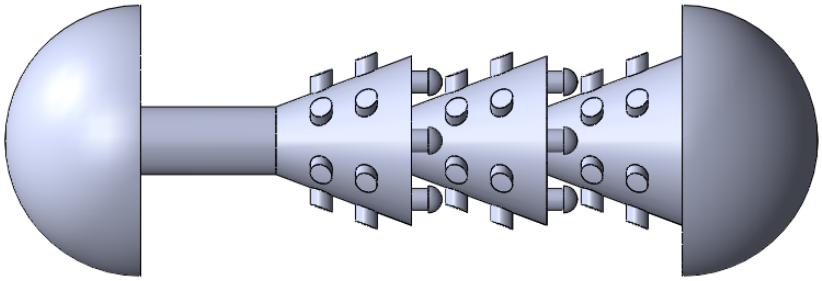

Figure 4-78 - MIMO - Base Feature AMM - Internal Cavity CAD

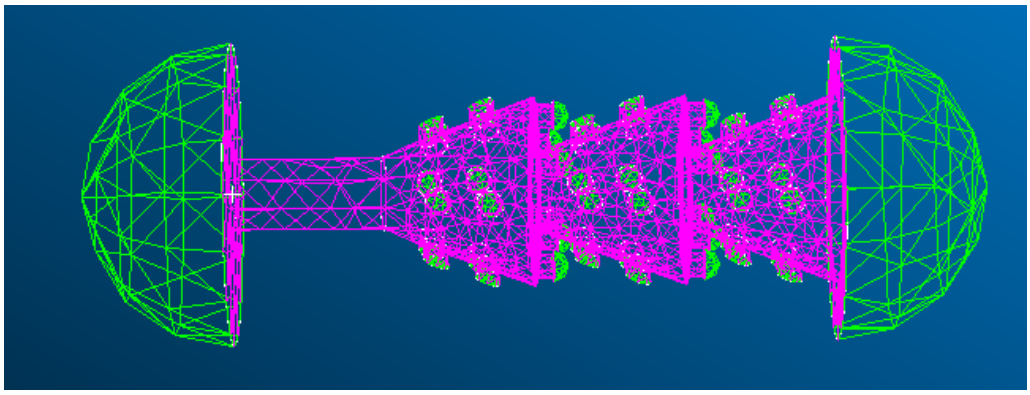

Figure 4-79 - MIMO - Base Feature AMM - Mesh

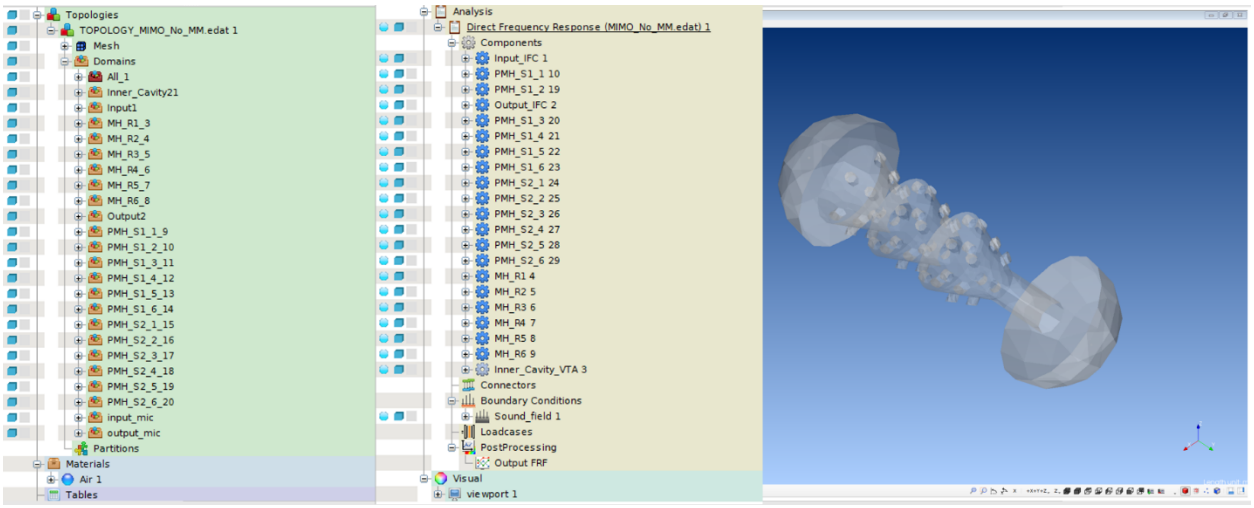

Figure 4-80 - MIMO - Base Feature AMM - ACTRAN Model Setup

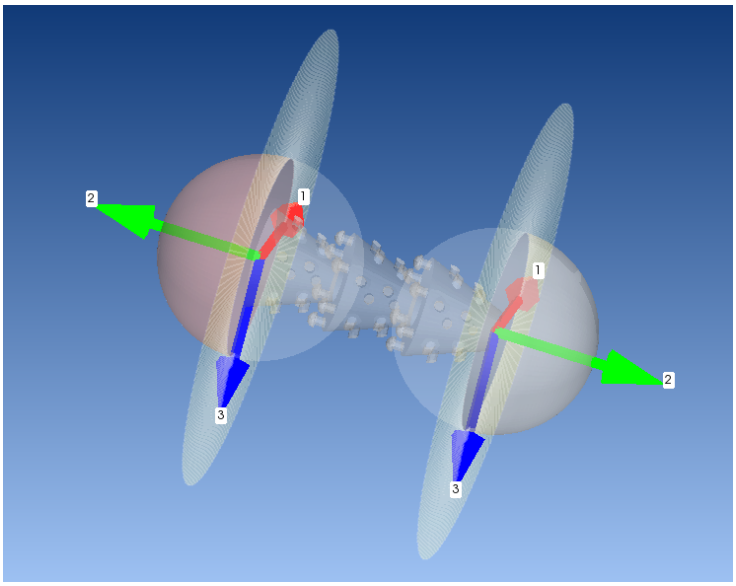

Figure 4-81 - MIMO - Base Feature AMM - IFC Side View

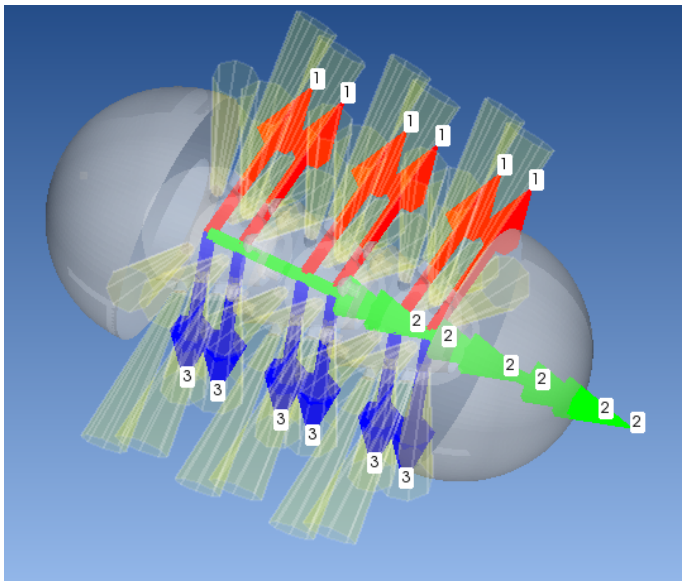

Figure 4-82 - MIMO - Base Feature AMM - IFC - Isometric View

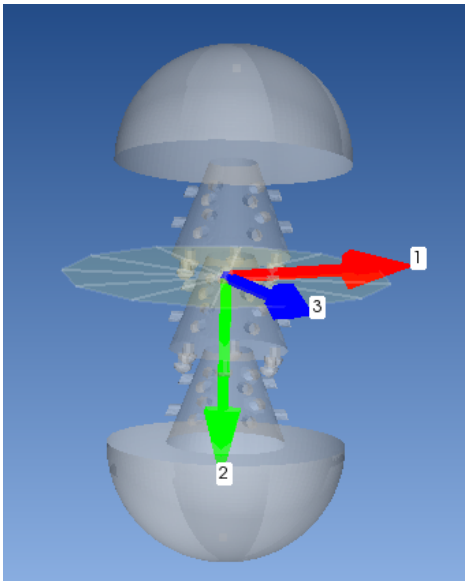

Figure 4-83 - MIMO - Base Feature Acoustic Metamaterials - Axial Perforations IFC - Forward View

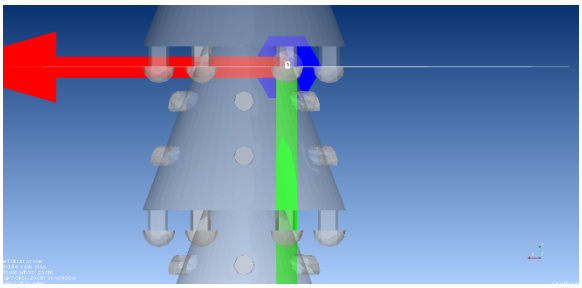

Figure 4-84 - MIMO - Base Feature Acoustic Metamaterials - Axial Perforations IFC - Enlarged View

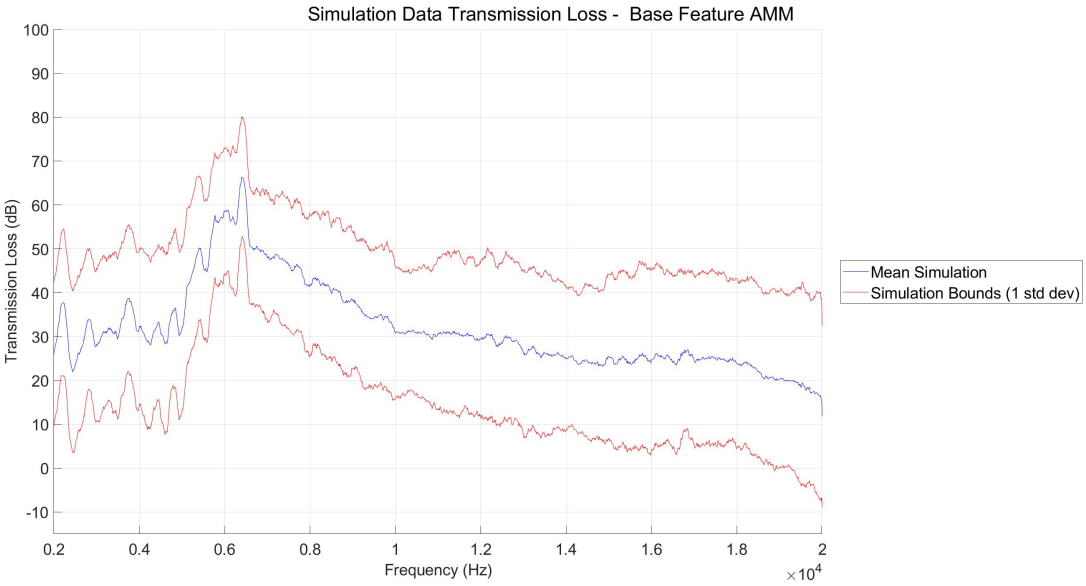

Figure 4-85 - MIMO - Base Feature AMM - Simulation Results

Average Transmission Loss (dB)				
20 Hz - 5 kHz	5 kHz - 10 kHz	10 kHz - 15 kHz	15 kHz - 20 kHz	20 Hz - 20 kHz
31.2	45.0	28.1	23.1	23.1

Table 4-11 - MIMO - Base Feature AMM - Simulation Data

4.3.3 Large Cavity Acoustic Metamaterials

The Large Cavity AMM acoustic simulation model consisted of 7 domains. The domains consisted of the internal cavity as a Finite Fluid Component as well as 4 rows of outer cell wall perforations, input, and output domains as IFCs.

Figure 4-86, Figure 4-87, and Figure 4-88 show the internal cavity solid model developed for the simulation in overall, vertical cross sectional, horizontal cross-sectional views. Figure 4-89 shows the MSC.PATRAN mesh model. Surface elements are shown in green and solid elements are shown in pink. Figure 4-90 shows the analysis tree for the ACTRAN model as well as the imported model. Figure 4-91 shows an isometric view of the IFC regions for the input and output domains as well as the IFC regions for the outer cell wall perforations. Figure 4-92 shows a top view of the outer cell wall perforations IFC region. Figure 4-93 shows an isometric view of the outer cell wall perforations IFC region.

The TL data is presented in Figure 4-94 and the corresponding tabular data is presented in Table 4-12. The data shows a wide peak at approximately 900 Hz followed by 2 large peaks at approximately 14 kHz and 17 kHz. The overall TL_{avg} has increased from previous configurations.

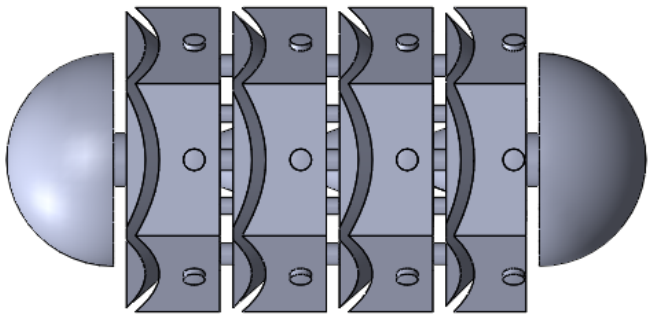

Figure 4-86 - MIMO - Large Cavity AMM - Internal Cavity CAD

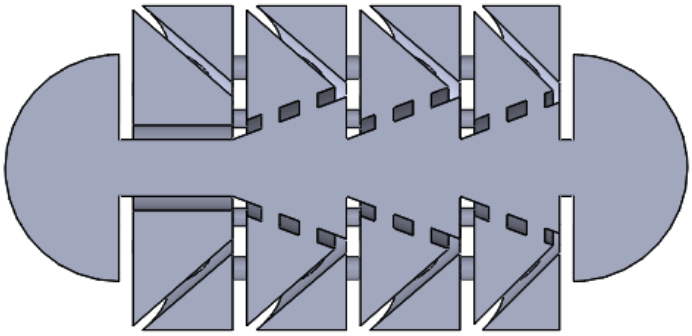

Figure 4-87 - MIMO - Large Cavity AMM - Internal Cavity CAD - Vertical Cross-Section View

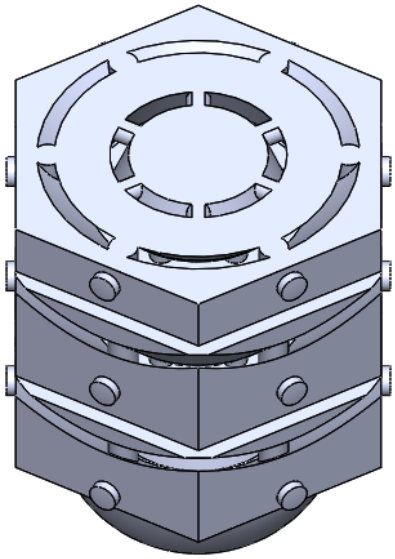

Figure 4-88 - MIMO - Large Cavity AMM - Internal Cavity CAD - Horizontal Cross-Section View

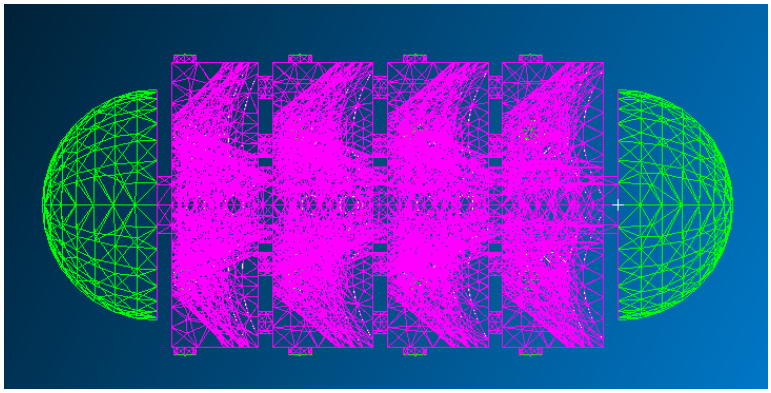

Figure 4-89 - MIMO - Large Cavity AMM - MSC.PATRAN Mesh

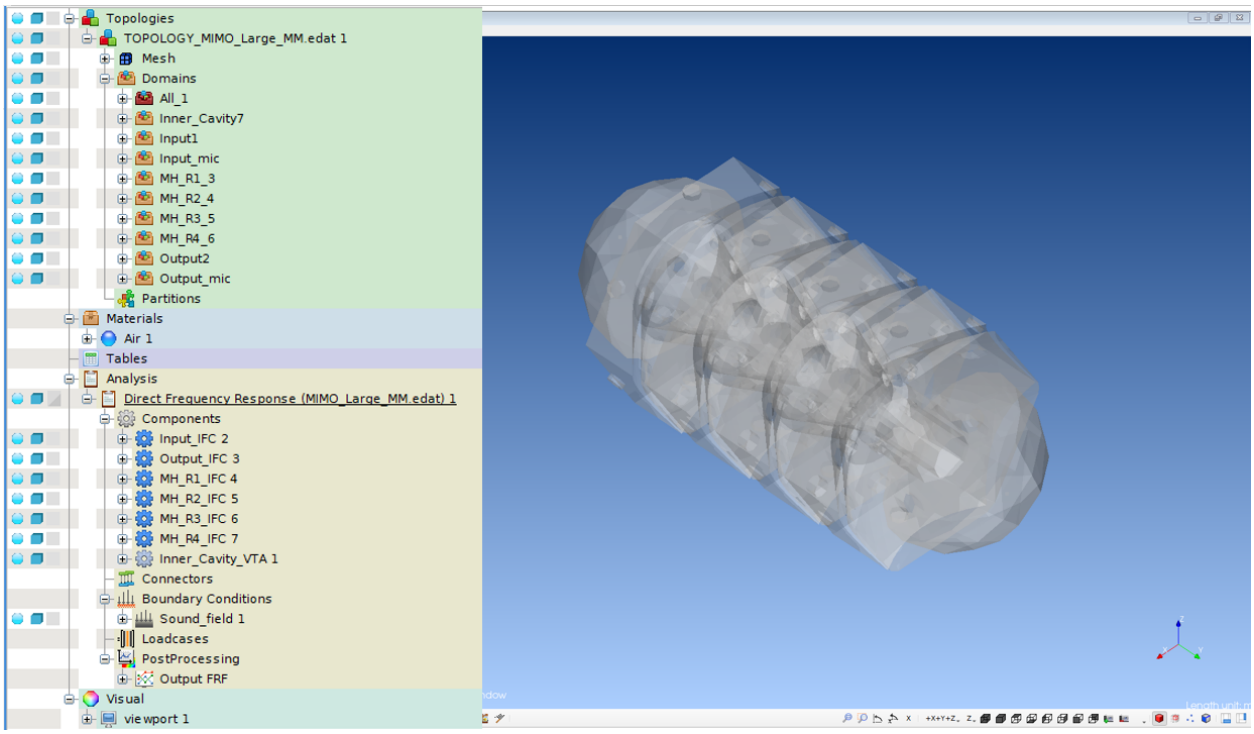

Figure 4-90 - MIMO - Large Cavity AMM - ACTRAN Model Setup

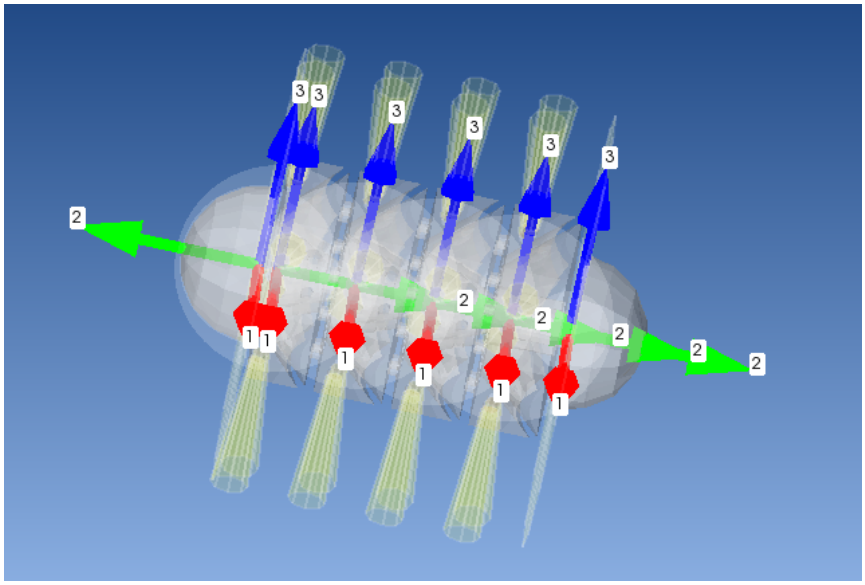

Figure 4-91 - MIMO - Large Cavity AMM - IFC Side View

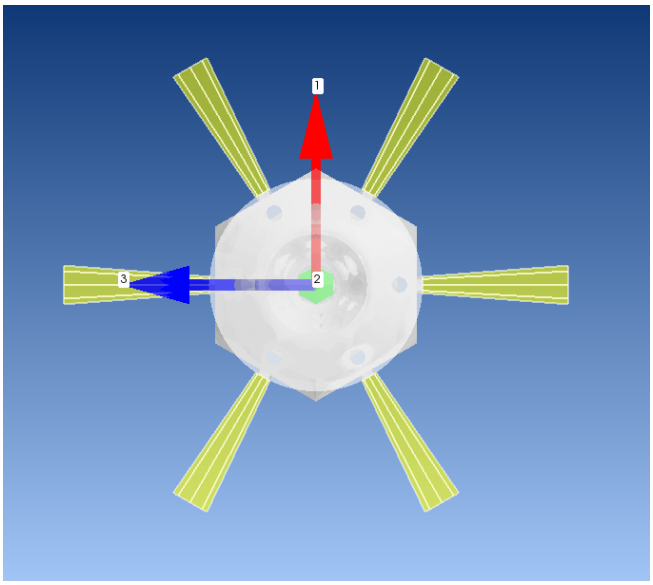

Figure 4-92 - MIMO - Large Cavity AMM - IFC Top View

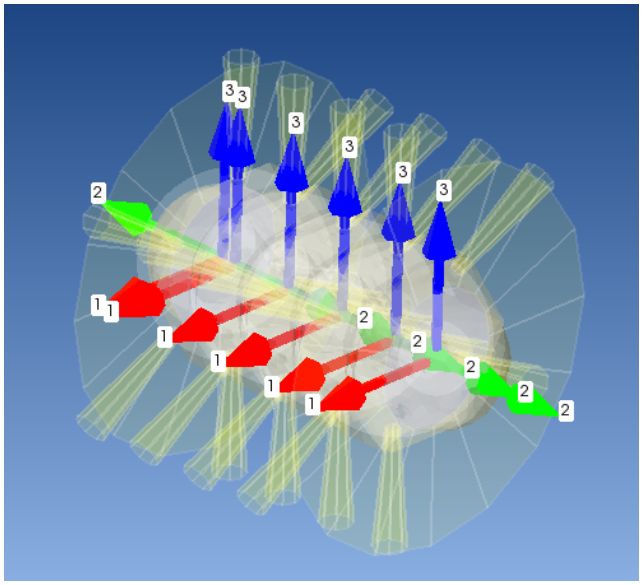

Figure 4-93 - MIMO - Large Cavity AMM - IFC Isometric View

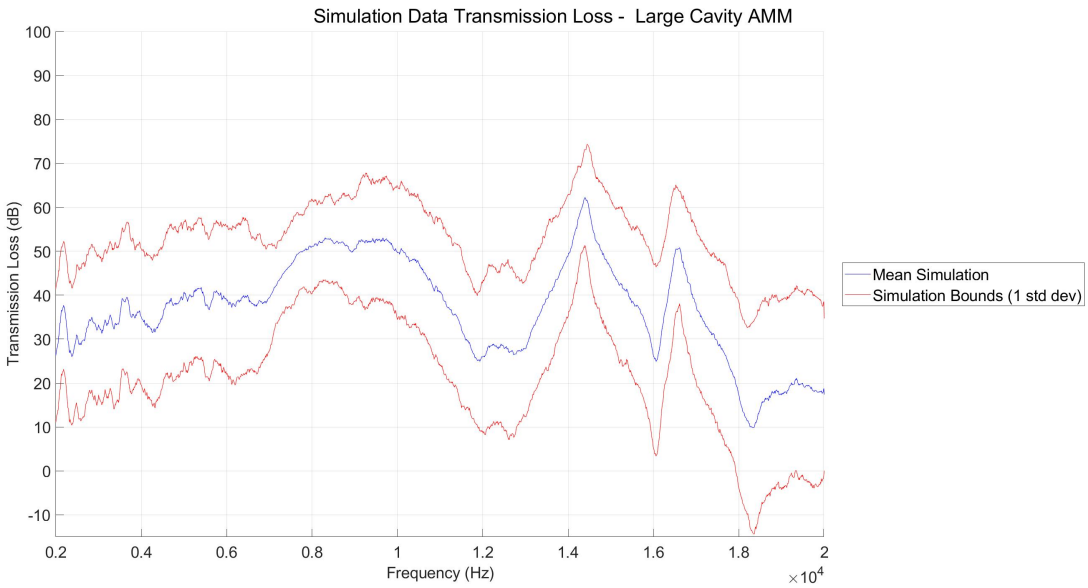

Figure 4-94 - MIMO - Large Cavity AMM - Simulation Results

Average Transmission Loss (dB)				
20 Hz - 5 kHz	5 kHz - 10 kHz	10 kHz - 15 kHz	15 kHz - 20 kHz	20 Hz - 20 kHz
34.8	45.7	39.8	28.1	28.1

Table 4-12 - MIMO - Large Cavity AMM - Simulation Data

4.3.4 Small Cavity Acoustic Metamaterials

The Small Cavity AMM acoustic simulation model consisted of 7 domains. The domains consisted of the internal cavity as a Finite Fluid Component as well as 4 rows of outer cell wall perforations, and input and output domains as IFCs.

Figure 4-95, Figure 4-96, and Figure 4-97 show the internal cavity solid model developed for the simulation in overall, vertical cross sectional, horizontal cross-sectional views, respectively. Figure 4-98 shows the MSC.PATRAN mesh model. Surface elements are shown in green and solid elements are shown in pink. Figure 4-99 shows the analysis tree for the ACTRAN

model as well as the imported model. Figure 4-100 shows an isometric view of the IFC regions for the input and output domains as well as the IFC regions for the outer cell wall perforations. Figure 4-101 shows a top view of the outer cell wall perforations IFC region. Figure 4-102 shows an isometric view of the outer cell wall perforations IFC regions.

The TL data is presented in Figure 4-103 and the corresponding tabular data is presented in Table 4-13. The data shows a wide peak at approximately 1 kHz followed by 2 large peaks at approximately 17 kHz and 19 kHz. The overall TL_{avg} has increased from previous configurations.

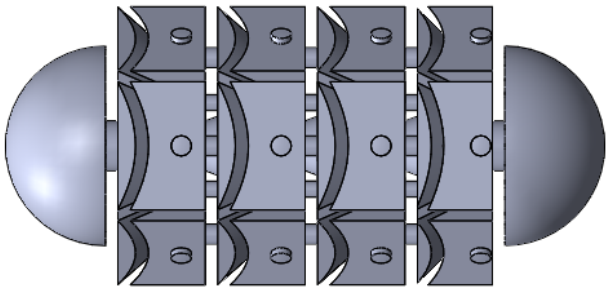

Figure 4-95 - MIMO - Small Cavity AMM - Internal Cavity CAD

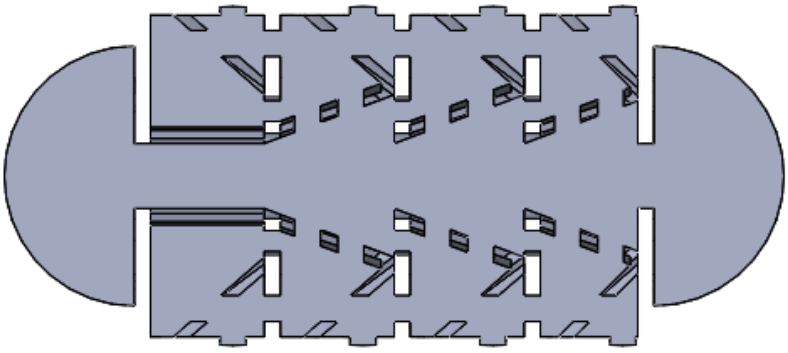

Figure 4-96 - MIMO - Small Cavity AMM - Internal Cavity CAD - Vertical Cross-Section View

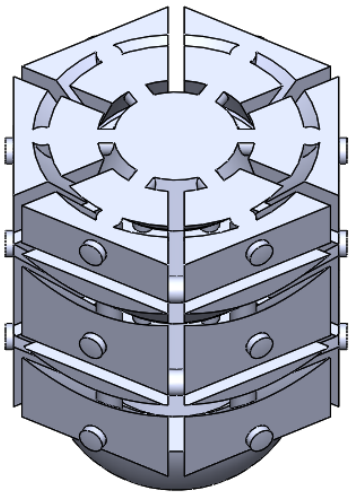

Figure 4-97 - MIMO - Small Cavity AMM - Internal Cavity CAD - Horizontal Cross-Section View

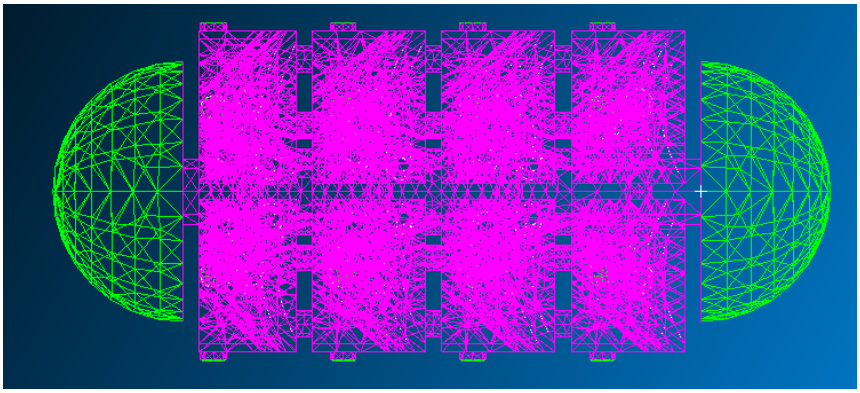

Figure 4-98 - MIMO - Small Cavity AMM - MSC.PATRAN Mesh

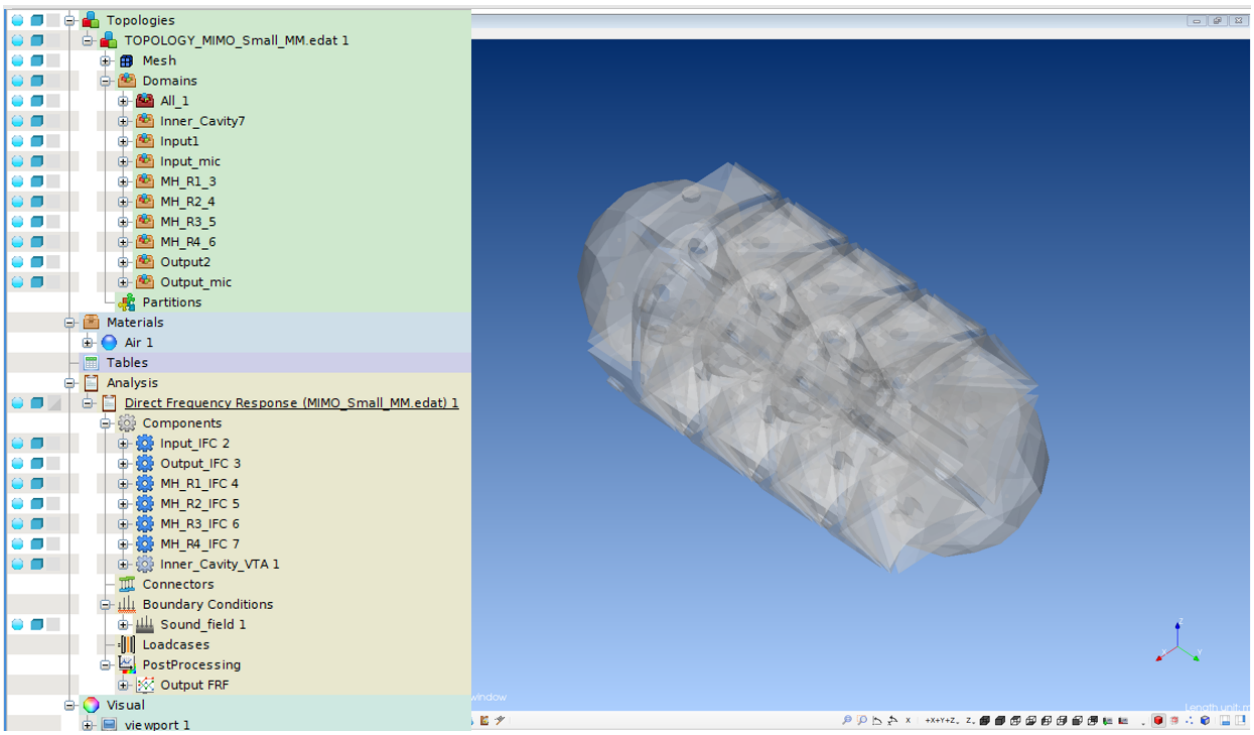

Figure 4-99 - MIMO - Small Cavity AMM - ACTRAN Model Setup

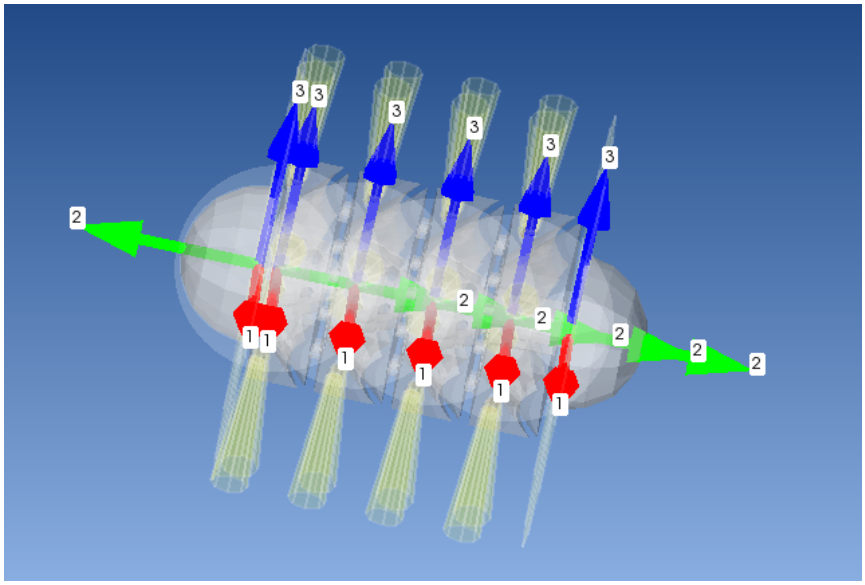

Figure 4-100 - MIMO - Small Cavity AMM - IFC - Side View

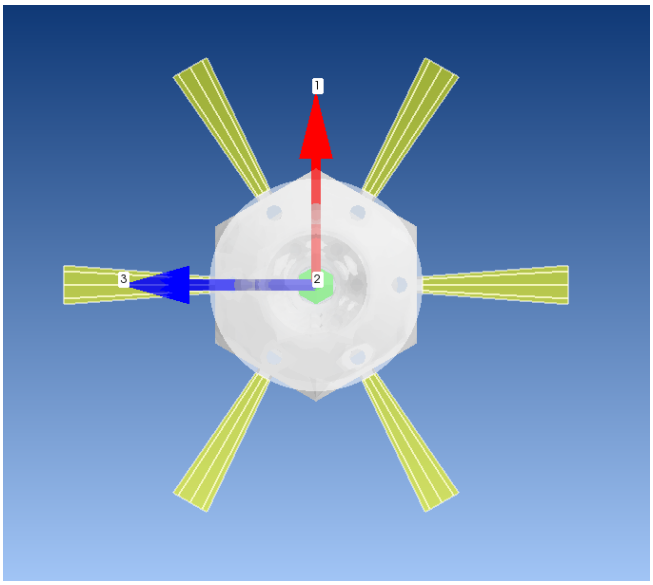

Figure 4-101 - MIMO - Small Cavity AMM - IFC - Top View

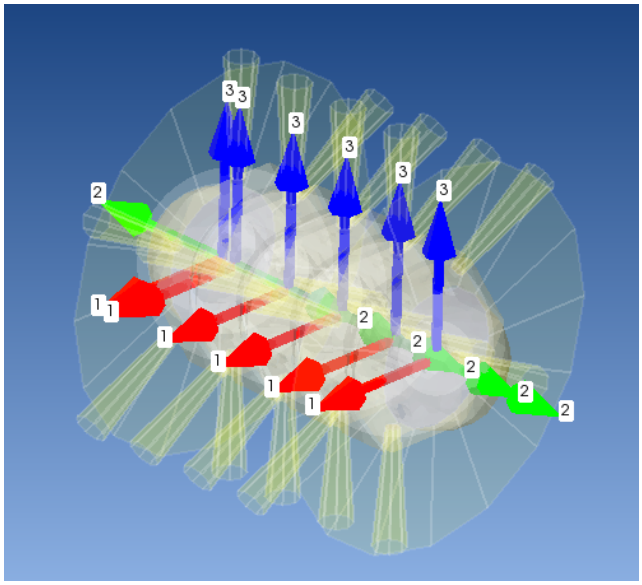

Figure 4-102 - MIMO - Small Cavity AMM - IFC - Isometric View

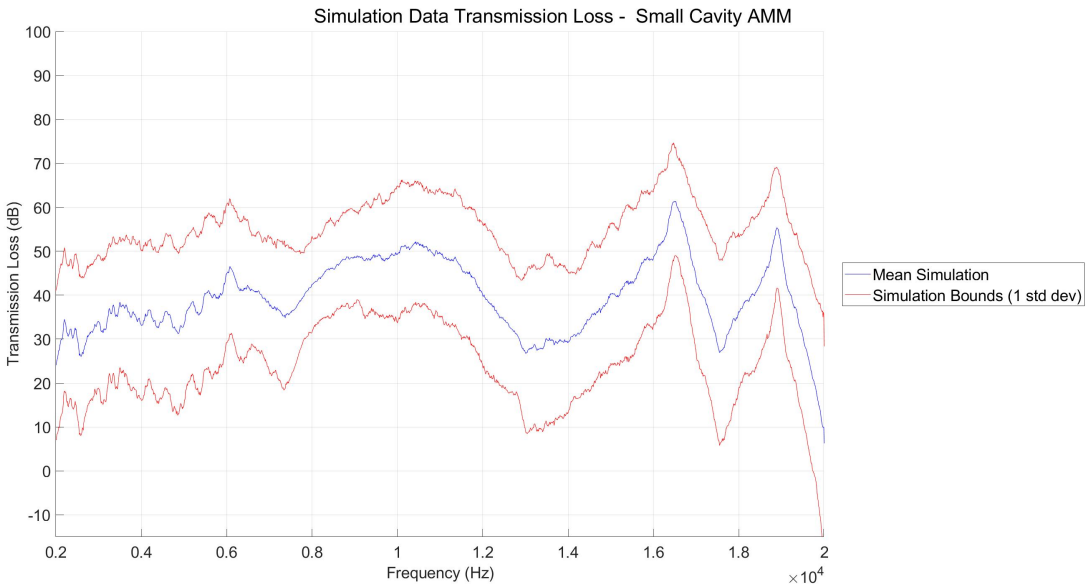

Figure 4-103 - MIMO - Small Cavity AMM - Simulation Results

Average Transmission Loss (dB)				
20 Hz - 5 kHz	5 kHz - 10 kHz	10 kHz - 15 kHz	15 kHz - 20 kHz	20 Hz - 20 kHz
34.0	42.6	38.8	41.2	41.2

Table 4-13 - MIMO - Small Cavity AMM - Simulation Data

4.4 Acoustic Simulation Summary

The MSC ACTRAN acoustic simulations were created in a way that allowed for characterization of the systems acoustic properties. The mesh size ensured model functionally throughout the entire acoustic spectrum. Within MSC ACTRAN, elements were categorized into domains that allowed the entire setup of the acoustic simulation to be specified. The specifications used on the IFC, Finite Fluid Components, and Virtual Instrumentation created a simulation model that replicated the physical setup used during experimental testing.

Within the small cavities of AMM, boundary layers provide significant energy losses. Consequently, the boundary layers must be properly incorporated into the system. The acoustic simulation models accounted for boundary layer conditions within the model using a comprehensive approach via the DBLNSF method.

The Diffused Sound Field allowed for characterization of the system. The use of randomly generated acoustic input noise from numerous directions allowed for system characterization without regards for variations in the physical setup that may be seen in experimental test or operational environments. The Number of Samples specification allowed the MUMPS solver to account for variations in the time domain as well as produce simulation statistics.

The resulting acoustic simulation data showed increasing values of TL as the system increased in complexity. Validation of the acoustic simulation results utilizing experimental testing results is discussed thoroughly in the subsequent chapter.

Chapter 5: Acoustic Simulation and Experimental Test Data Comparison

"Data will talk to you if you're willing to listen."

-Jim Bergeson [50]

A data comparison between the acoustic simulation data and the experimental test data was performed in order to validate the acoustic simulation results as well as determine the ability of the acoustic simulation to predict performance in operational settings. The data is compared using a plot of the TL for the experimental data, mean acoustic simulation data, and boundaries for 1 standard deviation of the acoustic simulation data. The results are shown in 5 bandwidths of the acoustic spectrum: 20 Hz to 5 kHz, 5 kHz to 10 kHz, 10 kHz to 15 kHz, 15 kHz to 20 kHz, and 20 Hz to 20 kHz. The comparison plots were generated with a MATLAB script, which is presented in Appendix A-9. The comparison plots presented have the experimental data shown in blue, the mean acoustic simulation data shown in green, and the boundaries for 1 standard deviation of the acoustic simulation shown in red.

The full comparison exercise of the experimental test data and the acoustic simulation data consisted of 9 SISO configurations and 4 MIMO configurations. The SISO configurations compared are the SP, SP with RP, CN, DN, DN with RP, SDN, SDN with RP, SDN with RAP, and SDN with RAP and COOP. The MIMO configurations compared are the SP, BF AMM, Large Cavity AMM, and the Small Cavity AMM.

Marginal deviations in the mean simulation data and the experimental test data were expected for a few reasons. Minor manufacturing tolerances and defects within the prototypes

were not included in the acoustic simulations. The acoustic simulations did not account for surface friction, surface roughness, structure deflection, and structural vibration. For the acoustic simulation, the structure walls were considered to be perfectly reflecting while the physical structure walls were not.

5.1 Single Input Single Output Systems Acoustic Simulation and Experimental Test Data Comparison

5.1.1 Straight Pipe

Comparison of the experimental testing data and the acoustic simulation data for the SP configuration is shown in Figure 5-1. The data shows good correlation across the acoustic spectrum. The simulation data captures the trends seen in the experimental data up to approximately 600 Hz. Above 600 Hz, the experimental data is lower than the mean simulation data, but the vast majority of the experimental data falls within a standard deviation of the mean simulation data. The tabular data is shown in Table 5-1. The TL_{avg} for the acoustic simulation data is much higher than the TL_{avg} for the experimental data.

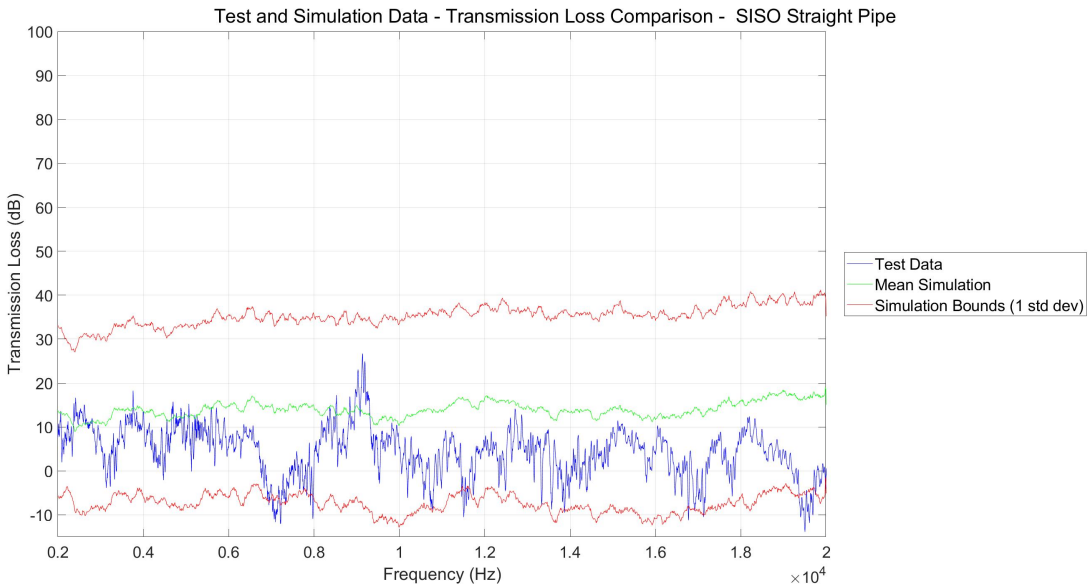

Figure 5-1 - SISO - Straight Pipe - Simulation and Testing Data Comparison

	Average Transmission Loss (dB)				
Configuration	20 Hz - 5 kHz	5 kHz - 10 kHz	10 kHz - 15 kHz	15 kHz - 20 kHz	20 Hz - 20 kHz
Test	8.5	5.8	2.5	2.6	2.6
Simulation	13.3	13.8	14.2	15.0	15.0

Table 5-1 - SISO - Straight Pipe - Simulation and Testing Data Comparison

5.1.2 Straight Pipe with Radial Perforations

The comparison of the experimental testing data and the acoustic simulation data for the SP with RP configuration is shown in Figure 5-2. The data shows good correlation across the acoustic spectrum. The simulation data captures the trends seen in the experimental data up to approximately 700 Hz. The experimental data is lower than the mean simulation data, but the vast majority of the experimental data falls within a standard deviation of the mean simulation

data. The tabular data is shown in Table 5-2. The TL_{avg} for the acoustic simulation data is much higher than the TL_{avg} for the experimental data. This phenomenon is discussed in section 5.3.

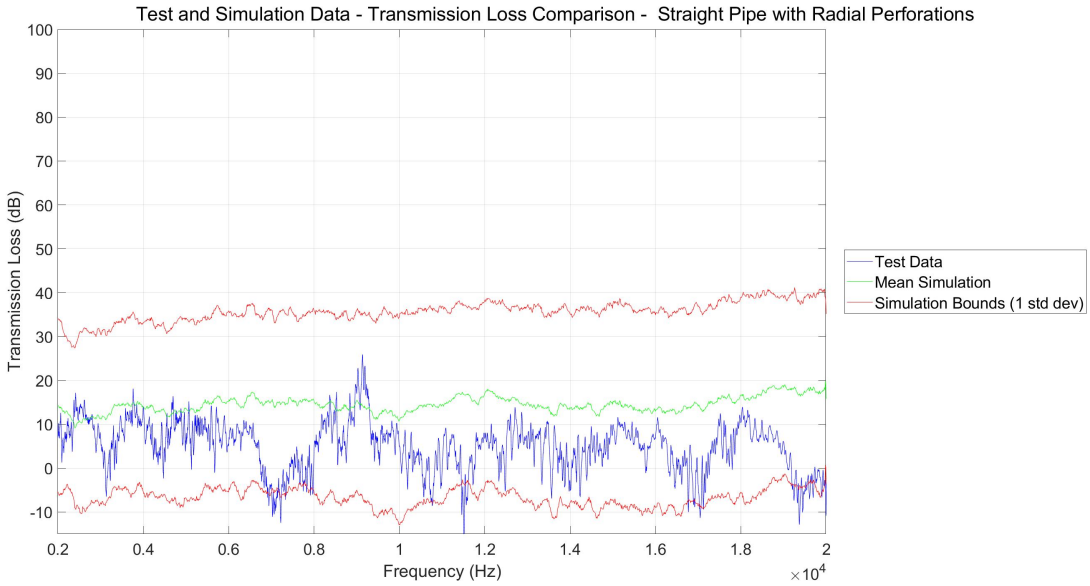

Figure 5-2 - SISO - Straight Pipe with Radial Perforations - Simulation and Testing Data Comparison

Average Transmission Loss (dB)					
Configuration	20 Hz - 5 kHz	5 kHz - 10 kHz	10 kHz - 15 kHz	15 kHz - 20 kHz	20 Hz - 20 kHz
Test	9.6	6.0	3.2	3.5	3.5
Simulation	13.8	14.4	14.6	15.5	15.5

Table 5-2 - SISO - Straight Pipe with Radial Perforations - Simulation and Testing Data Comparison

5.1.3 Converging Nozzle

Comparison of the experimental testing data and the acoustic simulation data for the CN configuration is shown in Figure 5-3. The data shows good correlation across the acoustic spectrum. The simulation data captures a dip in the data with a minimal phase shift at

approximately 900 Hz. The experimental data is lower than the mean simulation data, but the majority of the experimental data falls within a standard deviation of the mean simulation data. The tabular data is shown in Table 5-3. The TL_{avg} for the acoustic simulation data is much higher than the TL_{avg} for the experimental data. This phenomenon is discussed in section 5.3.

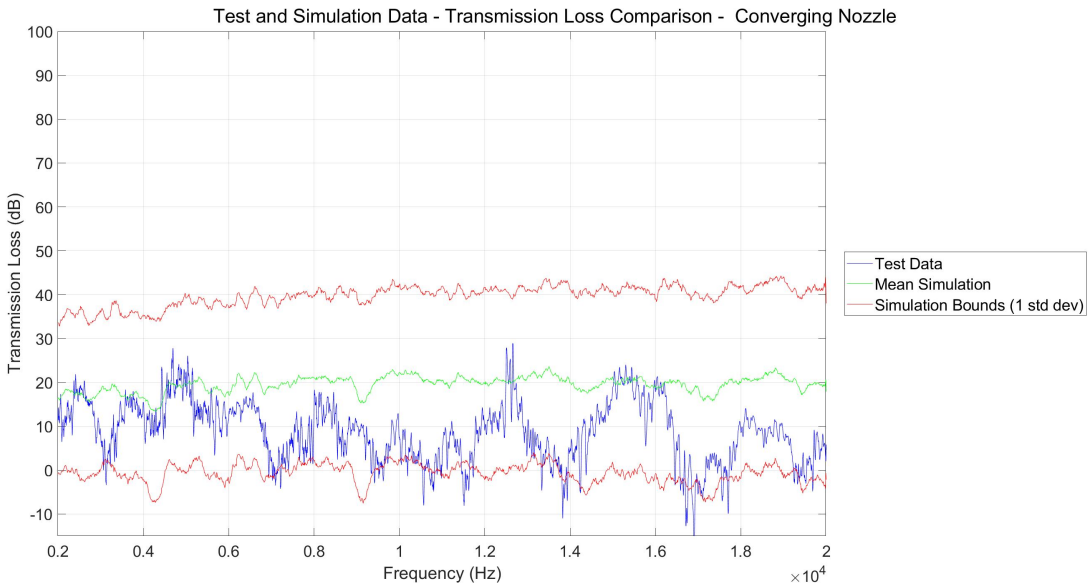

Figure 5-3 - SISO - Converging Nozzle - Simulation and Testing Data Comparison

	Average Transmission Loss (dB)				
Configuration	20 Hz - 5 kHz	5 kHz - 10 kHz	10 kHz - 15 kHz	15 kHz - 20 kHz	20 Hz - 20 kHz
Test	13.7	9.4	6.6	7.4	7.4
Simulation	18.3	19.8	20.5	19.7	19.7

Table 5-3 - SISO - Converging Nozzle - Simulation and Testing Data Comparison

5.1.4 Diverging Nozzle

Comparison of the experimental testing data and the acoustic simulation data for the DN configuration is shown in Figure 5-4. The data shows good correlation across the acoustic

spectrum. Furthermore, the acoustic simulation data exceptionally captures the trends seen in the experimental data up to approximately 700 Hz. The experimental data is lower than the mean simulation data, but the vast majority of the experimental data falls within a standard deviation of the mean simulation data. The tabular data is shown in Table 5-4. The TL_{avg} for the acoustic simulation data is higher than the TL_{avg} for the experimental data. The difference in the overall TL_{avg} between the experimental test data and the acoustic simulation data is much smaller than the previous configurations.

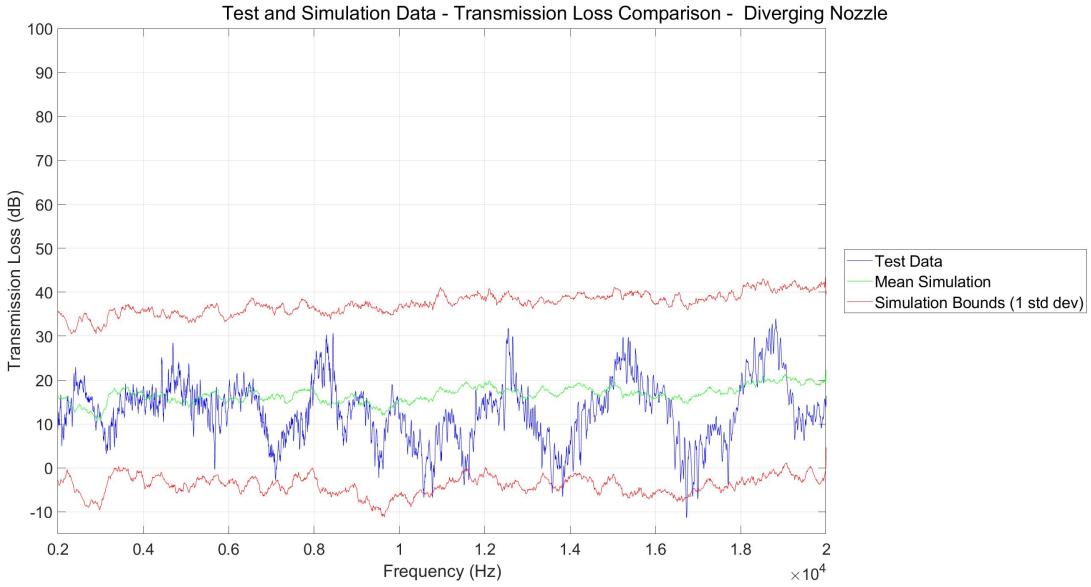

Figure 5-4 - SISO - Diverging Nozzle - Simulation and Testing Data Comparison

Average Transmission Loss (dB)					
Configuration	20 Hz - 5 kHz	5 kHz - 10 kHz	10 kHz - 15 kHz	15 kHz - 20 kHz	20 Hz - 20 kHz
Test	14.7	13.1	9.5	14.8	14.8
Simulation	17.3	15.7	17.3	18.0	18.0

Table 5-4 - SISO - Diverging Nozzle - Simulation and Testing Data Comparison

5.1.5 Diverging Nozzle with Radial Perforations

Comparison of the experimental testing data and the acoustic simulation data for the DN with RP configuration is shown in Figure 5-5. The data shows good correlation across the acoustic spectrum. Furthermore, the acoustic simulation data exceptionally captures the trends seen in the experimental test data up to approximately 700 Hz. The experimental data is lower than the mean simulation data, but the vast majority of the experimental data falls within a standard deviation of the mean simulation data. The tabular data is shown in Table 5-5. The TL_{avg} for the acoustic simulation data is higher than the TL_{avg} for the experimental data. This phenomenon is discussed in section 5.3.

Figure 5-5 - SISO - Diverging Nozzle with Radial Perforations - Simulation and Testing Data Comparison

Average Transmission Loss (dB)					
Configuration	20 Hz - 5 kHz	5 kHz - 10 kHz	10 kHz - 15 kHz	15 kHz - 20 kHz	20 Hz - 20 kHz
Test	15.6	15.1	11.4	16.5	16.5
Simulation	18.5	17.1	18.3	18.5	18.5

Table 5-5 - SISO - Diverging Nozzle with Radial Perforations - Simulation and Testing Data Comparison

5.1.6 Series of Diverging Nozzles

Comparison of the experimental testing data and the acoustic simulation data for the SDN configuration is shown in Figure 5-6. The data shows exceptional correlation across the acoustic spectrum. The simulation data captures multiple peaks and dips in the experimental test data across the acoustic spectrum with minimal phase shifts. The most prominent peaks and dips are seen at frequencies below 1 kHz, but these features are seen throughout the acoustic spectrum. The vast majority of the experimental data falls within a standard deviation of the mean simulation data. The tabular data is shown in Table 5-6. The TL_{avg} for the acoustic simulation data is higher than the TL_{avg} for the experimental data.

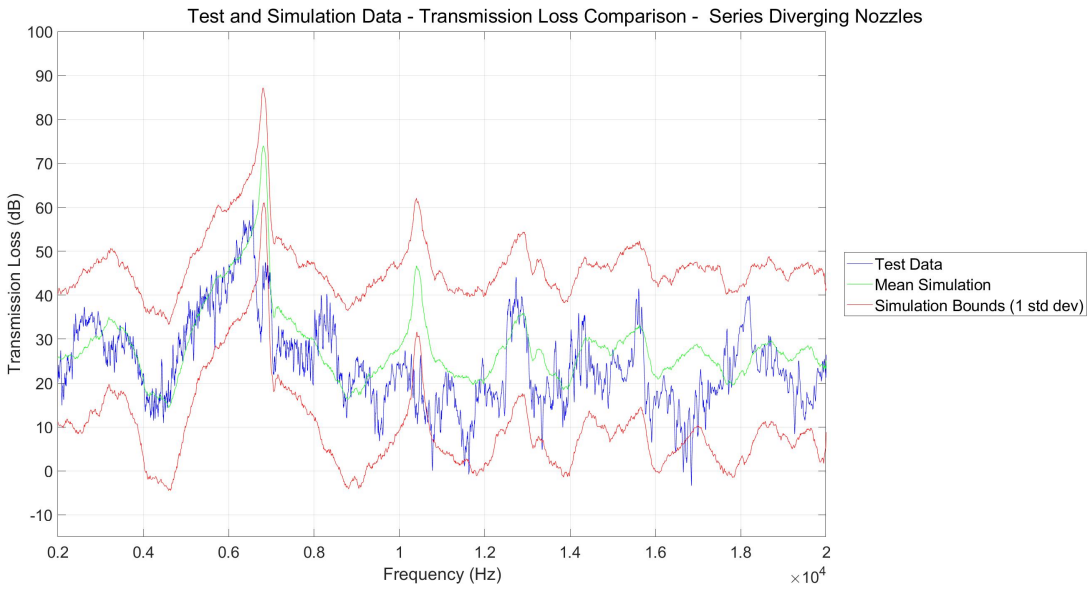

Figure 5-6 - SISO - Series of Diverging Nozzles - Simulation and Testing Data Comparison

	Average Transmission Loss (dB)				
Configuration	20 Hz - 5 kHz	5 kHz - 10 kHz	10 kHz - 15 kHz	15 kHz - 20 kHz	20 Hz - 20 kHz
Test	21.3	31.4	19.9	20.9	20.9
Simulation	24.2	34.3	26.9	26.1	26.1

Table 5-6 - SISO - Series of Diverging Nozzles - Simulation and Testing Data Comparison

5.1.7 Series of Diverging Nozzles with Radial Perforations

Comparison of the experimental testing data and the acoustic simulation data for the SDN with RP configuration is shown in Figure 5-7. The data shows exceptional correlation across the acoustic spectrum. The acoustic simulation data matches the trends seen in the experimental test data up to approximately 800 Hz. The remaining simulation data captures multiple peaks and dips in the experimental test data across the remaining acoustic spectrum with minimal phase shifts. The vast majority of the experimental data falls within a standard deviation of the

mean simulation data. The tabular data is shown in Table 5-7. The TL_{avg} for the acoustic simulation data is higher than the TL_{avg} for the experimental data.

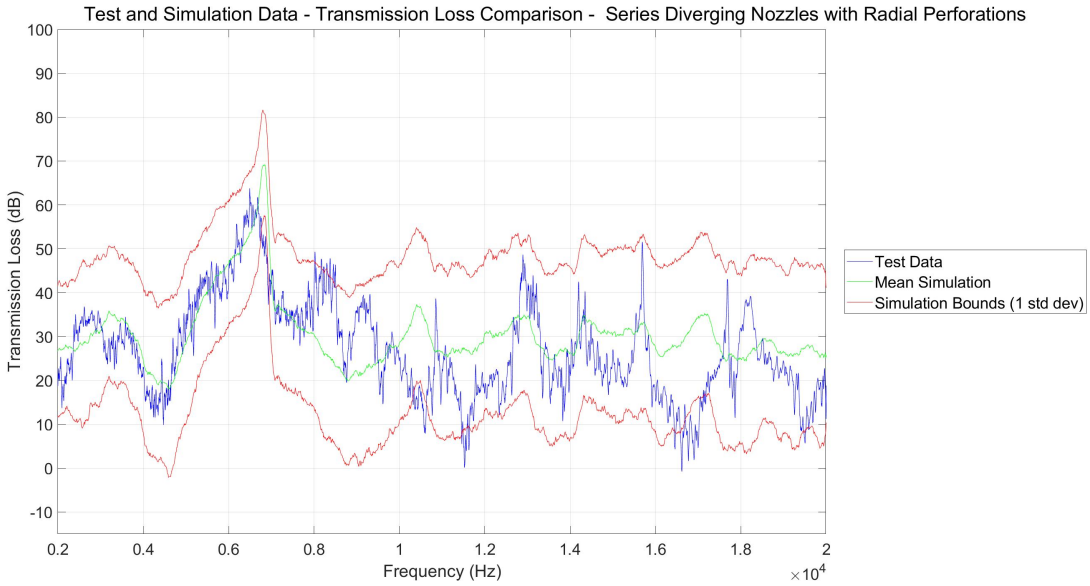

Figure 5-7 - SISO - Series of Diverging Nozzles with Radial Perforations - Simulation and Testing Data Comparison

	Average Transmission Loss (dB)				
Configuration	20 Hz - 5 kHz	5 kHz - 10 kHz	10 kHz - 15 kHz	15 kHz - 20 kHz	20 Hz - 20 kHz
Test	23.1	38.5	22.9	20.7	20.7
Simulation	27.2	35.3	29.8	28.5	28.5

Table 5-7 - SISO - Series of Diverging Nozzles with Radial Perforations - Simulation and Testing Data Comparison

5.1.8 Series of Diverging Nozzles with Radial and Axial Perforations

Comparison of the experimental testing data and the acoustic simulation data for the SDN with RAP configuration is shown in Figure 5-8. The acoustic simulation data exceptionally captures multiple peaks and dips in the experimental test data across the acoustic spectrum with

negligible phase shifts. The vast majority of the experimental data falls within a standard deviation of the mean simulation data. The tabular data is shown in Table 5-8. The TL_{avg} for the acoustic simulation data is comparable with the experimental test data across the spectrum. This phenomenon is discussed in section 5.3.

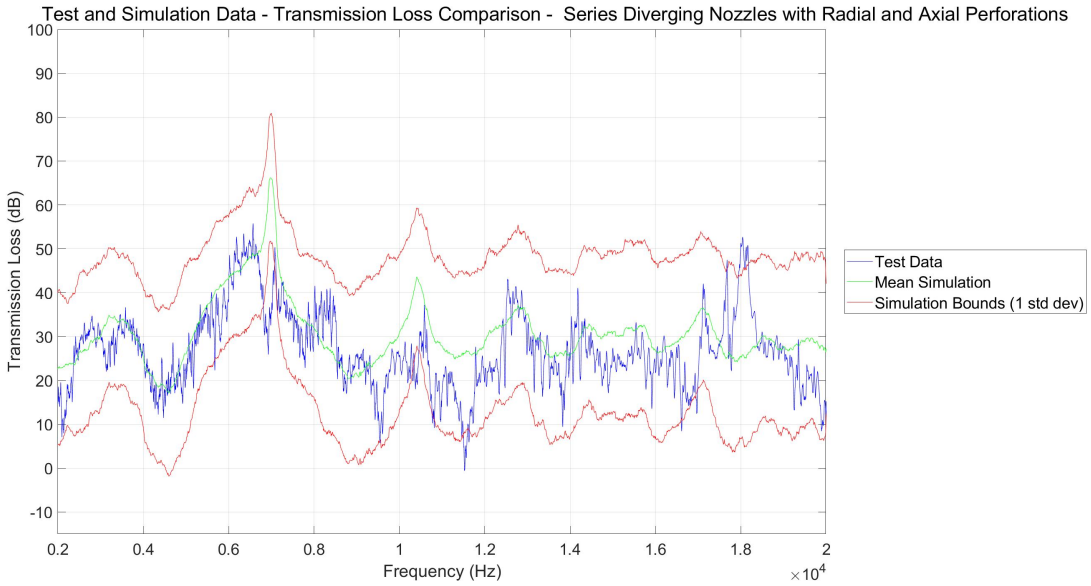

Figure 5-8 - SISO - Series of Diverging Nozzles with Radial and Axial Perforations - Simulation and Testing Data Comparison

Average Transmission Loss (dB)					
Configuration	20 Hz - 5 kHz	5 kHz - 10 kHz	10 kHz - 15 kHz	15 kHz - 20 kHz	20 Hz - 20 kHz
Test	25.4	32.1	23.8	26.1	26.1
Simulation	27.7	35.2	30.5	29.2	29.2

Table 5-8 - SISO - Series of Diverging Nozzles with Radial and Axial Perforations - Simulation and Testing Data Comparison

5.1.9 Series of Diverging Nozzles with Perforations and Axial Perforations and a Constricted Opening at the Output Plane

Comparison of the experimental testing data and the acoustic simulation data for the SDN with RP and a COOP configuration is shown in Figure 5-9. The data shows good correlation across the acoustic spectrum. The acoustic simulation data captures multiple peaks and dips in the experimental test data across the remaining acoustic spectrum with negligible phase shifts. The vast majority of the experimental data falls within a standard deviation of the mean simulation data. The tabular data is shown in Table 5-9.

The TL_{avg} for the simulation data is comparable with the experimental test data across the spectrum. In the 10 kHz to 15 kHz range, the simulation data TL_{avg} is higher than the experimental results as detailed in Table 5-9. However, the simulation data does capture the trends seen in the experimental data. The difference in the overall TL_{avg} between the experimental test data and the acoustic simulation data is much smaller than the previous configurations.

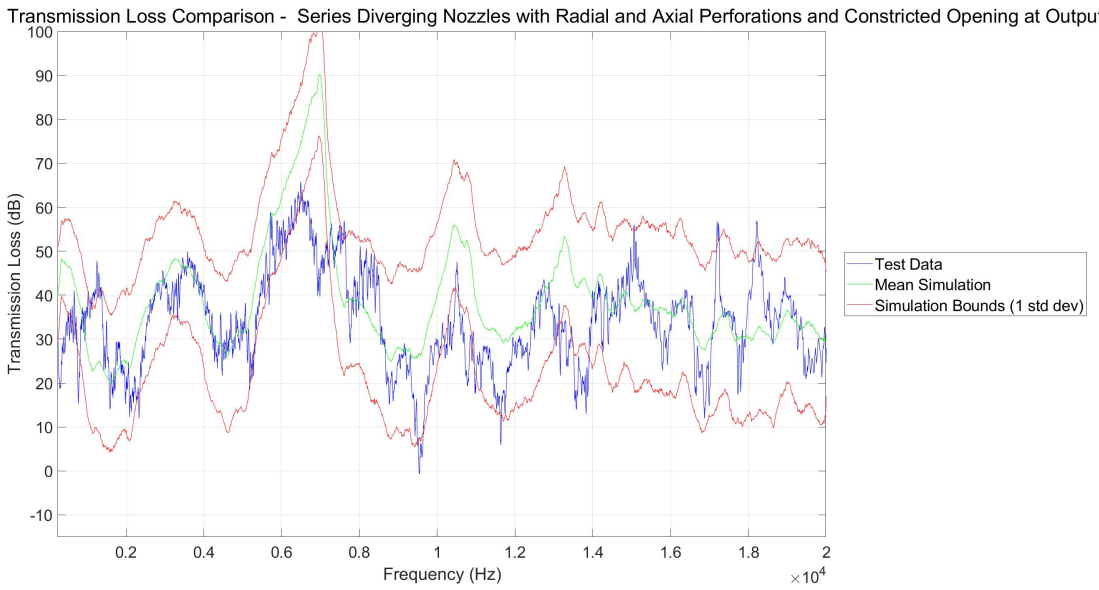

Figure 5-9 - SISO - Series of Diverging Nozzles with Radial and Axial Perforations and Constricted Opening at the Output - Simulation and Testing Data Comparison

Average Transmission Loss (dB)					
Configuration	20 Hz - 5 kHz	5 kHz - 10 kHz	10 kHz - 15 kHz	15 kHz - 20 kHz	20 Hz - 20 kHz
Test	31.9	39.2	30.3	34.3	34.3
Simulation	35.1	46.9	40.7	33.5	33.5

Table 5-9 - SISO - Series of Diverging Nozzles with Radial and Axial Perforations and Constricted Opening at the Output - Simulation and Testing Data Comparison

5.2 Multiple Input Multiple Output Systems Acoustic Simulation and Experimental Test Data Comparison

5.2.1 Straight Pipe

Comparison of the experimental testing data and the acoustic simulation data for the MIMO SP configuration is shown in Figure 5-10. The data shows exceptional correlation across the acoustic spectrum. The acoustic simulation data captures the trends seen in the

experimental data. All of the experimental data falls within a standard deviation of the mean simulation data. The tabular data is shown in Table 5-10. The TL_{avg} for the acoustic simulation data is lower than the TL_{avg} for the experimental data.

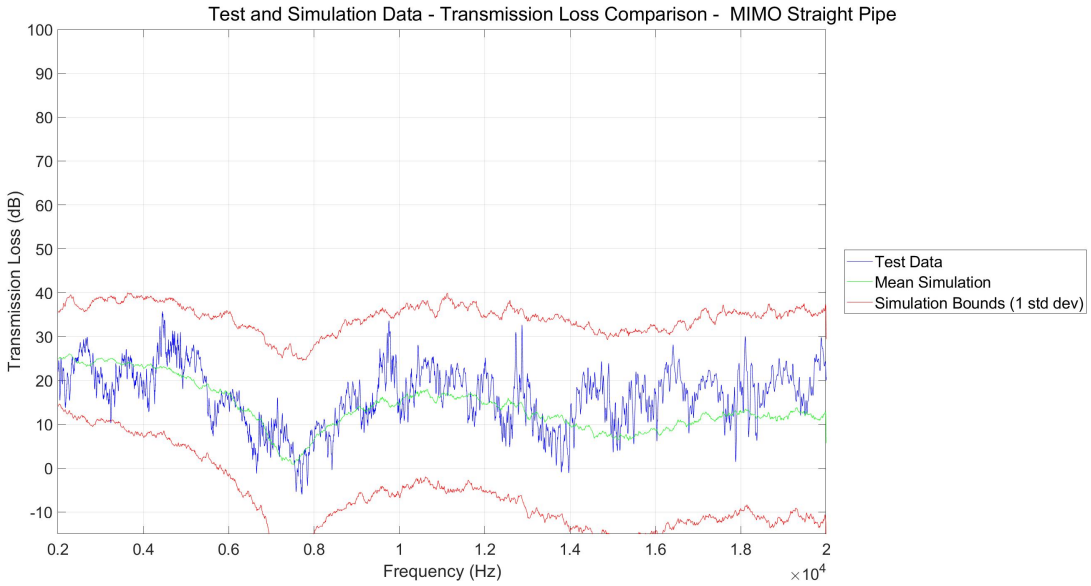

Figure 5-10 - MIMO - Straight Pipe - Simulation and Testing Data Comparison

	Average Transmission Loss (dB)				
Configuration	20 Hz - 5 kHz	5 kHz - 10 kHz	10 kHz - 15 kHz	15 kHz - 20 kHz	20 Hz - 20 kHz
Test	19.8	12.6	15.7	17.5	17.5
Simulation	23.5	11.7	13.4	10.6	10.6

Table 5-10 - MIMO - Straight Pipe - Simulation and Testing Data Comparison

5.2.2 Base Feature Acoustic Metamaterials

Comparison of the experimental testing data and the acoustic simulation data for the BF AMM configuration is shown in Figure 5-11. The data shows marginal correlation across the acoustic spectrum. The acoustic simulation data matches the majority of the trends seen in the

experimental data up to approximately 600 Hz. The majority of the remaining acoustic simulation data is higher than the experimental data, but the vast majority of the experimental data falls within a standard deviation of the mean simulation data. Between approximately 700 Hz and 900 Hz, the acoustic simulation data is higher than the experimental data. The tabular data is shown in Table 5-11. The TL_{avg} for the acoustic simulation data is lower than the TL_{avg} for the experimental data. This phenomenon is discussed in section 5.3.

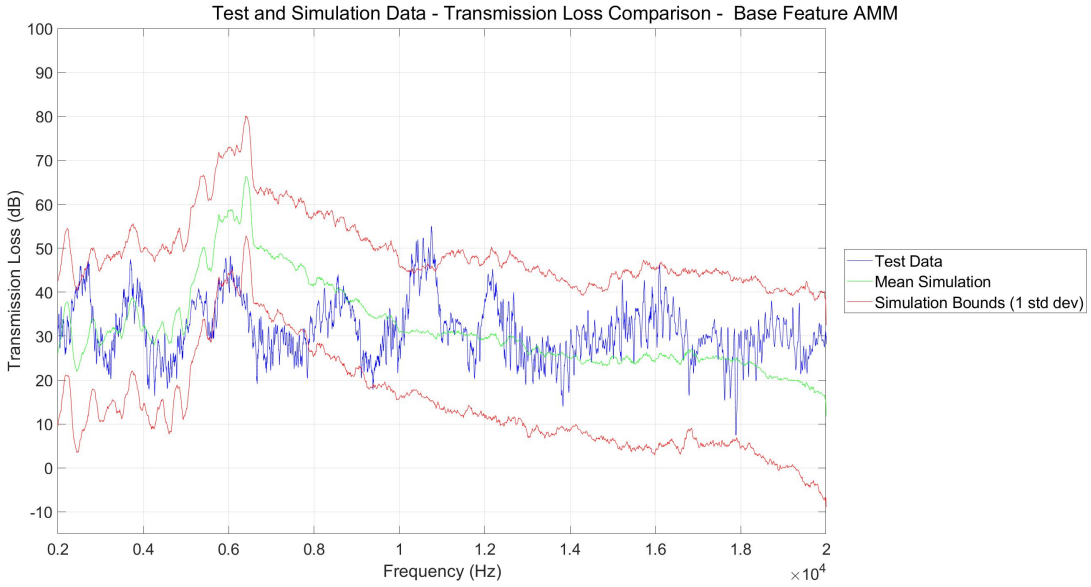

Figure 5-11 - MIMO - Base Feature AMM - Simulation and Testing Data Comparison

	Average Transmission Loss (dB)				
Configuration	20 Hz - 5 kHz	5 kHz - 10 kHz	10 kHz - 15 kHz	15 kHz - 20 kHz	20 Hz - 20 kHz
Test	27.1	32.5	31.8	29.9	29.9
Simulation	31.2	45.0	28.1	23.1	23.1

Table 5-11 - MIMO - Base Feature AMM - Simulation and Testing Data Comparison

5.2.3 Large Cavity Acoustic Metamaterials

Comparison of the experimental testing data and the acoustic simulation data for the Large Cavity AMM configuration is shown in Figure 5-12. The data shows good correlation across the acoustic spectrum. The majority of the experimental data falls within a standard deviation of the mean simulation data. The tabular data is shown in Table 5-12. The TL_{avg} for the acoustic simulation data is lower than the TL_{avg} for the experimental data. This phenomenon is discussed in section 5.3.

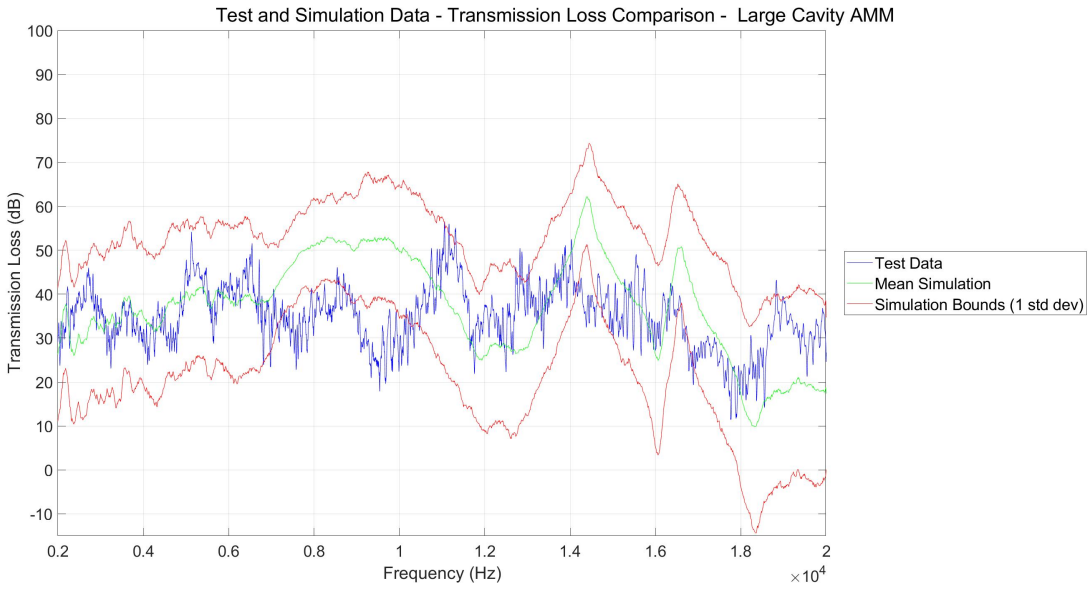

Figure 5-12 - MIMO - Large Cavity AMM - Simulation and Testing Data Comparison

Average Transmission Loss (dB)					
Configuration	20 Hz - 5 kHz	5 kHz - 10 kHz	10 kHz - 15 kHz	15 kHz - 20 kHz	20 Hz - 20 kHz
Test	28.0	36.2	38.6	30.4	30.4
Simulation	34.8	45.7	39.8	28.1	28.1

Table 5-12 - MIMO - Large Cavity AMM - Simulation and Testing Data Comparison

5.2.4 Small Cavity Acoustic Metamaterials

Comparison of the experimental testing data and the acoustic simulation data for the Small Cavity AMM configuration is shown in Figure 5-13. The data shows exceptional correlation across the acoustic spectrum. The acoustic simulation data captures multiple peaks and dips in the experimental data across the acoustic spectrum with minimal phase shifts. The majority of the experimental data falls within a standard deviation of the mean simulation data. The tabular data is shown in Table 5-13. The TL_{avg} for the acoustic simulation data is comparable to the experimental data across the spectrum. The difference in the overall TL_{avg} between the experimental test data and the acoustic simulation data is much smaller than seen in all of the previous configurations.

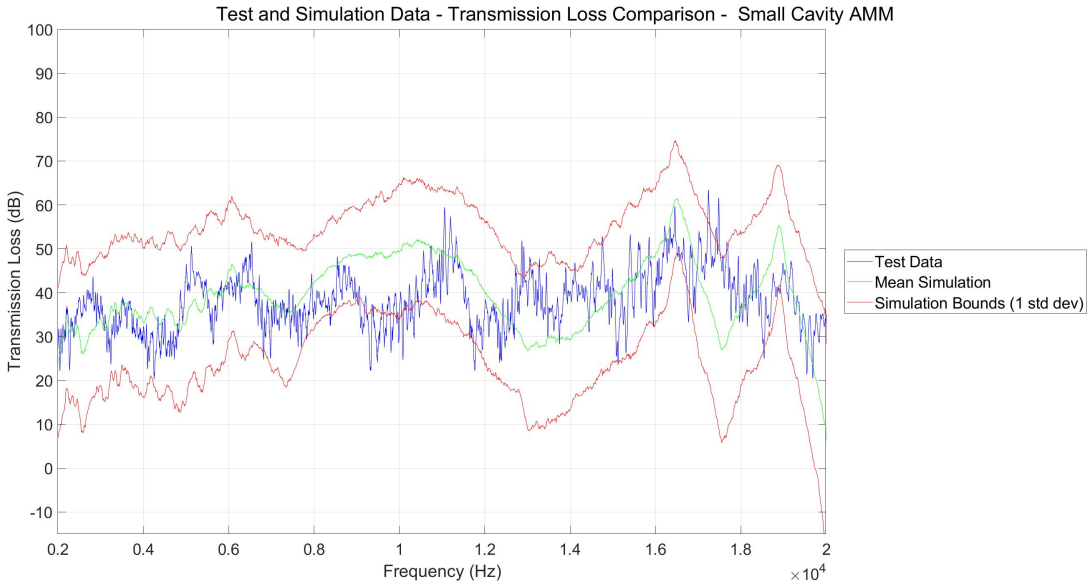

Figure 5-13 - MIMO - Small Cavity AMM - Simulation and Testing Data Comparison

Average Transmission Loss (dB)					
Configuration	20 Hz - 5 kHz	5 kHz - 10 kHz	10 kHz - 15 kHz	15 kHz - 20 kHz	20 Hz - 20 kHz
Test	27.1	37.8	39.1	41.5	41.5
Simulation	34.0	42.6	38.8	41.2	41.2

Table 5-13 - MIMO - Small Cavity AMM - Simulation and Testing Data Comparison

5.3 Acoustic Simulation and Experimental Test Data Comparison Summary

All of the acoustic simulations correlated reasonably well with the experimental test data, with some of the configurations having exceptional correlation. Overall, the acoustic simulations are a good representation of the experimental data. Within the SISO configurations, the values of the acoustic simulations overall TL_{avg} were higher than seen in the experimental results, while the opposite was seen in the MIMO configurations. This could be attributed to the factors detailed in the introduction for this chapter. Additionally, a large contributing factor is the way the simulation models the boundary layer. Acoustic boundary layers are small, ranging from 0.1 mm to 1 mm in size. [51] This small size partially explains why most acoustic equations neglect viscous and thermal effects. In a larger structure, like the SISO prototypes, the boundary layer would not have a large impact in the simulation results. Within a smaller structure, such as the MIMO configurations, the boundary layer would have a larger effect on the acoustic simulation results. Every acoustic simulation model captured the majority or all of the experimental test data within 1 standard deviation of the mean acoustic simulation data. Consequently, the acoustic simulations are a viable representation of the experimental test data and could be used to predict performance in operational environments.

Chapter 6: Conclusions

"Alright, let's get this thing wrapped up"

-George T. Flowers [52]

In this dissertation, the process of designing, testing, and simulating a complex system of AMM has been thoroughly discussed. Chapter 1 discussed the significance of the research and the acoustic principles used within this dissertation. Chapter 2 described the design process and the resulting designs in detail. Chapter 3 described the experimental testing process and accompanying results. Chapter 4 outlined the theory and setup of the acoustic simulation models and associated results. Chapter 5 made direct comparisons with the experimental testing results to the acoustic simulation results.

SISO experimental testing determined the fundamental design for the BF AMM. The BF AMM configuration was a 4-stage cell with an enclosed SDN with RAP and a COOP. The stage length of the cell was a quarter of an inch long; meaning, the overall thickness of the system was 1 inch. From the control configuration to the BF AMM configuration, the average transmission loss (TL_{avg}) across the acoustic spectrum went from 4.8 dB to 33.7 dB. Additionally, the BF performed well in the 2 kHz to 20 kHz range, with the TL_{avg} over 35 dB. These experimental results for the BF AMM formed the basis for the MIMO testing.

MIMO experimental testing determined the Small Cavity AMM to be the best performer. From the SP control panel to the Small Cavity AMM panel, the TL_{avg} increased from 16.4 dB to 33.8 dB across the acoustic spectrum. The Small Cavity AMM performed exceptionally in the 2

kHz to 20 kHz range, with the TL_{avg} equaling approximately 40 dB. These results formed the basis for the AMM Sphere testing.

The final stage of testing focused on an AMM Sphere. The Small Cavity AMM cell was modified to be curved for incorporation into a sphere. The AMM Sphere testing was performed at various distances as well as between multiple sound sources. The AMM Sphere test results were comparable in all the experimental test configurations with a TL_{avg} equaling approximately 28 dB. The AMM Sphere performed exceptionally well in the 2 kHz to 20 kHz. The system performance when subjected to multiple sound sources was not affected.

Overall, the acoustic simulations correlated reasonably well with the experimental data. The acoustic simulations encapsulated the majority or all of the experimental data within 1 standard deviation. The comparison of the experimental test data and the acoustic simulation data validated the acoustic simulation models and demonstrated the capability of the acoustic simulations to predict performance in operational environments.

The overall goals of this research were to design a passive, configurable, compact, and omnidirectional packaging that isolated MEMS devices from damaging high frequency acoustic environments by utilizing AMM. Additionally, the design was required to be operational in the 10 kHz to 20 kHz acoustic bandwidth. These goals have been met or exceeded. The system is both passive and configurable. The configurability of the design was based on a stage consisting of a perforated nozzle and AMM cavities. This stage was repeated in both series and in parallel allowing the design to vary in size. Four stages having an overall thickness of 1 inch validates the

requirement to have a compact footprint. The AMM Sphere tested in multiple configurations demonstrates the omnidirectionally of the system.

The requirement of the system to be operational in the 10 kHz to the 20 kHz acoustic bandwidth has been exceeded. Experimental testing in both the MIMO and AMM Sphere configurations showed the system to be operational from 2 kHz to 20 kHz. Additionally, the system performance when subjected to multiple sound sources was not adversely affected.

Outside the overall goals of the research, several supplementary features were implemented. The system is air permeable, therefore, adverse conditions such as stored heat, or the blockage of airflow are not introduced to the system. All of the configurations were tested in the CN and DN configurations with similar results. This is indicative of the structure having the ability to keep sound in as well as out.

This research has produced several contributions to the field of AMM. First, the development of a system, which successfully operates in three-quarters of the acoustic bandwidth, with special regards to the high frequency range, is innovative. Current AMM literature, as discussed in section 1.2, tends to operate in the lower half of the acoustic bandwidth. Additionally, current literature operates in narrow bandwidths while this research is extremely broadband. This project further adds improvement to the field of AMM by working omnidirectionally and with multiple sound sources. Finally, the configurability of the system to work with any MEMS device of any size creates countless opportunities for practical applications.

This work has merited 2 patent applications. The first, entitled “Metamaterial Design with Perforated Nozzles for Acoustic Noise Reduction,” is concerned with the concept of perforated

nozzles surrounded by AMM in the form of interconnected cavities. The second patent, entitled "Additive Manufacturing Acoustic Infill Metamaterial with Perforated Nozzles for Acoustic Noise Reduction," is concerned with the concept of perforated nozzles surrounded by additive manufacturing infill. While the Small Cavity AMM had a better overall performance, the difference in performance between the Infill AMM and Small Cavity AMM was marginal. However, the Infill Metamaterials were substantially easier to manufacture.

6.1 Future Work

Future work should focus on three main topics. The first topic should account for additional physics. In such a complex system, certain assumptions regarding variable and physical properties must be made. Future work should investigate the effects of surface roughness, additive manufacturing material, and structure rigidity on the system performance. Additional research into boundary layer refinement could include frictional effects.

The size of the nozzles; perforation size and location; number of stages; and AMM cavity size were arbitrarily chosen. The second topic future work should focus on is the optimization of the structure in order to refine these parameters for either general or specific applications. Finally, the use of the Infill AMM should be the subject of future work with regards to infill geometry selection. The tortuosity of the infill could be quantified for comparative purposes.

References

[1] J. Johnson, Thermal Agitation of Electricity in Conductors, Phys Rev.

[2] Inspiring Quotes, [Online]. Available: https://www.inspiringquotes.us/quotes/0N8g_NLsDT2ec. [Accessed 16 April 2021].

[3] J. Fraden, Handbook of Modern Sensors Physics, Designs, and Applications, Fifth Edition, Springer, 2016.

[4] S. Beeby, G. Ensell, M. Kraft and N. White, MEMS Mechanical Sensors, Norwood, MA: Artech House, Inc, 2004.

[5] C. P. Wright, Applied Measurement Engineering, How to Design Effective Mechanical Measurement Systems, Upper Saddle River, NJ: Prentice Hall, Inc., 1995.

[6] S. Khazaaleh, G. Korres, M. Eid, M. Rasras and M. F. Daqaq, "Vulnerability of MEMS Gyroscopes to Targeted Acoustic Attacks," *IEEE Access,* vol. 7, 2019.

[7] T. Trippel, O. Weisse, W. Xu, P. Honeyman and K. Fu, "WALNUT: Waging Doubt on the Integrity of MEMS Accelerometers with Acoustic Injection Attacks," *IEEE European Symposium on Security and Privacy,* 2017.

[8] Y. Son, H. Shin, D. Kim, Y. Park, J. Noh, K. Choi, J. Choi and Y. Kim, "Rocking Drones with Intentional Sound Noise on Gyroscopic Sensors," *USENIX Security Symposium,* vol. 24, 2015.

[9] AZ Quotes, [Online]. Available: www.azquotes.com/quote/1065587 . [Accessed 16 April 2021].

[10] Yale Law School, The Avalon Project, "Law of Caesar on Municipalities," Rome, Italy, 44 B.C..

[11] W. S. Gan, New Acoustics Based on Metamaterials, Singapore: Springer, 2018.

[12] A. Boardman, "Pioneers in metamaterials: John Pendry and Victor Veselago," *Journal of Optics,* vol. 13, no. 2, 2011.

[13] G. Ma and P. Sheng, "Acoustic metamaterials: From local resonances to broad horizons," *American Association for the Advancement of Science,* 2016.

[14] S. A. Cummer, "Chapter 8: Transformation Acoustics," in *Acoustic Metamaterials Negative Refraction, Imaging, Lensing, and Cloaking*, Springer, 2013, pp. 212-213.

[15] K. J. M. Bishop, "Acoustic Metamaterials, Living Bandgaps," *Nature Materials,* vol. 16, pp. 786-787, 2017.

[16] F. Zhang, G. Flowers, E. Perkins, R. Dean, D. Marghitu and J. Hung, "Metalenses, Acoustic Metamaterials: Air Permeable Super Sound Attenuators and Acoustic," Auburn University, Auburn Al, 2019.

[17] Y. Tang, S. Ren, H. Meng, F. Xin, L. Huang, T. Chen, C. Zhang and T. J. Lu, "Hybrid acoustic metamaterial as super absorber for broadband low-frequency sound," *Nature Scientific Reports,* 2017.

[18] C. Casarini, J. F. Windmill and J. C. Jackson, "3D printed small-scale acoustic metamaterials based on Helmholtz resonators with tuned overtones," in *IEEE Sensors*, Glasgow, Scotland, 2017.

[19] R. Ghaffarivardavagh, J. Nikolajczyk, S. Anderson and X. Zhang, "Ultra-open acoustic metamaterial silencer based on Fano-like interference," *PHYSICAL REVIEW,* vol. B 99, no. 024302, 2019.

[20] G. L. Huang and C. T. Sun, "Band Gaps in a Multiresonator Acoustic Metamaterial," *Journal of Vibration and Acoustics,* vol. 132, 2010.

[21] M. Chen, D. Meng, H. Jiang and Y. Wang, "Investigation on the Band Gap and Negative Properties of Concentric Ring Acoustic Metamaterial," *Hindawi Shock and Vibration,* p. 12, 2018.

[22] C. E. Wilson, Noise Control, Revised Edition, Malabar, FL: Krieger Publishing Company, 2006.

[23] MSC Software Company, "Damping in acoustic simulation," MSC Software Company, Detroit, MI, 2018.

[24] H. Lord, W. Gatley and H. Evensen, Noise Control for Engineers, Malabar, FL: Krieger Publishing Company, 1980.

[25] A. Pierce, Acoustics An Introduction to Its Physical Principles and Applications, McGraw Hill, 1981.

[26] J.-L. Migeot, J.-P. Coyette and G. Lielens, Acoustics Essential Concepts, Theory, and Models of Linear Acoustics for Engineers, Bruxelles, Belgiu, 2016.

[27] J. Ginsberg, Acoustics - A Textbook for Engineers and Physicists Vol. 1 Fundamentals, Dunwoody, GA: Springer, 2018.

[28] S. Temkin, Elements of Acoustics, John Wiley & Sons, Inc., 2001.

[29] M. L. Munjal, Acoustics of Ducts and Mufflers, Second Edition, Chichester, West Sussex, UK: Wiley, 2014.

[30] B. Nussbaum, "https://blog.prototypr.io," Medium.com, [Online]. Available: https://blog.prototypr.io/35-quotes-on-design-that-will-fuel-up-your-creativity-15060f732f1. [Accessed 19 April 2021].

[31] Stratasys Direct Manufacturing, "FDM Support Removal - Stratasys™ Support Center," [Online]. Available: https://support.stratasys.com/sitecore/api/downloadazurefile?id=f975cc4e-d52f-429a-aa41-3062776ca655. [Accessed April 2021].

[32] "FDM Machine/Material Reference," [Online]. Available: https://support.stratasys.com/sitecore/api/downloadazurefile?id=%7BB04BE3F0-E7C7-4266-BC6B-1EF4288C0086%7D. [Accessed 02 04 2021].

[33] Stratasys Direct Manufacturing, "Fortus 380mc and 450mc," [Online]. Available: https://www.stratasys.com/-/media/files/printer-spec-sheets/pss_fdm_fortus380mc450mc_0221a.pdf. [Accessed 2 4 2021].

[34] Stratasys Direct Manufacturing, "Advanced Prototyping and Production," [Online]. Available: https://www.stratasys.com/3d-printers/-/media/files/brochures/BR_FDM_Fortus450mc_0221a. [Accessed 2 4 2021].

[35] Stratasys Direct Manufacturing, "ASA," [Online]. Available: https://www.stratasys.com/-/media/files/material-spec-sheets/mds_fdm_asa_0920a.pdf. [Accessed 02 04 2021].

[36] Stratasys Direct Manufacturing, "www.stratasys.com," [Online]. Available: https://www.stratasys.com/3d-printers/fortus-380mc-450mc. [Accessed 26 April 2021].

[37] R. W. Emerson, "www.BrainyQuote.com," BrainyQuote.com, [Online]. Available: https://www.brainyquote.com/quotes/ralph_waldo_emerson_101056. [Accessed 19 April 2021].

[38] DEWEsoft , "www.dewesoft.com," [Online]. Available: https://dewesoft.com/products/daq-systems/mini. [Accessed 27 April 2021].

[39] PCB Piezotroics. An MTS Company, "www.pcb.com," [Online]. Available: https://www.pcb.com/products?m=378C10. [Accessed 27 April 2021].

[40] Klipsch Group, Inc., "www.klipsch.com," [Online]. Available: https://www.klipsch.com/products/rf-7-iii-floorstanding-speaker. [Accessed 27 April 2021].

[41] Klipsch Group, Inc., "www.klipsch.com," [Online]. Available: https://www.klipsch.com/products/rc-64-iii-center-channel-speaker. [Accessed 27 April

2021].

[42] Klipsch Group, Inc., "www.klipsch.com," [Online]. Available: https://www.klipsch.com/products/pro-200a. [Accessed 27 April 2021].

[43] Owens Corning, "www.owenscorning.com," [Online]. Available: https://www.owenscorning.com/en-us/insulation/products/700-series-fiberglas-insulation. [Accessed 27 April 2021].

[44] R. Marquand, Director, *Star Wars: Episode VI - Return of the Jedi.* [Film]. USA: Lucasfilm Ltd., 1983.

[45] T. Nelson, "www.quotemaster.org/," [Online]. Available: https://www.quotemaster.org/computer+simulation. [Accessed 24 May 2021].

[46] B. Williams, "IT History Society," IT History Society, [Online]. Available: https://www.ithistory.org/quotes/bob-williams. [Accessed 22 April 2021].

[47] Free Field Technologies SA, MSC Software Company, "Actran 19.1 Users Guide, Volume 1, Installation, Operations, Theory, and Utlities," Mont-Saint-Guibert, Belgium, 2019.

[48] MUMPS Consortium, "MUltifrontal Massively Parallel Solver (MUMPS 5.4.0) Users Guide," 2021.

[49] M. S. C. Free Field Technologies SA, "Actran 2020 User's Guide Vol. 2, Extended DAT Input File Syntax," Mont-Saint-Guibert, Belgium, 2020.

[50] J. Berges, "http://cliintel.com/," [Online]. Available: http://cliintel.com/6-of-the-best-quotes-about-business-data/. [Accessed 24 May 2021].

[51] C. Sambuc, G. Lielens and J.-P. Coyette, "Numerical modelling of visco-thermal acoustics using finite elements," in *International Conference on Noise and Vibration Engineering*, Mont-Saint-Guibert, Belgium, 2014.

[52] B. Griffin, Interviewee, *Famous ME Professor Quotes.* [Interview]. 2007.

Appendix A. MATLAB Scripts

A-1 Straight Pipe Transfer Matrix

```
%%This matlab script generates the transfer matrix for a straight pipe given
%%symbolic expressions for the system geometry
%%Brittany Griffin, 2021

%%Variables
   %%S - cross-sectional area
   %%x - x location
   %%x1 - x location of input
   %%x2 - x location of output
   %%c - speed of sound
   %%w - angular frequency
   %%t - time
   %%k - wave number
   %%L - length of nozzle
   %%rho - density of air

clc
clear
close all

syms x1 x2 c w t k x L S TM_SP rho

%Define the transfer Matrix
   G_x_a=exp(-1i*k*x);
   G_x_b=exp(1i*k*x);
   G_x_c=exp(-1i*k*x)/(rho*c);
   G_x_d=-exp(1i*k*x)/(rho*c);
```

```
    G_x=[G_x_a,G_x_b;G_x_c,G_x_d];

%Create G(x1) and G(x2)
    G_x1=subs(G_x,x,x1);
    G_x2=subs(G_x,x,x2);

%Define and simplify Transfer Matrix
    Transfer_Matrix_SP=G_x1*G_x2^-1;

    Transfer_Matrix_SP=rewrite(Transfer_Matrix_SP,'sincos'); %changes e^ to sin/cos
    Transfer_Matrix_SP=expand(Transfer_Matrix_SP); %expands factored terms
    Transfer_Matrix_SP=simplify(Transfer_Matrix_SP);%simplifies equation
    Transfer_Matrix_SP=subs(Transfer_Matrix_SP,x2-x1,L);
    Transfer_Matrix_SP=subs(Transfer_Matrix_SP,x1-x2,-L);
    Transfer_Matrix_SP=simplify(Transfer_Matrix_SP);%simplifies equation

    %%Area Correction
    Transfer_Matrix_SP(2,1)=Transfer_Matrix_SP(2,1)*S;
    Transfer_Matrix_SP(2,2)=Transfer_Matrix_SP(2,2)*S/S;
    pretty_equation(Transfer_Matrix_SP)%displays equation in a user friendly format
```

A-2 Straight Pipe Numerical Comparison with Test

```
%%Brittany Griffin, 2021

clc
clear
close all

%%Input Parameters
   pipe_length=6;  %%length of nozzle in inches
   radius=1.25; %%Radius of pipe in inches

%%Data Acquisition Properties
   sample_rate=100000;
   pretrigger_time_input=0; %msec

%%Bandwidth
   starting_freq=20;
   ending_freq=20000;

%%Step Counts
   time_step=1/sample_rate;
   white_noise_steps=10*sample_rate; %%10 sec

%%Pretriggger
   pretrigger_time=pretrigger_time_input*10^-3;
   starting_index=pretrigger_time*sample_rate+1;

%%File Indexes
   start_index=starting_index;
```

```
    end_index=start_index+white_noise_steps;

%%Constants
    P0=20*1e-6; %reference pressure [Pa]
    c=343; %Speed of sound in air [m/s]
    rho=1.225; %density of air [kg/m^3]
    Z_air=c*rho; %Acoustic impedance of Air

%%%%Test Data
    %%Data File Information and naming convention
        test_files_to_import="LB_001";
        jpeg_name=" Straight Pipe";
        legend_labels=" Straight Pipe";
        graph_title=jpeg_name;

    %%Import Data
        import_file_name_test=test_files_to_import+".txt";
        run_data_test=importdata(import_file_name_test);
        ch1_test=run_data_test(:,1);
        ch2_test=run_data_test(:,2);

    %%File Indexes
        start_index_test=starting_index;
        end_index_test=start_index_test+white_noise_steps;

    %%Crop file
        ch1_test=ch1_test(start_index_test:end_index_test);
        ch2_test=ch2_test(start_index_test:end_index_test);
```

```
%%Calculate FFT
    nfft_ch1_test=length(ch1_test);
    FFT_ch1_temp=fft(ch1_test,nfft_ch1_test)/nfft_ch1_test;
    index_ch1_test=round(nfft_ch1_test/2);
    FFT_ch1_test=FFT_ch1_temp(1:index_ch1_test);
    f_ch1_test=abs(FFT_ch1_test);

    nfft_ch2_test=length(ch2_test);
    FFT_ch2_temp=fft(ch2_test,nfft_ch2_test)/nfft_ch2_test;
    index_ch2_test=round(nfft_ch2_test/2);
    FFT_ch2_test=FFT_ch2_temp(1:index_ch2_test);
    f_ch2_test=abs(FFT_ch2_test);

%Calculate Frequency Vector
    frequency_test=sample_rate*(0:(nfft_ch1_test/2))/nfft_ch1_test;
    frequency_test=frequency_test';

%Convert FFT to  dB and calculate Tau and Transmission Loss
    y=size(f_ch1_test);
    y=max(y);

%Preallocate for speed
    f_ch1_ dB_test=zeros(1,y);
    f_ch2_ dB_test=zeros(1,y);
    tau_test=zeros(1,y);
    TL_test=zeros(1,y);

    for j=1:y
    %%Convert Pa to  dB
```

```
        f_ch1_ dB_test(j)=20*log10(f_ch1_test(j)/P0);
        f_ch2_ dB_test(j)=20*log10(f_ch2_test(j)/P0);

      %%Transmission Coefficient
        tau_test(j)=(f_ch2_test(j)^2)/(f_ch1_test(j)^2);
        TL_test(j)=-10*log10(tau_test(j));
      end

   %%Find index of Bandwidth
      steps_in_a_Hz=round(2*(length(frequency_test))/sample_rate);
      BW_start_index=starting_freq*steps_in_a_Hz+1;
      BW_ending_index=ending_freq*steps_in_a_Hz+1;

   %%Crop vectors
      frequency_test=frequency_test(BW_start_index:BW_ending_index);
      f_ch1_ dB_test=f_ch1_ dB_test(BW_start_index:BW_ending_index);
      f_ch2_ dB_test=f_ch2_ dB_test(BW_start_index:BW_ending_index);
      tau_test=tau_test(BW_start_index:BW_ending_index);
      TL_test=TL_test(BW_start_index:BW_ending_index);

   %%Find Averages
      tau_avg_test=mean(tau_test);
      TL_avg_test=mean(TL_test);

%%%%Numerical Simulation
   %%Only in the frequency domain
   %%Geometry (Needs to be metric)
      radius_metric=radius*2.54/100;
      length_metric=pipe_length*2.54/100;
```

```
cross_section_area=pi()*radius_metric^2;

%%Input Pressure (already cropped)
P_in_num=f_ch1_ dB_test;
frequency_num=frequency_test';

%%Calculate input Velocity
u_in=Z_air*P_in_num;

%%Calculate wave number as a function of frequency
 k=2*pi()*frequency_num./c;

%%Define the transfer Matrix
TM_nozzle_11=cos(k.*length_metric);
TM_nozzle_12=rho*c*1i*sin(k.*length_metric);
TM_nozzle_21=cross_section_area*1i*sin(k.*length_metric)/(rho*c);
TM_nozzle_22=cos(k.*length_metric);

%%Calculate Output Pressure and velocity as real components
P_out_num=TM_nozzle_11.*P_in_num+(TM_nozzle_12.*u_in);
P_out_num=abs(real(P_out_num));

u_out_num=TM_nozzle_21.*P_in_num+TM_nozzle_22.*u_in;
u_out_num=abs(real(u_out_num));

 %%Transmission Coefficient and Loss
tau_num=(P_out_num.^2)./(P_in_num.^2);
tau_avg_num=mean(tau_num);
TL_num=-10*log10(tau_num);
```

```
    TL_avg_num=mean(TL_num);

%%%%Simulation Data
  %%Import Data
    import_file_name_sim="SISO_SP.txt";
    run_data_sim=importdata(import_file_name_sim);

    run_data_sim=run_data_sim.data;
    frequency_sim=run_data_sim(:,1);
    number_of_analysis_runs=size(run_data_sim);
    number_of_analysis_runs=(number_of_analysis_runs(2)-1)/2;

    for x=1:number_of_analysis_runs
      input_sim_all_runs(:,x)=run_data_sim(:,x);
      y=x+number_of_analysis_runs;
      output_sim_all_runs(:,x)=run_data_sim(:,y);
    end

  %%First simulation run has high error by nature since runs need to
  %%converge, therefore remove first row of data

    input_sim=input_sim_all_runs;
    input_sim(:,1)=[];
    output_sim=output_sim_all_runs;
    output_sim(:,1)=[];

  %%Transmission Coefficient and Loss
    length_of_sim_vector=size(input_sim);
```

```
    for k=1:length_of_sim_vector(2)
        for j=1:length_of_sim_vector(1)
            tau_sim(j,k)=(output_sim(j,k)^2)/(input_sim(j,k)^2);
            TL_sim(j,k)=-10*log10(tau_sim(j,k));
        end
    end

    for m=1:length_of_sim_vector(1)
        tau_avg_sim(m)=mean(tau_sim(m,:));
        TL_avg_sim(m)=mean(TL_sim(m,:));
        TL_std_dev_sim(m)=std(TL_sim(m,:));
    end

    tau_avg_sim_value=mean(tau_avg_sim);
    TL_avg_sim_value=mean(TL_avg_sim);

%%%%Bounds
  TL_sim_lower_bound=TL_avg_sim-TL_std_dev_sim;
  TL_sim_upper_bound=TL_avg_sim+TL_std_dev_sim;

 %%Plots
  font_size=14;
  chart_title=["Straight Pipe Test Data, Numerical Solution, and Simulation Data Transmission
Loss Comparison"];
  sgtitle(chart_title,'FontSize',font_size+4,'FontWeight','bold');
  set(gcf,'WindowState','maximized');

  %%Plot Limits
    smoothing_factor=250;
```

```
    TL_min=-10;
    TL_max=60;

  %%Plot TL
    semilogx(frequency_test,smooth(TL_test,smoothing_factor),'r');
    hold on
    semilogx(frequency_num,TL_num,'b');
    semilogx(frequency_sim,smooth(TL_avg_sim,smoothing_factor/20),'g');

    xlim([starting_freq,ending_freq]);
%       ylim([TL_min,TL_max])
    xlabel('Frequency (Hz)','fontsize',font_size);
    ylabel('Transmission Loss (dB)','fontsize',font_size);
    grid on;
    test_legend=string(['Test Mean=',num2str(TL_avg_test,'%1.2f')]);
    num_legend=string(['Numerical Mean=',num2str(TL_avg_num,'%1.2f')]);
    sim_legend=string(['Simulation Mean=',num2str(TL_avg_sim_value,'%1.2f')]);
    legend(test_legend,num_legend,sim_legend,'fontsize',font_size,'location','eastoutside');
    comparison_plot_settings=gca;
    comparison_plot_settings.FontSize=font_size;

%%Save Figure as JPG
  filename=jpeg_name+" comparison";
  saveas(figure(1),filename,'jpg');
  close(figure(1))
```

A-3 Nozzle Transfer Matrix

```
%%This matlab script generates the transfer matrix for a nozzle given
%%symbolic expressions for the system geometry
%%Brittany Griffin, 2021
%%Variables
   %%s1 - input cross-sectional area
   %%s2 - output cross-sectional area
   %%x - x location
   %%x1 - x location of input
   %%x2 - x location of output
   %%c - speed of sound
   %%w - angular frequency
   %%t - time
   %%k - wave number
   %%L - length of nozzle

clc
clear
close all

syms s1 s2 x x1 x2 c w t k L  TM_Nozzle

%Define the transfer Matrix
   G_x_a=exp(1i*w*t)*exp(-1i*k*x)/x;
   G_x_b=exp(1i*w*t)*exp(1i*k*x)/x;
   G_x_c=(s2*x*exp(1i*w*t)*exp(-1i*k*x)*(1-(1i/(k*x))))/(c*(x2^2));
   G_x_d=-(s2*x*exp(1i*w*t)*exp(1i*k*x)*(1+(1i/(k*x))))/(c*(x2^2));
```

```
    G_x=[G_x_a,G_x_b;G_x_c,G_x_d];

%Create G(x1) and G(x2)
    G_x1=subs(G_x,x,x1);
    G_x2=subs(G_x,x,x2);

%Define and simplify Transfer Matrix
    Transfer_Matrix_Nozzle=G_x1*G_x2^-1;

    Transfer_Matrix_Nozzle=rewrite(Transfer_Matrix_Nozzle,'sincos');
    Transfer_Matrix_Nozzle=expand(Transfer_Matrix_Nozzle);
    Transfer_Matrix_Nozzle=simplify(Transfer_Matrix_Nozzle);
    Transfer_Matrix_Nozzle=subs(Transfer_Matrix_Nozzle,x2-x1,L);
    Transfer_Matrix_Nozzle=subs(Transfer_Matrix_Nozzle,x1-x2,-L);
    Transfer_Matrix_Nozzle=simplify(Transfer_Matrix_Nozzle);

%Area Correction
    Transfer_Matrix_Nozzle(2,1)=Transfer_Matrix_Nozzle(2,1)*s1;
    Transfer_Matrix_Nozzle(2,2)=Transfer_Matrix_Nozzle(2,2)*s1/s2;

%Inverse Matrix
    Transfer_Matrix_Nozzle_inverse=simplify(expand(inv(Transfer_Matrix_Nozzle)));
```

A-4 Nozzle Numerical Comparison with Test

```
%%Brittany Griffin, 2021

clc
clear
close all

%%Input Parameters
   pipe_length=6;  %%length of nozzle in inches
   radius=1.25; %%Radius of pipe in inches

%%Data Acquisition Properties
   sample_rate=100000;
   pretrigger_time_input=0; %msec

%%Bandwidth
   starting_freq=20;
   ending_freq=20000;

%%Step Counts
   time_step=1/sample_rate;
   white_noise_steps=10*sample_rate; %%10 sec

%%Pretriggger
   pretrigger_time=pretrigger_time_input*10^-3;
   starting_index=pretrigger_time*sample_rate+1;

%%File Indexes
   start_index=starting_index;
```

```
    end_index=start_index+white_noise_steps;

%%Constants
    P0=20*1e-6; %reference pressure [Pa]
    c=343; %Speed of sound in air [m/s]
    rho=1.225; %density of air [kg/m^3]
    Z_air=c*rho; %Acoustic impedance of Air

%%%%Test Data
    %%Data File Information and naming convention
        test_files_to_import="LB_001";
        jpeg_name=" Straight Pipe";
        legend_labels=" Straight Pipe";
        graph_title=jpeg_name;

    %%Import Data
        import_file_name_test=test_files_to_import+".txt";
        run_data_test=importdata(import_file_name_test);
        ch1_test=run_data_test(:,1);
        ch2_test=run_data_test(:,2);

    %%File Indexes
        start_index_test=starting_index;
        end_index_test=start_index_test+white_noise_steps;

    %%Crop file
        ch1_test=ch1_test(start_index_test:end_index_test);
        ch2_test=ch2_test(start_index_test:end_index_test);
```

```
%%Calculate FFT
    nfft_ch1_test=length(ch1_test);
    FFT_ch1_temp=fft(ch1_test,nfft_ch1_test)/nfft_ch1_test;
    index_ch1_test=round(nfft_ch1_test/2);
    FFT_ch1_test=FFT_ch1_temp(1:index_ch1_test);
    f_ch1_test=abs(FFT_ch1_test);

    nfft_ch2_test=length(ch2_test);
    FFT_ch2_temp=fft(ch2_test,nfft_ch2_test)/nfft_ch2_test;
    index_ch2_test=round(nfft_ch2_test/2);
    FFT_ch2_test=FFT_ch2_temp(1:index_ch2_test);
    f_ch2_test=abs(FFT_ch2_test);

%Calculate Frequency Vector
    frequency_test=sample_rate*(0:(nfft_ch1_test/2))/nfft_ch1_test;
    frequency_test=frequency_test';

%Convert FFT to  dB and calculate Tau and Transmission Loss
    y=size(f_ch1_test);
    y=max(y);

%Preallocate for speed
    f_ch1_ dB_test=zeros(1,y);
    f_ch2_ dB_test=zeros(1,y);
    tau_test=zeros(1,y);
    TL_test=zeros(1,y);

    for j=1:y
    %%Convert Pa to  dB
```

```
        f_ch1_ dB_test(j)=20*log10(f_ch1_test(j)/P0);
        f_ch2_ dB_test(j)=20*log10(f_ch2_test(j)/P0);
    %%Transmission Coefficient
        tau_test(j)=(f_ch2_test(j)^2)/(f_ch1_test(j)^2);
        TL_test(j)=-10*log10(tau_test(j));
    end

  %%Find index of Bandwidth
    steps_in_a_Hz=round(2*(length(frequency_test))/sample_rate);
    BW_start_index=starting_freq*steps_in_a_Hz+1;
    BW_ending_index=ending_freq*steps_in_a_Hz+1;

  %%Crop vectors
    frequency_test=frequency_test(BW_start_index:BW_ending_index);
    f_ch1_ dB_test=f_ch1_ dB_test(BW_start_index:BW_ending_index);
    f_ch2_ dB_test=f_ch2_ dB_test(BW_start_index:BW_ending_index);
    tau_test=tau_test(BW_start_index:BW_ending_index);
    TL_test=TL_test(BW_start_index:BW_ending_index);

  %%Find Averages
    tau_avg_test=mean(tau_test);
    TL_avg_test=mean(TL_test);

%%%%Numerical Simulation
  %%Only in the frequency domain
  %%Geometry (Needs to be metric)
    radius_metric=radius*2.54/100;
    length_metric=pipe_length*2.54/100;
    cross_section_area=pi()*radius_metric^2;
```

```
%%Input Pressure (already cropped)
   P_in_num=f_ch1_ dB_test;
   frequency_num=frequency_test';

%%Calculate input Velocity
   u_in=Z_air*P_in_num;

%%Calculate wave number as a function of frequency
    k=2*pi()*frequency_num./c;

%%Define the transfer Matrix
   TM_nozzle_11=cos(k.*length_metric);
   TM_nozzle_12=rho*c*1i*sin(k.*length_metric);
   TM_nozzle_21=cross_section_area*1i*sin(k.*length_metric)/(rho*c);
   TM_nozzle_22=cos(k.*length_metric);

%%Calculate Output Pressure and velocity as real components
   P_out_num=TM_nozzle_11.*P_in_num+(TM_nozzle_12.*u_in);
   P_out_num=abs(real(P_out_num));

   u_out_num=TM_nozzle_21.*P_in_num+TM_nozzle_22.*u_in;
   u_out_num=abs(real(u_out_num));

 %%Transmission Coefficient and Loss
   tau_num=(P_out_num.^2)./(P_in_num.^2);
   tau_avg_num=mean(tau_num);
   TL_num=-10*log10(tau_num);
   TL_avg_num=mean(TL_num);
```

```
%%%%Simulation Data
  %%Import Data
    import_file_name_sim="SISO_SP.txt";
    run_data_sim=importdata(import_file_name_sim);

    run_data_sim=run_data_sim.data;
    frequency_sim=run_data_sim(:,1);
    number_of_analysis_runs=size(run_data_sim);
    number_of_analysis_runs=(number_of_analysis_runs(2)-1)/2;

    for x=1:number_of_analysis_runs
      input_sim_all_runs(:,x)=run_data_sim(:,x);
      y=x+number_of_analysis_runs;
      output_sim_all_runs(:,x)=run_data_sim(:,y);
    end

  %%First simulation run has high error by nature since runs need to
  %%converge, therefore remove first row of data

    input_sim=input_sim_all_runs;
    input_sim(:,1)=[];
    output_sim=output_sim_all_runs;
    output_sim(:,1)=[];

  %%Transmission Coefficient and Loss
    length_of_sim_vector=size(input_sim);
    for k=1:length_of_sim_vector(2)
      for j=1:length_of_sim_vector(1)
```

```
            tau_sim(j,k)=(output_sim(j,k)^2)/(input_sim(j,k)^2);
            TL_sim(j,k)=-10*log10(tau_sim(j,k));
        end
    end

    for m=1:length_of_sim_vector(1)
        tau_avg_sim(m)=mean(tau_sim(m,:));
        TL_avg_sim(m)=mean(TL_sim(m,:));
        TL_std_dev_sim(m)=std(TL_sim(m,:));
    end
    tau_avg_sim_value=mean(tau_avg_sim);
    TL_avg_sim_value=mean(TL_avg_sim);

%%%%Bounds
  TL_sim_lower_bound=TL_avg_sim-TL_std_dev_sim;
  TL_sim_upper_bound=TL_avg_sim+TL_std_dev_sim;

 %%Plots
  font_size=14;
  chart_title=["Straight Pipe Test Data, Numerical Solution, and Simulation Data Transmission
Loss Comparison"];
  sgtitle(chart_title,'FontSize',font_size+4,'FontWeight','bold');
  set(gcf,'WindowState','maximized');

  %%Plot Limits
    smoothing_factor=250;
    TL_min=-10;
    TL_max=60;
```

```
    %%Plot TL
        semilogx(frequency_test,smooth(TL_test,smoothing_factor),'r');
        hold on
        semilogx(frequency_num,TL_num,'b');
        semilogx(frequency_sim,smooth(TL_avg_sim,smoothing_factor/20),'g');

        xlim([starting_freq,ending_freq]);
        xlabel('Frequency (Hz)','fontsize',font_size);
        ylabel('Transmission Loss (dB)','fontsize',font_size);
        grid on;
        test_legend=string(['Test Mean=',num2str(TL_avg_test,'%1.2f')]);
        num_legend=string(['Numerical Mean=',num2str(TL_avg_num,'%1.2f')]);
        sim_legend=string(['Simulation Mean=',num2str(TL_avg_sim_value,'%1.2f')]);
        legend(test_legend,num_legend,sim_legend,'fontsize',font_size,'location','eastoutside');
        comparison_plot_settings=gca;
        comparison_plot_settings.FontSize=font_size;

%%Save Figure as JPG
    filename=jpeg_name+" comparison";
    saveas(figure(1),filename,'jpg');
    close(figure(1))

            clc
clear
close all

%%Input Parameters
    L_input=6;  %%length of nozzle in inches
    R1_input=.5; %%Radius of nozzle input radius in inches
    R2_output=1.25; %%Radius of nozzle output radius in inches
```

```
%%Data Acquisition Properties
   sample_rate=100000;
   pretrigger_time_input=0; %msec

%%Bandwidth
   starting_freq=20;
   ending_freq=20000;

%%Step Counts
   time_step=1/sample_rate;
   white_noise_steps=10*sample_rate; %%10 sec

%%Pretriggger
   pretrigger_time=pretrigger_time_input*10^-3;
   starting_index=pretrigger_time*sample_rate+1;

%%File Indexes
   start_index=starting_index;
   end_index=start_index+white_noise_steps;

%%Constants
   P0=20*1e-6; %reference pressure [Pa]
   c=343; %Speed of sound in air [m/s]
   rho=1.225; %density of air [kg/m^3]
   Z_air=c*rho; %Acoustic impedance of Air

%%%%Test Data
   %%Data File Information and naming convention
```

```
    test_files_to_import="LB_005";
    jpeg_name=" Diverging Nozzle";
    legend_labels=" Diverging Nozzle";
    graph_title=jpeg_name;

%%Import Data
    import_file_name_test=test_files_to_import+".txt";
    run_data_test=importdata(import_file_name_test);
    ch1_test=run_data_test(:,1);
    ch2_test=run_data_test(:,2);

%%File Indexes
    start_index_test=starting_index;
    end_index_test=start_index_test+white_noise_steps;

%%Crop file
    ch1_test=ch1_test(start_index_test:end_index_test);
    ch2_test=ch2_test(start_index_test:end_index_test);

%%Calculate FFT
    nfft_ch1_test=length(ch1_test);
    FFT_ch1_temp=fft(ch1_test,nfft_ch1_test)/nfft_ch1_test;
    index_ch1_test=round(nfft_ch1_test/2);
    FFT_ch1_test=FFT_ch1_temp(1:index_ch1_test);
    f_ch1_test=abs(FFT_ch1_test);

    nfft_ch2_test=length(ch2_test);
    FFT_ch2_temp=fft(ch2_test,nfft_ch2_test)/nfft_ch2_test;
    index_ch2_test=round(nfft_ch2_test/2);
```

```
    FFT_ch2_test=FFT_ch2_temp(1:index_ch2_test);
    f_ch2_test=abs(FFT_ch2_test);

%Calculate Frequency Vector
    frequency_test=sample_rate*(0:(nfft_ch1_test/2))/nfft_ch1_test;
    frequency_test=frequency_test';

%Convert FFT to  dB and calculate Tau and Transmission Loss
    y=size(f_ch1_test);
    y=max(y);

%Preallocate for speed
    f_ch1_ dB_test=zeros(1,y);
    f_ch2_ dB_test=zeros(1,y);
    tau_test=zeros(1,y);
    TL_test=zeros(1,y);

    for j=1:y
    %%Convert Pa to  dB
        f_ch1_ dB_test(j)=20*log10(f_ch1_test(j)/P0);
        f_ch2_ dB_test(j)=20*log10(f_ch2_test(j)/P0);

    %%Transmission Coefficient
        tau_test(j)=(f_ch2_test(j)^2)/(f_ch1_test(j)^2);
        TL_test(j)=-10*log10(tau_test(j));
    end

%%Find index of Bandwidth
    steps_in_a_Hz=round(2*(length(frequency_test))/sample_rate);
```

```
    BW_start_index=starting_freq*steps_in_a_Hz+1;
    BW_ending_index=ending_freq*steps_in_a_Hz+1;

  %%Crop vectors
    frequency_test=frequency_test(BW_start_index:BW_ending_index);
    f_ch1_ dB_test=f_ch1_ dB_test(BW_start_index:BW_ending_index);
    f_ch2_ dB_test=f_ch2_ dB_test(BW_start_index:BW_ending_index);
    tau_test=tau_test(BW_start_index:BW_ending_index);
    TL_test=TL_test(BW_start_index:BW_ending_index);

  %%Find Averages
    tau_avg_test=mean(tau_test);
    TL_avg_test=mean(TL_test);

%%%%Numerical Simulation
  %%Only in the frequency domain
  %%Geometry (Needs to be metric)
    R2=R1_input*2.54/100;
    R1=R2_output*2.54/100;
    L=L_input*2.54/100;
    s1=pi()*R1^2;
    s2=pi()*R2^2;
    x1=L*R1/(R2-R1);
    x2=x1+L;

  %%Input Pressure (already cropped)
    P_in_num=f_ch1_ dB_test;
    frequency_num=frequency_test';
```

```
%%Calculate input Velocity
    u_in=Z_air*P_in_num;

%%Calculate wave number as a function of frequency
     k=2*pi()*frequency_num./c;

%%Define the transfer Matrix
    TM_nozzle_11=-(sin(L.*k) - k.*x2.*cos(L.*k))./(k.*x1);
    T12_placeholder=c*x2*1i/(s2*x1);
    TM_nozzle_12=T12_placeholder*sin(L.*k);
    TM21_placeholder_1=s1*s2*1i/(c*x2^2);
    TM21_placeholder_2=x2*1i/(c*x2^2);
    TM21_placeholder_3=x1*x2*1i/(c*x2^2);
    TM21_placeholder_3=TM21_placeholder_3.*(k.^2);

TM_nozzle_21=(TM21_placeholder_1.*sin(L.*k))+(TM21_placeholder_2.*cos(L.*k))+(TM21_pla
ceholder_3.*sin(L.*k));
    TM_nozzle_21=TM_nozzle_21./(k.^2);
    TM_nozzle_22=(s1.*(sin(L.*k) + k.*x1.*cos(L.*k))).*(k.*s2.*x2);

%%Calculate Output Pressure and velocity as real components
    P_out_num=TM_nozzle_11.*P_in_num+(TM_nozzle_12.*u_in);
    P_out_num=abs(real(P_out_num));

    u_out_num=TM_nozzle_21.*P_in_num+TM_nozzle_22.*u_in;
    u_out_num=abs(real(u_out_num));

 %%Transmission Coefficient and Loss
    tau_num=(P_out_num.^2)./(P_in_num.^2);
```

```
    tau_avg_num=mean(tau_num);
    TL_num=-10*log10(tau_num);
    TL_avg_num=mean(TL_num);

%%%%Simulation Data
  %%Import Data
    import_file_name_sim="SISO_DN.txt";
    run_data_sim=importdata(import_file_name_sim);

    run_data_sim=run_data_sim.data;
    frequency_sim=run_data_sim(:,1);
    number_of_analysis_runs=size(run_data_sim);
    number_of_analysis_runs=(number_of_analysis_runs(2)-1)/2;

    for x=1:number_of_analysis_runs
      input_sim_all_runs(:,x)=run_data_sim(:,x);
      y=x+number_of_analysis_runs;
      output_sim_all_runs(:,x)=run_data_sim(:,y);
    end

  %%First simulation run has high error by nature since runs need to
  %%converge, therefore remove first row of data

    input_sim=input_sim_all_runs;
    input_sim(:,1)=[];
    output_sim=output_sim_all_runs;
    output_sim(:,1)=[];

  %%Transmission Coefficient and Loss
```

```
    length_of_sim_vector=size(input_sim);

    for k=1:length_of_sim_vector(2)
      for j=1:length_of_sim_vector(1)
        tau_sim(j,k)=(output_sim(j,k)^2)/(input_sim(j,k)^2);
        TL_sim(j,k)=-10*log10(tau_sim(j,k));
      end
    end

    for m=1:length_of_sim_vector(1)
      tau_avg_sim(m)=mean(tau_sim(m,:));
      TL_avg_sim(m)=mean(TL_sim(m,:));
      TL_std_dev_sim(m)=std(TL_sim(m,:));
    end

    tau_avg_sim_value=mean(tau_avg_sim);
    TL_avg_sim_value=mean(TL_avg_sim);

%%%%Bounds
  TL_sim_lower_bound=TL_avg_sim-TL_std_dev_sim;
  TL_sim_upper_bound=TL_avg_sim+TL_std_dev_sim;

 %%Plots
  chart_title=["Nozzle Test Data, Numerical Solution, and Simulation Data Transmission Loss
Comparison"];
  sgtitle(chart_title);
  set(gcf,'WindowState','maximized');

  %%Plot Limits
```

```
    smoothing_factor=250;
    TL_min=-10;
    TL_max=60;

  %%Plot TL
    semilogx(frequency_test,smooth(TL_test,smoothing_factor),'r');
    hold on
    semilogx(frequency_num,TL_num,'b');
    semilogx(frequency_sim,smooth(TL_avg_sim,smoothing_factor/20),'g');

    xlim([starting_freq,ending_freq]);
%       ylim([TL_min,TL_max])
    xlabel('Frequency (Hz)');
    ylabel('Transmission Loss (dB)');
    grid on;
    test_legend=string(['Test Mean=',num2str(TL_avg_test,'%1.2f')]);
    num_legend=string(['Numerical Mean=',num2str(TL_avg_num,'%1.2f')]);
    sim_legend=string(['Simulation Mean=',num2str(TL_avg_sim_value,'%1.2f')]);
    legend(test_legend,num_legend,sim_legend,'fontsize',12,'location','eastoutside');


%%Save Figure as JPG
  filename=jpeg_name+" comparison";
  saveas(figure(1),filename,'jpg');
  close(figure(1))
```

A-5 White Noise Generator

```
%%This matlab script generates a wave file of white noise
%%Brittany Griffin, 2021

clc
clear
close all

sample_rate=44100; %sample rate supported by media player
time_step=1/sample_rate;

%%10 sec of white noise
   time_duration_white_noise=10;
   number_of_steps_WN=time_duration_white_noise*sample_rate;
   output_file_white_noise=wgn(number_of_steps_WN,1,1)';

%%combine vectors
   output_file=[output_file_white_noise];

%generate .wav file
   audiowrite('white_noise.wav',output_file,sample_rate,'BitsPerSample',32);

%Check file
   num_steps=size(output_file);
   num_steps=num_steps(2);
   max_time=num_steps*time_step;
   time=linspace(0,max_time,num_steps);
```

```
%%FFT
    nfft1=length(output_file);
    FFT_ch1_temp=fft(output_file,nfft1)/nfft1;
    index1=round(nfft1/2);
    FFT_ch1=FFT_ch1_temp(1:index1);
    f_ch1=abs(FFT_ch1);
    frequency_ch1=sample_rate*(0:(nfft1/2-1))/nfft1;

%%Plot
    %%Plots
        chart_title=["White Noise"];
        sgtitle(chart_title);
        set(gcf,'WindowState','maximized');

     %%Plot time
        figure(1),subplot(3,1,1),plot(time,output_file);
        figure(1),subplot(3,1,1),title('Time');
        figure(1),subplot(3,1,1),xlabel('Time (s)');
        figure(1),subplot(3,1,1),ylabel('Sound Level');
        figure(1),subplot(3,1,1),grid on;

    %%Plot Spectrograms

figure(1),subplot(3,1,2),pspectrum(output_file,sample_rate,'spectrogram','Reassign',true,'frequ
encylimits',[20,20000])
        figure(1),subplot(3,1,2),title('Input Sound Spectrogram');
        figure(1),subplot(3,1,2),caxis([-150 0]);

    %%Plot FFT
```

```
    subplot(3,1,3),loglog(frequency_ch1,f_ch1);
    subplot(3,1,3),title('FFT');
    subplot(3,1,3),xlim([20 20000]);
    subplot(3,1,3),xlabel('Frequency (Hz)');
    subplot(3,1,3),ylabel('Sound Level');
    subplot(3,1,3),grid on;

%%Save as JPG and export code
    saveas(figure(1),'white noise','jpg');
    close all
```

A-6 Test Input Sound Verification

```
%%This script was generated to plot recorded input sound data
%%White noise only, 10s duration
%%Brittany Griffin, 2020

clc
clear
close all
close all hidden

%%Make sure these are correct%%
   sample_rate=100000;
   pretrigger_time_input=0; %msec
   test_time=10;

%Step Counts
   time_step=1/sample_rate;
   noise_steps=test_time*sample_rate;

%%Pretriggger
   pretrigger_time=pretrigger_time_input*10^-3;
   starting_index=pretrigger_time*sample_rate+1;

%%File Indexes
   start_index=starting_index;
   end_index=start_index+noise_steps;

%%Constants
```

```
    P0=20*1e-6; %reference pressure [Pa]
    time_const=343; %Speed of sound in air [m/s]
    p=1.225; %density of air [kg/m^3]
    w0=10^-12; %reference sound power [W]
    I0=10^-12; %reference sound intensity [W/m^2]

%%Master matrix and define variables
    test_matrix= ["SISO"," Straight Pipe","LB_001"];

%%Automate File names and graph titles
    files_to_import=test_matrix(1,3);
    legend_labels=test_matrix(1,2);

%%Plot Limits
    time_max_amp=50;
    time_min_amp=-time_max_amp;
    time_min=0;
    time_max=10;
    spectrogram_limits=[-100,0];
    smoothing_factor_test=1;
    fft_min_amp=5;
    fft_max_amp=100;
    tau_min=-.1;
    tau_max=10;
    TL_min=-10;
    TL_max=75;

%%Bandwidth
    starting_freq=20;
```

```
    ending_freq=20000;

%%Import Data
    import_file_name=test_matrix(1,3)+".txt";
    run_data=importdata(import_file_name);
    ch1_full=run_data(:,1);
    ch2_full=run_data(:,2);

%%Crop file
    ch1=ch1_full(start_index:end_index);
    ch2=ch2_full(start_index:end_index);

    time_steps=end_index-start_index+1;
    time_duration=time_steps/sample_rate;
    time=linspace(0,time_duration,time_steps)';

    ch1_RMS_Pa=max(ch1);
    ch2_RMS_Pa=max(ch2);

%convert to  dB
    ch1_ dB=20*log10(ch1_RMS_Pa/P0);
    ch2_ dB=20*log10(ch2_RMS_Pa/P0);

%%Calculate FFT
    nfft1=length(ch1);
    FFT_ch1_temp=fft(ch1,nfft1)/nfft1;
    index1=round(nfft1/2);
    FFT_ch1=FFT_ch1_temp(1:index1);
    f_ch1=abs(FFT_ch1);
```

```
    nfft2=length(ch2);
    FFT_ch2_temp=fft(ch2,nfft2)/nfft2;
    index2=round(nfft2/2);
    FFT_ch2=FFT_ch2_temp(1:index2);
    f_ch2=abs(FFT_ch2);

%Calculate Frequency Vector
    frequency_full=sample_rate*(0:(nfft1/2))/nfft1;
    frequency_full=frequency_full';

%Convert FFT to  dB and calculate Tau and Transmission Loss
    y=size(f_ch1);
    y=max(y);

%Preallocate for speed
    f_ch1_ dB_full=zeros(1,y);
    f_ch2_ dB_full=zeros(1,y);
    tau_Full=zeros(1,y);
    TL_full=zeros(1,y);

    for j=1:y
      %%Convert Pa to  dB
        f_ch1_ dB_full(j)=abs(20*log10(f_ch1(j)/P0));
        f_ch2_ dB_full(j)=abs(20*log10(f_ch2(j)/P0));
      %%Transmission Coefficient and Loss
        tau_full(j)=(f_ch2(j)^2)/(f_ch1(j)^2);
        TL_full(j)=-10*log10(tau_full(j));
    end
```

```
%%Find index of Bandwidth
    steps_in_a_Hz=round(2*(length(frequency_full))/sample_rate);
    BW_start_index=starting_freq*steps_in_a_Hz+1;
    BW_ending_index=ending_freq*steps_in_a_Hz+1;

%%Crop vectors
    frequency=frequency_full(BW_start_index:BW_ending_index);
    f_ch1_ dB=f_ch1_ dB_full(BW_start_index:BW_ending_index);
    f_ch2_ dB=f_ch2_ dB_full(BW_start_index:BW_ending_index);
    tau=tau_full(BW_start_index:BW_ending_index);
    TL=TL_full(BW_start_index:BW_ending_index);

%%Find Averages
    tau_avg_full_BW=mean(tau);
    TL_avg_full_BW=mean(TL);

    tau_avg_full_BW_all_runs=tau_avg_full_BW;
    TL_avg_full_BW_all_runs=TL_avg_full_BW;

%%Plots
    chart_title="Test Input Acoustic Noise - Recorded";
    sgtitle(chart_title);
    set(gcf,'WindowState','maximized');

%%Plot time
    figure(1),subplot(3,1,1),plot(time,ch1,'color','b');
    figure(1),subplot(3,1,1),title('Input Sound Time History');
    figure(1),subplot(3,1,1),xlim([time_min,time_max]);
```

```
   figure(1),subplot(3,1,1),ylim([time_min_amp,time_max_amp]);
   figure(1),subplot(3,1,1),xlabel('Time (s)');
   figure(1),subplot(3,1,1),ylabel('Sound Level (Pa)');
   figure(1),subplot(3,1,1),grid on;
   input_time_legend=string([num2str(ch1_ dB,'%1.0f'),' dB (Max)']);
   figure(1),subplot(3,1,1),legend(input_time_legend,'fontsize',12,'location','eastoutside');


%%Plot Spectrograms

figure(1),subplot(3,1,2),pspectrum(ch1,sample_rate,'spectrogram','Reassign',true,'frequencylim
its',[starting_freq,ending_freq])
   figure(1),subplot(3,1,2),title('Input Sound Spectrogram');
   figure(1),subplot(3,1,2),caxis(spectrogram_limits);

%%Plot FFT
   subplot(3,1,3),loglog(frequency,smooth(f_ch1_ dB,smoothing_factor_test),'color','b');
   subplot(3,1,3),title('Input Sound FFT');
   subplot(3,1,3),xlim([starting_freq,ending_freq]);
   subplot(3,1,3),ylim([fft_min_amp,fft_max_amp])
   subplot(3,1,3),xlabel('Frequency (Hz)');
   subplot(3,1,3),ylabel('Sound Level (dB)');
   subplot(3,1,3),grid on;
   subplot(3,1,3),legend('Input','fontsize',12,'location','eastoutside');

%%Save Figure as JPG
   saveas(figure(1),'Input Noise.jpg');
```

A-7 Test Data Plotter and Comparison

```
%%This script was generated to plot selected test runs, generate comparison
%%plots, and write values to table
%%2 channels, 1 in and 1 out
%%White noise only, 10s duration
%%Brittany Griffin, 2021

clc
clear
close all
close all hidden

%%Make sure these are correct%%
   sample_rate=100000;
   pretrigger_time_input=0; %msec
   test_time=10;

%Step Counts
   time_step=1/sample_rate;
   noise_steps=test_time*sample_rate;

%%Pretriggger
   pretrigger_time=pretrigger_time_input*10^-3;
   starting_index=pretrigger_time*sample_rate+1;

%%File Indexes
   start_index=starting_index;
   end_index=start_index+noise_steps;
```

```
%%Constants
   P0=20*1e-6; %reference pressure [Pa]

%%Master matrix and define variables
   test_matrix= ["SISO"," Straight Pipe","LB_001";"SISO"," Straight Pipe with Radial
Perforations","LB_003";"SISO"," Converging Nozzle","LB_005";"SISO"," Diverging
Nozzle","LB_004";"SISO"," Converging Nozzle with Radial Perforations","LB_009";"SISO","
Diverging Nozzle with Radial Perforations","LB_008";"SISO"," Diverging Nozzle with Constricted
Opening at Output","LB_0024";"SISO"," Diverging Nozzle with Axial
Perforations","LB_0026";"SISO"," Series Converging Nozzles","LB_0011";"SISO"," Series
Diverging Nozzles","LB_0010";"SISO"," Series Converging Nozzles with Radial
Perforations","LB_0015";"SISO"," Series Diverging Nozzles with Radial
Perforations","LB_0014";"SISO"," Series Converging Nozzles with Radial and Axial
Perforations","LB_0019";"SISO"," Series Diverging Nozzles with Radial and Axial
Perforations","LB_0018";"SISO"," Series Diverging Nozzles with Radial and Axial Perforations
and Constricted Opening at Output","LB_0022";"Size"," Base Feature AMM with 2 Inch Stages
Converging Nozzles ","Panel_001";"Size"," Base Feature AMM with 2 Inch Stages Diverging
Nozzles ","Panel_002";"Size"," Base Feature AMM with 4 Stages and 2 Inch Stages Diverging
Nozzles ","Panel_003";"Size"," Base Feature AMM with 1 Inch Stages Converging Nozzles
","Panel_004";"Size"," Base Feature AMM with 1 Inch Stages Diverging Nozzles
","Panel_005";"Size"," Base Feature AMM with 4 Stages and 1 Inch Stages Diverging Nozzles
","Panel_006";"Size"," Base Feature AMM with Half Inch Stages Converging Nozzles
","Panel_0010";"Size"," Base Feature AMM with Half Inch Stages Diverging Nozzles
","Panel_0011";"Size"," Base Feature AMM with 4 Stages with a Half Inch Stages Diverging
Nozzles ","Panel_0012";"Size"," Base Feature AMM with Quarter Inch Stages Converging
Nozzles ","Panel_0013";"Size"," Base Feature AMM with Quarter Inch Stages Diverging Nozzles
","Panel_0014";"Size"," Base Feature AMM with 4 Stages and Quarter Inch Stages Diverging
Nozzles ","Panel_0015";"MIMO"," MIMO Straight Pipe ","Panel_0016";"MIMO"," Base Feature
```

```
AMM Converging Nozzles ","Panel_0018";"MIMO"," Base Feature AMM Diverging Nozzles
","Panel_0019";"MIMO"," 4-stage Base Feature AMM Diverging Nozzles
","Panel_0020";"MIMO"," Large Cavity AMM Converging Nozzles ","Panel_0021";"MIMO","
Large Cavity AMM Diverging Nozzles ","Panel_0023";"MIMO"," 4-stage Large Cavity AMM
Diverging Nozzles ","Panel_0026";"MIMO"," Small Cavity AMM Converging Nozzles
","Panel_0027";"MIMO"," Small Cavity AMM Diverging Nozzles ","Panel_0029";"MIMO"," 4-
stage Small Cavity AMM Diverging Nozzles ","Panel_0032";"MIMO"," Infill AMM Converging
Nozzles ","Panel_0033";"MIMO"," Infill AMM Diverging Nozzles ","Panel_0035";"MIMO"," 4-
stage Infill AMM Diverging Nozzles ","Panel_0038";"Sphere"," Sphere at a Nominal Distance
Joint Horizontal","Sphere_0002";"Sphere"," Sphere at a Nominal Distance Joint
Vertical","Sphere_0001";"Sphere"," Sphere at a Close Distance Joint
Horizontal","Sphere_0003";"Sphere"," Sphere at a Close Distance Joint
Vertical","Sphere_0004";"Sphere"," Sphere between Speakers Joint
Horizontal","Sphere_0005";"Sphere"," Sphere between Speakers Joint
Vertical","Sphere_0006";"Sphere"," Sphere at an Extended Distance Joint
Horizontal","Sphere_0007";"Sphere"," Sphere at an Extended Distance Joint
Vertical","Sphere_0008"];
   display_list=(test_matrix(:,1)+"     "+test_matrix(:,2));

%%User selects runs for comparison
   [selected_runs]=listdlg('ListString',display_list,'ListSize',[750 500],'name','Available
Data','PromptString','Select the Configurations for Analysis, No more than 5 for Comparison
Plots');
   number_of_runs=size(selected_runs);
   number_of_runs=number_of_runs(2);

%%Automate File names and graph titles
   files_to_import=test_matrix(selected_runs,3);
   jpeg_name=test_matrix(selected_runs,2);
```

```
    legend_labels=test_matrix(selected_runs,2);
    graph_title=jpeg_name;

%%Plot Limits
    time_max_amp=50;
    time_min_amp=-time_max_amp;
    time_min=0;
    time_max=10;
    spectrogram_limits=[-75,0];
    smoothing_factor_test=250;
    fft_min_amp=5;
    fft_max_amp=100;
    tau_min=-.1;
    tau_max=10;
    TL_min=-10;
    TL_max=75;

%%Bandwidth
    starting_freq=20;
    ending_freq=20000;

%%Bandwidths for comparison
    width_of_band=750;
    lower_limit=20;
    upper_limit=20000;
    number_of_bands=round((upper_limit-lower_limit)/width_of_band);
    placeholder=lower_limit;
    comparison_bandwidth=round((upper_limit-lower_limit)/number_of_bands);
```

```
    for q=1:number_of_bands
      freq_matrix(q,:)=[placeholder,placeholder+comparison_bandwidth];
      placeholder= placeholder+comparison_bandwidth;
    end

    number_of_freq_bands=size(freq_matrix);

%%Data plotting Loops
    for i=1:number_of_runs

      %%Import Data
        import_file_name=files_to_import(i)+".txt";
        run_data=importdata(import_file_name);
        ch1_full=run_data(:,1);
        ch2_full=run_data(:,2);

      %%Crop file
        ch1=ch1_full(start_index:end_index);
        ch2=ch2_full(start_index:end_index);

        time_steps=end_index-start_index+1;
        time_duration=time_steps/sample_rate;
        time=linspace(0,time_duration,time_steps)';

        ch1_RMS_Pa=max(ch1);
        ch2_RMS_Pa=max(ch2);

      %convert to  dB
        ch1_ dB=20*log10(ch1_RMS_Pa/P0);
```

```
    ch2_ dB=20*log10(ch2_RMS_Pa/P0);

%%Calculate FFT
    nfft1=length(ch1);
    FFT_ch1_temp=fft(ch1,nfft1)/nfft1;
    index1=round(nfft1/2);
    FFT_ch1=FFT_ch1_temp(1:index1);
    f_ch1=abs(FFT_ch1);

    nfft2=length(ch2);
    FFT_ch2_temp=fft(ch2,nfft2)/nfft2;
    index2=round(nfft2/2);
    FFT_ch2=FFT_ch2_temp(1:index2);
    f_ch2=abs(FFT_ch2);

%Calculate Frequency Vector
    frequency_full=sample_rate*(0:(nfft1/2))/nfft1;
    frequency_full=frequency_full';

%Convert FFT to  dB and calculate Tau and Transmission Loss
    y=size(f_ch1);
    y=max(y);

%Preallocate for speed
    f_ch1_ dB_full=zeros(1,y);
    f_ch2_ dB_full=zeros(1,y);
    tau_full=zeros(1,y);
    TL_full=zeros(1,y);
```

```
    for j=1:y
      %%Convert Pa to  dB
        f_ch1_ dB_full(j)=abs(20*log10(f_ch1(j)/P0));
        f_ch2_ dB_full(j)=abs(20*log10(f_ch2(j)/P0));
      %%Transmission Coefficient and Loss
        tau_full(j)=(f_ch2(j)^2)/(f_ch1(j)^2);
        TL_full(j)=-10*log10(tau_full(j));
    end

%%Find index of Bandwidth
    steps_in_a_Hz=round(2*(length(frequency_full))/sample_rate);
    BW_start_index=starting_freq*steps_in_a_Hz+1;
    BW_ending_index=ending_freq*steps_in_a_Hz+1;

%%Crop vectors
    frequency=frequency_full(BW_start_index:BW_ending_index);
    f_ch1_ dB=f_ch1_ dB_full(BW_start_index:BW_ending_index);
    f_ch2_ dB=f_ch2_ dB_full(BW_start_index:BW_ending_index);
    tau=tau_full(BW_start_index:BW_ending_index);
    TL=TL_full(BW_start_index:BW_ending_index);

%%Find Averages
    tau_avg_full_BW=mean(tau);
    TL_avg_full_BW=mean(TL);

    tau_avg_full_BW_all_runs(i)=tau_avg_full_BW;
    TL_avg_full_BW_all_runs(i)=TL_avg_full_BW;
```

```
%%Comparison Plot Matrix and export to table
   for k=1:number_of_freq_bands(1)

   %%Define Bands
      comparison_starting_freq=freq_matrix(k,1);
      comparison_ending_freq=freq_matrix(k,2);
      BW_start_index_compare=comparison_starting_freq*steps_in_a_Hz+1;
      BW_ending_index_compare=comparison_ending_freq*steps_in_a_Hz+1;

   %%Crop tau and TL vectors
      TL_compare=TL_full(BW_start_index_compare:BW_ending_index_compare);
      tau_compare=tau_full(BW_start_index_compare:BW_ending_index_compare);

   %%Find Averages and write to matrix
      tau_avg=mean(tau_compare);
      TL_avg=mean(TL_compare);
      display_tau_table_data(i,k)=tau_avg;
      display_TL_table_data(i,k)=TL_avg;
   end

   font_size=14;

%%Plots
   chart_title=[graph_title(i)];
   sgtitle(chart_title,'fontsize',font_size+4,'FontWeight','bold');
   set(gcf,'WindowState','maximized');

%%Plot time
   figure(1),subplot(3,2,1),plot(time,ch1,'color','b');
```

```
        set(gca,'Fontsize',font_size);
        figure(1),subplot(3,2,1),title('Input Sound Time History');
        figure(1),subplot(3,2,1),xlim([time_min,time_max]);
        figure(1),subplot(3,2,1),ylim([time_min_amp,time_max_amp]);
        figure(1),subplot(3,2,1),xlabel('Time (s)','fontsize',font_size);
        figure(1),subplot(3,2,1),ylabel('Sound Level (Pa)','fontsize',font_size);
        figure(1),subplot(3,2,1),grid on;
        input_time_legend=string([num2str(ch1_ dB,'%1.0f'),' dB (Max)']);

figure(1),subplot(3,2,1),legend(input_time_legend,'fontsize',font_size,'location','eastoutside');

        figure(1),subplot(3,2,2),plot(time,ch2,'color','b');
        set(gca,'Fontsize',font_size);
        figure(1),subplot(3,2,2),title('Output Sound Time History','fontsize',font_size);
        figure(1),subplot(3,2,2),xlim([time_min,time_max]);
        figure(1),subplot(3,2,2),ylim([time_min_amp,time_max_amp]);
        figure(1),subplot(3,2,2),xlabel('Time (s)','fontsize',font_size);
        figure(1),subplot(3,2,2),ylabel('Sound Level (Pa)','fontsize',font_size);
        figure(1),subplot(3,2,2),grid on;
        output_time_legend=string([num2str(ch2_ dB,'%1.0f'),' dB (Max)']);

figure(1),subplot(3,2,2),legend(output_time_legend,'fontsize',font_size,'location','eastoutside');

    %%Plot Spectrograms

figure(1),subplot(3,2,3),pspectrum(ch1,sample_rate,'spectrogram','Reassign',true,'frequencylim
its',[starting_freq,ending_freq])
        set(gca,'Fontsize',font_size);
        figure(1),subplot(3,2,3),title('Input Sound Spectrogram','fontsize',font_size);
```

```
        figure(1),subplot(3,2,3),caxis(spectrogram_limits);

figure(1),subplot(3,2,4),pspectrum(ch2,sample_rate,'spectrogram','Reassign',true,'frequencylim
its',[starting_freq,ending_freq])
        set(gca,'Fontsize',font_size);
        figure(1),subplot(3,2,4),title('Output Sound Spectrogram','fontsize',font_size);
        figure(1),subplot(3,2,4),caxis(spectrogram_limits);

    %%Plot FFT
        subplot(3,2,5),loglog(frequency,smooth(f_ch1_ dB,smoothing_factor_test),'color','b');
        set(gca,'Fontsize',font_size);
        subplot(3,2,5),hold on;
        subplot(3,2,5),title('Input and Output Sound FFT','fontsize',font_size);
        subplot(3,2,5),xlim([starting_freq,ending_freq]);
        subplot(3,2,5),ylim([fft_min_amp,fft_max_amp])
        subplot(3,2,5),xlabel('Frequency (Hz)','fontsize',font_size);
        subplot(3,2,5),ylabel('Sound Level (dB)','fontsize',font_size);
        subplot(3,2,5),grid on;
        subplot(3,2,5),loglog(frequency,smooth(f_ch2_ dB,smoothing_factor_test));
        subplot(3,2,5),legend('Input','Output','fontsize',font_size,'location','eastoutside');

    %%Plot TL
        subplot(3,2,6),semilogx(frequency,smooth(TL,smoothing_factor_test),'color','b');
        set(gca,'Fontsize',font_size);
        subplot(3,2,6),title('Transmission Loss','fontsize',font_size);
        subplot(3,2,6),xlim([starting_freq,ending_freq]);
        subplot(3,2,6),ylim([TL_min,TL_max]);
        subplot(3,2,6),xlabel('Frequency (Hz)','fontsize',font_size);
        subplot(3,2,6),ylabel('Magnitude (dB)','fontsize',font_size);
```

```
        subplot(3,2,6),grid on;
        label={'TL_a_v_g= '};
        tau_legend=[label,num2str(TL_avg_full_BW,'%1.1f'),' dB'];
        tau_legend=strcat(tau_legend(1),tau_legend(2),tau_legend(3));
        subplot(3,2,6),legend(tau_legend,'fontsize',font_size,'location','eastoutside');

      %%Save Figure as JPG
        filename=jpeg_name(i);
        saveas(figure(1),filename,'jpg');
        close all
   end

%%Generate frequency vector
  center_freq=(freq_matrix(:,1)+freq_matrix(:,2))/2;

%%Write averages to excel

export_table=[legend_labels,num2str(TL_avg_full_BW_all_runs','%2.2f'),num2str(tau_avg_full_
BW_all_runs','%1.4f')];
%    writematrix(export_table,'comparison_table.xlsx');

   headers=["Configuration",(center_freq+"Hz")',"TL_avg"];

data_rows=[legend_labels,display_TL_table_data,num2str(TL_avg_full_BW_all_runs','%2.2f')];
   expanded_export_table=[headers;data_rows];

%    writematrix(expanded_export_table,'full_TL_data_comparison_table.xlsx');
%%%%Comparison Plots
  color=['b','r','g','c','m','k',[0,0,128]/256,[64,224,208]/256,[112,128,144]/256];
```

```
%%TL Plot
    set(gcf,'WindowState','maximized');
    comparison_plot_settings=gca;
    comparison_plot_settings.FontSize=font_size;

      for j=1:number_of_runs
        if j==1
          hold on
        end
        scatter(center_freq,display_TL_table_data(j,:),'filled',color(j));
        fitted_curve_function=fit(center_freq,display_TL_table_data(j,:)','smoothingspline');
        fitted_curve=feval(fitted_curve_function,[lower_limit:upper_limit]);
        plot([lower_limit:upper_limit],fitted_curve,color(j),'HandleVisibility','off');
        clear fitted_curve fitted_curve_function
      end

      title('Test Data Comparison - Transmission
Loss','fontsize',font_size+6,'FontWeight','bold');
      xlabel('Frequency (Hz)','fontsize',font_size+4);
      ylabel('Transmission Loss (dB)','fontsize',font_size+4);
      xlim([starting_freq,ending_freq]);
      ylim([TL_min,TL_max]);
      legend(legend_labels,'location','southoutside','fontsize',font_size+4);
      grid on;

    %%Save and Close
      saveas(figure(1),'TL Comparison','jpg');
      close all
```

A-8 Simulation Data Plotter

```
%%This script was generated to plot
%%simulation results
%%2 channels, 1 in and 1 out
%%White noise only, 10s duration
%%Brittany Griffin, 2020

clc
clear
close all
close all hidden

%%Make sure these are correct%%
   sample_rate=100000;
   pretrigger_time_input=0; %msec

%Step Counts
   time_step=1/sample_rate;
   white_noise_steps=10*sample_rate; %%10 sec

%%Pretriggger
   pretrigger_time=pretrigger_time_input*10^-3;
   starting_index=pretrigger_time*sample_rate+1;

%%File Indexes
   start_index=starting_index;
   end_index=start_index+white_noise_steps;
```

```
%%Constants
   P0=20*1e-6; %reference pressure [Pa]

%%Master matrix and define variables
      test_matrix= ["Panel"," MIMO Straight Pipe ","Panel_0016","MIMO_SP";"Panel"," Base
Feature AMM","Panel_0020","MIMO_No_MM";"Panel"," Large Cavity
AMM","Panel_0026","MIMO_Large_MM";"Panel"," Small Cavity
AMM","Panel_0032","MIMO_Small_MM";"Non Uniform Input"," SISO Straight
Pipe","LB_001","SISO_SP";"Non Uniform Input"," Straight Pipe with Radial
Perforations","LB_003","SISO_SP_MH";"Non Uniform Input"," Converging
Nozzle","LB_005","SISO_CN";"Non Uniform Input"," Diverging
Nozzle","LB_004","SISO_DN";"Non Uniform Input"," Diverging Nozzle with Radial
Perforations","LB_008","SISO_DN_MH";"Non Uniform Input"," Series Diverging
Nozzles","LB_0010","SISO_SDN";"Non Uniform Input"," Series Diverging Nozzles with Radial
Perforations","LB_0014","SISO_SDN_MH";"Non Uniform Input"," Series Diverging Nozzles with
Radial and Axial Perforations","LB_0018","SISO_SDN_MH_PMH";"Non Uniform Input"," Series
Diverging Nozzles with Radial and Axial Perforations and Constricted Opening at
Output","LB_0022","SISO_SDN_MH_PMH_PP"];
      display_list=[test_matrix(:,1)+"     "+test_matrix(:,2)];

%%User selects runs for comparison
   [selected_runs]=listdlg('ListString',display_list,'ListSize',[750 500],'name','Available
Data','PromptString','Select the Configuration for Comparison');
   number_of_runs=size(selected_runs);
   number_of_runs=number_of_runs(2);

%%Automate File names and graph titles
   files_to_import_test=test_matrix(selected_runs,3);
   files_to_import_sim=test_matrix(selected_runs,4)+"_combined";
```

```
    jpeg_name=test_matrix(selected_runs,2);
    graph_title=jpeg_name;

%%Automate Plot Limits for SISO and MIMO
    if test_matrix(selected_runs,1)=="Non Uniform Input"
        lower_plot_limit=250;
    else
        lower_plot_limit=2000;
    end

%%Plot Limits
    smoothing_factor_test=250;
    smoothing_factor_sim=20;
    tau_min=-.1;
    tau_max=1.1;
    TL_min=-15;
    TL_max=100;

%%Bandwidths of Interest
    starting_freq=20;
    ending_freq=20000;

    freq_matrix=[20,5000;5000,10000;10000,15000;15000,20000];
    number_of_freq_bands=size(freq_matrix);

   for i=1:number_of_runs
    %%%%Sim Data
        %%Import Data
            import_file_name_sim=files_to_import_sim(i)+".txt";
```

```
    run_data_sim=importdata(import_file_name_sim);
    frequency_sim=run_data_sim(:,1);
    number_of_analysis_runs=size(run_data_sim);
    number_of_analysis_runs=(number_of_analysis_runs(2)-1)/2;

    for x=1:number_of_analysis_runs
      input_sim(:,x)=run_data_sim(:,x);
      y=x+number_of_analysis_runs;
      output_sim(:,x)=run_data_sim(:,y);
    end

  %%Transmission Coefficient and Loss
    length_of_sim_vector=size(input_sim);

    for k=1:length_of_sim_vector(2)
      for j=1:length_of_sim_vector(1)
        tau_sim(j,k)=(output_sim(j,k)^2)/(input_sim(j,k)^2);
        TL_sim(j,k)=-10*log10(tau_sim(j,k));
      end
    end

    for m=1:length_of_sim_vector(1)
      tau_sim_avg(m)=mean(tau_sim(m,:));
      TL_sim_avg(m)=mean(TL_sim(m,:));
      TL_sim_std_dev(m)=std(TL_sim(m,:));
    end

%%%%Bounds
  TL_sim_entire_avg=mean(TL_sim_avg);
```

```
    TL_sim_lower_bound=TL_sim_avg-TL_sim_std_dev;
    TL_sim_upper_bound=TL_sim_avg+TL_sim_std_dev;

%%%%Comparison Plot Matrix and export to table
    for k=1:number_of_freq_bands(1)
    %%Define Bands
        comparison_starting_freq=freq_matrix(k,1);
        comparison_ending_freq=freq_matrix(k,2);

        %%Sim
            sim_start_index=find(comparison_starting_freq==frequency_sim);
            sim_end_index=find(comparison_ending_freq==frequency_sim);

        %%Crop tau and TL vectors
            tau_compare_sim=tau_sim_avg(sim_start_index:sim_end_index);
            TL_compare_sim=TL_sim_avg(sim_start_index:sim_end_index);

        %%Find Averages and write to matrix
            tau_avg_sim=mean(tau_compare_sim);
            TL_avg_sim=mean(TL_compare_sim);
            display_tau_table_data_sim(k,1)=tau_avg_sim;
            display_TL_table_data_sim(k,1)=TL_avg_sim;
    end

    %Average Values
        TL_sim_entire_avg=mean(TL_avg_sim);

    %%Export to table
        export_table=[display_TL_table_data_sim;TL_avg_sim];
```

```
        xlswrite('Simulation Data',export_table',i);

    %%%%Plots
        font_size=14;
        figure(1),chart_title=["Simulation Data Transmission Loss - "+jpeg_name(i)];
        figure(1),sgtitle(chart_title,'fontsize',font_size+4,'FontWeight','bold');
        figure(1),set(gcf,'WindowState','maximized');
        comparison_plot_settings=gca;
        comparison_plot_settings.FontSize=font_size;

        hold on;
        plot(frequency_sim,smooth(TL_sim_avg,smoothing_factor_sim),'b');
        plot(frequency_sim,smooth(TL_sim_lower_bound,smoothing_factor_sim),'r');

plot(frequency_sim,smooth(TL_sim_upper_bound,smoothing_factor_sim),'r','HandleVisibility','
off');

        xlim([lower_plot_limit,ending_freq]);
        ylim([TL_min,TL_max])
        xlabel('Frequency (Hz)','fontsize',font_size);
        ylabel('Transmission Loss (dB)','fontsize',font_size);
        grid on;
        legend_labels=["Mean Simulation","Simulation Bounds (1 std dev)"];
        legend(legend_labels,'location','eastoutside','fontsize',font_size);


    %%Save Figure as JPG
        filename=jpeg_name(i)+" Sim Data.jpg";
        saveas(figure(1),filename);
```

```
    close all

  %%clear variables
  clear ch1_full_test ch2_full_test ch1_test ch2_test frequency_full_test TL_full_test
tau_full_test input_sim_all_runs output_sim_all_runs input_sim output_sim frequency_sim
TL_sim_avg TL_sim_std_dev tau_sim_lower_bound
 end
```

A-9 Test and Simulation Comparison

```
%%This script was generated to plot selected test runs and compare with
%%simulation results
%%2 channels, 1 in and 1 out
%%White noise only, 10s duration
%%Brittany Griffin, 2020



clc
clear
close all
close all hidden

%%Make sure these are correct%%
   sample_rate=100000;
   pretrigger_time_input=0; %msec

%Step Counts
   time_step=1/sample_rate;
   white_noise_steps=10*sample_rate; %%10 sec

%%Pretriggger
   pretrigger_time=pretrigger_time_input*10^-3;
   starting_index=pretrigger_time*sample_rate+1;

%%File Indexes
   start_index=starting_index;
   end_index=start_index+white_noise_steps;
```

```
%%Constants
   P0=20*1e-6; %reference pressure [Pa]

%%Master matrix and define variables
      test_matrix= ["Panel"," MIMO Straight Pipe ","Panel_0016","MIMO_SP";"Panel"," Base
Feature AMM","Panel_0020","MIMO_No_MM";"Panel"," Large Cavity
AMM","Panel_0026","MIMO_Large_MM";"Panel"," Small Cavity
AMM","Panel_0032","MIMO_Small_MM";"Non Uniform Input"," SISO Straight
Pipe","LB_001","SISO_SP";"Non Uniform Input"," Straight Pipe with Radial
Perforations","LB_003","SISO_SP_MH";"Non Uniform Input"," Converging
Nozzle","LB_005","SISO_CN";"Non Uniform Input"," Diverging
Nozzle","LB_004","SISO_DN";"Non Uniform Input"," Diverging Nozzle with Radial
Perforations","LB_008","SISO_DN_MH";"Non Uniform Input"," Series Diverging
Nozzles","LB_0010","SISO_SDN";"Non Uniform Input"," Series Diverging Nozzles with Radial
Perforations","LB_0014","SISO_SDN_MH";"Non Uniform Input"," Series Diverging Nozzles with
Radial and Axial Perforations","LB_0018","SISO_SDN_MH_PMH";"Non Uniform Input"," Series
Diverging Nozzles with Radial and Axial Perforations and Constricted Opening at
Output","LB_0022","SISO_SDN_MH_PMH_PP"];
      display_list=[test_matrix(:,1)+"     "+test_matrix(:,2)];

%%User selects runs for comparison
   [selected_runs]=listdlg('ListString',display_list,'ListSize',[750 500],'name','Available
Data','PromptString','Select the Configuration for Comparison');
   number_of_runs=size(selected_runs);
   number_of_runs=number_of_runs(2);

%%Automate File names and graph titles
   files_to_import_test=test_matrix(selected_runs,3);
```

```
    files_to_import_sim=test_matrix(selected_runs,4)+"_combined";
    jpeg_name=test_matrix(selected_runs,2);
    graph_title=jpeg_name;

%%Automate Plot Limits for SISO and MIMO
    if test_matrix(selected_runs,1)=="Non Uniform Input"
        lower_plot_limit=250;
    else
        lower_plot_limit=2000;
    end

% lower_plot_limit=20;

%%Plot Limits
    smoothing_factor_test=250;
    smoothing_factor_sim=20;
    tau_min=-.1;
    tau_max=1.1;
    TL_min=-15;
    TL_max=100;

%%Bandwidths of Interest
    starting_freq=20;
    ending_freq=20000;

    freq_matrix=[20,5000;5000,10000;10000,15000;15000,20000];
    number_of_freq_bands=size(freq_matrix);

   for i=1:number_of_runs
```

```
%%%%Test Data
    %%Import Data
        import_file_name_test=files_to_import_test(i)+".txt";
        run_data_test=importdata(import_file_name_test);
        ch1_full_test=run_data_test(:,1);
        ch2_full_test=run_data_test(:,2);

    %%Crop file
        ch1_test=ch1_full_test(start_index:end_index);
        ch2_test=ch2_full_test(start_index:end_index);

    %%Calculate FFT
        nfft1=length(ch1_test);
        FFT_ch1_temp=fft(ch1_test,nfft1)/nfft1;
        index1=round(nfft1/2);
        FFT_ch1=FFT_ch1_temp(1:index1);
        f_ch1=abs(FFT_ch1);

        nfft2=length(ch2_test);
        FFT_ch2_temp=fft(ch2_test,nfft2)/nfft2;
        index2=round(nfft2/2);
        FFT_ch2=FFT_ch2_temp(1:index2);
        f_ch2=abs(FFT_ch2);

    %Calculate Frequency Vector
        frequency_full_test=sample_rate*(0:(nfft1/2))/nfft1;
        frequency_full_test=frequency_full_test';

    %Convert Calculate Tau and Transmission Loss
```

```
    y=size(f_ch1);
    y=y(1);

  %Preallocate for speed
    tau_full_test=zeros(1,y);
    TL_full_test=zeros(1,y);

  %%Transmission Coefficient and Loss
    for j=1:y
      tau_full_test(j)=(f_ch2(j)^2)/(f_ch1(j)^2);
      TL_full_test(j)=-10*log10(tau_full_test(j));
    end

  %%Find index of Bandwidth
    steps_in_a_Hz=round(2*(length(frequency_full_test))/sample_rate);
    BW_start_index=starting_freq*steps_in_a_Hz+1;
    BW_ending_index=ending_freq*steps_in_a_Hz+1;

  %%Crop vectors
    frequency_test=frequency_full_test(BW_start_index:BW_ending_index);
    tau_test=tau_full_test(BW_start_index:BW_ending_index);
    TL_test=TL_full_test(BW_start_index:BW_ending_index);

%%%%Sim Data
  %%Import Data
    import_file_name_sim=files_to_import_sim(i)+".txt";
    run_data_sim=importdata(import_file_name_sim);
    frequency_sim=run_data_sim(:,1);
    number_of_analysis_runs=size(run_data_sim);
```

```
    number_of_analysis_runs=(number_of_analysis_runs(2)-1)/2;

    for x=1:number_of_analysis_runs
      input_sim(:,x)=run_data_sim(:,x);
      y=x+number_of_analysis_runs;
      output_sim(:,x)=run_data_sim(:,y);
    end

  %%Transmission Coefficient and Loss
    length_of_sim_vector=size(input_sim);

    for k=1:length_of_sim_vector(2)
      for j=1:length_of_sim_vector(1)
        tau_sim(j,k)=(output_sim(j,k)^2)/(input_sim(j,k)^2);
        TL_sim(j,k)=-10*log10(tau_sim(j,k));
      end
    end

    for m=1:length_of_sim_vector(1)
      tau_sim_avg(m)=mean(tau_sim(m,:));
      TL_sim_avg(m)=mean(TL_sim(m,:));
      TL_sim_std_dev(m)=std(TL_sim(m,:));
    end

%%%%Bounds
  TL_sim_entire_avg=mean(TL_sim_avg);
  TL_sim_lower_bound=TL_sim_avg-TL_sim_std_dev;
  TL_sim_upper_bound=TL_sim_avg+TL_sim_std_dev;
```

```
    %%%%Comparison Plot Matrix and export to table
      for k=1:number_of_freq_bands(1)
      %%Define Bands
        comparison_starting_freq=freq_matrix(k,1);
        comparison_ending_freq=freq_matrix(k,2);

        %%Test
          BW_start_index_compare=comparison_starting_freq*steps_in_a_Hz+1;
          BW_ending_index_compare=comparison_ending_freq*steps_in_a_Hz+1;

        %%Sim
          sim_start_index=find(comparison_starting_freq==frequency_sim);
          sim_end_index=find(comparison_ending_freq==frequency_sim);

        %%Crop tau and TL vectors

TL_compare_test=TL_full_test(BW_start_index_compare:BW_ending_index_compare);

tau_compare_test=tau_full_test(BW_start_index_compare:BW_ending_index_compare);
          tau_compare_sim=tau_sim_avg(sim_start_index:sim_end_index);
          TL_compare_sim=TL_sim_avg(sim_start_index:sim_end_index);

        %%Find Averages and write to matrix
          tau_avg_test=mean(tau_compare_test);
          TL_avg_test=mean(TL_compare_test);
          display_tau_table_data_test(k,1)=tau_avg_test;
          display_TL_table_data_test(k,1)=TL_avg_test;

          tau_avg_sim=mean(tau_compare_sim);
```

```
            TL_avg_sim=mean(TL_compare_sim);
            display_tau_table_data_sim(k,1)=tau_avg_sim;
            display_TL_table_data_sim(k,1)=TL_avg_sim;
        end

        %Average Values
           TL_test_entire_avg=mean(TL_avg_test);
           TL_sim_entire_avg=mean(TL_avg_sim);

        %%Export to table

export_table=[display_TL_table_data_test,display_TL_table_data_sim;TL_avg_test,TL_avg_sim]
;
           xlswrite('Test and Sim Comparison',export_table',i);

     %%%%Plots
        font_size=14;

        figure(1),chart_title=["Test and Simulation Data - Transmission Loss Comparison -
"+jpeg_name(i)];
        figure(1),sgtitle(chart_title,'fontsize',font_size+4,'FontWeight','bold');
        figure(1),set(gcf,'WindowState','maximized');

        plot(frequency_test,smooth(TL_test,smoothing_factor_test),'b');
        hold on;
        plot(frequency_sim,smooth(TL_sim_avg,smoothing_factor_sim),'g');
        plot(frequency_sim,smooth(TL_sim_lower_bound,smoothing_factor_sim),'r');

plot(frequency_sim,smooth(TL_sim_upper_bound,smoothing_factor_sim),'r','HandleVisibility','
```

```
off');

    xlim([lower_plot_limit,ending_freq]);
    ylim([TL_min,TL_max])
    xlabel('Frequency (Hz)','fontsize',font_size);
    ylabel('Transmission Loss (dB)','fontsize',font_size);
    grid on;
    legend_labels=["Test Data","Mean Simulation","Simulation Bounds (1 std dev)"];
    legend(legend_labels,'fontsize',12,'location','eastoutside','fontsize',font_size);

    comparison_plot_settings=gca;
    comparison_plot_settings.FontSize=font_size;

  %%Save Figure as JPG
    filename=jpeg_name(i)+" Test and Sim Comparison.jpg";
    saveas(figure(1),filename);
    close all

  %%clear variables
  clear ch1_full_test ch2_full_test ch1_test ch2_test frequency_full_test TL_full_test
tau_full_test input_sim_all_runs output_sim_all_runs input_sim output_sim frequency_sim
TL_sim_avg TL_sim_std_dev tau_sim_lower_bound
 end
```